

**LOW COHERENCE FIBRE OPTIC FABRY-PEROT SENSORS SUITABLE  
FOR MULTIPLEXED STRAIN MEASUREMENT**

A thesis submitted

by

**Kaddu Ssenyomo Charles**

for the degree of

**DOCTOR OF PHILOSOPHY**



Department of Applied Physics

Victoria University

1995

## **DECLARATION**

I, **Kaddu S Charles**, declare that the thesis titled,

**Low Coherence Fibre Optic Fabry-Perot Sensors Suitable for Multiplexed Strain Measurement**

is my own work and has not, been submitted previously, in whole or in part, in respect of any other academic award.



**Kaddu S Charles**

dated the 11th day of December, 1995.

## **ACKNOWLEDGEMENTS**

I wish to thank my supervisors, Professor David Booth and Dr. Stephen Collins for their constant guidance, useful comments, suggestions and discussions in all aspects of this research. I am also grateful to Dr. Jakub Szajman and Dr. Leo Cussen for their assistance in the vacuum laboratory. I wish also to extend my thanks to all other academic staff, technical staff, administrative staff and fellow post-graduate students in the department of Applied Physics for their love and assistance. Special thanks to Darol Garchev for all the time put in during the fabrication of in-fibre Bragg grating-based Fabry-Perot interferometers. I am also indebted to Olex Cables for the BIT fusion splicer.

Finally a lot of thanks to my wife Kaddu Jane, my sons ; Kaddu Ronald, Kaddu Ivan and Kaddu Daniel for their constant support, encouragement and inspiration during the period of this research in Australia away from my family.

## **ABSTRACT**

This thesis contains an investigation of the potential of low finesse in-fibre Fabry-Perot interferometer sensors for the measurement of strain. There are a number of areas of modern engineering applications where there is a need for an alternative to conventional resistive strain gauges; particularly where a number of such sensors can be multiplexed onto a common carrier so that one system can be used for multi-point strain measurements. Hence, the emphasis is on low finesse sensors which are suitable for multiplexing.

This thesis concentrates on the use of white light interferometer (WLI) techniques to measure the optical path changes produced in the sensors by the application of strain. Since thermal effects also produce phase changes in the fibre Fabry-Perot interferometer (FFPI) which are undistinguishable from strain changes the investigations have included both thermal and strain responses of the sensors.

An analysis is presented of the methods which can be used to determine the centre of the WLI pattern and the signal-to-noise required for reliable identification of this centre. This analysis is then extended to predict the performance of multiplexed systems and define the optimum reflectivity for  $n$  identical serially multiplexed sensors.

Two approaches were investigated for making low finesse fibre Fabry-Perot systems. The first was based on internal dielectric mirrors and fusion splicing techniques and the second involved

the use of in-fibre Bragg gratings as reflectors. For both cases manufacturing techniques are described in detail.

Structural strain monitoring using optical fibre strain sensors requires a sensor with high tensile strength. For sensors made using dielectric coatings and fusion splicing this necessitated the development of techniques for coating only the core region of the fibre and also for splice strengthening by annealing using a CO<sub>2</sub> laser.

Experimental measurements have been made for strain and temperature sensing using single and multiplexed fusion spliced sensors. These measurements have been combined with modelling to predict the maximum number of sensors which can be serially multiplexed given practical values of sensor parameters, launched power from the source, receiver optical efficiency and system noise.

The need to find sensors with improved tensile properties led to the development of a totally new type of low coherence fibre Fabry-Perot sensor based on multiple independent Fabry-Perot interferometers, using grating pairs at different wavelengths with the same grating spacing. These multiple FFPI sensors are almost overlapping in the fibre and so the sensor has a total length only slightly longer than the grating spacing. The reflected light from these complex grating structures forms a synthetic low coherence source which can have greatly improved coherence properties compared to the reflection from a FFPI consisting of a single grating pair.

The performance of these multiple grating-based FFPI sensors has been modelled and experimental measurements are presented with dual and triple FFPI sensors to confirm the predictions.

<b>Contents</b>	<b>Page</b>
<b>Chapter 1 Introduction</b>	1.1
1.1 Aims of the research	1.6
1.2 Content summary	1.8
<b>Chapter 2 Optical fibre sensor systems</b>	2.1
2.1 Light sources	2.2
2.1.1 Semiconductor sources	2.2
2.1.2 Incandescent lamps and lasers	2.3
2.2 Optical fibres	2.4
2.3.1 Properties of optical fibres	2.5
2.3.2 Intrinsic loss mechanisms in optical fibres	2.8
2.4 Light detectors	2.11
2.5 Sensor limitations	2.12
2.6 Conclusion	2.14
<b>Chapter 3 Review of strain measurement techniques</b>	3.1
3.1 Introduction to strain	3.1
3.2 Conventional methods of strain measurement	3.4
3.2.1 Mechanical strain gauges	3.5
3.2.2 Acoustic strain gauges	3.5
3.2.3 Electrical strain gauges	3.7
3.2.3.1 Inductance strain gauges	3.7
3.2.3.2 Capacitance strain gauges	3.7
3.2.3.3 Resistance strain gauges	3.8
3.2.4.4 Semiconductor strain gauges	3.10
3.2.4.5 Summary of conventional strain measurement techniques	3.10
3.3 Optical fibre strain sensing	3.11
3.3.1 Microbend strain gauge	3.12
3.3.2 Interferometric strain gauges	3.13

	3.4	Conclusion	3.25
<b>Chapter 4</b>		<b>Multiplexed interferometric fibre optic sensors</b>	4.1
	4.1	Frequency division multiplexing	4.1
	4.2	Time-division multiplexing	4.3
	4.3	Wavelength division multiplexing	4.5
	4.4	Polarisation multiplexing	4.6
	4.5	Coherence multiplexing	4.7
	4.5.1	Introduction to WLI	4.8
	4.5.2	WLI multiplexed sensors	4.10
	4.6	Conclusion	4.11
<b>Chapter 5</b>		<b>Development of intrinsic fibre Fabry-Perot sensors</b>	5.1
	5.1	Fabrication process	5.1
	5.1.1	Background	5.1
	5.1.2	Basic considerations	5.6
	5.1.3	Monitor design and operating principles	5.7
	5.1.4	Monitoring of the deposition of titanium films	5.10
	5.1.5	Monitoring of sputter deposition of TiO <sub>2</sub>	5.12
	5.1.6	Comparison of optical fibre thickness monitor with a quartz crystal monitor	5.15
	5.1.7	Conclusion	5.17
	5.2	Refractive index of titanium dioxide film	5.17
	5.3	Entire face coated intrinsic FFPI cavities and results	5.21
	5.3.1	Core region only coated FFPI	5.23
	5.3.2	Fusion spliced fibre Fabry-Perot sensors	5.25
	5.3.3	Annealing of fusion spliced FFPI cavities and results	5.26
	5.4	Conclusion	5.28
<b>Chapter 6</b>		<b>Predicted performance</b>	6.1

6.1	Reflection transfer function of a fibre Fabry-Perot interferometer (FFPI)	6.2
6.2	Thermal properties of the FFP sensor	6.5
6.3	FFPI strain response	6.6
6.4	Apparent strain analysis	6.10
6.5	White light interferometry (WLI)	6.12
6.5.1	WLI sensing with multimode laser diodes	6.13
6.5.2	Central fringe determination	6.16
6.5.3	Chi-squared fitting	6.19
6.5.4	Centre of the central fringe	6.21
6.6	Modelling of multiplexed system performance	6.22
6.6.1	Interferometer transfer function	6.24
6.6.2	Multiplexed sensors	6.28
6.7	Conclusion	6.36

**Chapter 7 Experimental measurements with fusion-spliced  
sensors** 7.1

7.1	measurements with one sensor	7.1
7.1.1	Thermal characteristics of the FFPIs	7.1
7.1.2	Thermal results	7.2
7.1.3	Results for static strain	7.4
7.2	Summary of temperature and strain measurements	7.6
7.3	White light interferometry measurements	7.7
7.3.1	WLI measurements with a single FFPI sensor	7.7
7.3.2	Experimental arrangement for temperature measurement	7.7
7.3.3	Central fringe determination	7.9
7.3.4	Computer simulations	7.9

7.3.5	Experimental results	7.13
7.3.6	Temperature measurements	7.15
7.3.7	Static strain measurements	7.18
7.3.7.1	Correction for thermally induced strain	7.20
7.3.7.2	Static strain results	7.22
7.4	Conclusion	7.22
7.5	Measurements with low coherence multiplexed fusion-spliced FFPI sensors	7.23
7.5.1	Introduction	7.23
7.5.2	Temperature measurements	7.25
7.5.2.1	Experimental arrangement	7.25
7.5.2.2	Signal processing and results	7.26
7.6	Static strain measurements	7.28
7.6.1	Experimental arrangement and results	7.28
7.7	System limitation	7.32
7.8	Conclusion	7.38
<b>Chapter 8</b>	<b>Grating fibre Fabry-Perot interferometers</b>	<b>8.1</b>
8.1	Bragg grating writing techniques	8.5
8.2	Holographic technique	8.6
8.3	Phase mask technique	8.7
8.4	Characteristics of in-fibre Bragg gratings	8.8
8.5	Temperature or strain characteristics of a Bragg grating sensor	8.10
8.6	Bragg grating characterisation	8.11
8.6.1	Thermal sensitivity of IFBG	8.11
8.6.2	Static strain sensitivity of IFBG	8.14
8.7	Fabrication of dual FFP pairs based on Bragg gratings	8.15
8.7.1	Fabrication results	8.18

8.7.2	Predicted performance of a dual FFP interferometer based on Bragg gratings	8.20
8.7.3	Computer simulations	8.24
8.7.4	Experimental results	8.31
8.7.5	Results with triple FFPI sensor	8.33
8.7.6	Mechanical strength of grating sensors	8.36
8.7.7	Conclusion	8.37
<b>Chapter 9</b>	<b>Conclusion and future work</b>	9.1
9.1	Conclusion	9.1
9.2	Future work	9.4
<b>References</b>		R1
<b>Publications resulting from this thesis</b>		P1
<b>Symbols and acronyms</b>		S1

## CHAPTER 1

### INTRODUCTION

Fibre optic strain sensors have significant potential for the testing and surveying of various structures in mechanical and civil engineering [Fuhr *et al.*, 1992; Escobar *et al.*, 1992]. Examples include glass fibre reinforced anchors, stress monitoring in the evaluation of the structural integrity of buildings, bridges, dams, storage tanks or prestressed elements. These optical strain sensors will have to provide broad dynamic range, high strain resolution and, in certain applications, absolute measurements (e.g. for quasi-static strain measurements [Ohba *et al.*, 1989]). The sensors may be embedded within or surface bonded to the structure and can monitor the material not only throughout its initial processing but also during long term use. Therefore the development of reliable fibre optic sensors and their integration within a structure (composite) is important for the further development of smart structures. These have been discussed by many authors [Udd, 1989; Measures, 1990].

To be successful, these optical fibre monitoring sensor systems will require reliable and high performance sensors. Optical fibre sensors have a number of unique advantages over conventional sensors that make them extremely amenable to monitoring of several parameters. These advantages, in particular, include small size and light weight, capacity to withstand harsh

operating temperatures and pressures, immunity to electromagnetic interference, ability to lend themselves to multiplexing, compatibility with composite materials, and an all passive, all dielectric configuration. The small size of optical fibres allow them to be consolidated into composite materials, usually without degrading structural integrity. The feature of immunity from electromagnetic interference reduces the need for shielding and greatly lowers cost, while their dielectric nature avoids the possible creation of electrical pathways when embodied within structures. Optical fibres as sensing elements have been developed and used to monitor parameters, including strain [Butter and Hocker, 1978], temperature [Hocker, 1979], magnetic and electric fields [Dakin *et al.*, 1977], acoustic vibrations [Alcoz *et al.*, 1990], chemical concentration [Jackson, 1985], by determining changes in optical intensity, phase, polarisation, wavelength, pulse propagation time or modal content.

Optical fibre interferometric sensors using highly coherent sources have received most attention for scientific and industrial applications due to their high resolution. However, these sensors face some drawbacks including limited unambiguous measurement range (which, for normal interferometric sensors, can only be determined to within one period of the interferometer transfer function) and the requirement for highly stabilised sources. These sensors have had only limited application in monitoring strain, displacement and temperature because of their lack of self initialisation. For example, if there is any interruption to the interferometer (by, say, turning off the power) all the gathered information is lost and new initial conditions must be determined when the power is reconnected. These shortcomings may be overcome by the use of white light interferometry (WLI) which employs a low coherence source. This is discussed further in section 4.5.1.

The usefulness of optical fibres in sensor systems may be enhanced if multiplexed or quasi distributed configurations are adopted, since information can be obtained from several sites using a single instrumentation system. This is particularly attractive for large composite

structures like hulls of boats or aircraft wings for which strain or other measurands need to be monitored over a large area. Optical fibre sensors can be multiplexed by methods which are not possible with conventional measurement systems and successful multiplexing is essential if a cost-effective structural sensor monitoring system is to be developed. A consideration of multiplexed performance is an important part of the analysis of the sensors developed during this investigation.

Of particular interest in this thesis is the construction of a multiplexed optical fibre sensor system for the measurement of strain using white light interferometry. This sensor system could also be useful in monitoring temperature. Such an optical fibre strain sensor would be the optical equivalent of an electrical resistive strain gauge. Electrical strain gauges are the primary means of measurement in stress analysis. Although these gauge types work reliably in a large range of applications, the increased use of new materials (like composites) and use of materials in an extended range of environments (including high and low temperature environments) leaves room for a range of alternative gauges that are more compatible with these materials and unaffected by these environments. Resistance strain gauges employ thin film metallic foils in the form of folded grids, and are bonded with a suitable adhesive to the structure for which strain measurements are required [Neurbert, 1967]. These gauges are thin, fragile, may be difficult to handle and cannot be multiplexed easily. Proper and careful bonding procedures of these electrical gauges is essential (which at times may be cumbersome and time consuming) if the integrity of these gauges is to be maintained over long periods and large temperature variations. Unfortunately existing electrical strain gauges are vulnerable to electromagnetic interference; this necessitates that they be shielded, thus making them expensive and possibly significantly altering the overall integrity and weight of the monitored structure. The optical sensor system developed here allows several sensors on a single strand of single mode optical fibre with no requirement for shielding.

The ultimate goal of strain sensing has been the measurement of an arbitrary state of strain. In practical strain gauging, the magnitudes and directions of the principal strains and stresses are unknown. These have been obtained by taking three independent strain measurements using three or four resistive strain gauges [Neurbert, 1967] which are arranged at different angles to each other, forming the strain rosette. Such a resistive strain rosette has to be screened from electromagnetic interference. The analogue of this, namely an optical fibre strain rosette based on a Fabry-Perot interferometer has been reported [Valis *et al.*, 1990] and does not require shielding as it simply uses four dielectric optical fibres. This efficient integrated optical sensor has fewer optical components and hence the operational costs may be lower.

Using single-mode optical fibres, the two interferometric configurations which have been studied extensively for strain applications are the Michelson [Measures, 1990; Valis *et al.*, 1991] and Mach-Zehnder types [Hocker, 1979; Sirkis, 1988]. These have shown good strain sensitivity. However neither of these methods offer both high resolution and the ability to measure the parameter of interest in a highly localised region of the structure. These sensors are unable to be deployed in an array on a single fibre; neither do they possess the self referencing property which is vital in ensuring a practical sensor.

When measurement of strain over several sites of a structure is performed using conventional technology, it is necessary to festoon the structure with a multitude of strain gauges. This presents multiplexing and calibration problems. Optical fibre technology provides a simpler method for gathering data from many points, with negligible crosstalk. An early attempt at strain monitoring in structures using optical fibre Mach-Zehnder interferometers suffered from lack of localisation, and failed to give the absolute value of the measurand [Rowe *et al.*, 1986; Sirkis, 1988]. These requirements (localisation and initialisation), along with the need to multiplex several sensors on single strand of fibre sharing the same optoelectronics, are of paramount importance if these devices are to play a major role as reliable and accurate sensors.

The advantages of multiplexed fibre optic sensor systems in a number of application areas have been recognised [Brooks *et al.*, 1985; Dakin, 1987; Kersey and Dandridge, 1988]. However, these schemes have been limited by high levels of excess induced noise [Brooks *et al.*, 1985]. In other instances the measurements were hampered by low phase detection sensitivity and the sensing scheme required long lengths of delay fibres [Brooks *et al.*, 1987] which may cause some practical difficulties. An intrinsic multiplexed scheme [Kersey and Dandridge, 1986] suffered from high levels of optical cross-talk arising from multiple reflections occurring in the system. Better multiplexing approaches are desirable for performance and cost reasons. The need to devise an optical fibre sensor system that can be used reliably and be able to offer absolute measurements when applied to a structure is a major challenge in optical strain gauge development. The performance of such a sensor system has to be comparable to, or even better than, the conventional resistive strain gauge. It is useful therefore to consider the criteria for multiplexing of sensors and of modern strain gauge measurement, so that the practical requirements can be fulfilled.

The overall capacity of a sensor network to gather information is limited by the bandwidth and signal-to-noise ratio of detected optical signals and the need to avoid undesirable cross modulation between signals from apparently independent sensors. The choice of a suitable fibre optic multiplexing scheme has to take into account, among other factors, the method of separating each sensor's information from the single data stream, the number of addressable sensors for the proposed scheme and the allowable cross talk level [Brooks *et al.*, 1985; Kersey, 1988b].

Furthermore, for optical fibre strain gauges to be competitive with conventional strain sensors, it is logical to base the suitability of optical fibre strain sensors on the existing standards of strain gauging [Neubert, 1967; Handerek *et al.*, 1992]. These require that, in order for the gauge to be applied in inaccessible areas, it ought to have a small size and be of low weight, so

as not to significantly alter the mass of the monitored structure. It is desirable that the gauge have minimal temperature sensitivity while exhibiting a high strain sensitivity. The gauges are normally surface bonded or embedded within structures, and should be able to monitor the structure when it is subjected to a time-varying stress, without experiencing fatigue. The gauge should possess the feature of remote sensing which gives the possibility of conducting measurements in the laboratory and external environments. The gauge assembly should allow easy, demountable, secure connection to a signal processing unit located remotely from the sensor assembly. The strain gauge should have a straightforward attachment to the structure, so that lengthy procedures which require specialised expertise are not necessary.

These are very exacting requirements which cannot be satisfied by a single sensor which can operate in all situations and environments. Thus it is necessary to develop a variety of sensors which can perform adequately in a limited range of situations. The sensor and sensing techniques investigated in this thesis represents one of these possibilities. The work involves construction techniques of the sensor, and an investigation of its performance and limitations.

### **1.1 Aims of the research**

The aims of the research were to:

- fabricate an optical fibre sensor suitable for the measurement of strain, and
- evaluate the performance of the strain sensor when used in a suitable multiplexed system.

In order to meet the aforementioned requirements of both multiplexing and strain gauging, a sensor had to be sought which provided an attractive alternative to the resistive strain gauge.

as not to significantly alter the mass of the monitored structure. It is desirable that the gauge have minimal temperature sensitivity while exhibiting a high strain sensitivity. The gauges are normally surface bonded or embedded within structures, and should be able to monitor the structure when it is subjected to a time-varying stress, without experiencing fatigue. The gauge should possess the feature of remote sensing which gives the possibility of conducting measurements in the laboratory and external environments. The gauge assembly should allow easy, demountable, secure connection to a signal processing unit located remotely from the sensor assembly. The strain gauge should have a straightforward attachment to the structure, so that lengthy procedures which require specialised expertise are not necessary.

These are very exacting requirements which cannot be satisfied by a single sensor which can operate in all situations and environments. Thus it is necessary to develop a variety of sensors which can perform adequately in a limited range of situations. The sensor and sensing techniques investigated in this thesis represents one of these possibilities. The work involves construction techniques of the sensor, and an investigation of its performance and limitations.

### **1.1 Aims of the research**

The aims of the research were to:

- fabricate an optical fibre sensor suitable for the measurement of strain, and
- evaluate the performance of the strain sensor when used in a suitable multiplexed system.

In order to meet the aforementioned requirements of both multiplexing and strain gauging, a sensor had to be sought which provided an attractive alternative to the resistive strain gauge.

The two optical fibre sensors which exhibit both high sensitivity and localised measurements are the intrinsic fibre Fabry-Perot interferometer (FFPI) and in-fibre Bragg grating sensors. In-fibre Bragg gratings (IFBGs) are currently used for a variety of sensing applications [Meltz *et al.*, 1989; Morey *et al.*, 1994] and in development of a range of devices including, optical filters and Fabry-Perot filters [Morey *et al.*, 1992]. These devices are attractive for sensing applications due to their intrinsic nature and wavelength-encoded operation. The wavelength encoding is an absolute parameter, a feature that is useful for quasi-static measurements. In this thesis the concentration has been on FFPI sensors. IFBGs have been used, as described later, but only to construct one type of FFPI. If IFBGs are made to form an intrinsic FFPI gauge then the device formed has the potential to realise an FFPI gauge with high mechanical strength. The useful characteristics of the intrinsic FFPI gauges include:

- Light is guided within the fibre. This ensures robustness as optical alignments are insensitive to external influences.
- The possible range of FFPI gauge length (a few millimetres to several centimetres) allows the fabrication of sensors which span the measurement range of available resistive gauges (0.2 mm - 102 mm, [Dally and Riley, 1978]).
- The gauge diameter does not exceed that of the fibre itself. This allows the easy embodiment of strain sensors within the composite material.
- An intrinsic optical FFPI gauge offers lead insensitivity since light is guided to and from the sensor within the same fibre.
- An FFPI optical fibre gauge is amenable to serial multiplexing because it is a single fibre and can be addressed from one end.

- The Fabry-Perot fibre optic strain sensor has the unique ability of being easily embodied within composite materials, whereas resistive strain gauges normally require a surface for attachment.
- The gauge can be coated with suitable material to protect the fibre from moisture absorption [Mason *et al.*, 1992].

The construction and practical demonstration of a multiplexed optical fibre Fabry-Perot sensor system for the measurement of strain using white light interferometry is described in this thesis. Two approaches were investigated in making low finesse fibre Fabry-Perot interferometers, one is based on a dielectric coating and fusion splicing technique, the other on Bragg grating reflectors configured to make an FFPI. A multimode laser diode or a super-luminescent diode as low coherence sources were used, one for the fusion spliced FFPI sensor measurements and other for Bragg grating-based FFP sensor measurements. The sensor elements were fabricated using a single-mode fibre (Corning Flexcore 780, 5/125  $\mu\text{m}$ ). An absolute measurement is achieved through self-calibration, and each time the system is turned on self calibration is executed. A single receiver interferometer at the output selectively reconstructs the interference associated with individual sensors when its optical path difference is tuned to match that of each sensor (to within the coherence length of the source). The sensing scheme used in this research took advantage of the principle of white light interferometry which has important advantages over other methods in overcoming problems of measurement ambiguity and intensity fluctuations. It offers extended unambiguous measurement range and has the ability to determine absolute path imbalances. The combination of white light interferometry and intrinsic multiplexed fibre Fabry-Perot sensors offers a multiplexed sensor system having the additional features of localisation and lead insensitivity.

## 1.2 Content summary

Chapter 2 gives a short introduction to the optical fibre sensing system by considering the general optical fibre sensor requirements and the basic components of such a measurement system. Chapter 3 looks at the progress that has been achieved with optical methods and non-optical alternatives for the measurement of strain. A discussion of optical fibre temperature sensors is also given in this chapter since the fibre Fabry-Perot (FFP) sensor is also sensitive to temperature. In chapter 4 a brief discussion on the various interferometric multiplexed optical fibre sensing schemes is presented, with an indication of the progress of these multiplexed sensor systems. Chapter 5 gives details of the process which has been used for fabrication of the intrinsic fibre optic Fabry-Perot sensors, which involved a vacuum deposition technique followed by fusion splicing. It is apparent from the attention given to optimal fusion parameters that care has to be taken in choosing the proper coating films. This is followed by the predicted performance of these sensors with a calculation of their thermal and strain sensitivities in chapter 6. The sensors' co-dependency on temperature and strain presents problems when monitoring static strain. This results in a change in phase of light propagating along a structurally integrated optical fibre subject to a change in temperature but without any applied force, and this effect is termed 'thermally induced strain'. A method used to minimise thermally induced strain is also analysed. White light interferometric sensing using multimode laser diode sources is discussed. An analytical model which predicts the maximum possible number of in-line FFP sensors that can be serially multiplexed using low coherence demodulation is also given in this chapter. This is followed by the results obtained with both single sensor and multiplexed sensor measurements of temperature and strain, which are reported in chapter 7. This chapter includes a comparison of experimental results with the analytical model given in chapter 6. System limitations are discussed to appraise the overall sensing scheme and system

performance. A new technique used to construct a “dual/triple FFPI” sensor based on in-fibre Bragg grating reflectors and the measurements obtained with this sensor using low coherence interferometry are discussed in chapter 8. This technique could be a promising alternative for use for certain applications including high stress monitoring. Finally, chapter 9 gives the final conclusion for this thesis together with suggestions for future work.

## CHAPTER 2

### OPTICAL FIBRE SENSOR SYSTEMS

An optical fibre sensing system in its basic form consists of an optical source, an optical fibre link, a sensor (modulator) and a detector. For measurement purposes, the light propagating within the fibre will be characterised by one or more features such as intensity, phase, pulse propagation time, wavelength or polarisation. The parameter to be measured (measurand) modulates one or more of the aforementioned properties of light, and this modulated light is collected by the same or different fibre and returned to the detector where it is converted to an electrical signal. Light modulation can occur within the fibre itself, where it is directly modulated by the measurand. Such a sensor is called *intrinsic* and examples include temperature measurement using an in-fibre Bragg grating sensor [Wosinski *et al.*, 1994] and strain measurement using a fibre Michelson interferometer [Valis *et al.*, 1991]. Alternatively in an *extrinsic* sensor the optical fibre may simply guide light to and from a location at which an optical sensor head is located, as in liquid flow detection [Nguyen *et al.*, 1984]. Extrinsic sensors suffer from low efficiency because of light losses and also tend to be bulky and fragmented in nature. Intrinsic sensors, on the other hand, have the advantage of high sensitivity and versatility, and also high stability since light is contained in the fibre and no special sensor heads are required. In the following sections the basic components of optical fibre sensors are discussed.

## 2.1 Light sources

The sensing system contains an appropriate light source having spatial and spectral power distribution  $S(x, y, z, \lambda)$ . The power distribution is typically symmetrical around the central wavelength,  $\lambda$ , with a full width at half maximum,  $\Delta\lambda$ . The coherence length of such a source  $l_c$  is given approximately by [Culshaw and Dakin, 1988]  $l_c \approx \lambda^2/\Delta\lambda$ . Typical optical fibre sensor light sources are semiconductor sources (light emitting diodes (LEDs), superluminescent diodes (SLDs), laser diodes), incandescent lamps and highly coherent lasers (gas, ion, solid state).

### 2.1.1 Semiconductor sources

Semiconductor sources are the primary optical sources used for communication and sensor applications. Their small size and configuration, which allow for efficient launching of light into optical fibres, long life, relatively low cost and low power consumption and significant optical output power has given them prominence over alternative sources. Semiconductor optical sources are forward biased p-n junctions which emit light through electron-hole pair recombination radiative processes. These devices exist in two different forms having different optical properties, the basic device being the light emitting diode and the other the laser diode.

The LED relies on spontaneous emission as a means of photon generation. The optical output power generated by the LED ideally varies linearly with the forward driving current [Gloge, 1977]. However with increased temperature the optical output power decreases and a change in spectral emission towards longer wavelength is observed [Bergh and Dean, 1976]. LEDs have a poor coupling efficiency into single mode fibre due to their relatively large emitting areas. Typical line-widths of LEDs operating in the region of 800 - 900 nm at room temperature, are between 25 and 50 nm while those of LEDs emitting in longer wavelength regions is between 50 and 160 nm [Senior, 1992]. Two types of devices have been designed for high radiance,

namely the surface emitting LED and the edge emitting LED. If the edge emitting LED is driven with an increased current density, population inversion occurs, and this provides single pass gain by stimulated emission amplification. Such a device, called a superluminescent diode has a higher optical output power than an LED, a more uni-directional output and narrower spectral line-width (20 to 30 nm) [Culshaw and Dakin, 1988]. However, the output power of this device is non-linear with driving current and decreases with an increase in temperature. One end of this device is made optically lossy to suppress laser action.

The small emitting area of a laser diode is well suited for launching light into single-mode fibres. This device has far more stringent requirements than the LED, and its operation relies on a threshold current at which stimulated emission takes over from spontaneous emission. The threshold current of laser diodes is a function of temperature and ageing [Culshaw and Dakin, 1988]. These devices need some form of optical power monitoring along with thermal and electrical stabilisation. The efficiency of laser action reduces in the visible region making it quite difficult to produce lasers at wavelengths shorter than red. Similarly, reports regarding long-wavelength laser diodes have indicated that they are rather inferior in terms of power and phase noise obtainable in comparison with typical 800 nm laser diodes. Typical line widths of commonly used laser diodes are between 1 and 5 nm [Senior, 1992].

### **2.1.2 Incandescent lamps and lasers**

Among other optical sources briefly discussed are the incandescent (incoherent) lamps and lasers which have been used for varied sensing or industrial applications. Tungsten-halogen lamps are usually used in situations where broadband sources are required. They have a limited life of about 2000 hours, and have a very poor coupling efficiency into optical fibres. For operation, incandescent lamps rely on an electrically heated tungsten filament which converts most of its input electrical energy into radiant energy. Its non-symmetrical spectral radiance approximates that of a black body which has a temperature and wavelength dependence

described by Planck's law. Although it has a broad spectrum, which spans the useful optical fibre region (400 to 1000 nm), much of the power is wasted because the spectral power distribution spreads beyond the low attenuation window for most fibres. For applications requiring effectively a single wavelength, the spectral energy density is too low for measurements with reasonable signal-to-noise ratios. Consequently, incandescent sources have been used only for simple intensity modulated sensors.

Lasers which are available include solid state lasers (e.g. neodymium YAG, with wavelengths 1064 nm or 1320 nm), gas lasers (e.g. He-Ne, 632.8 nm or 1150 nm), and ion lasers (e.g. Ar<sup>+</sup>, 457.9 nm to 514.5 nm [Culshaw and Dakin, 1989]). These lasers, when pumped with an appropriate energy source, may exhibit a high degree of coherence and stability and have been used for various scientific and industrial applications. Although these sources offer, in some instances, several wavelengths they have not been used much in sensing applications mainly because of their size. Fibres having cores doped with an appropriate rare earth ion (for example Er<sup>3+</sup> emitting at 800, 980 and 1550 nm) [Urquhart, 1988] may be used as amplifiers, or they can be configured as lasers or broadband superluminescent sources. Sources based on pumped monomode optical fibres for fibre optic interferometric sensors have not yet received significant attention; this may be because of the noise arising from spontaneous emission sets the limit on the signal-to-noise ratio. Optical fibre amplifiers may be of interest in applications involving multiplexed fibre sensor networks when it is desirable to increase the number of sensor elements in a network.

## **2.2 Optical fibres**

Single mode step index fibres were used exclusively in this work because monomode fibre systems have optimum resistance to fibre perturbation. Furthermore, unlike multimode step index fibres, single mode step index fibres maintain the spatial coherence of the transmitted

beam, have very low loss and thus are compatible with interferometric sensor systems [Jackson, 1994]. They have a step index structure with a transparent core of refractive index  $n_1$  surrounded by a transparent material of lower refractive index  $n_2$  which forms the cladding (figure 2.1). Electromagnetic waves at optical frequencies are confined and guided through the core by total internal reflection.

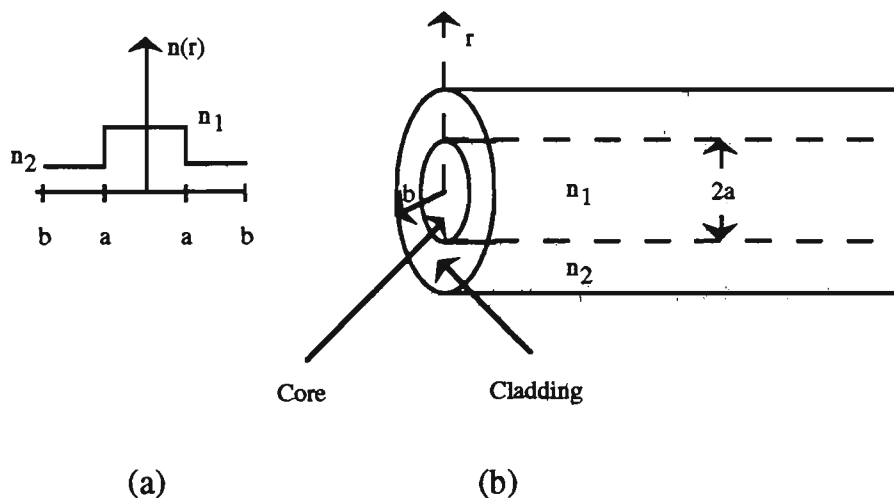


Fig. 2.1 Step index fibre (a) refractive index profile, (b) fibre geometry.

### 2.3.1 Properties of optical fibres

The basic properties of light propagating in an optical fibre are illustrated using a simple ray model, even though this model has significant limitations when considering single-mode optical fibres. A ray incident at an angle  $\theta$  at the core-cladding interface, which is greater than the critical angle  $\theta_c$ , will be totally internally reflected at the interface as shown in figure 2.2.

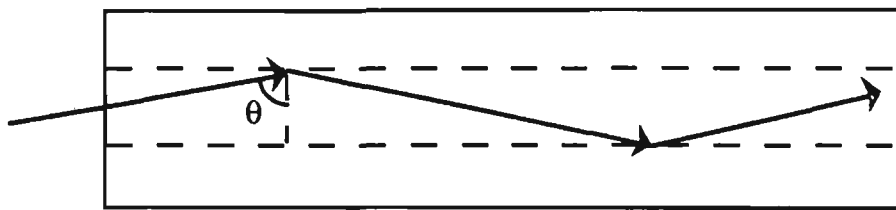


Fig. 2.2 The transmission of light ray in optical fibre.

The symmetry of the fibre ensures that the same ray will undergo similar total internal reflection at all core-cladding interfaces and thus be guided through the core. Only rays incident at angles greater than the critical angle  $\theta_c$  are guided whereas others are partially reflected only. The critical angle  $\theta_c$  (for a step index fibre) is given by [Jenkins and White, 1976]

$$\theta_c = \sin^{-1}\left(\frac{n_2}{n_1}\right). \quad (2.1)$$

For polychromatic light equation 2.1 becomes non-unique since the refractive index varies with wavelength.

An important consideration is the maximum angle of acceptance  $\theta_a$  for a light ray into an optical fibre. Figure 2.3 shows a meridional ray (A) striking the fibre core at an angle  $\theta_a$  with respect to the axis of the fibre. This ray is refracted at the air-core interface and then transmitted to the core-cladding interface at the critical angle  $\theta_c$ . Rays entering the fibre at an angle  $\theta < \theta_a$  will meet the core-cladding boundary at an angle greater than the critical angle and hence be guided along the core. Rays entering the fibre at angles  $\theta > \theta_a$  will be only partially reflected at the core-cladding boundary and thus will suffer high loss in propagating in the core. This  $\theta_a$  defines the acceptance cone for rays which will propagate in the core with low loss. The acceptance angle  $\theta_a$  can be expressed in terms of refractive indices of the media involved,

namely air ( $n_0$ ), the core ( $n_1$ ) and cladding ( $n_2$ ). This expression leads to the numerical arpeture (NA) given by [Senior, 1992]

$$NA = n_0 \sin \theta_a = \sqrt{n_1^2 - n_2^2} . \quad (2.2)$$

This definition of NA is true for meridional rays but for skew rays which do not pass through the axis of the fibre, the equation needs to be modified by a geometrical factor [Senior, 1992].

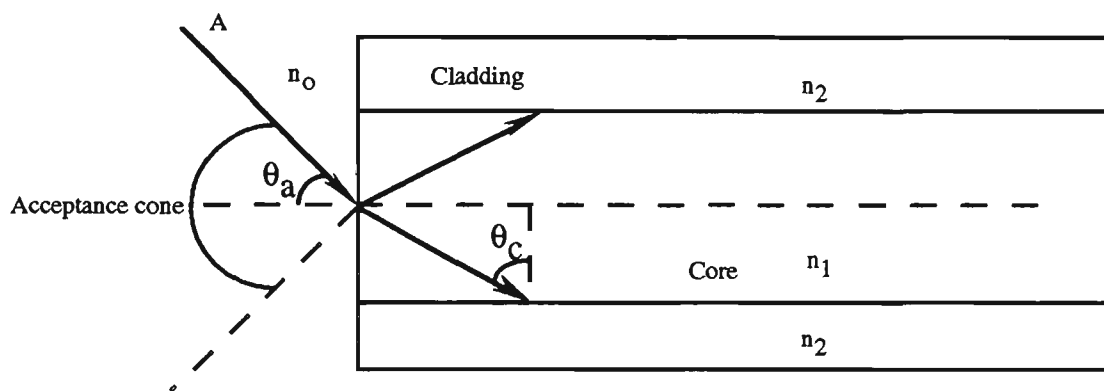


Figure 2.3 Acceptance angle for a single mode fibre

For fibre of diameter approaching the wavelength of light, the ray theory fails and the propagation of light in an optical fibre must be described by electromagnetic wave theory. Interference between wave components produces standing waves, orthogonal to the direction of propagation, which are called modes. The modes that will propagate are called *guided* modes while the others are *leaky* modes [Culshaw and Dakin, 1988]. The guided modes do not have a unique optical path for the injected light to follow as it propagates through the optical fibre, but a large number of paths, which have different propagation constants. The propagation constant  $\beta$  of any guided mode in the fibre is defined [Senior, 1992] by

$$\beta_2 < \beta < \beta_1 , \quad (2.3)$$

where

$$\beta_2 = 2\pi n_2/\lambda \quad \text{and} \quad \beta_1 = 2\pi n_1/\lambda, \quad (2.3a)$$

where  $\lambda$  is the free space wavelength of the propagating light. The number of modes in the fibre,  $N$ , has been shown [Senior, 1992] to be equal to  $4V^2/\pi$ , where  $V$  is the normalised frequency of the fibre given by  $(2\pi a/\lambda)(n_1^2 - n_2^2)^{1/2}$ . When  $V < 2.405$  then only the lowest order spatial mode can propagate and the fibre is classified as single mode; otherwise it is multimode.

The refractive index of glasses used in optical fibres varies with wavelength and so wave velocity is a function of wavelength, which produces dispersion. Dispersion mechanisms within the fibre cause broadening of the transmitted light pulses as they travel along the fibre, primarily limiting the maximum possible modulation bandwidth for a particular length of optical fibre. Velocity variation caused by the variation of material refractive index of the fibre is described as material dispersion. In fibre waveguides dispersion due to the structures themselves is known as waveguide dispersion. The single mode step index fibre has the additional advantage of low intermodal dispersion, because only one mode is transmitted, and thus has very low loss and high bandwidth compared with multimode fibre.

### **2.3.2 Intrinsic loss mechanisms in optical fibres**

The losses occurring in single mode fibres are caused primarily by the combined effect of absorption and scattering (Rayleigh and Mie) in the optical fibre waveguide [Senior, 1992].

Absorption in the ultra-violet range is due to electronic transitions in glass. There are absorption peaks in the infra-red region associated with vibrations of a range of bonds, principally oxygen-

silicon bonds. The major impurity absorption loss at wavelengths of 1.37, 1.23 and 0.95  $\mu\text{m}$  are due mainly to OH absorption. Careful manufacturing processes can reduce some of these losses.

The scattering loss due to small-scale localised refractive index variations, caused by localised density variations throughout the glass fibre, is called Rayleigh scattering. These variations act as scattering objects imbedded in an otherwise homogeneous structure. Rayleigh scattering is dominant at shorter wavelengths because of its  $1/\lambda^4$  dependence. It is dependent on the temperature at which the preform was drawn and the scattering produces an attenuation coefficient ( $\gamma_R$ ) which is given by the Rayleigh scattering formula [Senior, 1992]

$$\gamma_R = \frac{1}{\lambda^4} \left\{ \frac{8\pi^3 n^8 p^2 \beta_c k T_f}{3} \right\}, \quad (2.4)$$

where  $\lambda$  is the optical wavelength,  $n$  is the refractive index,  $p$  is average photo-elastic coefficient,  $\beta_c$  is the compressibility at a fictive temperature  $T_f$  (the temperature at which glass attains a state of thermal equilibrium and is closely related to the annealing temperature of glass) and  $k$  is Boltzmann's constant.

Mie scattering is caused by scattering from larger refractive index variations. This arises from the non-perfect cylindrical structure of the fibre waveguide which may result from irregularities in the core-cladding interface, core-cladding refractive index variations along the fibre length, diameter variations, strain and bubbles (all comparable in size to the guided wavelength). Mie scattering may be reduced by careful manufacturing processes [Senior, 1992].

Optical fibres can also suffer radiation losses at bends or curves on their path. Higher order modes are susceptible to radiation loss at bends which are large in comparison with the fibre diameter (macroscopic bends). Explicit wavelength dependent bending loss has been shown to

exist for a specified bend radius. Large losses can be induced at a definite critical bend radius,  $R_c$  (for single mode fibres), which is given by [Senior, 1992]

$$R_c = \frac{20\lambda}{(n_1 - n_2)} \left( 2.748 - 0.996 \frac{\lambda}{\lambda_c} \right)^{-3}, \quad (2.5)$$

where  $n_1$  and  $n_2$  are the core and cladding refractive indices respectively,  $\lambda$  is the wavelength of the propagating light, and  $\lambda_c$  is the cut off wavelength for the single mode fibre. Random stresses in a fibre which may be due to cabling processes or temperature variations cause microscopic bends and may result in light coupling out of the fibre [Palais, 1988]. These losses may cause significant errors in the case of intensity based measurements.

A further loss consideration with any optical fibre sensing system is the interconnection loss effects between system components [Senior, 1992]. There is always a thin film of air trapped between any two interconnected optical components. Accordingly, there are losses associated with connectors since a portion of light will be reflected back into the transmitting fibre at the interface because of the Fresnel reflection associated with the changes in refractive index at the interface. For normal incidence at a simple glass-air boundary, the reflected fraction of light ( $R$ ) is given by the Fresnel equation [Born and Wolf, 1969]

$$R = \left[ \frac{n_1 - n_a}{n_1 + n_a} \right]^2, \quad (2.6)$$

where  $n_1$  and  $n_a$  are the core and air refractive indices respectively. This intrinsic joint loss can be minimised through use of index matching fluid in the gap between jointed fibres or by the use of physical contact joints.

The total intrinsic loss is fairly small around the 800 to 900 nm region. This first low-loss window is commonly used for fibre optic sensing because high power sources and sensitive

detectors operating in this wavelength region are inexpensive. In the region from 1300 nm to about 1600 nm, glass losses are lower which makes it practical for long distance optical communication links. This region is sometimes referred to as the second window. These low loss regions are bounded on the short wavelength side by scattering and on the longer wavelength side by infrared absorption.

## 2.4 Light detectors

Optical detectors rely on the absorption of an incident photon with appropriate energy to produce either an electron-hole pair (in the case of semiconductors) or generate a free electron (in vacuum photodiode or photomultiplier tubes) [Andonovic and Uttamchandani, 1989]

Internal photoemission devices (semiconductor photodiodes), with or without internal (avalanche) gain, provide good performance and are compatible with optical fibre systems. In semiconductor photodetectors, incoming photons generate an electron-hole pair to produce an electrical current. These devices are well-suited for optical fibre based systems because of their small size, light weight, low cost, fast response and use of low operating voltages. In order to create an electron-hole pair, an incoming photon should have enough energy to raise an electron across the band gap. Photo-conductive detectors are reverse-biased devices and the electric field developed across the p-n junction sweeps mobile carriers (holes or electrons) to their respective majority sides ( $p$  and  $n$  material).

A planar diffusion p-n junction is a photodiode whose frequency and spectral response are governed by the thickness of semiconductor layers and doping concentration. It is characterised by a low efficiency and low responsivity because of its relatively large  $p$  and  $n$  doped regions and small depletion region. Further improvement in the performance of the device led to the p-i-n photodetector with a wider intrinsic semiconductor layer between the  $p$  and  $n$  regions. In fibre sensor systems the p-i-n photodetector is used most commonly because of its high

efficiency. For greater sensitivity an avalanche photodiode with an internal gain is used [Senior, 1992]. Its disadvantages are that it requires a relatively high voltage (100 - 200 volts) for its operation and it is intrinsically noisier than the p-i-n device. For this work, the detector used was a p-i-n silicon photodetector which has a peak responsivity around the 800 nm region of the spectrum.

## 2.5 Sensor limitations

The performance of sensor systems is limited in general by several types of noise, which may mask the signal. Thermal (or Johnson) noise arising from the thermal random motion of electrons within the detector load resistor and from within active elements in the amplifier sets the lowest noise limit of system components. The thermal noise mean square current in the load resistor is given by [Palais, 1988]

$$\overline{i^2} = \frac{4kTB}{R_L} \quad , \quad (2.7)$$

where  $k$  is Boltzmann's constant,  $T$  is the absolute temperature,  $B$  is the receiver's electrical bandwidth and  $R_L$  is the load resistance.

In photodetectors the incoming optic signals generate random discrete charge carriers, giving rise to a signal disturbance called shot noise. Shot noise increases with an increase in optic power and is due to the quantised nature of charge (electrons and holes) and light (photons). Also, other sources of noise exist which will further degrade the performance of the sensing network. The most relevant are those associated with (a) the type of source being used and (b) the sensing scheme used.

Fluctuations in the amplitude or intensity of the output from semiconductor injection lasers leads to optical intensity noise called laser amplitude noise. These fluctuations result from a

range of effects which affect the process responsible for laser action. Also, when a laser diode is used as a source for an interferometer of path difference,  $l$ , an optical phase shift  $\Delta\phi$  is induced in the interferometer arising from a source frequency instability  $\Delta\nu$ , giving rise to laser frequency noise given by [Culshaw and Dakin, 1989]

$$\Delta\phi = 2\pi n_1 l \Delta\nu / c , \quad (2.8)$$

where  $c$  is the speed of light in free space.

A white light interferometer may suffer from environmental noise which may be due to vibration during the scanning of the receiver interferometer. In addition, a multiplexed sensor network may be a source of noise due to cross-talk between sensor channels, and which is dependent on the multiplexing scheme and source coherence length [Kersey, 1988b; Brooks *et al.*, 1987]. It is possible to minimise some of the aforementioned noise limitations, and cross-talk noise may be reduced by proper choice of sensor type (e.g. low finesse FFP to reduce the effect of multiple reflections). The choice of sensor components (broadband sources) may play a major role in reducing phase noise since a white light interferometer has very low levels of phase noise because of its operation near zero optical path difference [Chen *et al.*, 1992]. Both thermal noise and dark current noise may be reduced by lowering the temperature of the photodetector, but shot noise represents a fundamental irreducible level. Vibrational effects can usually be reduced to an acceptable level by careful system design. Suitable packaging of the interferometer such as putting the sensor in a styrofoam enclosure and using a vibration isolated table may significantly minimise the environmental noise. These have been used in this work to minimise some of the noise sources as outlined in section 7.7.

## 2.6 Conclusion

In conclusion, the components of an optical fibre sensor and their limitations have been discussed very briefly. Optical sensing systems are usually subject to a variety of types of noise including shot noise and electronic noise arising from the electronic circuitry. Different sensing applications will require different types of fibres. Single-mode fibres are used when preservation of spatial coherence is to be maintained, such as in interferometric sensors or polarisation sensors. Multimode fibres are used when no phase or polarisation information is required, e.g. in intensity-based measurements. The choice of light source depends upon the selected modulation mechanism but the choice of modulation must be made concurrently with the multiplexing scheme. The detector to be used must have spectral characteristics which match those of the source. In the work described in the thesis the low coherence source was (mostly) a multimode laser diode (LT016MD) of nominal centre wavelength of 810 nm and coherence length of  $\sim 150 \mu\text{m}$ . The choice of this light source was a compromise between its higher optical power and its fairly low coherence length. In later stages of this work a superluminescent diode of centre wavelength 835 nm and coherence length of  $\sim 70 \mu\text{m}$  was also used for the measurements with in fibre Bragg-based fibre Fabry-Perot interferometers. During the initial stages of the research, involving the fabrication of in-line fibre Fabry-Perot sensors, a single-mode communications fibre ( $\lambda = 1300 \text{ nm}$ ,  $10/125 \mu\text{m}$ ) was used as test fibre because of its low cost. Once the technique of sensor fabrication was mastered, a single mode Flexcore 780 fibre (Corning  $5/125 \mu\text{m}$ ) was used for the white light interferometry sensor measurements. All measurements used a silicon p-i-n detector.

## CHAPTER 3

### REVIEW OF STRAIN MEASUREMENT TECHNIQUES

#### 3.1 Introduction to strain

The fundamental objective of strain monitoring is the safety of loaded structures. Strain refers to the fractional deformation produced in a body by the application of stress [Neubert, 1967]. Associated with each type of stress is a corresponding type of strain, i.e tensile, compressional or shear. A simple case of pure tensile stress is shown in figure 3.1, in which a rod of diameter  $d$  experiences an elongation  $\Delta L$  due to the applied stress  $F$ . The rod similarly experiences a corresponding lateral contraction  $\Delta d$ .

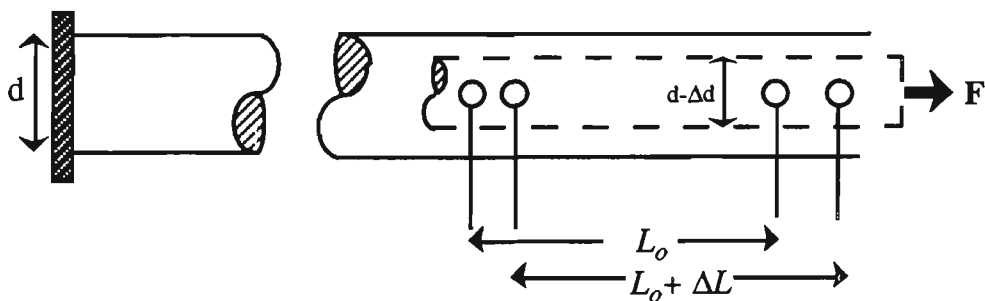


Figure 3.1 Elongation of stressed structure.

Consider an element of length  $L_o$  which is elongated to  $L_o + \Delta L$  The tensile strain ( $\epsilon$ ) is defined as the ratio of the increase in length to the original length, i.e.

$$\epsilon = \frac{\Delta L}{L_o} . \quad (3.1)$$

Strain is a dimensionless quantity but convention is to use microstrain ( $\mu\epsilon$ ) (i.e. strain  $\times 10^{-6}$ ). The strain suffered by a rod in compression is defined in a similar manner, namely the ratio of the decrease in length to the original length. Hooke's law establishes that, up to a limit, the relation between stress and the corresponding strain is linear [Dally and Riley, 1978]. This relationship allows for the determination of structural stresses from strain measurements. The stress required to produce a given strain is dependent on the nature of the material under stress. The stress ( $\sigma$ ) per unit strain ( $\epsilon$ ) defines the elastic modulus ( $E_e$ ) of the material, i.e.

$$E_e = \sigma / \epsilon . \quad (3.2)$$

The typical stress-strain relationship for most metals is illustrated in figure 3.2

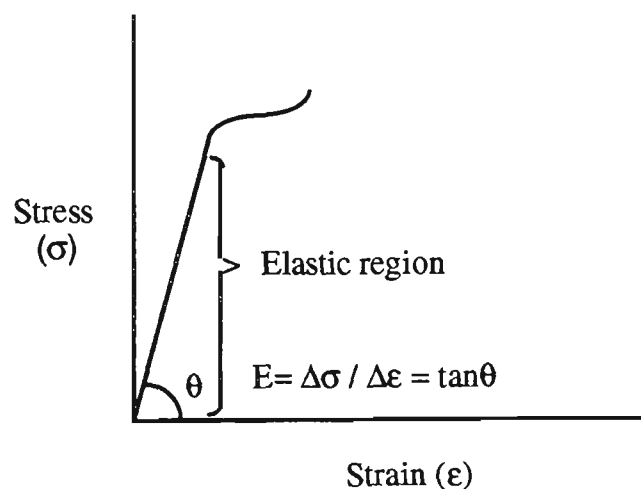


Figure 3.2 Stress / strain relationship of most metals.

Associated with the elongation is a corresponding lateral contraction of a structure, as can be seen from fig. 3.1. In the elastic region, the ratio of the lateral strain to the longitudinal strain (Poisson's ratio) is a constant which has a value of approximately 0.3 for most commonly used metals.

Where accurate strain measurements are not possible, stresses can be estimated theoretically and structural safety achieved by very conservative design. This becomes unacceptable as the demand for minimum weight and maximum strength and performance increases. The requirement in industries, such as the aircraft industry, for maximum strength-to-weight ratio in the materials calls for an accurate and reliable means of strain monitoring. It is fortunate that most of the critical regions of a structure under stress occur invariably on its surface [Neubert, 1967]. In monitoring these stresses, one important consideration is the sensing gauge length. Strains cannot be measured at a point with any type of strain gauge and, consequently, at a given point strains cannot be measured without some degree of error. This error will have a dependence on the gauge length. This may be illustrated by the simple (though important) case of a cantilever under a bending moment, where the strain on the top surface varies linearly from zero to a maximum at the clamped end [Neubert, 1967], as shown in figure 3.3. A strain gauge bounded by points Q and P would measure an intermediate value somewhere between ( $\epsilon_Q$ ) and ( $\epsilon_P$ ). It is evident from figure 3.3 that one requirement of a strain measuring device should generally be high spatial resolution (small gauge size) so as to give near point-wise measurements. This linear stress-strain relationship for the simple cantilever has been exploited in this research as a means to test the strain sensitivity of sensors.

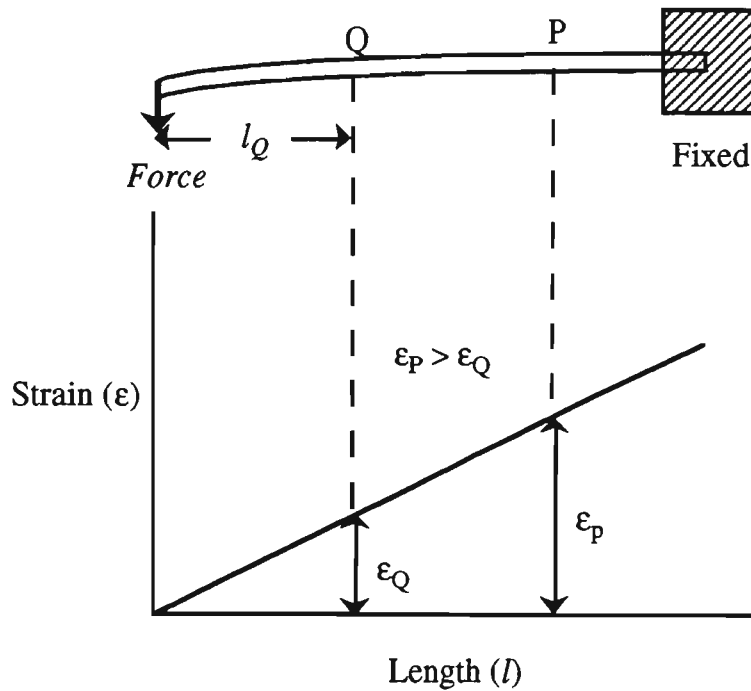


Figure 3.3 Strain distribution along axis of a stressed cantilever.

### 3.2 Conventional methods of strain measurement

Over the years, strain measurement techniques have been sought so as to produce a gauge which embraces the desired qualities of high spatial resolution and strain sensitivity with minimal temperature sensitivity, ease of gauge attachment and negligible effect of the gauge on the structure, stability of gauge calibration with time and dynamic loading, ease of multiplexing, and distinct direction sensitivity with low transverse sensitivity [Neubert, 1967]. This section reviews some of the basic methods of strain measurement. The principles employed in strain gauge construction can be used as a classification for these gauges into the following categories.

### 3.2.1 Mechanical strain gauges

These are devices which measure extension ( $\Delta l$ ) when attached to a test structure under load, and are called extensometers. The elongation of a stressed structure over base lengths (5 - 20 cm) is measured by an extensometer clamped to the structure. Considerable mechanical magnification ( $\sim 4000$ ) using composite lever systems is necessary in order to provide the experimenter with a suitable measurement of strain [Hetényi, 1950]. The commonly used types were the lever type extensimeter due to Kennedy and the Haggenger extensimeter [Dally and Riley, 1978]. Measurements down to 50  $\mu\text{m}$  were possible with these gauges [Hetényi, 1950]. Their size and weight limit the frequency response and thus they are better suited for quasi-static measurements.

### 3.2.2 Acoustic strain gauges

An acoustic-mechanical strain gauge utilises the change in natural vibrational frequency of a steel wire (attached between two knife blades one fixed and other movable) which occurs when it is subjected to stress, as shown in figure 3.4. The natural frequency ( $f$ ) of vibration of a taut wire fixed at both ends, length ( $L_w$ ) is given by [Neubert, 1967]

$$f_j = \frac{j}{2l} \sqrt{\frac{\sigma}{\rho}} \quad ,$$

where

$$\sigma = \frac{E\Delta L}{L_w} \quad (3.3)$$

Here  $j$  is the order of vibration (i.e. harmonic),  $\sigma$  is the tension,  $\rho$  is the volume density of the wire and  $E$  is its Young's modulus.

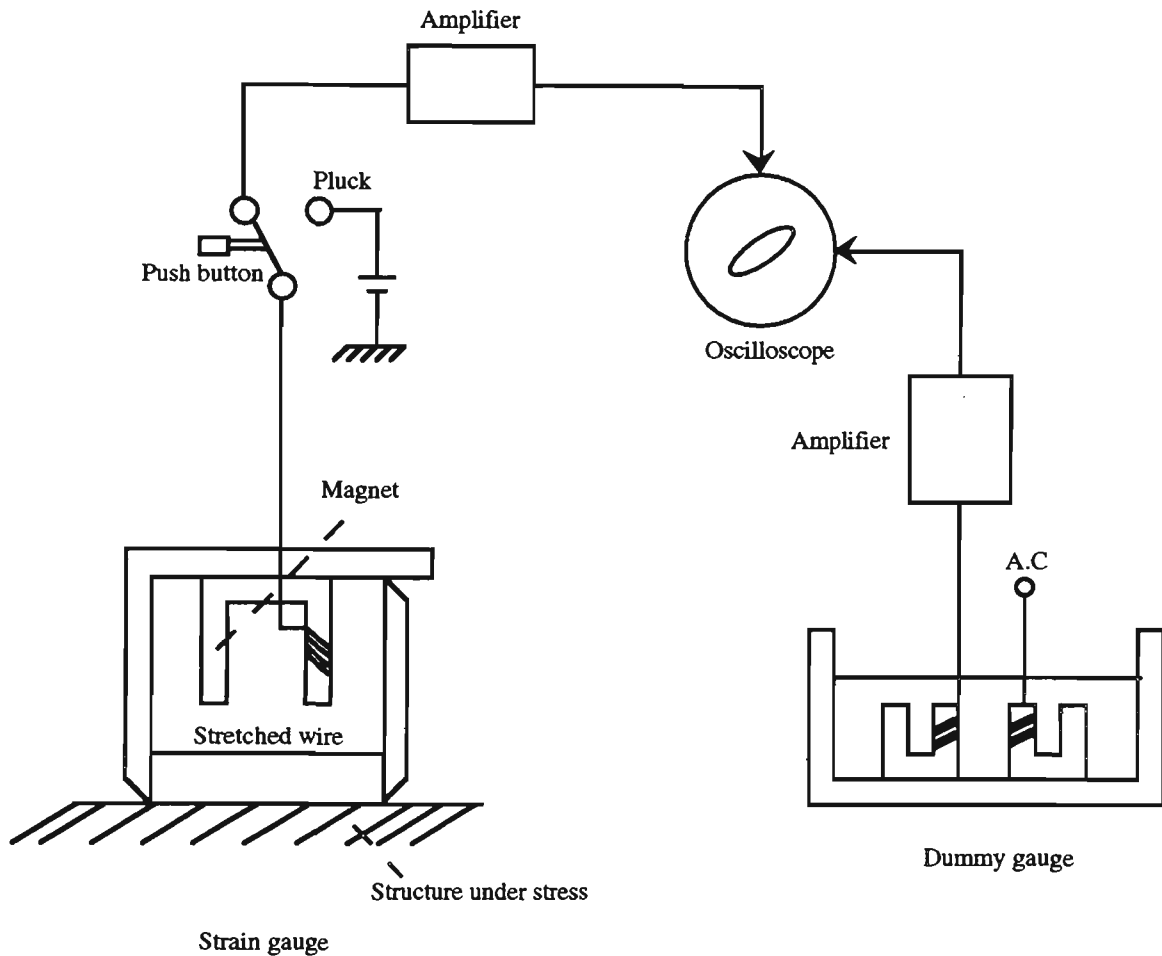


Figure 3.4 Acoustic strain gauge [Neubert, 1967]

It can be seen that for any harmonic the natural frequency is dependent upon the tension in the wire, which in turn is dependent upon the elongation of the wire caused by the stress in the structure under test. The steel wire shown between the two knife blades is plucked by a current impulse in a small electromagnet. Then, the magnet and coil arrangement is used to detect the natural frequency of the vibrating wire. The change in frequency of vibration of the wire was determined by measuring a phase shift, with a dummy gauge providing a reference signal.

Commercially available gauge lengths varied between 0.02 and 0.1 m. These gauges have exhibited a high sensitivity, with a possible determination of displacements of the order of 2.5 nm [Dally and Riley, 1978]. On light structures the tensile stresses of the taut wire may affect the strength of the structure and alter the stress under investigation [Neubert, 1967].

### **3.2.3 Electrical strain gauges**

Electrical strain gauges are the most widely used gauges for structural stress analysis with inductance, resistance, and semiconductor gauges dominating the market.

#### **3.2.3.1 Inductance strain gauges**

Inductance strain gauges exploit the transformation of a linear displacement of an armature into an inductance variation. This is obtained from the relative movement of the armature placed between a primary and secondary coil arrangement which varies the mutual inductance between the windings. Several inductance gauges have been devised with the transverse armature type offering the highest sensitivity to strain [Neubert, 1967]. Although these gauge types have exhibited good strain sensitivity e.g.  $\sim 10^{-5} \mu\epsilon$  per cm indicator deflection, they are not easy to handle, are expensive and suffer from unwanted contributions from resistance variations with strain, which makes them unpopular for strain measurement.

#### **3.2.3.2 Capacitance strain gauges**

A capacitance strain gauge utilises a variation of capacitance between two capacitor plates, due to changes in distance between the plates when subjected to a stress. They have been used for the measurement of both static and dynamic strain. Capacitance gauges, when bonded or clamped onto flat surfaces, have been shown to operate within a temperature range of -250 to 650°C. Strain resolution down to 1  $\mu\text{m}$  has been obtained with a capacitance gauge of length 25

mm and capacitor gap separation of 0.25 mm [Dally and Riley, 1978]. Capacitance strain gauges are limited in their practical application because the accurate determination of small capacitance variations is difficult, since their extremely narrow air gap results in large errors due to temperature variations [Neubert, 1967].

### 3.2.3.3 Resistance strain gauges

The resistance of a conductor of uniform cross-section area  $A$ , length  $L$  and resistivity  $K$  is given by [Hetenyi, 1950]

$$R = KL/A \quad (\Omega) \quad (3.4)$$

Kelvin in 1856 noted that the electrical resistance of a conductor varies with stress. This variation of resistance with stress (due to elongation and lateral contraction) has been taken advantage of in resistance strain gauges. A resistance strain gauge is a length of thin metallic foil looped back on itself many times (to increase sensitivity) attached to an insulating backing material [Hetenyi, 1950] as shown in figure 3.4.

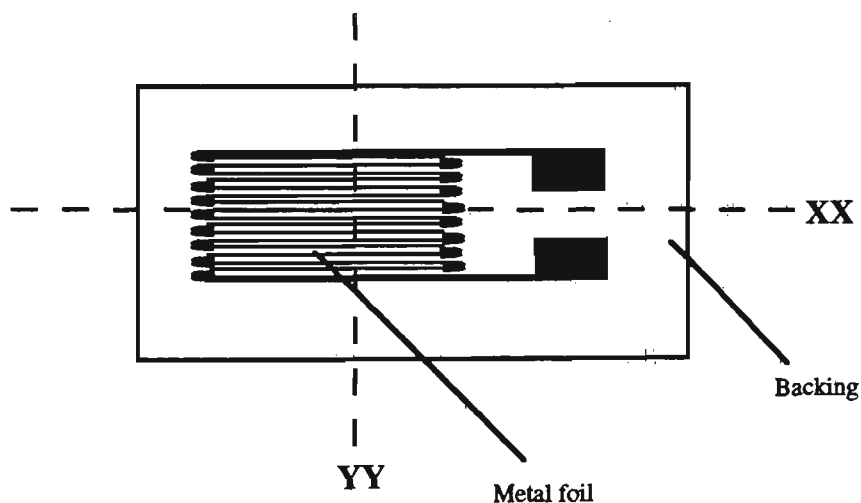


Fig. 3.4 Typical resistance strain gauge.

The gauge is sensitive to the strain along its axial direction XX. However, due to Poisson's ratio there may be transverse strains in the YY direction of about 2%. Consequently, a large length to width ratio is desirable for minimal transverse strain sensitivity. The gauge is usually protected from humidity by a water-proof layer of suitable lacquer [Dally and Riley, 1978]. The gauge sensitivity (G) or gauge factor can be expressed in terms of Poisson's ratio ( $\nu$ ) and resistivity (K) by [Neubert, 1967]

$$G = \frac{\Delta R / R}{\Delta L / L} = 1 + 2\nu + \frac{\Delta K / K}{\Delta L / L}, \quad (3.5)$$

where  $\Delta R/R$  is the fractional change in resistance,  $\Delta L/L$  is the strain, and  $\Delta K/K$  is the fractional change in resistivity of the gauge material. Even though most metals have  $\nu = 0.3$  the value of the gauge factor of commercial resistive strain gauges is 2, owing to the contribution to the gauge factor from changes of resistivity with strain [Neubert, 1967].

Resistance strain gauges are usually operated using balanced bridge circuits. The electrical resistance of the strain gauge varies not only with strain, but also with temperature, and the gauge factor has a temperature dependence as well. These deviations from ideal behaviour can cause significant errors if not properly accounted for. The error due to thermal output can be minimised by connecting into an adjacent arm of the Wheatstone bridge circuit an identical compensating or dummy gauge attached to an identical unstrained structure. Resistance changes are normally very small and typically, for a 120  $\Omega$  resistance strain gauge with a strain gauge factor of 2, the corresponding change in resistance is about  $10^{-3} \Omega$  for a strain of about 10  $\mu\text{m}$ . Strain resolution depends ultimately on the bridge used. Typically for commercial bridges the strain indicator will resolve  $\pm 2 \mu\epsilon$  with an accuracy of  $\pm 0.1\%$  of the reading or 5  $\mu\text{m}$  whichever is greater [Dally and Riley, 1978].

#### 3.2.4.4 Semiconductor strain gauges

Semiconductor strain gauges are produced from single crystals of germanium or silicon doped with the required amount of impurity atoms from group 3 or 5 of the periodic table. These devices exploit the variation of resistance in semiconductor strips with stress (piezoresistive effect). The fractional resistance variation ( $\Delta R/R$ ) with strain ( $\Delta L/L$ ) is given by [Neubert, 1967]

$$\frac{\Delta R / R}{\Delta L / L} = 1 + 2\vartheta + m , \quad (3.6)$$

where  $\vartheta$  is Poisson's ratio and  $m$  is the product of the piezoresistive coefficient with the Young's modulus of the semiconductor gauge in its longitudinal direction. The advantage of semiconductor gauges is that their sensitivity to strain is an order of magnitude higher than resistance gauges. However, these gauges are limited by several drawbacks. These include their non-linear fractional resistance variation with strain, the dependence of the gauge factor on doping concentration and temperature, the dependence of gauge resistance on temperature and the variation of gauge sensitivity with strain levels. Meaningful and reliable strain measurements using semiconductor strain gauges require sophisticated and precarious compensation techniques.

#### 3.2.4.5 Summary of conventional strain measurement techniques

From the foregoing discussion of conventional methods of strain measurement, the following general conclusions may be drawn:

- Mechanical strain gauges tend to be bulky and do not allow remote monitoring since an operator must be in attendance.

- Acoustic strain transducers are not suitable for light structures, and their long wire lengths do not satisfy the requirement for small gauge size.
- Inductance strain gauges and capacitance gauges are cumbersome, expensive and difficult to implement for large scale monitoring.
- The high strain sensitivity of a semiconductor gauge is attractive but account must be taken of the gauge's non-linear fractional resistance variation with strain, and its temperature instabilities.
- The most suitable gauge for strain monitoring is the resistive strain gauge. However, this gauge is susceptible to electromagnetic interference and like all conventional strain measurement gauges, does not lend itself easily to multiplexing.

Clearly, all these gauges have one or more undesirable quality. If these drawbacks can be overcome or minimised by optical fibre strain gauges then they will be competitive with existing conventional strain sensors. It is hoped that fibre optic strain sensors will prove to be more versatile than conventional strain gauges. By assessing the performance of optical strain gauges, their advantages and limitations can be evaluated so that the situations in which they are likely to be more effective than the alternatives can be clarified.

### **3.3 Optical fibre strain sensing**

Strain measurement using optical fibres is of special importance because other measurands (e.g. pressure and flow rate) may be converted to a displacement, and finally measured as a strain in an optical fibre. Various optical fibre strain measurement methods have been investigated and their operation and performance are reviewed here.

### 3.3.1 Microbend strain gauge

Microbend strain sensors are based on distortion-induced modulation of the optical transmission through an optical fibre. Light loss in the fibre is due to coupling from propagation modes in the fibre to radiation modes. It has been observed that when the wave number of distortion equals the difference in wave number between propagation and radiation modes a strong loss occurs [Giallorenzi *et al.*, 1982]. For an optical fibre experiencing a periodic distortion along its axis, the power propagating in the fibre couples from propagation modes into radiation modes with longitudinal propagation constants  $\beta$  and  $\beta'$  respectively such that

$$\beta - \beta' = \pm 2\pi/\Lambda_M,$$

where  $\Lambda_M$  is the wavelength of the periodic mechanical distortion. The microbend strain gauge employs a multimode fibre placed in a corrugated structure which is subjected to a stress. The stress causes an increase in the magnitude of the fibre bends, resulting in reduced transmitted intensity. Figure 3.5 shows an optical fibre sensor based on intensity induced microbend losses.

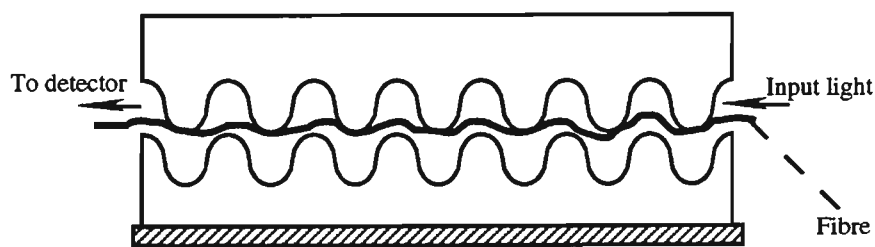


Figure 3.5 Microbend intensity based sensor.

The wavelength of the periodic mechanical perturbation depends upon the modal properties of the fibre used (and is typically in the mm range) [Giallorenzi *et al.*, 1982]. Microbend sensors have demonstrated only a limited ability for structural monitoring both in tensile [Lagakos *et al.*, 1981; Mardi, *et al.*, 1992] and bending strain [Rogers, 1988], due to their low sensitivity. A microbend sensor for monitoring acoustic vibration [Fields and Cole, 1980] had difficulties in optimising the optical fibre and acoustic transduction for adequate sensitivity. The method, though simple, is only useful when monitoring fairly large strains or displacements, and when the requirements in regard to high spatial resolution and accuracy of measurement are not critical.

### 3.3.2 Interferometric strain gauges

Single-mode optical fibre interferometric sensors have been shown to possess the greatest measurement resolution for a wide range of measurands including strain and temperature. Interferometric optical fibre sensors are based primarily on the detection of the optical phase change induced in the radiation field as it propagates along the optical fibre. Since temperature as well as strain changes the optical phase, the following discussion of interferometric strain sensors will also include their temperature sensing properties.

The initial experimental investigations of Butter and Hocker [1978] demonstrated that strain could be monitored using optical fibres. They used a Mach-Zehnder interferometer with bulk optic components and fibre arms bonded onto a cantilever beam. The strain gauge sensitivity ( $G = \Delta\phi/\epsilon L$ ) obtained from their experimental results of  $1.2 \times 10^7 \text{ m}^{-1}$  ( $\lambda = 633 \text{ nm}$ ) compared favourably with the theoretical prediction of  $1.25 \times 10^7 \text{ m}^{-1}$  which was obtained using parameters for bulk-silica. Pseudo-localisation of their system was obtained by bonding a desired length of optical fibre to the cantilever beam. The method detected changes of measurand by incremental fringe counting, and also continuous observation was needed as to

monitor the change of path difference. In such an arrangement it is not always very easy to maintain the stability or obtain repeatability.

A hybrid bulk and fibre optic Mach-Zehnder interferometer for the measurement of temperature [Hocker, 1979] over a 1 m length of fibre (insulated in an enclosure) yielded good temperature phase sensitivity. This employed a He-Ne laser ( $\lambda = 633 \text{ nm}$ ) as source and a Mach-Zehnder interferometer comprised of bulk optical components and two lengths of single-mode fibres, for the sensing and the reference arms. Temperature changes in the sensing arm resulted in a displacement of the fringes at the output, which were used as a measure of temperature. The average fringe shift per unit temperature obtained with this arrangement was  $13.2 \pm 0.5 \text{ fringe } ^\circ\text{C}^{-1}\text{m}^{-1}$ , while the predicted value was  $17.0 \text{ fringes } ^\circ\text{C}^{-1}\text{m}^{-1}$ . The bulk optic components used in the system created alignment problems and the requirement that the motion of the optical fringes be observed physically was an added disadvantage. A technique of mode-mode interference of the two orthogonal linear polarisations of the  $\text{HE}_{11}$  mode in a single high birefringent fibre for temperature sensing has been demonstrated [Eickhoff, 1981]. The two orthogonal linear polarisations constitute the two arms of the interferometer. By equally exciting these modes, the status of the interferometer could be obtained via the phase difference between these two beams. The value of phase sensitivity per unit temperature per unit length ( $\Delta\phi / \Delta T.L$ ) obtained with this scheme of  $1.66 \text{ rad K}^{-1}\text{m}^{-1}$  was in agreement with earlier reported data. This sensor has the advantage of using a single fibre only.

A Mach-Zehnder interferometer comprising both bulk and fibre optic sensing and reference arms was also used in investigating the static thermal sensitivity of bare and jacketed single-mode fibres [Lagakos, *et al.* 1981a]. Their experimental observations were consistent with theoretical predictions, and values of temperature phase sensitivity ( $\Delta\phi/\phi\Delta T$ ) for bare and the jacketed fibre of  $0.68 \times 10^{-5}/^\circ\text{C}$  and  $1.80 \times 10^{-5}/^\circ\text{C}$  ( $\lambda = 0.6328 \text{ }\mu\text{m}$ ) respectively were obtained using a core silica fibre whose cladding was doped with 5%  $\text{B}_2\text{O}_3$ . The disadvantage of their system was the use of both bulk and fibre optical components which created alignment

problems. A more rugged all fibre Mach-Zehnder interferometer [Uttam *et al.*, 1985] was used for the measurement of static strain. This is of advantage because it has no optical interface within the sensing region. However, the limitation of this scheme was that the fibre itself is sensitive to the measurand of interest throughout its entire length and this demands the confinement of the sensitivity to the required locality. For the measurement of dynamic strain a heterodyned Mach-Zehnder interferometer of bulk optical components [Uttam *et al.*, 1985] was used and gave a strain sensitivity of  $0.6 \text{ mV}/\mu\epsilon/\text{Hz}$ . Heterodyne detection ensured that the interferometer output was independent of power fluctuations of the laser source. The scheme was limited mainly by the electronics used.

A Michelson interferometer is more attractive for high sensitivity strain and thermal measurements than the Mach-Zehnder interferometer because in the Michelson interferometer the optical signal traverses the sensing element twice. This was exploited in an all-fibre Michelson temperature sensor which utilised signal recovery based on laser frequency ramping with digital phase tracking [Corke *et al.*, 1983]. Their arrangement relied on the creation of a moving fringe pattern at the output of an unbalanced Michelson fibre interferometer by linearly ramping the laser injection current. Although this scheme was introduced as a temperature sensor, it was to become the first fibre optic strain gauge system to meet the requirements of localisation through a signal recovery technique. Signal recovery was obtained by frequency ramping of the diode laser output and employing a digital phase tracking technique. This allowed measurements of static parameters and also eliminated the requirement of active phase compensation in the fibre arm. A sensitivity of  $141 - 208 \text{ rad } ^\circ\text{C}^{-1}\text{m}^{-1}$  was obtained for a 2 cm length of sensing fibre.

An early attempt at strain monitoring in structural materials using optical fibres, suffered from lack of localisation and poor signal recovery [Rowe *et al.*, 1986]. They embedded Corning 50/125  $\mu\text{m}$  fibre (with the jacket removed) in graphite epoxy material. The sensing interferometer was a Mach-Zehnder interferometer and the use of multimode mode fibre

warranted the use of RF interferometry. In 1988 Sirkis constructed a Mach-Zehnder fibre optic strain gauge that attempted to localise the sensing region by means of a geometrical difference between the sensing and reference fibre arms and by adhering the optical fibres only where the strain measurement was to be done. More recently, these problems (i.e. localisation and signal recovery) were addressed by using an all-fibre Michelson interferometer embedded in a composite material [Valis *et al.*, 1991]. Phase demodulation performed using a passive single-mode  $3 \times 3$  directional coupler techniques, which had advantages of simplicity and also does not involve active elements. Localisation was achieved by using a pair of mirror-ended optical fibres of different lengths. The strain phase sensitivity obtained experimentally for the embodied sensors was  $2 \times (1.07 \pm 0.15) \times 10^7$  rad/m ( $\lambda = 632.8$  nm). The drawback of the scheme was the need to provide a high degree of common mode rejection for the two fibres. To overcome the problem partially, the fibres were mechanically paired and connectorised, but this was cumbersome.

Induced optical birefringence has been exploited in the analysis of both static and dynamically induced strains in optical structures [Varnham *et al.*, 1983]. They used a polarisation optic strain sensor utilising a dual  $45^\circ$  configuration which was constructed from single mode high birefringence bow-tie fibre. This was achieved by splicing the birefringence fibre to two similar fibres such that the axes of birefringence were rotated approximately  $45^\circ$  with respect to each other. Laser light was injected into a length of high birefringent fibre which was lightly looped to form a polariser. The length that followed the loop effectively has one x-polarised mode excited and thus provided linearly polarised light which was injected into a sensing length of the same fibre which formed a dual  $45^\circ$  splice. The localised nature of the sensor stimulated interest in the embodiment of optical fibre sensors into structural materials for stress monitoring. The jointing scheme, which employed adhesives, had a negative effect on the sensitivity of the system. Similar sensor schemes for simultaneous recovery of phase and polarisation in interferometers made from birefringent components have been reported [Akhavan *et al.*, 1985, Corke *et al.*, 1985], in which the high resolution of the interferometric sensor is combined with

the larger measurement range of the polarisation sensor. The last scheme has been exploited in strain monitoring in an all fibre system, where the two polarisation modes of a high birefringence fibre were used as two fibre Fabry-Perot cavities [Akhavan *et al.*, 1985]. In their system, a 10 cm length of high birefringent fibre was used as the sensing element configured to form an interferometer with amplitude division at the normally cleaved input face of the fibre, and reflection at the distal end face of the same fibre. The fibre is equivalent to two interferometers, each corresponding to the orthogonal polarisation modes. The two independent outputs correspond to two fibre Fabry-Perot cavities. The value of phase sensitivity ( $\Delta\phi/\Delta l$ ) obtained with this set up for a 10 cm length of sensing fibre was  $6.5 \times 10^6$  rad m<sup>-1</sup>. The advantage of the system was its intrinsic temperature compensation. The resolution of the system was limited by the signal analyser used, and it would have been desirable for the absolute values of both phases for the fast and slow axes to have been determined. In a similar development, a technique which allows the simultaneous measurement of strain and temperature applied to a sensing fibre have been demonstrated [Farahi *et al.*, 1990, Faramarz *et al.*, 1990] utilising a birefringent optical fibre configured as a fibre Fabry-Perot. Measurements were done using a 7 cm length of sensing fibre [Faramarz *et al.*, 1990] which was enclosed in an electrically heated furnace. Strain and temperature sensitivities of  $10.601 \pm 0.021$  rad/ $\mu\epsilon$ ,  $10.730 \pm 0.015$  rad/ $\mu\epsilon$  and  $8.681 \pm 0.031$  rad/ $^{\circ}\text{C}$ ,  $8.084 \pm 0.023$  rad/ $^{\circ}\text{C}$  were obtained respectively for the slow and fast axes. This scheme has advantages because it could realise an interferometric strain gauge with inherent temperature compensation. However, the scheme had limitations in measurement range since the unambiguous range was only  $2\pi$  radians and, also, it lacked the strain sensitivity required to make a short (in the mm range) gauge for high resolution ( $< 1 \mu\epsilon$ ) measurements. Similar interferometric sensor schemes employing tension-induced modal birefringence in single-mode fibres have exhibited limited sensitivity as has been discussed elsewhere [Blake *et al.*, 1987; Ohtsuka and Tanaka, 1990; Charasse *et al.*, 1991].

Interferometric strain gauges based on the use of internal mirrors in single mode fibres have attracted significant interest [Lee and Taylor, 1988; Mason, 1992; Measures, 1992; Atkins *et*

*al.*, 1994]. Lee and Taylor [1988] demonstrated that Fabry-Perot based fibre optic sensors can be fabricated with reflective fusion splices. This was an important development because it allowed the embodiment of these sensors into structural materials or their adherence to structures, with minimal intrusion, for the measurement of temperature [Lee *et al.*, 1988a, 1989] and strain [Valis *et al.*, 1990b; Kaddu *et al.*, 1993]. The manufacturing technique used to fabricate these FFP sensors was based on titanium dioxide sputtering (this is discussed further in chapter 5), except for Valis *et al.* [1990b] who used reflective fusion splices based on metal vapour deposition. Dielectric mirrors as opposed to metallic mirrors have a low absorption in a broad spectral range. The advantage of this fusion splicing technique is that it allows for the creation of internal mirrors of varied reflectances [Kaddu *et al.*, 1993]. The strain sensitivity ( $\Delta\phi/\phi\epsilon$ ) obtained experimentally of  $0.840 \pm 0.004$  ( $\lambda = 1300$  nm, FFP gauge length = 4 mm) compared closely with the predicted result of 0.74 which was calculated using bulk silica parameters. Sensors of this type could well be suited for use in high strain sensitivity measurements in a localised region of the structure, and several of them can be multiplexed on a single strand of fibre. This is useful, as a large number of sensors may be addressed without the usual multiplexing problem of power loss in splitters. Recently, intrinsic fibre optic Fabry-Perot strain sensors fabricated in single-mode fibres have been used for the measurement of combustion chamber pressure [Atkins *et al.*, 1994]. The FFP interferometer was embedded in a metal rod placed in contact with one or more diaphragms that were exposed to the chamber pressure. The pressure causes the longitudinal compression of the rod thereby straining the embedded FFP sensor. The signal from the FFP interferometer which serves as a strain transducer allows for the determination of the pressure. The pressure sensitivity obtained experimentally using a 4 mm FFPI was  $6.5 \times 10^{-7}$  rad/pA ( $\lambda = 1.3$   $\mu$ m).

An extrinsic Fabry-Perot cavity formed by an air gap between an input single mode fibre and a reflective multimode fibre (i.e. a low finesse Fabry-Perot) has been used as a strain gauge [Murphy *et al.*, 1991, Lesko *et al.*, 1992]. The Fresnel reflection from the glass-air interface formed at the cleaved end of the input single-mode fibre (reference reflection) and the reflection

from the air-glass interface at the far end of the air gap due to the reflective multimode fibre (sensing reflection) interfere in the input/output fibre. The fibres are held in a silica tube and are able to move longitudinally under the influence of a stress. This causes a change in the air gap length, thus changing the phase difference between the reference and sensing reflections. Measurements obtained using the optical fibre strain gauge compared closely with those obtained using a resistance strain gauge. The extrinsic optical strain gauge may be limited to low levels of strain because its signal-to-noise ratio decreases with increase in the air gap. Furthermore, the use of cleaved fibre ends separated by small air gaps as reflectors may not generally be suitable for deployment in a practical sensor cable.

Field deployment of optical fibre interferometric sensors for strain or temperature measurement requires an analogue or digital sensor output so as to be meaningful to the end user. A development in this direction has been a fibre Fabry-Perot strain sensor for the monitoring of strain on the wings of an aircraft [Murphy *et al.*, 1992]. Fibre Fabry-Perot sensors were surface bonded to the underside of the wings of an F-15 aircraft to monitor both static and dynamic strain. The wing was loaded from 0 to 17615 kg (gross weight) and the sensor exhibited a high performance with a minimum detectable resolution of  $0.01 \mu\epsilon$  for a gauge length of 19.03 mm. Measurements with the optical gauge agreed closely with the resistive strain gauge. In a similar development, intrinsic fibre Fabry-Perot fibre optic strain sensors were used for vibration damping and also for controlling the shape of a space-based radar satellite [Mason, 1992]. Two FFP sensors based on internal mirrors were surface bonded onto the main beam of the radar. The information provided by the sensor was used for controlling the shape. Strain resolution to better than  $10 \mu\epsilon$  was obtained with a 9 mm gauge length. The advantage of intrinsic FFP sensors is that the system could well be extended to a serially multiplexed array of FFP sensors, which could probably be used to control other aspects of the structure like position or stiffness.

Local internal stress analysis in composite materials has been demonstrated using a Fabry-Perot fibre optic strain sensor [Lesko *et al.*, 1992] which provided accurate strain measurements. An extrinsic FP sensor of the type described by Murphy *et al.*[1991] was used as the optical strain gauge and results were in agreement with those obtained using a resistance strain gauge. Using a 4 mm gauge length, the phase sensitivity of the FFP was found to be  $5.6 \text{ deg } \mu\epsilon^{-1}\text{cm}^{-1}$ . The disadvantage of the system was the incremental nature of the sensor readout which necessitates sensor initialisation whenever the power to the sensor is interrupted.

A technique for the measurement of the absolute value of optical path length using an optical fibre sensor strain gauge when applied to quasi-static strain measurements has been reported [Ohba *et al.*, 1989]. A frequency modulated laser diode and dual Fabry-Perot resonators were used; one Fabry-Perot operated as a sensing element and the other as a reference. By sweeping the frequency of the laser diode, the phase at the output of the interferometer could be varied, even for a constant path difference. This allowed the determination of absolute path imbalance in the reference etalon by simultaneously observing, in transmission, the number of fringes from the sensing and reference interferometers. This scheme is of interest because it could be extended to a multiplexed system by simply cascading several fibre Fabry-Perot resonators. The measurement range of the system was limited by the unstable operation of the laser, which mode hopped due to frequency modulation of the source, and the sensitivity was limited by the source coherence length. The ambiguity and initialisation problems, as related to interferometric strain sensors which use incremental read out, was further addressed in a technique which utilised two orthogonally polarised identical interference signals (one in the vertical and the other in the horizontal), which were phase shifted with respect to each other [Furstenau *et al.*, 1992]. The interference phase difference between the two signals depends on the birefringence of the interferometer arms, and this birefringence varies with the stress. Simultaneous measurement of the continuously varying phase difference between the two signals yields an analogue (polarimetric) output, which could be used for initialisation of the incremental read out. The relative phase shift per unit strain (optical fibre gauge factor) of 0.794 obtained

experimentally was in agreement with reported data. However, although the problem of ambiguity was eliminated, but the cost was a corresponding reduction in the resolution of the system.

Further improvement in resolution can be made by using white light interferometry (WLI) [Al-Chalabi *et al.*, 1983] which solves the ambiguity problem by allowing absolute measurement of the differential phase and potentially has a greater multiplexing ability. A fibre optic sensor system exploiting the principles of WLI, using a Mach-Zehnder interferometer having both fibre and bulk optical components, has been demonstrated for the measurement of static strain [Gerges *et al.*, 1987]. They used a homodyne signal processing approach to lock the interferometer to the quadrature point nearest to maximum visibility. This scheme has the advantage of an extended unambiguous measurement range and the ability to measure absolute path imbalances. A WLI interferometric temperature sensor using two in-line fibre optic Fabry-Perot interferometers of equal cavity length, one used as the sensor and the other as the receiver interferometer, was reported [Chung and Taylor, 1990]. Although this sensing arrangement performed well for low temperatures it suffered from a decrease in visibility with temperature rise as the cavity length difference between the two fibre Fabry-Perot interferometers (FFPIs) increased. This necessitated the changing of FFP pairs with slightly different lengths in order to cover the temperature range of 26 - 108°C (a procedure that may be unsuitable for field deployment). An optical force and temperature sensor [Picherit *et al.*, 1990] based on two single-mode fibres, one weakly birefringent and the other strongly birefringent, used the principle of WLI to simultaneously recover the force and temperature information. The two birefringent fibres formed the sensing interferometer while the receiver interferometer was a Michelson with mechanical scanning. The low birefringence fibre is more sensitive to force or pressure, whereas the highly birefringence fibre responds more readily to temperature and these were exposed to a force field and a temperature field respectively. By scanning the receiver interferometer, phase information caused by force and temperature could be simultaneously recovered. Using a 40 cm length of low birefringence fibre ( $\lambda = 1300$  nm) a strain resolution

of about  $0.1 \mu\text{m}$  was achieved, while a 15 cm length of high birefringence fibre was able to resolve  $\sim 1^\circ\text{C}$ . The system was limited by low strain and temperature resolution despite the use of long lengths of sensing fibres. An optical fibre Young's interferometer using white light interferometry techniques has been demonstrated for the measurement of temperature and strain [Chen *et al.*, 1991c], with temperature and strain sensitivities of  $115.2 \text{ rad } ^\circ\text{C}^{-1}\text{m}^{-1}$  and  $0.78 \text{ rad}/\mu\epsilon$  respectively. The sensing interferometer arms (i.e. sensing and reference) consist of single-mode fibres and sections of free space. These fibres are set at a known distance (analogous to the slit separation in Young's double slit experiment) from each other. The free space section is used to provide the spatial scan covering the operating range. The output signal was processed using a CCD array. This arrangement has advantages of simplicity in construction and also the ability to minimise the spatial coherence mismatch associated with conventional electronically scanned receiving interferometers. The use of two arms, however, may constitute a common mode rejection problem. The principles of white light interferometry have been utilised in miniature pressure or temperature probes for physiological applications (for example; measurement of blood temperature) [Meggitt, 1994]. The sensing interferometer was an extrinsic FP formed between a cleaved end of a single-mode fibre and a mirrored surface. The mirrored surface was in the form of a short length of a silvered  $600 \mu\text{m}$  diameter stub, which was set in a miniaturised aluminium tube into which the cleaved end of the sensing fibre had been retrofitted to form a sensing cavity of  $\sim 100 \mu\text{m}$ . A bulk optic FP with one mirror scanned by a piezo-electric transducer was used to recover the signal. The sensor temperature resolution was determined to be  $\sim 0.02^\circ\text{C}$ , and was limited by system noise only.

Fibre optic Bragg gratings have also been used for strain or temperature measurements [Morey *et al.*, 1989; Meltz *et al.*, 1989; Kersey and Berkoff, 1992; Braddy *et al.*, 1994]. Linear in-fibre gratings are characterised by a regular periodic variation of the core refractive index which is produced by UV photon absorption [Meltz *et al.*, 1989]. The ability of the grating wavelength to respond to strain or temperature changes in the fibre grating has allowed its use as a strain or temperature sensor. The intrinsic nature of in-fibre Bragg gratings and wavelength encoded

operation make them attractive for sensing applications. However, the use of Bragg gratings requires accurate tracking of small wavelength shifts of the order of a hundredth of a nanometre. Although some work on wavelength demodulation techniques with limited resolution have been reported using filtering concepts [Melle *et al.*, 1993], the accurate determination of the shift in the Bragg wavelength of a fibre Bragg grating sensor remains a problem to be solved. Accurate measurement of wavelength with precision relies on costly and slow devices such as optical spectrum analysers or monochromators which are impractical for field deployment owing to their size and weight. Sensitive phase shift techniques based on unbalanced fibre interferometers have been used to detect Bragg wavelength shifts and provided higher resolution than could be obtained with simpler methods of wavelength determinations [Kersey *et al.*, 1992a]. In such systems the output phase depends on the wavelength, such that it becomes possible to monitor the shift in wavelength of stressed in-fibre Bragg gratings. This gives high performance for a single grating, but the method is not well-suited for interrogating a large number of grating sensors.

A major advance in the field of optical fibre strain gauging has been the measurement of an arbitrary state of strain using a fibre optic strain rosette. An optical fibre strain rosette is the analogue of an electrical strain rosette (chapter 1) and has been based either on localised polarimeters [Measures *et al.*, 1988] or a fibre optic Michelson interferometer [Measures, 1990, 1990a]. The former sensor is limited in its strain sensitivity, while the later suffers from the need to maintain common-mode strain-rejection of the four optical fibre leads. An optical fibre rosette which combines the high strain sensitivity of the Michelson interferometer with the single fibre referencing property of the polarimeter is based on a fibre Fabry-Perot strain gauge [Valis *et al.*, 1990]. The performance of this device is comparable to that of an electrical strain rosette. However, a common weakness for these optical fibre strain rosettes is the lack of self initialisation, because they are based on incremental read out measurements. Hence they cannot be used for absolute measurements nor can they re-initialise themselves after power turn off.

There has been significant progress in the development of fibre optic strain gauges. A commercially available optical fibre strain gauge has been reported [Mason *et al.*, 1992]. This gauge is capable of operating with either a Fabry-Perot for localised measurements or a polarimetric sensor for integrated measurements. The Fabry-Perot configuration uses an intrinsic cavity with semi-reflective splices. However, there still remains the one major problem, in that the absolute relative phase is lost when the system is switched off.

Intrinsic fibre optic interferometric strain sensors may face considerable limitations if cross sensitivities of temperature and strain are not accounted for. This is discussed further in section 6.4. It has been shown [Mardi *et al.*, 1992] that, by using special types of coated optical fibres (for example, standard single-coat, dual-coat or hermetic), the effects of temperature may be minimised. The standard single coat fibre had a single layer of acrylate coating applied to the cladding, the second fibre had a dual acrylate coating applied to the cladding while the hermetic fibre had a thin amorphous carbon layer between the cladding and the standard acrylate coating. For these fibres, the extra coating is much more sensitive to strain than to temperature, and thus it enhances the fibres' strain sensitivity making it much more sensitive to strain than to temperature. Consequently, for an optical fibre coated with a thick layer, and subjected to a longitudinal stress, the fibre experiences a tension/compression in the longitudinal direction, which is primarily controlled by the properties of the coating. Thus the axial extension/contraction is much larger than would the case be for an uncoated fibre. Longitudinal strain has been found to increase 13 fold for a teflon-plastic coated cladding compared to an uncoated fibre [Budiansky *et al.*, 1979]. It has also been possible to enhance or reduce the strain phase sensitivity of an optical fibre by choosing an appropriate value of the relative refractive index difference between the core and cladding [Egalon and Rogowski, 1993]. They showed that strain sensitivity can be significantly altered by choosing a large value of the relative refractive index difference because the larger the value, the smaller the induced strain phase shift. The details are not discussed in this work but can be found in that paper. A better approach to minimisation of temperature effects on strain measurements has been demonstrated

by use of temperature compensation techniques [Hogg *et al.*, 1991] in which temperature effects appearing as apparent strain were addressed analytically by their scheme which used a fibre Fabry-Perot interferometer. In this present research, thermally induced apparent strains have been experimentally determined for an unloaded cantilever under ambient temperature fluctuations and then added algebraically to the observed strain measurements in order to correct for ambient temperature fluctuations, (section 7.3.7.1).

### 3.4 Conclusion

There are a variety of appropriate optical fibre sensors available for the measurement of strain as discussed above. The choice of sensor is dependent upon the desired qualities of a strain gauge and also the multiplexing approach. None of the optical fibre strain gauges described embraces all the desired qualities of an ideal strain gauge (section 3.2). The microbend sensor, although simple lacks the accuracy and high spatial resolution required of a practical strain gauge. It also relies on a complex corrugated structure, is bulky and therefore is not suitable for strain gauging.

A Mach-Zehnder interferometer used as strain gauge provides good strain sensitivity. However, it has a poor degree of localisation, contradicting the requirement of a small gauge. Although as indicated in the foregoing review, the Michelson interferometer can be used for strain measurements, the need to provide a high degree of common mode rejection may limit the usefulness of this device for slowly varying measurands such as strain and temperature. Single fibre approaches (i.e dual mode, polarimetric, fibre Fabry-Perot and Bragg sensors) are preferred as they eliminate the problems associated with lead pairing. They are better suited to quasi-static strain measurements than the fibre Michelson interferometer. However, they may require some form of source modulation for signal processing purposes, unless used in conjunction with white light interferometry.

Polarimetric sensors have been used as a means of extending the unambiguous measurement range, but with a concomitant reduction in resolution, which is not a desired quality for practical strain gauging. Polarisation maintaining fibres can only offer a coarse means for the measurement of strain even though long path lengths are used. The need to use additional optical components in the vicinity of the fibre (analyser and in some cases Soleil-Babinet compensator and Wollaston prisms) to recover the phase information can severely restrict the practical use of these sensors. Dual mode strain sensors are similarly limited in sensitivity.

From the foregoing discussion it can be understood that the preferred choice of optical fibre strain gauge is either the intrinsic fibre Fabry-Perot or in-fibre Bragg grating. Both of these gauges have the ability to measure strain in a highly localised region of the structure, are intrinsic, sensitive and lend themselves to multiplexing. Both of these sensors are lead insensitive since a single input and output fibre is used. The Bragg sensor can provide absolute strain encoding but is a lower strain-resolution device than the in-line fibre Fabry-Perot. In order to appreciate the characteristics of two beam interferometric strain gauges, these gauges have been classified according to their optical configuration as Mach-Zehnder, Michelson, low finesse Fabry-Perot, Polarimetric, modal and fibre Bragg interferometric sensors. Table 3.1 gives a brief summary of the characteristics of these configurations.

sensor type	Number of lead fibres	Axial strain sensitivity	Requirement of fusion splice	Degree of localisation	Multiplexability	Multi-parameter sensing capability
Mach-Zehnder	4	High (0.1134 rad $\mu\epsilon^{-1}\text{cm}^{-1}$ $\lambda=633$ nm) [Valis <i>et al.</i> , 1991]	Not required	poor	Very high	Moderate
Michelson	2	Very high (0.2269 rad $\mu\epsilon^{-1}\text{cm}^{-1}$ $\lambda=633$ nm) [Valis <i>et al.</i> , 1991]	Not required	Fair	Low	Moderate
Fibre Fabry-Perot (intrinsic) Low finesse	1	Very high ( 0.1186 rad $\mu\epsilon^{-1}\text{cm}^{-1}$ $\lambda=1300$ nm) {equivalent to 0.244 rad $\mu\epsilon^{-1}\text{cm}^{-1}$ $\lambda = 633$ nm) [Kaddu <i>et al.</i> , 1993]	Required	Good	Very high	Moderate

Dual-mode	1	Low (0.0021 $\text{rad}\mu\epsilon^{-1}\text{cm}^{-1}$ , $\lambda=780 \text{ nm}$ ) [Lu and Blaha 1989]	Required	Good	Low	Moderate
Polarimetric	1	Low (0.0021 $\text{rad}\mu\epsilon^{-1}\text{cm}^{-1}$ , $\lambda=633 \text{ nm}$ ) [Hogg <i>et al.</i> , 1989]	Required	Good	Low	High
In-fibre Bragg grating	1	Low ( $\Delta\lambda/\mu\epsilon =$ 0.703 $\text{pm}/\mu\epsilon$ , $\lambda=821.5 \text{ nm}$ ) [Melle <i>et al.</i> , 1993]	Not required	Good	Very high	Moderate

Table 3.1 Comparison of localised fibre optic strain gauges

In conclusion, the concept of strain in relation to structural stress analysis has been introduced. Conventional and optical strain measurement techniques have been discussed. In order to realise a suitable practical optical fibre sensor system used in a multiplexed configuration for the measurement of static strain over several sites of a structure, it is proposed that low finesse FFP sensors be used and demodulated using white light interferometry. Accordingly, in-line fibre Fabry-Perot sensors were fabricated and investigated. The sensor was surface adhered onto a

mild steel cantilever beam for longitudinal strain analysis. The FFP strain gauge satisfies many of the criteria for strain gauging. This device may be regarded as the optical analogy of the resistance strain gauge. A second alternative device receiving much interest, the in-fibre Bragg grating has been taken advantage of in this work in constructing for the first time an intrinsic double/triple grating-based fibre Fabry-Perot, called, in this work, “ a dual or a triple FFP interferometer”. The dual/triple FFP interferometer is based on low IFBG reflectors which are introduced into the core of the same fibre in such a way that two/three pairs of IFBG reflectors, with each grating pair reflecting a different wavelength, form the dual/triple FFP sensing element. Although, a diffraction phase mask can write reflection Bragg gratings into the cores of optical fibres (subject to UV exposure) at only one wavelength, these grating pairs, were written using the same diffraction phase mask. This optical device has the advantage that it does not rely on a fusion splice, is amenable to multiplexing and can be used to measure several parameters including strain and temperature using WLI techniques. The details of the fabrication of the dual/triple FFPI sensors and measurements obtained using these devices are discussed in chapter 8.

## **CHAPTER 4**

### **MULTIPLEXED INTERFEROMETRIC FIBRE OPTIC SENSORS**

With the increasing usage of optical fibre sensors in engineering structure applications, a large number of sensors may be required in order to monitor the potentially varied number of parameters of interest, including strain. In such structural systems, the use of an efficient, cost-effective multiplexed sensor system is often desirable. Various approaches to sensor multiplexing have been reported, which may be divided into several categories including frequency, time-division, polarisation, and coherence multiplexing [Dakin, 1987; Kersey and Dandridge, 1988, 1988a]. The development of an efficient multiplexing technique could lead to a general improvement in competitiveness with conventional technologies in a broad range of applications. In doing so, it has to be observed that the actual multiplexing method chosen has a significant impact on the overall sensitivity. This is usually the case when the method of signal recovery involves unbalanced interferometers as the performance is normally limited by the laser phase noise [Jackson, 1994]. This chapter briefly discusses some of the commonly used multiplexed interferometric optical fibre sensor schemes with an indication of their relative degree of success.

#### **4.1 Frequency division multiplexing**

Frequency-division multiplexing (FDM) in interferometric fibre sensors uses a frequency modulated laser source (typically a laser diode) along with a network of unbalanced

interferometers to produce a phase generated carrier output signal. Two main approaches have been used to provide phase generated carrier outputs, namely (a) a frequency ramped laser modulation [Giles *et al.*, 1983] known as frequency modulated continuous wave (FMCW), and (b) a sinusoidal frequency modulation of a laser diode. The principle of FMCW relies on the beating between two chirped optical signals, which are delayed in time with respect to each other. The period of the beat frequency produced at each interferometer output is dependent upon the frequency excursion of the chirp, the chirp rate and the interferometer path imbalance. A different optical path difference is assigned to each interferometer, thereby allowing the beat frequency associated with each sensor element to be unique and separable. Giles *et al.*, [1983] investigated the FMCW method based on coherence sensing with a modulated laser diode. The minimum detectable phase shift was limited by induced intensity noise. In this early FMCW work, in which no attempt was made to extract signals from individual sensors, the raw multiplexed outputs were seen to be noisy with intermodulation terms visibly seen.

Another implementation using the FMCW technique was demonstrated in a serial network of three Mach-Zehnder interferometric fibre optic sensors, with each sensor having a different path imbalance (28, 49 and 84 m) [Sakai, 1987]. This work produced relatively poor detection sensitivities of  $\sim 1000 \mu\text{rad}/\sqrt{\text{Hz}}$  primarily due high levels of phase noise which may have been produced by the large path sensor imbalances. Additional problems included non-linearity in laser modulation and intrinsic sensor cross-modulation effects.

The second FDM approach is based on the use of sinusoidally frequency-modulated diode laser sources to provide phase generated carrier outputs [Dandridge *et al.*, 1987]. This multiplexed sensor scheme used a sinusoidally-modulated laser diode which exhibited improved sensitivities ( $\sim 20 \mu\text{m rad}/\sqrt{\text{Hz}}$ ) compared to the methods reported by Giles *et al.*, [1983] and Sakai *et al.* [1987] employing FMCW. Although the method of FMCW is simple in concept and has the capability to determine absolute path imbalance in each sensor, its sensitivity is limited by the large phase noise due to laser injection current-driven frequency modulation.

Furthermore, any deviation of the frequency versus time relationship from linearity increases the uncertainty in the beat frequency and hence the path imbalance [Culshaw and Dakin, 1989].

#### **4.2. Time-division multiplexing**

The concept of time-division multiplexing, used in combination with fast electronics, is a well-known technique in communication and radar systems. It normally requires a repetitive short pulse whose duration is chosen in such a way that returning pulses, from each sensor, are separated in time and therefore do not overlap at the photodetector. The repetition rate must be low enough to allow a pulse to return from the most distant element of the sensing array before the following pulse returns from the nearest sensing element [Brooks *et al.*, 1987]. The time differences between sensor returns, are achieved by arranging differing total signal propagation delays for each sensing element.

A technique of time division multiplexing which involved the use of differential path-matched interferometry demodulation with a compensating interferometer was used in addressing and demodulating an eight-element interferometric sensor array [Kersey *et al.*, 1988c, 1988d]. The arrangement is based on a transmissive tapped serial array which utilises low coupling-ratio fibre splitters to couple light from each sensor to the output fibre bus. The output signals were demodulated using phase generated carrier techniques applied to one arm of the compensator. The system, however, was limited by high levels of intrinsic optical cross-talk between sensor elements ranging from  $\sim -49$  dB to  $\sim -25$  dB, which may have been generated by multiple cross coupling in the network. The use of large path imbalances between sensor coils is another drawback of the system.

The issue of phase noise effects in the form of cross-talk, which affect the sensitivity in FMCW and TDM multiplexing systems has been addressed in an array of two unbalanced interferometers monitored in transmission [Brooks *et al.*, 1986, 1987], and in a serial array of two reflective Michelson interferometers [Santos and Jackson, 1991] utilising time division

addressing with their status read by coherence tuned sensing. The attractive features of coherence sensing (section 4.5.1) namely, large unambiguous measurement range and self initialisation, were combined with TDM which enabled sensors of identical path imbalances to be addressed. This is attractive as each sensor has equal sensitivity, but a large amount of noise was introduced by the gating process used to select a particular channel which affected the overall sensitivity. Sensitivities of better than  $40 \mu\text{rad}/\sqrt{\text{Hz}}$  at signal frequencies above 600 Hz were reported by Brooks *et al.*, while Santos and Jackson obtained detection sensitivities of  $20 \mu\text{rad}/\sqrt{\text{Hz}}$  at 3 kHz and  $0.3 \mu\text{rad}/\sqrt{\text{Hz}}$  at 1 Hz with a crosstalk of -65 dBV. The requirement of long delay fibres may introduce high intrinsic fibre losses which could limit the number of usefully addressed sensors.

A Mach-Zehnder 'ladder topology' (parallel arrangement) illuminated with a highly coherent source (subject to frequency modulation) to enable signal recovery using phase generated carrier techniques was demonstrated with ten sensors [Kersey and Dandridge, 1989]. Optical pulses were generated using an acousto-optic modulator and long fibre delay coils positioned between each sensor provided the necessary time delays between signals from different sensors. For a two-sensor network, detection sensitivities observed were about  $15 \mu\text{rad}/\sqrt{\text{Hz}}$  at a frequency of 1 kHz with a sensor-to-sensor crosstalk level of about 50 dB. Although this type of network is attractive in terms of number of sensors being addressed, problems of polarisation fading in each interferometer sensor and fluctuating sensitivity limits their usefulness. McGarrily and Jackson [1992] attempted to solve the problem of polarisation fading by using a reflective binary tree arrangement which was capable of supporting up to eight fibre Michelson sensors. In reflective mode, polarisation fading is minimised because reflections would be at normal incidence (where light is unpolarised). Michelson sensors with Faraday rotator mirrors were used instead of coated fibre ends, further reducing the polarisation. The phase sensitivity of this system was  $25 \mu\text{rad}/\sqrt{\text{Hz}}$  in a 1 kHz bandwidth. The system was mainly limited by the phase noise of the laser.

### 4.3 Wavelength division multiplexing

Wavelength division multiplexing (WDM) has been used primarily in communication systems [Lin *et al.*, 1988]. The multiplexing scheme involves guiding optical power to each sensor, and back to a corresponding photodetector via a route which depends on a wavelength designated for interrogation of that particular channel. The WDM multiplexing scheme is theoretically the most efficient technique possible, as all the light from a particular source could in principle be directed to a corresponding photodetector with minimal excess loss [Kersey and Dandridge, 1988a]. However, the use of this technique in optical sensor applications has not received much practical attention for reasons of the complexity of optical devices required to selectively tap a certain wavelength from a fibre bus to its respective sensor elements. Furthermore, the cross-talk between sensors is dependent upon the degree of wavelength discrimination, which is reported to be of the order of about 15 to 20 dB [Kersey, 1991]. Consequently, WDM is not an attractive option for the multiplexing several optical fibre sensors.

It has been possible to experimentally demonstrate a multiplexed sensor array when the concepts of WDM are combined with TDM [Kersey, 1991]. In this work, Kersey demonstrated, for the first time, a 14 element multiplexed interferometric sensor array based on hybrid WDM/TDM, operated at two different wavelengths. Although, the scheme performed quite well, it had a high level of cross modulation. A recent (intensity based) technique worth mentioning, is the wavelength division multiplexing of three fibre temperature sensors, based on the temperature dependence of differential spectral transmittance or reflectance of dielectric edge multilayer filters [Wang *et al.*, 1995]. As both the refractive indices and thicknesses of dielectric layers are temperature dependent, their transmittance or reflectance are also functions of temperature, and thus the intensity at a given wavelength is also a function of temperature. A resolution of 0.5 °C was obtained with this multiplexing scheme in the range of 30 - 120 °C, but the arrangement had a series of drawbacks including cross-talk, low SNR due to the high losses introduced by the filters (which were simply glued to the fibres) and the dependence of the sensor output on the modal power distribution in the fibre. A better alternative could be to

use in fibre Bragg grating sensors instead of the multilayer dielectric filters and employ phase sensitive techniques, although low optical power levels returned to the detector may pose a signal-to-noise problem.

#### **4.4 Polarisation multiplexing**

Polarimetric sensors utilise the relative change in optical path length which occurs between two orthogonally polarised modes of a high birefringence fibre when it is subjected to an external influence. This scheme is attractive because of the simplicity of its single fibre configuration. Simultaneous recovery of phase and polarisation information in interferometers made from birefringent components, in which the high resolution of interferometric sensors was combined with the larger unambiguous measurement range of polarimetric devices, has been exploited [Kersey *et al.*, 1989]. A polarimetric multiplexed fibre sensor scheme addressed in coherence has been reported [Chen *et al.*, 1991a], which involved an array of 10 pressure sensors on a length of a high birefringent fibre. A Michelson interferometer was used as the processing interferometer, thereby introducing a matching time delay to bring the two polarisations back into coherence by adjusting one of its mirrors. The spatial resolution obtained with this scheme was about 4 cm. Cross-talk between sensing units and spurious peaks occurred as the number of sensing elements along the fibre increased, which limited the sensitivity. In a similar fashion a network of three polarimetric sensors was read in coherence [Santos and Leite, 1993], using a low coherence source. The phase sensitivities obtained for the three successive sensors were  $26 \mu\text{rad}/\sqrt{\text{Hz}}$ ,  $35 \mu\text{rad}/\sqrt{\text{Hz}}$ , and  $21 \mu\text{rad}/\sqrt{\text{Hz}}$ , respectively. It was found that the dominant noise was due to electronic noise arising from the electronic circuitry which was due to low levels of optical power in the system. The method of polarisation multiplexing does not seem to be well-suited for multiplexing a large number of sensors.

## 4.5 Coherence multiplexing

Coherence interferometry is a sensing scheme based on two interferometers in series, a sensing interferometer and a receiving interferometer. The method requires that the source coherence length be much less than the path imbalances of both the sensing and receiving interferometers. This means that the two beams from either one of the interferometers are mutually incoherent and, therefore unable to give a significant fringe contrast. A fringe pattern is obtained at the output of the two serially connected interferometers when the path imbalance of the receiving interferometer is matched to that of the sensing interferometer [Al-Chalabi *et al.*, 1983] to within the coherence length of the source. This method has been utilised in addressing several interferometric fibre optic sensors by coherence multiplexing [Brooks *et al.*, 1985]. The scheme allowed for the simultaneous demodulation of an array of fibre optic interferometric sensors with an equal number of parallel receiving interferometers, each of which had its own detector. Laser sources of moderate coherence lengths (greater than 1 m) have been used in such sensing schemes. Kersey and Dandridge [1986], investigated a coherence multiplexed system of two interferometric optical fibre sensors, operated with a frequency-modulated laser source, in which it was shown that the relative excess noise in the system increased with an increase in source coherence length. Excess noise is due to interferometric conversion of laser frequency-jitter induced phase in each of the interferometers in the optical system.

Sensor systems based on coherence multiplexing have been limited by high levels of phase noise and sensor cross-talk. This is because, when lasers of moderate coherence lengths are used as the light sources, the interferometer path imbalances are large since the coherence length is also large (in the 2-20 m range [Brooks *et al.*, 1985]). While this has the advantage that stringent tolerances in optical path compensation between the interferometer pairs are not necessary, it gives rise to large levels of source-induced noise (due to the unmatched optical path) which severely degrades the sensors' sensitivity. Furthermore, these systems are susceptible to environmental instabilities because of the long lengths of the sensing fibres. Feedback techniques may be used to provide compensation, but this removes the passive nature

of the sensor and may increase the complexity of the system. Although coherence multiplexing has several advantages, including the ability to provide the absolute value of the measurand and offers a large unambiguous measurement range, it is only attractive when multiplexing a few sensors because, as the number of sensors increases, the signal decreases and this eventually results in a poor signal-to-noise ratio. The level of cross-talk and source induced noise can be avoided or substantially reduced by exploiting the principles of *low coherence interferometry*, usually known as *white light interferometry* (WLI), in which broad band sources (for example a light emitting diode or a superluminescent diode) and nearly balanced interferometers are used. The term WLI is normally applied to a sensing technique in which the coherence length of the source is very much less than that of a laser, and light emitting diodes are often used as source for this technique. The very low coherence length of these sources (typically in the micron range), means that highly tunable and stable receiving interferometers are required so that the sensor imbalance is matched within the source coherence length. The terms low coherence interferometry and white light interferometry have generally been used interchangeably.

#### **4.5.1 Introduction to white light interferometry**

The principle and application of WLI to optical fibre sensors has been discussed by Bosselman and Ulrich [1984] and it has been shown that several sensors can be passively multiplexed and demodulated using a single receiving interferometer. The sensing interferometer acts as a filter which produces a channelled spectrum with a periodicity that is inversely proportional to the optical path imbalance [Koch and Ulrich, 1990]. An interference pattern is obtained by matching the imbalance in the receiving interferometer to that of the sensing interferometer. In contrast to conventional interferometric sensors which generally operate as incremental sensors, WLI provides a means of identifying both the absolute optical interference fringe order and the phase in an unbalanced sensing interferometer. This is possible because of the limited coherence length of the source which allows recognition of the central fringe. A disadvantage of using white light interferometry is the requirement of two interferometers which may increase

the complexity over a single measuring system, but the method of WLI provides other advantages including high immunity to perturbations of the transmission medium, support for self initialisation which is particularly important for the measurement of slowly varying parameters. White light interferometry sensor systems have been used to monitor measurands such as displacement [Gerges *et al.*, 1990; Martin *et al.*, 1991], pressure [Chen *et al.*, 1990, 1991a; Norton, 1992], strain [Gerges *et al.*, 1987, Chen *et al.*, 1991c], temperature [Xu *et al.*, 1993; Kaddu *et al.*, 1994], and refractive index [Trouchet *et al.*, 1992] and provided good sensitivity. White light interferometry has also been used for the measurement of spurious polarisation cross couplings and rejections in high birefringence fibres. Such a measurement is of particular application to intrinsic interferometric sensors such as the fibre gyroscope [Lefevre, 1990].

The sensing interferometer in white light interferometry may be of any type (Michelson, Mach-Zehnder or Fabry-Perot) and may be either intrinsic or extrinsic. The receiving interferometers are normally scanned either mechanically (temporal domain), to provide a wide measurement range at low repetition, or electronically with, for example, a CCD photodiode array (spatial domain) offering fast read-out over a limited measurement range. A simple implementation of spatial scanning [Chen *et al.*, 1991] used a tilted Fizeau interferometer, formed using two optical flats with a small angular displacement. Another scheme used a bulk Michelson receiver interferometer with a tilted mirror to provide a spatial fringe pattern [Koch and Ulrich, 1990]. The main advantage of electronic scanning is that the CCD array is read without moving parts. However, in these systems, the interferogram is produced by overlapping two expanded beams and detected using a CCD array, and so the fringe visibility is reduced due to a spatial coherence mismatch [Chen *et al.*, 1991]. Moreover a charge coupled detector is a source of high noise, and the need to collimate the beam followed by its expansion requires bulk optic devices which may compromise the stability of the receiving interferometer. The method of electronic scanning requires a trade off between resolution and dynamic range [Chen *et al.*, 1990a], which may be critical in terms of operating range (which is set by CCD spacing and

length) for certain applications including coherence multiplexing where large operating ranges may be required.

Receiving interferometers have also been scanned using a piezo-electric transducer (PZT) in which several turns of optical fibre are wound around a PZT stretcher. Variation of the applied voltage provides a limited scanning range. A scheme well-suited for use with multiplexing several sensors is a receiving interferometer with a mechanically scanned (temporal domain) mirror. This scheme requires high mechanical stability, in order to obtain a precise measurement of receiver path imbalance to yield the optimal correlation with that of the sensor interferometer. It has advantages of higher signal-to-noise ratio than electronically scanned systems [Chen *et al.*, 1992], simplicity, and a large operating measurement range [Koch and Ulrich, 1991] and, therefore, a large dynamic range which is useful when several sensors are multiplexed.

#### **4.5.2 WLI multiplexed sensors**

The technique of WLI allows an array of interferometric sensors to be multiplexed by exploiting the coherence properties of the light from a low coherence source. A number of multiplexing configurations for interferometric sensors using low coherence processing have been developed, including tapered monomode fibres used as remote sensors in low coherence multiplexed systems [Giovannini *et al.*, 1993], low coherence reflectometry in multiplexed sensor measurements on an array of remotely located cavities [Sorin, 1993], and white light path-matched differential interferometry [Santos and Jackson, 1991]. Santos and Jackson, [1991] used a parallel array of two fibre Michelson interferometers applied to the measurement of quasi-static and dynamic parameters. The scheme combined the principles of WLI with TDM addressing, using a bulk optic Michelson interferometer as the receiver interferometer.

An absolute displacement sensor [Koch and Ulrich, 1990] utilising two parallel coupled transducers, both of the Michelson type with an electronically scanned white light

interferometer, provided a good displacement resolution of 20 nm with a limited measurement range of 80  $\mu\text{m}$ . A low coherence technique [Ribeiro *et al.*, 1993] was used to identify the individual sensors in a multiplexed array and to interrogate their measurement status. In its basic configuration, the output from a low coherence source was directed into a bulk receiving transmission Michelson interferometer. The output signal was then injected into a  $2 \times 2$  directional coupler and used to illuminate two bulk Michelson sensing interferometers. The system resolution was better than 50 nm with a displacement range of about 200  $\mu\text{m}$ . In this case the receiving interferometer output light is sent to the sensing interferometer because there is reciprocity between the sensing and receiving interferometers. The advantage of the system was its minimal cross-talk, but the use of bulk optic sensors and the requirement of additional 3 dB couplers, with increased number of sensor elements to be multiplexed, were its serious drawbacks. The multiplexing potential of low coherence demodulated fibre Fabry-Perot sensors of different cavity lengths [Nellen *et al.*, 1994], configured in a parallel arrangement was exploited for the measurement of axial strain. Temporal scanning was accomplished using a bulk Michelson interferometer. The measured Fabry-Perot phase sensitivity of  $(1.69 \pm 0.07) \times 10^7$  ( $\lambda = 840 \text{ nm}$ ) agreed closely with the calculated value of  $1.73 \times 10^7$ . The disadvantages of their system was that the number of sensors for parallel multiplexing was limited by the necessity to use a chain of  $2 \times 2$  couplers. In addition there are as many fibre paths as there are sensors.

#### 4.6 Conclusion

The optical multiplexing methods introduced and described briefly here, offer a variety of means of polling a number of interferometric sensors for parameter monitoring. Not all of these methods offer a practical solution to sensor multiplexing. In sensor multiplexing, the major requirement is to address and separate effectively several separate parameters (or the same parameter at separate location) simultaneously on a common optical highway. The methods of FMCW, TDM, and polarisation multiplexing are limited by phase induced noise and cross-talk, which degrade the sensitivity of the system. The method of wavelength division multiplexing

requires complex optical components which are expensive and unattractive for a practical multiplexed sensor scheme.

For this research it is proposed that the technique of white light interferometry be used to multiplex an array of intrinsic fibre Fabry-Perot sensors in series. The method of low coherence multiplexing has the advantages of high signal-to-noise ratio, immunity to source noise, high spatial resolution, and the ability to offer absolute measurements. The principles of white light interferometry can be used in many applications, including slowly varying parameters with several attractive features such as a wide unambiguous measurement range suitable for low coherence multiplexing, and its support of totally passive interferometric sensors.

## CHAPTER 5

# DEVELOPMENT OF INTRINSIC FIBRE FABRY-PEROT SENSORS

This chapter describes the details of the design and construction of practical in-line intrinsic fibre-optic Fabry-Perot sensors based upon a fusion splicing technique. The fundamental requirements of optical fibre sensing and multiplexing given in chapter 1 are applied to the specific problem of fabricating such sensing interferometers. Current opinions about fibre Fabry-Perot fabrication are discussed to appreciate the method which was chosen.

### 5.1 Fabrication Process

#### 5.1.1 Background

In 1889 Charles Fabry and Alfred Perot [Vaughan, 1989] first introduced their concepts on interference due to waves successively reflected between two partially reflecting silvered plane glass plates set accurately in parallel. Since that time, there have been very large numbers of applications involving the use of the Fabry-Perot interferometer including spectral analysis, metrology and parameter monitoring. The fibre Fabry-Perot (FFP) etalon has proven to be useful in a wide variety of applications [Mitchell, 1989; Beheim *et al.*, 1989; Meggitt, 1994] including, for example, as an optical spectrum analyser [Douglas *et al.*, 1981], as a laser diode

frequency stabiliser, and as a sensing element for the measurement of temperature [Lee *et al.*, 1988a, 1989], strain [Murphy *et al.*, 1992], ultrasonic pressure [Alcoz *et al.*, 1990], gas pressure in internal combustion engines [Atkins *et al.*, 1994], and electric and magnetic fields [Yoshino *et al.*, 1982]. In its basic form, an FFP interferometer consists of a single mode fibre (in some cases a multimode fibre [Gunderson, 1990]) with reflectors at its ends or formed within a continuous length of fibre. The reflector mirrors may be metallic or dielectric, single- or multi-layered, and may be attached or deposited using various vacuum techniques. Normally fibre optic Fabry-Perot interferometers employ single-mode fibres because of their ability to guide the light coherently, and so they can be used as interferometer arms. Furthermore, single-mode interferometers allow some design flexibilities which are not possible with multimode configurations. The FFP as a sensor element monitors external perturbations via its spectral reflectance. The spectral reflectance variations can be produced by any perturbation which changes the optical path length between the mirrors. This change in optical path will produce a phase change which can be related to the parameter being measured. The FFP interferometers can be pigtailed and made with arbitrary free spectral ranges (resonator lengths as high as 200 m and as low as 6  $\mu\text{m}$  have been realised). They can be insensitive to polarisation changes, have minimal intrinsic loss, can have a range of finesse values up to very high values (a finesse of 1000 has been reported [Stone and Stulz, 1991]), and can be tuned over more than one free spectral range. An optical fibre Fabry-Perot has the added advantage over a conventional Fabry-Perot (FP) of simplicity in that there is no need for precise mirror alignment. The FFP sensor elements have been manufactured from single-mode fibres by a variety of methods, and the current state of the art of single-mode FFP fabrication is briefly described in the following paragraphs.

Yoshino *et al.*, [1982] fabricated high finesse FFP resonators by depositing multilayer dielectric films onto the ends of polished single-mode fibres using vacuum deposition techniques. In a second method, a lapping technique was employed to fabricate high finesse FFP resonators from a piece of single-mode fibre by carefully polishing its ends, and gluing properly prepared

small size multilayer dielectric mirrors using epoxy resins [Stone, 1985]. Both of these FFP resonators performed well as spectrum analysers and tunable filters, but have had limited application for parameter monitoring because of the non-linearities associated with high finesse FP resonators. A summary of these construction methods used for single-mode FFP sensors is given in figure 5.1.

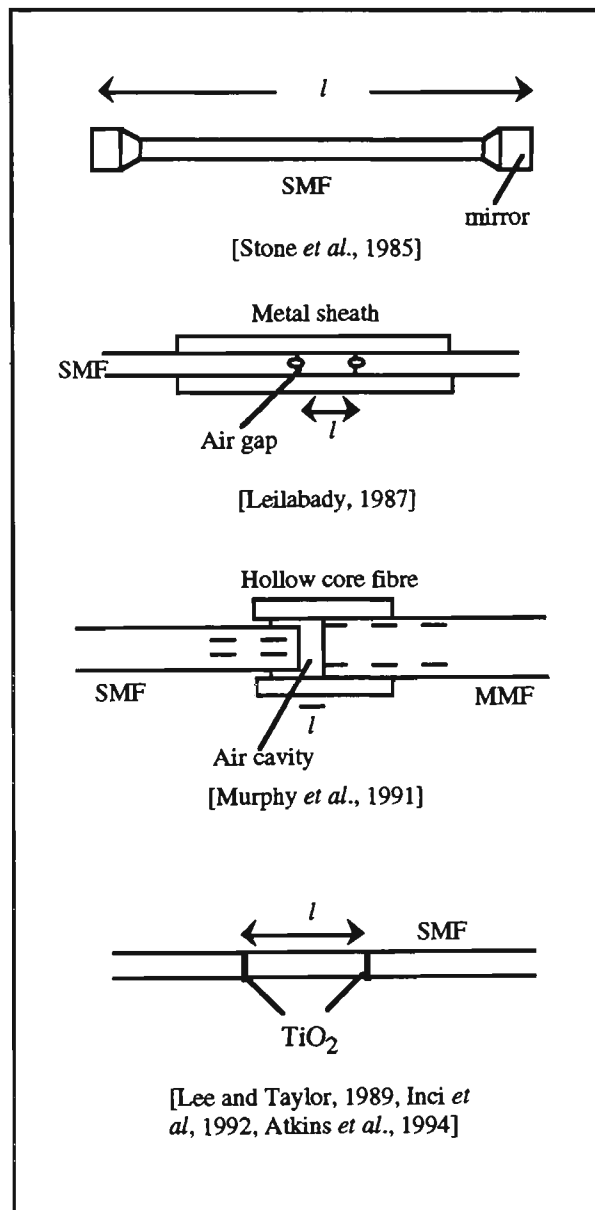


Figure 5.1. Different methods of single-mode FFP fabrication.

Leilabady [1987] developed an extrinsic FFP sensor based on two semi-reflective air gaps. A semi-reflective air gap was fabricated by low-heat fusion splicing of only the cladding regions of two ends of single-mode fibres, forming an air gap in the core region of the fibre. The second air gap was produced in a similar manner to form the FFP cavity. The cavity was then protected using a metallic sheath. Murphy *et al.*, [1991] also reported an extrinsic FFP interferometer based on an air gap cavity. The construction of the sensor involved a single-mode fibre used as the input-output fibre, and a multimode fibre used merely as a reflector. These fibres were placed inside a hollow silica tube, forming an air gap that acts as a low finesse Fabry-Perot cavity (figure 5.1). This type of sensors performed well for a particular application, but the overall size of the sensors is large in comparison with the cross-sectional area of the leading fibre.

Short intrinsic FFP gauges (1-2 mm) used to monitor surface heat transfer rates on turbine blades [Kidd *et al.*, 1992] were produced by applying aluminium coatings on the end of a cleaved single-mode fibre. An internal mirror was formed with the aid of a strengthening bored ceramic tube into which the sensing fibre was held after gluing the coated end to an uncoated lead fibre. A critical issue with this type of sensor is its long term temperature stability. Changes in the physical structure of the glue mean that the joint is expected to become unstable after exposure to elevated temperatures, thus limiting the sensor performance. The reflectors used in this scheme are generally not suitable for use in a practical sensor. Lee and Taylor [1988, 1989] described a technique of fabricating semi-reflective splices in a continuous length of fibre based on a fusion splicing technique. A cleaved single-mode fibre (SMF) whose end was coated with TiO<sub>2</sub> using sputter deposition, was spliced onto a similar uncoated fibre to form the first mirror. A second semi-reflective splice fabricated in a similar way was added to form the FFP cavity. Reflectances of ~ 1-2% were realised using this technique. A further technique of fabricating intrinsic FFP sensors in a continuous length of fibre has been used [Inci *et al.*, 1992] where high reflectivity values (~ 25%) have been realised. The technique is based upon electron beam evaporation of titanium dioxide thin films onto ends of cleaved

single-mode fibres followed by their fusion splicing to similar uncoated fibres to form an internal mirror. Atkins *et al.*, [1994] fabricated low finesse FFP sensors (used for monitoring pressures in internal combustion engines) in a single-mode fibre using techniques similar to Lee and Taylor, based on titanium dioxide sputtering with mirror reflectance in the 2 - 4% range.

Fibre optic Fabry-Perot sensor fabrication by repetitive application of a two stage process involving the vacuum deposition of a mirror coating onto a fibre end, followed by fusion splicing to similar uncoated fibre, produces sensors having the inherent advantages of intrinsic sensing. These sensors have the potential of withstanding reasonable mechanical stresses or high temperature operation. The low finesse intrinsic fibre optic sensors for this work were fabricated by a similar fusion splicing technique.

The objectives of this work included building a number of in-line fibre Fabry-Perot interferometers along a continuous length of single-mode fibre. Techniques had to be developed to fabricate several sensors by depositing titanium dioxide on the ends of cleaved fibres and fusion splicing to similar uncoated fibres in a manner similar to the one used by Lee and Taylor [1989]. These methods involved the sputter deposition of TiO<sub>2</sub> onto the entire face of a single-mode fibre or onto a confined region ~ 25 µm in diameter which included the core. A number of FFP sensors were fabricated using these techniques and the absorption and reflectances were measured during fabrication. The physical properties of TiO<sub>2</sub> films are known to depend strongly on the conditions under which the films are deposited [Bennett *et al.*, 1989], and thus the refractive index of titanium dioxide thin films had to be estimated after deposition from the transmission spectrum of the film which was obtained using an optical spectrum analyser. Optimum fusion parameters were determined, thus yielding reflective splices with good reflectivity and adequate tensile strength. These reflective splices were then used to form the fibre optic Fabry-Perot interferometers. The details of the procedures of the sputter deposition of TiO<sub>2</sub> on the ends of single-mode fibres or onto a localised region of the core, and application of these reflective splices to form physical sensors is discussed in the

following sections. In this work, a novel CW carbon dioxide laser technique was used to anneal the sensing region of the fabricated FFPs so as to realise sensors of reasonable tensile stress (section 5.3.3).

### 5.1.2 Basic considerations

In optical fibre Fabry-Perot fabrication using dielectric or metallic mirrors, the properties desirable in a coating material differ according to the fabrication technique adopted. Fusion spliced based FFP sensors formed in a single-mode fibre require coating materials of high melting points ( $> 1550^{\circ}\text{C}$ ; the softening point of glass). A second important consideration for coating materials is the sensor stability which will determine sensor reliability, since some materials may be susceptible to effects which cause long-term drift in performance. The refractive index of the chosen material should be as high as possible so as to provide the desired reflectance with as thin a film as possible. When multiplexing a small number of sensors, a reasonably high reflectance is desirable to ensure that signals are large enough to give good signal-to-noise ratios. Finally, the absorption loss of the coating film, should be low at the operating wavelength.

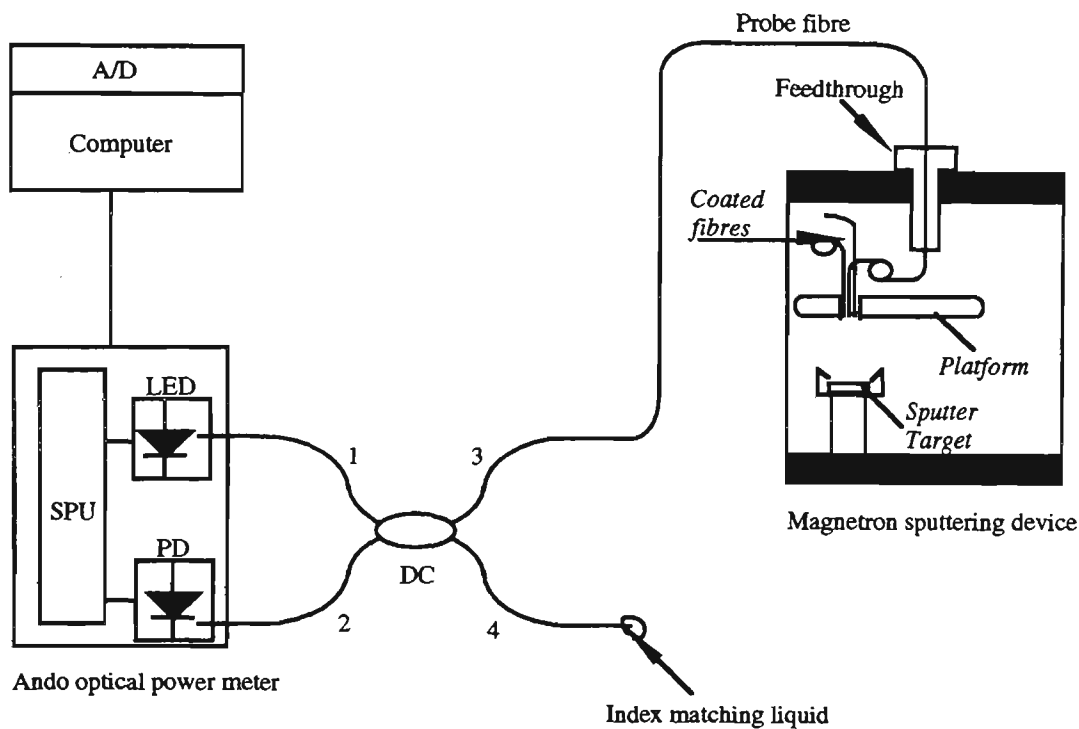
A variety of coating materials are available including aluminium, silver, gold and a range of dielectrics including titanium dioxide [Stuart, 1983]. Titanium dioxide satisfies most of the aforementioned qualities desirable of a fibre fusion spliced based reflective mirror. It has long been established as a suitable coating material [Pulker *et al.*, 1976] having a wide spectral range over which its optical absorption is a minimum (600 nm - 1600 nm), and is therefore suitable for sensing applications. A variety of vacuum deposition methods are available which can be used to deposit optical thin films onto various substrates including thermal evaporation [Stuart, 1983], chemical vapour-phase deposition [Severin and Severijns, 1990; Severin, 1990], electron beam and sputter deposition [Behrisch and Wittmaack, 1991]. Each method has its own advantages and disadvantages and some materials can only be deposited by a limited range

of techniques. Titanium dioxide films can be produced by sputter deposition of titanium in an argon-oxygen atmosphere. This method offers good composition of the deposited film and thus films produced in this way tend to have good homogeneity.

A planar magnetron sputtering device was used to deposit titanium thin films on the ends of cleaved single-mode fibres. It was also used to sputter titanium dioxide (used for all the FFP sensor mirrors) by controlling the amount of oxygen in the chamber. In order to meet the optical specifications for the deposited film material, a number of parameters had to be monitored including sputtering plasma pressure and film thickness. The absence of a suitable monitor for the film thickness in the sputtering environment necessitated the design and fabrication of a monitor of the coating thickness during deposition, which would be appropriate for the sputter chamber and small enough to be placed immediately beside the coated fibres. Using this simple all-fibre thin film thickness monitor it was possible to obtain, during deposition, a reasonable indication of the thickness of the coating being deposited on the sensing fibre.

### **5.1.3 Monitor design and operating principles**

The concept of the optical-fibre-based thin film thickness monitor is illustrated schematically in figure 5.3. The optical monitor consists of a single-mode fibre ( $5/125\ \mu\text{m}$ ,  $\lambda = 850\ \text{nm}$ ) introduced into the vacuum system, as indicated, via a special feedthrough arrangement, and cemented into the feedthrough with vacuum sealant. The feedthrough itself was installed in the vacuum chamber using a viton o-ring, and a long loop of fibre is provided for the monitor fibre (inside the vacuum system) to allow sufficient length for cleaving many times. Light from an 840 nm LED was launched into the fibre via port 1 of a  $2 \times 2$  directional coupler and the power reflected from the distal end of the probe fibre was monitored by a photodiode. Port 4 of the optical fibre coupler was index matched to avoid unwanted reflections.



SPU - Signal processing unit, PD - Photodiode, LED - Light emitting diode and DC - Directional coupler.

Figure 5.3 Schematic diagram of the optical fibre thin film thickness monitor

The LED was modulated at 270 Hz to improve the SNR using a phase-sensitive signal processing technique, which allows the rejection of unwanted optical radiation from the discharge plasma. For thin films, where the total optical path within the film is less than the coherence length of the LED source, the optical intensity received at port 2 varies according to the thickness of the film deposited. During a deposition run, the probe fibre (along with other fibres to be coated) was held in a convenient fabricated holder and positioned above the sputter target. The probe fibre was cleaved before each deposition, after which no further end preparation was necessary. During deposition of thin films, the reflectance signals were recorded on-line using a personal computer interfaced to the ANDO AQ-2105 optical power meter which was used as the source/detector for the measurements.

This reflectance ( $R$ ) of a single layer thin film on the end of a fibre for a uniform thickness ( $d$ ) and at normal incidence (see figure 5.4) is given by [Inci *et al.*, 1992]

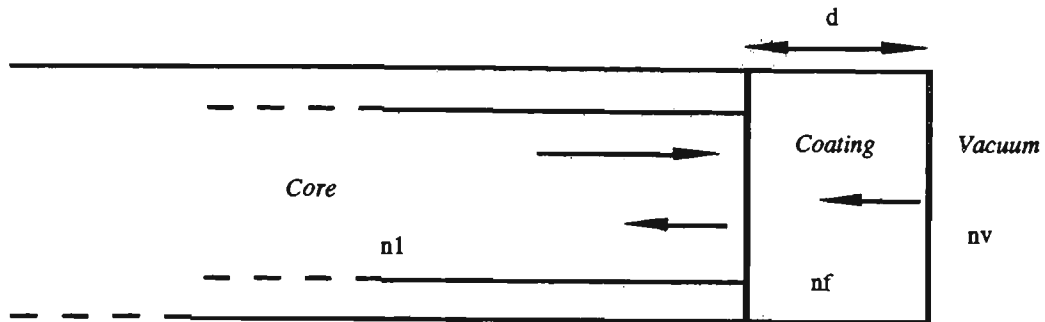


Figure 5.4 Cleaved end of SMF coated with thin film.

$$R = \frac{u - v + w \cos \phi}{u + v + w \cos \phi}, \quad (5.5)$$

$$\text{where } u = (n_1^2 + n_f^2)(n_f^2 + n_v^2), \quad (5.5a)$$

$$v = 4n_1 n_f^2 n_v, \quad (5.5b)$$

$$w = (n_1^2 - n_f^2)(n_f^2 - n_v^2), \quad (5.5c)$$

$$\phi = 4\pi n_f d / \lambda, \quad (5.5d)$$

and  $n_1$ ,  $n_f$ ,  $n_v$ , are the refractive indices of the fibre core, film, and vacuum respectively, while  $\lambda$  is the free space wavelength of the incident beam,  $d$  the thickness of the film and  $\phi$  the round-trip phase shift in the film. In the case of a dielectric film,  $R$  oscillates sinusoidally (for a perfectly coherent source) as the film thickness increases during deposition. However, when using low coherent sources such as LEDs, interpretation of the reflectance curves requires consideration of the finite spectral width of the source. The consequence of this is a reduction in

the peak-peak variation of R as the film increases in thickness. The measurement of R requires calibration of the monitor at the start of every deposition run. The intensity of the beam ( $I_R$ ) received at the photodiode may be expressed as [Caranto *et al.*, 1993]

$$I_R = I_0\gamma(\zeta + R), \quad (5.6)$$

where  $I_0$  is the intensity of the incident beam launched into arm 1 of the coupler (figure 5.3),  $\gamma$  the overall total loss factor of the system which incorporates coupling and fibre insertion losses, and  $\zeta$  the term associated with the return power (e.g. Rayleigh scattering) from regions of the fibre away from the end being coated. In this arrangement,  $I_0$ ,  $\gamma$ , and  $\zeta$  are assumed constant during deposition. Thus, the monitor can be calibrated by determining the return power of two known reflectances, namely a cleaved end ( $R \sim 3.6\%$ ) and an end coated with a thick (> 100 nm) layer of silver ( $R \sim 98.7\%$ ). This simple form of calibration was conducted at the start of every deposition run so that any variations in source intensity between runs did not affect the calibration. For such a calibration, a fibre coated with a thick layer of silver was fused to the monitor fibre for high reflectance measurement and then immediately removed after the measurement was completed.

#### 5.1.4 Monitoring of the deposition of titanium films

The initial investigation of coating material studied two materials: titanium and titanium dioxide. The former, whilst attractive because it offered a higher value of reflectance, was found to have a high absorption loss in the wavelength region of interest (800nm – 1300nm) making it impractical to implement fibre Fabry-Perots (FFPs) for a multiplexed sensor design. The latter, however, had minimal optical absorption losses over the 800 nm - 1300 nm wavelength region. Thus, titanium metallic mirrors were not found to be useful as semi-reflective mirrors in this work and, accordingly, titanium dioxide films were used for the FFP sensor mirrors for all the FFPs prepared using fusion splicing. The performance of the thickness monitor and the

techniques used to estimate film thickness are quite different for absorbing and non-absorbing films. This is illustrated below and in the next section.

Ti was sputtered in the presence of argon onto the cleaved end of the probe fibre, at a background pressure of  $10^{-2}$  mbar for a duration of 300 seconds. The DC power to the titanium target was 200 W. Figure 5.5 shows a plot of experimentally determined reflectance against deposition time. During coating, the reflectance initially first drops from an uncoated value of about 4% to almost 1%. This may be due to the very thin coating layer (thickness very much less than a wavelength) having an effective refractive index between the glass and air and thus reducing the reflectivity. Continued deposition leads to a progressively thicker film with reflectance eventually reaching a steady value for thicknesses greater than the skin depth. During this phase the reflectance of the film increases markedly to about 45%. After about 200 seconds the reflected intensity remains essentially constant. The deposition rate was determined from the reflectance peak (expected at 65 nm thickness), which occurred at 144 seconds (thus, implying a rate of  $27 \text{ nm min}^{-1}$ ). In earlier stages of deposition, thickness of the film can be inferred from a measurement of its reflectance.

### **5.1.5 Monitoring of sputter deposition of $\text{TiO}_2$**

Titanium dioxide films used for the fabrication of intrinsic FFP sensors were obtained by reactive sputtering of a titanium target in an argon-oxygen pre-mixture (80% argon and 20% oxygen). The base pressure in the chamber was  $10^{-6}$  mbar, and during sputtering an argon-oxygen mixture was added, raising the pressure to  $6 \times 10^{-3}$  mbar. The target was operated at a DC voltage of 580 V with discharge current of 0.3 A. A microscope glass slide was coated simultaneously with the optical fibres and was used to determine the transmission

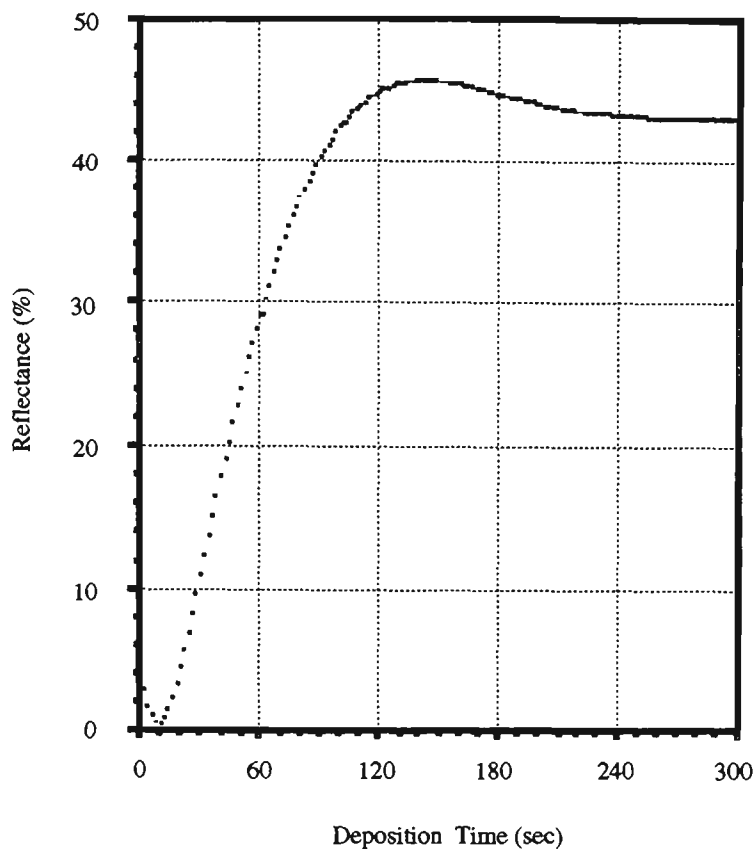


Figure 5.5 Reflectance of titanium against deposition time.

characteristics of the film using an optical spectrum analyser. This enabled the determination of the refractive index of the film as described in section 5.2. The fibres to be coated were mechanically (jacket) stripped and cleaned using isopropyl alcohol. During stripping, care was taken to not cause mechanical damage to the surfaces. After the fibre jacket had been removed and fibres cleaned, the fibres were cleaved using a York FK11 cleaver. No further cleaning processes were undertaken. These fibres, along with the probe fibre were conveniently held in a special holder which was placed on the substrate platform ready for  $\text{TiO}_2$  deposition. The back-reflected intensity was monitored as a function of time and a graph of the reflectance as monitored by the optical thickness monitor over deposition time is shown in figure 5.6.

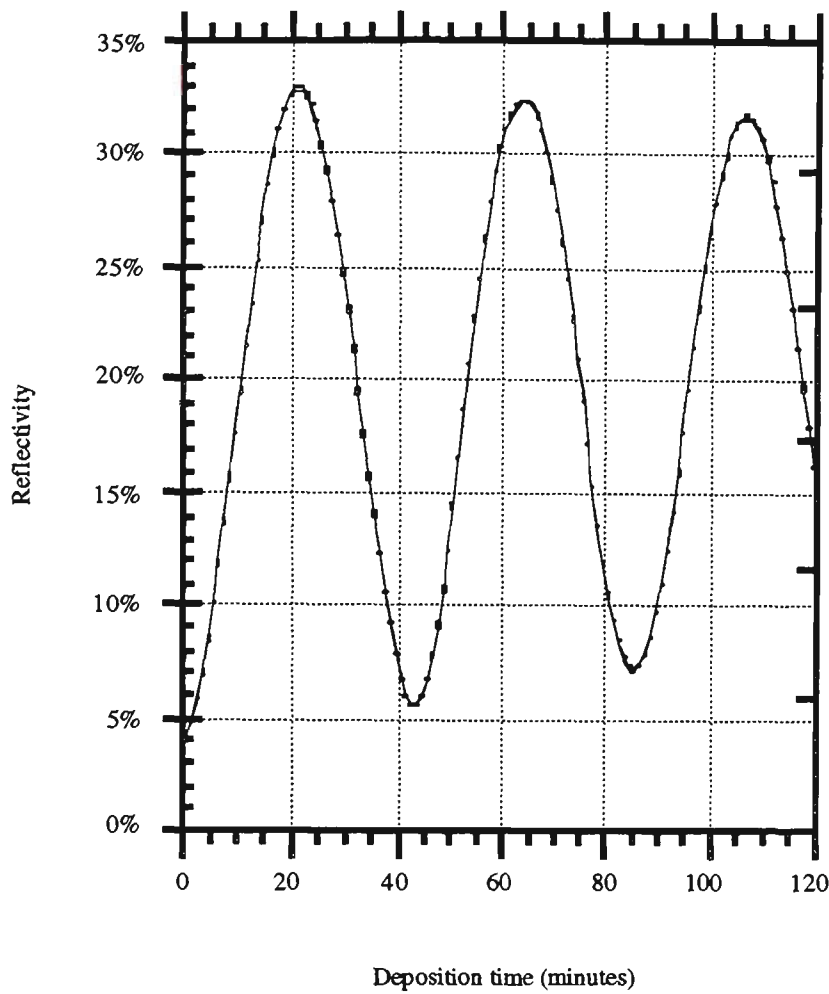


Figure 5.6 The reflectance of the titanium dioxide film against deposition time.

The decaying amplitude of the ‘oscillations’ is attributed to the low coherence length ( $\sim 18 \mu\text{m}$ ) of the LED used. As the thickness of the film grows, the optical path difference between the interfering beams approaches the coherence length of the source, and hence there is a decrease in the fringe contrast. It can be seen from the graph of reflectance versus deposition time (figure 5.6) that the maxima, corresponding to odd multiples of a quarterwave ( $\lambda/4$ ) film thickness, are periodic yielding a constant deposition rate of  $4.5 \text{ nm min}^{-1}$ . The maximum quarter wave reflectance is  $\sim 33\%$ .

Figure 5.7 shows the comparison between experimental and expected reflectance as a function of thickness, again assuming a constant deposition rate. The experimentally measured

reflectance is shown as data points joined by full line 1 while the calculated values shown by line 2, were obtained assuming a Gaussian spectral profile of the LED source. The experimental data shows a strong correlation with theory, with the slight discrepancy being probably caused by an error in the assumed value of the effective coherence length of the source.

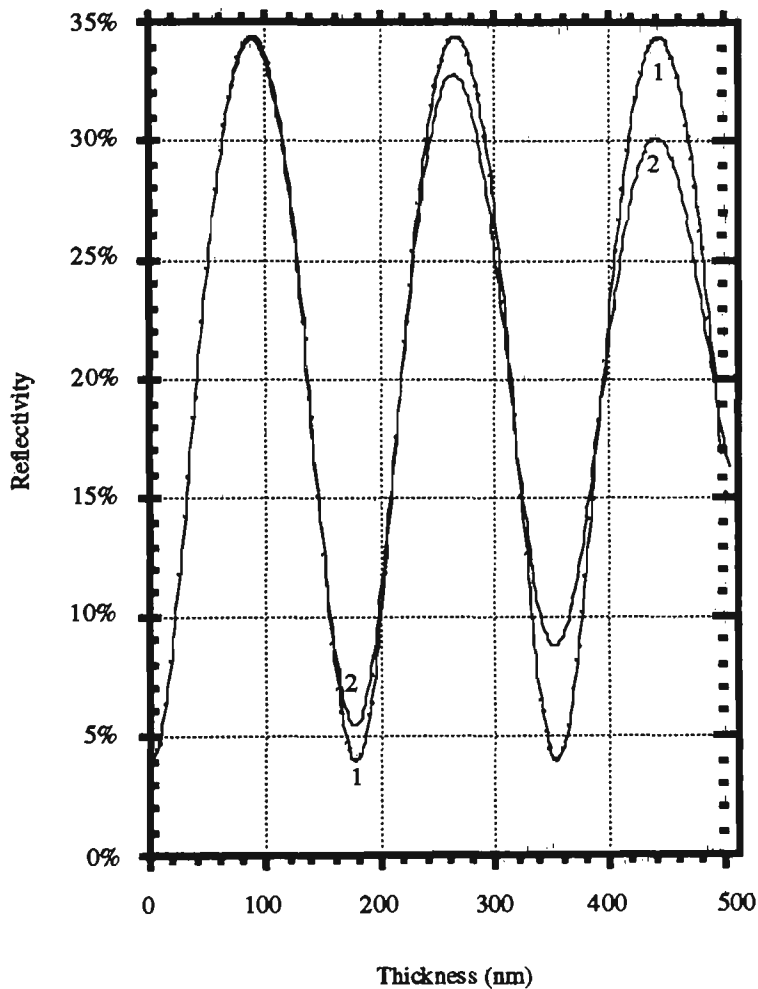


Figure 5.7 The experimental (line 1) and theoretical (line 2) reflectance of titanium dioxide against thickness.

### **5.1.6 Comparison of optical fibre thickness monitor with a quartz crystal monitor**

As a further check on the proper operation of the optical fibre thickness monitor, it was compared with the measurements obtained using a quartz crystal monitor. This later monitor depends on the change in resonant frequency of a quartz crystal as the coating is deposited on its surface. Calibration of thickness as a function of resonant frequency change relies upon a knowledge of density of the thin film which is not always the same as the bulk density. In addition, direct reading of thickness is possible only with the knowledge of a further calibration factor which is related to a variety of other geometrical and electronic factors. Conventionally these factors and the actual density are combined into one single calibration factor which needs to be determined experimentally for a given coating material and coating arrangement. The two monitors were compared using coatings of ZnS films in a conventional vacuum evaporation system. Figure 5.8 shows measured film reflectance plotted against apparent thickness obtained from the crystal monitor (overall calibration factor = 1).

The quarter wave thickness for ZnS determined from this graph was 81.0 nm. Comparison with the accepted value of 91.3 nm obtained using  $n_f = 2.3$ , gives a calibration factor for the crystal monitor of approximately 1.13 which is in good agreement with that obtained by other means for this monitor.

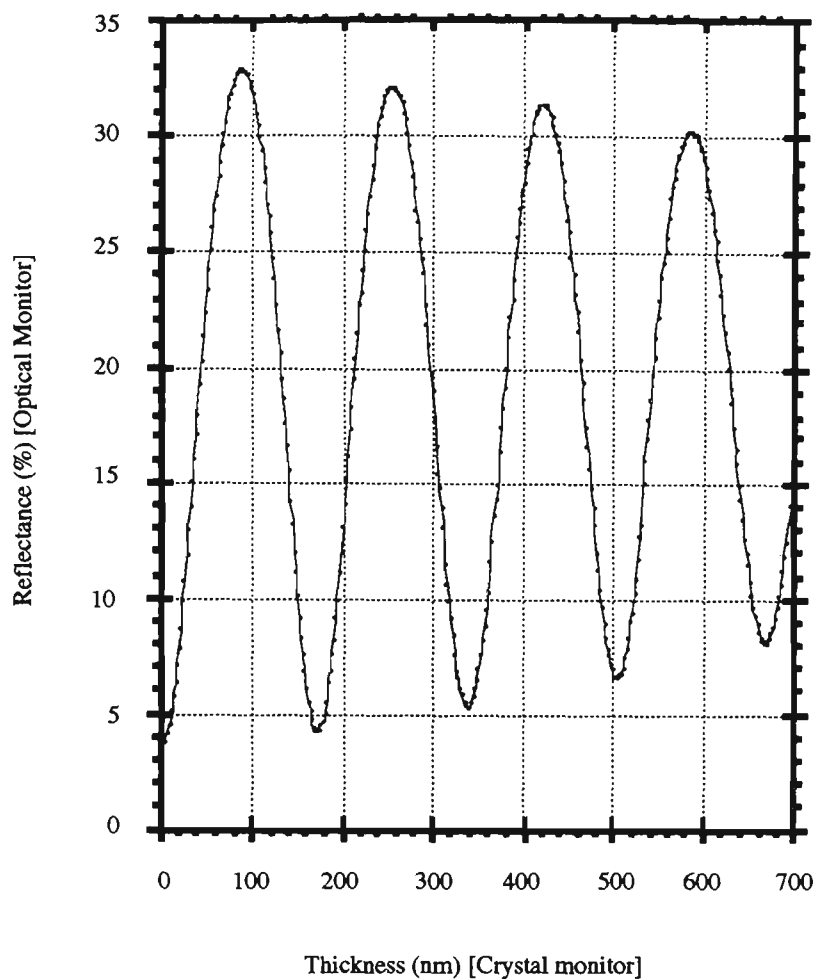


Figure 5.8 The reflectance of ZnS determined by the optical fibre thickness monitor against the apparent thickness measured by a quartz crystal microbalance

### 5.1.7 Conclusion

The optical-fibre-based thin film thickness monitor which was developed has performed as expected and the results obtained are in good agreement with theory. The monitor can also be used to calibrate a quartz crystal monitor, since the occurrence of quarter wave peaks/troughs provides a useful datum for dielectric films. Furthermore, it was used in determining the reflectance of deposited titanium dioxide thin films which are of interest for this work. In the case of metals, the transfer function restricts the range of film thickness, since reflectance reaches a peak for relatively thin coatings. The system may be extended to multilayer coating

process through careful monitoring of the  $\lambda/4$  turning points, but it should be noted that interpolation for thicker films may prove difficult, due to the reduction in fringe visibility associated with the LED source. This could be overcome with the use of a laser diode source having a longer coherence length.

## 5.2 Refractive index of titanium dioxide film

The refractive index of  $\text{TiO}_2$  films was obtained from the transmission characteristics of a clean microscope glass slide which was coated alongside the fibre ends during deposition of  $\text{TiO}_2$  films. Using an optical spectrum analyser (AQ-6310B), a sample glass slide coated with a thin film of  $\text{TiO}_2$  was analysed for its transmission in the 770 - 870 nm range. Refractive index was evaluated numerically in a similar manner to Swanepoel [1983], in which the refractive index is determined from the peaks of the transmission spectrum of a thin film deposited on a thick finite transparent substrate.

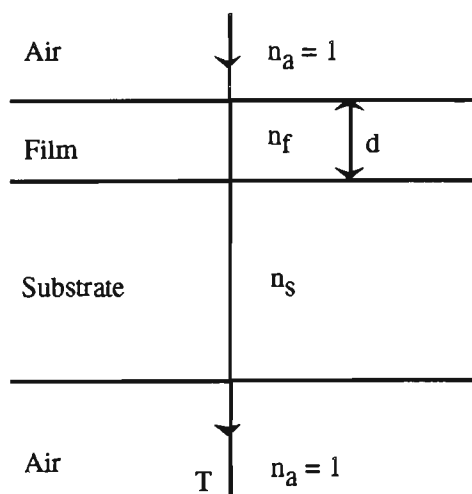


Figure 5.9 Light at normal incidence on a finite transparent substrate coated with a thin film.

The transmission (T) of a thin film deposited on a thick layer of substrate, as illustrated in figure 5.9, is given by Swanepoel [1983] as:

$$T = \frac{Ax}{B - Cx \cos \phi + Dx^2}, \quad (5.7)$$

where  $A = 16n_f^2 n_s,$  (5.7a)

$$B = (n_f + 1)^3 (n_f + n_s^2), \quad (5.7b)$$

$$C = 2(n_f^2 - 1)(n_f^2 - n_s^2), \quad (5.7c)$$

$$D = (n_f - 1)(n_f - n_s^2), \quad (5.7d)$$

$$x = \exp(-\alpha d), \quad (5.7e)$$

and  $\phi$  is, as previously, the total round-trip phase shift in the film. Here  $n_f$  and  $n_s$  are the refractive indices of the film and substrate respectively,  $\alpha$  is the film absorption coefficient,  $d$  the film thickness and  $\lambda$  the free space wavelength. The two extreme cases of interference, equation 5.7 are given by

$$T_{max} = \frac{Ax}{B - Cx + Dx^2}, \quad (5.8)$$

$$T_{min} = \frac{Ax}{B + Cx + Dx^2}. \quad (5.8a)$$

It is assumed that the  $TiO_2$  film is non absorbing, and therefore  $x = 1$ . Substituting  $x = 1$  in equations 5.7 and 5.8a yields

$$T_{max} = \frac{2n_s}{n_s^2 + 1} \quad (5.9)$$

Clearly, the maxima of the interference fringes as given by  $T_{max}$  in equation 5.9 is a function of only the refractive index of the substrate  $n_s$ . Likewise substituting for  $x = 1$  in equation 5.8a gives

$$T_{min} = \frac{4n_f^2 n_s}{n_f^4 + n_f^2(n_s^2 + 1) + n_s^2} \quad (5.10)$$

which can be rewritten as

$$n_f = [M + (M^2 - n_s^2)^{1/2}]^{1/2} \quad (5.10a)$$

where

$$M = \frac{2n_s}{T_{min}} - \frac{n_s^2 + 1}{2}$$

Thus, the refractive index of the film  $n_f$  can be calculated from  $T_{min}$  using equation 5.10a. The refractive index ( $n_s$ ) of the substrate alone at a particular wavelength can be calculated from the interference-free transmission ( $T_s$ ) of a clean glass slide, using [Born and Wolf, 1969]

$$T_s = \frac{(1 - R)^2}{1 - R^2} \quad (5.11a)$$

where, for normal incidence, the intensity reflection coefficient,  $R$ , at the air-glass interface is given by the Fresnel equation (section 2.3.2)

$$R = \left[ \frac{n_s - 1}{n_s + 1} \right]^2. \quad (5.11b)$$

Substituting for R in equation 5.11a gives

$$T_s = \frac{2n_s}{n_s^2 + 1}$$

and

$$n_s = \frac{1}{T_s} + \left( \frac{1}{T_s^2} - 1 \right)^{1/2} \quad (5.11c)$$

Using the above method on the titanium dioxide slides, the average values of the refractive indices of titanium dioxide and glass substrate were found to be 2.41 and 1.56 respectively. In the latter case, an error of 1% in the value of  $T_s$  leads to an uncertainty of about 3% in the value of  $n_s$ .

### 5.3 Entire-face coated intrinsic FFPI cavities and results

Preliminary tests on the FFPI fabrication technique were performed with a 1300 nm single mode fibre (8/125  $\mu\text{m}$ ) since this was readily available and much cheaper than the Corning 780 Flexcore fibre used for the sensors. A single-mode fibre end coated with a titanium dioxide ( $n = 2.41$ ,  $\lambda = 840$  nm) film of thickness  $\sim 87$  nm ( i.e.  $\lambda/4$  thickness) was fusion spliced to a similar uncoated cleaved fibre using a BIT fusion splicer model BSF-50. This splicer was chosen because it allowed easy variation of all process settings and could readily perform multiple fusion cycles. Careful control over fusion parameters, which was possible with this splicer, was essential for the production of adequate Fabry-Perot mirrors. The two fibres were either aligned manually using the microscope of the fusion splicer, which allows for horizontal and vertical viewing, or automatically aligned by maximising the light transmitted through the

core using the local injection and detection technique. Once alignment of the fibres was achieved, the fusion process proceeds via programs incorporated in the splicer. For a chosen program a series of parameters defines the arc current, duration and speed of approach of the fibres during the controlled fusion cycle. This allowed optimisation of the fusion process for a particular fibre type and fusion requirement. The fibres were cleaned using a lower arc current of 5 mA and were set a distance of 50  $\mu\text{m}$  apart from their butt position prior to the cleaning arc lasting for 0.5 seconds. Then, they were set 30  $\mu\text{m}$  apart prior to being heated with an initial electric arc of 10 mA for a duration of 0.5 seconds. These fibres were driven towards each other at an initial speed of 100  $\mu\text{m/s}$  and a final closing speed of 80  $\mu\text{m/s}$ . During the final fusing arc of 10 mA at a distance of 10  $\mu\text{m}$ , the molten fibre ends are pushed into each other to the overrun distance of 3  $\mu\text{m}$  in a time of 0.5 seconds. During the fusion process the reflectance was monitored using an arrangement similar to that used to monitor the reflectance during  $\text{TiO}_2$  deposition. Secondary electric arc current pulses of 10 mA and duration of 0.5 seconds were required to improve the mechanical strength of the splice and could be used to tailor the reflectance of the reflective splice to a desired value. Normally, between 7 and 15 current pulses were required for each fused splice. Once the desired reflectance was achieved fabrication of that mirror was complete. The cavity length was set by then cleaving the spliced fibre at the desired distance from the first mirror. The York cleaver applied an axial tension of 2 N to the first splice, which indicated that it can withstand a strain of approximately +2000 microstrain. The second mirror was formed by fusing this cleaved face onto a similar fibre whose end face is coated with  $\text{TiO}_2$  to form an in-line FFP cavity as shown in figure 5.10. The mechanical strength of the second splice was improved in a similar manner as before by application of secondary arcs until the required effective reflectance of the mirrors was obtained.

After the cavity was fabricated, its optical transmission was monitored to enable evaluation of the sensor signal loss. It was found that the mechanical strength of these sensors and the fusion-induced change in reflectance of the dielectric coating was critically dependent on the

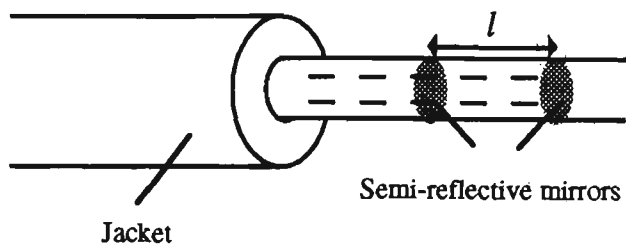


Figure 5.10 Schematic in-line fibre Fabry-Perot cavity formed using fusion splicing technique.

details of the fusion splicing process. In some circumstances it was necessary to use an annealing technique (section 5.3.3) to improve the splice mechanical strength. The most critical parameters were the fusing current and fusing time. The splicer fusion current and fusing time could be varied between 5-25 mA and 0.1-9.9 seconds respectively. The strength of the splices and mirror losses were also dependent on the alignment during the fusion process. Any slight misalignment between the fusing fibres during the fusion process resulted in weak splices and very high transmission losses. The success rate of good splices was critically dependent on the end faces of the coated fibres, and hence on the uniformity of the film. In addition, the nature of the cleaved end face of the uncoated fibre being fusion spliced to the coated fibre also influences the quality of the final splice. Lower losses and good splices required fibre ends which were cleaved accurately normal to the fibre axis. A bad end surface could be seen to slip off the end of a similar fibre as they were being butted together prior to fusion. Of the total of 98 fabricated samples of  $\text{TiO}_2$  face coated fibres, 19 splices (~ 20%) were good splices. The rest either did not fuse properly or were misaligned in their x- or y-direction. A good splice, when observed through the microscope of the fusion splicer, looks like a perfect cylinder with uniform continuity at the splice point. A high percentage of the defective splices may be due to the various reasons cited above (i.e. the non-uniformity of the deposited film, the degree of perpendicularity of the cleaved fibre ends), and also the coating of the entire fibre face which limits the automatic self alignment due to the forces of surface tension of the fused glass. Table

5.1 gives a summary of results of the optimal fusion parameters used during fabrication of FFPs for fibres coated with a thin film of TiO<sub>2</sub> (~ 87 nm).

<b>Cleaning</b>	<b>Fusing</b>	<b>Sub arcs</b>
Cleaning current = 5 mA	<u>Initial</u> <u>Final</u> Initial arc = 10 mA,      Final arc = 10 mA	Overrun = 0
Distance = 50 μm	Initial distance = 30 μm,      Final distance = 10 μm	Current = 10 mA
Time = 0.5 sec	Time = 0.5 sec,      Overrun = 3 μm	Subarcs = 7 - 15
	Time = 0.5 sec	Time = 0.5 sec

Table 5.1 Summary of optimal fusion splicer parameters

### 5.3.1 Core region only coated FFPI

The fabricated FFP sensors discussed in the previous section, generally failed under low tension when a tensile load was applied at the end of fibres inside which the cavity was contained. A possible reason for this structural failure may be that having the entire end face coated with reflective film, does not allow glass-to-glass fusion of the fibres. Coating the entire fibre is unnecessary since the guided light is confined to the core, and by maximising glass-to-glass fusion (of the cladding), the tensile strength of the FFPI could be improved [Measures, 1992, Kaddu *et al.*, 1993].

In order to improve the mechanical strength of fabricated FFPs, a localised region coating technique involving the core was employed, and in certain circumstances this was followed by

an annealing process using a CW CO<sub>2</sub> laser (section 5.3.3). The fabrication of a core-region-only coated FFPI involved the deposition of titanium dioxide mirrors onto a 25 μm diameter region which includes the core of an 8/125 μm cleaved optical fibre (first mirror), the fusion splicing of this coated end to a second single-mode fibre, and the distal cleaving and fusing to a core-region-only coated fibre (second mirror) to form an in-line cavity. Figure 5.11 shows a cleaved optical fibre with a thin film coating of the core region.

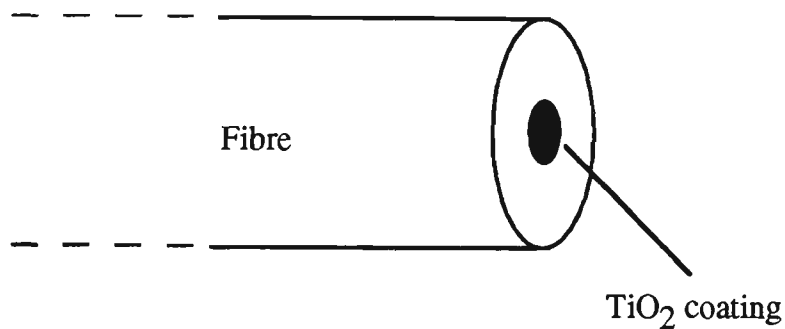


Figure 5.11 Core-region-only coated end face with a 25 μm diameter coating (not to scale).

A core-region-only coating of the fibre was achieved by depositing TiO<sub>2</sub> film through a 25 μm diameter aperture. The fibres were prepared for coating in the usual manner. Alignment of the fibre core and aperture was achieved by maximising the light transmitted through the aperture using a photodetector. With maximum transmission, the XYZ micromanipulator for fibre alignment was locked and the whole assembly was placed inside the vacuum chamber. The reflectance of the mirrors were monitored using an optical thin film monitor (section 5.1.3) [Caranto *et al.*, 1993]. The experimental arrangement is similar to the one shown in figure 5.3 which employed a 2 × 2 directional coupler to monitor the reflection from the coated face. Core-region-only FFP in-line cavities were fabricated in a similar manner to that described in section 5.3. The fusion parameters used were the same as those given in table 5.1, namely a fusing current of 10 mA for both initial and final arc current, 0.5 second arc duration with a 3 μm overrun. Interestingly, the work of Hogg *et al.*, [1991], which involved coating the core

region of a single-mode fibre using metallic coatings of aluminium and fusion splicing to a similar uncoated fibre, did not require reduction of fusion current. However, this was not the case with this investigation which used dielectric coatings.

### 5.3.2 Fusion spliced fibre Fabry-Perot sensors

The construction of in-line FFP cavities, either face coated or core-region only coated, was an essential step leading to the fabrication of a serial array of intrinsic FFP sensors formed in a continuous length of fibre. By repeated coating and fusion splicing, as outlined in section 5.3, several in-line cavities were fabricated. The ends of the fibres which formed the first and second cavity are stripped, cleaved and fusion spliced to form two in-line FFP sensors. Several FFP sensors of cavity length of few millimetres to a few centimetres and of mirror reflectances between 4 - 20% were produced using this technique. These sensors were later tested experimentally in a physical environment to measure strain and temperature, either as single

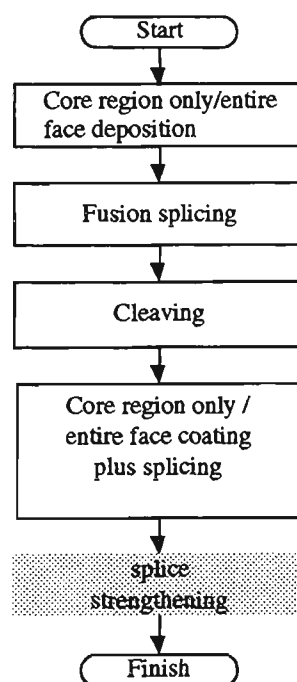


Figure 5.12 Fabrication process of FFPs.

sensors or multiplexed sensors using WLI techniques (chapter 7). Figure 5.12 gives a summary of the steps taken during fabrication of FFPI used in this work, which in some cases were followed by a strengthening of the fusion splices.

### 5.3.3 Annealing of fusion spliced FFPI cavities and results

The mechanical strength of reflective splices in single-mode intrinsic FFP sensors is of great importance if these sensors are to be useful for applications which involve large mechanical stresses. Efforts in this work have been directed towards achieving improved splice strength of fabricated FFP sensors (via core-region-only coated FFP sensors (section 5.3.1)). To achieve higher splice strength for high stress applications, an annealing technique using a 200 W CW carbon dioxide laser beam was employed. Although the arc fusion splicing technique used for fibre optic Fabry-Perot fabrication is very attractive because of its low loss and good reproducibility, the mechanical strength around the splice region is weakened by the arc [Hatakeyama, *et al.*, 1978]. Strength reduction at the heated part of the fibres has long been studied [Miyajima *et al.*, 1985], and reasons suggested for this reduction have been based on mechanical damage to the fibre surface [Krause *et al.*, 1981], devitrification [Tachikura and Haibara, 1985], surface corrosion by OH at high temperatures [Krause *et al.*, 1981a], and thermal stress resulting from localised heating. A single-mode fused silica fibre when placed in a 10.6  $\mu\text{m}$  CO<sub>2</sub> laser beam absorbs the infrared heat radiation and this has been exploited to anneal the fusion splices within a short length of fibre (~ 20 mm). This infrared laser is appropriate, because of its large beam diameter of ~ 20 mm and the 80 - 90% absorption of the CO<sub>2</sub> radiation by silica fibre [Woolsey and Lamb, 1992]. Samples (68) of normally-spliced uncoated fibres were investigated and the CO<sub>2</sub> laser operation was optimised for maximum strength of the annealed splices. The laser used was a molecular gas system using a CO<sub>2</sub>/N<sub>2</sub>/He mixture, active length of 4 m with a continuous DC discharge. The output CO<sub>2</sub> laser specifications were wavelength, 10.6  $\mu\text{m}$ ; output power, 200 W CW; efficiency, 7%;

beam divergence, 0.06%. The fibre used was single-mode (8/125  $\mu\text{m}$ ) at 1300 nm, and samples were carefully prepared prior to fusing to avoid surface scratches and particle contamination. After fusion splicing, the splice was placed centrally in the path of the CW CO<sub>2</sub> laser beam for 10 seconds. The splice region was manually rotated about the axis of the fibre (for uniform heating) as it was pulled transversely to the CO<sub>2</sub> laser beam using a fibre jig. For all measurements, the splice was mounted nearly orthogonal to the CO<sub>2</sub> laser axis. The tensile strength was measured and compared with non-annealed splices, taking non-spliced fibres as a reference. The average breaking strength of normal uncoated fusion splices after annealing was 8.5 N, which was a marked improvement compared to a breaking strength of 4.5 N for a normal uncoated splice and comparable to 13.0 N for unspliced fibre. The tensile strength of the fibre splices was measured by a motor driven tension spring balance under 1.5 N/min weighting velocity. This improvement in uncoated splice strength after annealing with the CW CO<sub>2</sub> laser led to further work to establish the effectiveness of CO<sub>2</sub> laser annealing on coated splices.

Nineteen (19) samples of TiO<sub>2</sub> face coated fusion spliced fibres were annealed with the CW CO<sub>2</sub> laser, even if deformation had been detected during the fusion process. The six good splices were then tested for tensile mechanical strength and it was found that the mechanical strength of these splices had also generally improved compared to non-irradiated splices. Furthermore, it was observed that all the splices that were CO<sub>2</sub> laser treated (i.e. annealed) broke at a distance away from the splice point, whereas all the untreated splices (those not exposed to the CO<sub>2</sub> laser beam) broke at the splice point. This was a good evidence that the splices had been strengthened by the annealing process. For the good TiO<sub>2</sub> entire-face coated splices, an average breaking strength of 3.5 N ( $\sim 3500 \mu\epsilon$ ) was obtained for the laser treated splices compared to 3.0 N ( $\sim 3000 \mu\epsilon$ ) for the TiO<sub>2</sub> entire-face coated splices which had not been exposed to the CW CO<sub>2</sub> laser beam. Because of the difficulties involved, both in coating TiO<sub>2</sub> to a confined region of the single-mode core of approximately 25  $\mu\text{m}$  and also making a finished product of a core-region-only coated intrinsic FFP sensor, it was deemed necessary

not to break these sensors just to investigate their mechanical strength. Therefore, no measurements are available for the mechanical strength of core-region coated FFP sensors. However, it could be argued that, since only a small region near the core was coated (which left a larger portion of glass-to-glass fusion) it is likely that their mechanical strength would be in excess of +3.5 N (that exhibited by entire face coated splices) after annealing with the CW carbon dioxide laser. A summary of the mechanical strength of the various splices is given in table 5.2.

#### **5.4 Conclusion**

The details of the steps taken for the design and production of practical fusion-spliced intrinsic FFP sensors for the measurement of strain or temperature have been described. Titanium dioxide reflection coatings as internal mirrors with high stability and high index of refraction have been exploited. This allowed the formation of reflective splices in a continuous length of fibre as required for a multiplexed sensor arrangement. The optical and mechanical properties of the splice are critically dependent on the end face properties of the fibres and perpendicular end faces are required. The optimum fusion splicing parameters required for these splices were investigated. The TiO<sub>2</sub> film deposited on the fibre end may weaken the splice strength, and thus a localised deposition technique involving the core is of practical importance for fabricating FFP sensors of improved strength. A CW CO<sub>2</sub> laser technique used to anneal the splices could be an alternative route to improve the mechanical strength of the reflective splices, since the fibre breaks away from the splice after annealing with the laser. Short FFP cavities suitable for near point-wise sensing (4 - 20 mm) and low reflectance (4 - 20%) have been produced. These FFP sensors were experimentally tested for thermal and strain performance, and the results are described in chapter 7.

Splice type	Average breaking strength	Breaking point	Samples
Normal (uncoated) splices	4.5 N	at the splice	25
Normal (uncoated) splices when laser treated	8 N	away from splice	32
TiO <sub>2</sub> entire face coated splices (untreated)	3 N	at the splice	12
TiO <sub>2</sub> entire face coated splices when laser treated	3.5 N	> ± 15 mm from splice point	6
Core-region-only coated splices	No breaking strength measurements done.		

Table 5.2 Summary of mechanical strength of various splices under different conditions.

## **CHAPTER 6**

### **PREDICTED PERFORMANCE**

The details regarding the fabrication of intrinsic fibre Fabry-Perot sensors were discussed in chapter 5. In this chapter, the concept of reflection transfer function of these sensors is introduced prior to consideration of their thermal and strain phase sensitivities. Apparent strain, or thermally induced equivalent strain, which may be defined as the change in phase of light propagating along a structurally integrated optical fibre subject to a change in temperature but without any applied force [Measures, 1992], is an issue which needs to be addressed when measuring static strain and is thus discussed in section 6.4. A calculation of this effect, based on an FFP bonded to a cantilever beam, is given. Multimode laser diodes, were used as optical sources in much of the work described in this thesis since they provide large output power and exhibit good coupling efficiency into single mode fibres. However, their use in WLI based systems requires some consideration of the interference effects produced by individual longitudinal modes. WLI interferometry measurements require an unambiguous determination of the central fringe, therefore, some of the methods used to identify this fringe will be briefly introduced. The discussion also includes a model used to estimate the expected performance of a number of identical in-line fibre Fabry-Perot sensors multiplexed in series using white light interferometry.

## 6.1 Reflection transfer function of a fibre Fabry-Perot interferometer (FFPI)

An intrinsic fibre Fabry-Perot interferometer (FFP) is illustrated schematically in figure 6.1. Two dielectric mirrors are introduced within the fibre by vacuum deposition techniques followed by fusion splicing (chapter 5) or by writing Bragg gratings into the core of the fibre (chapter 8).

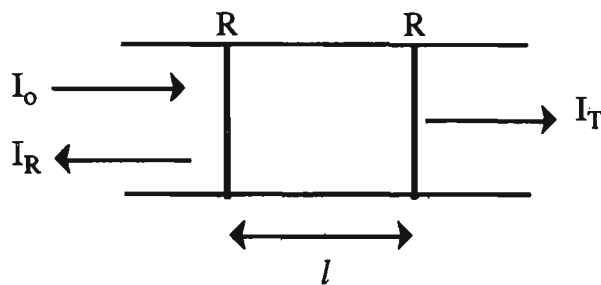


Figure 6.1 Diagram of FFPI interferometer.

Using conventional multiple beam-interferometry theory (a reasonable assumption in the case of a single mode fibre), the intensity of light reflected from the FFPI with mirrors of equal reflectance  $R$ , as a function of phase can be expressed as [Born and Wolf, 1969]

$$I_R = \frac{2RI_o(1 - \cos\phi)}{1 + R^2 - 2R \cos\phi}, \quad (6.1a)$$

$$= \frac{4RI_o \sin^2(\phi/2)}{(1 - R)^2 + 4R \sin^2(\phi/2)}, \quad (6.1b)$$

$$= \frac{FI_o \sin^2(\phi/2)}{1 + F \sin^2(\phi/2)}, \quad (6.1c)$$

$$= F \sin^2(\phi/2) A(\phi). \quad (6.1d)$$

Here  $I_0$  is the intensity of the incident beam,  $F$  is the finesse which is a measure of the sharpness of the fringes and is given by

$$F = \frac{4R}{(1 - R)^2} , \quad (6.2)$$

and  $A(\phi)$  is the Airy shape function of the FFPI [Born and Wolf, 1969] given by

$$A(\phi) = \frac{I_0}{1 + F \sin^2(\phi / 2)} . \quad (6.3)$$

Here  $\phi$  is the round trip phase difference between two successive beams and is given by

$$\phi = 4\pi n l / \lambda , \quad (6.4)$$

where  $n$  is the refractive index of the core,  $l$  is the distance between the sensing mirrors and  $\lambda$  is the free space wavelength. The transfer function ( $I_R/I_0$ ) implicit in equations 6.1 is periodic with reflection minima separated by  $\Delta\phi = 2\pi$ , corresponding to a change in optical cavity length ( $nl$ ) of the FFPI equal to  $\lambda/2$ . Equation 6.1 is plotted in figure 6.2 for various values of reflectance and illustrates the increased sharpness of the fringes with increased reflectance. The Fabry-Perot interferometer may be characterised by two quantities, namely the finesse  $F$  and the free spectral range ( $\Omega_f$ ). The free spectral range  $\Omega_f$  (in frequency units) is given by [Kist *et al.*, 1985]

$$\Omega_f = \frac{c}{2nl} , \quad (6.5)$$

where  $c$  is the speed of light in a vacuum, and  $l$  is the cavity length.

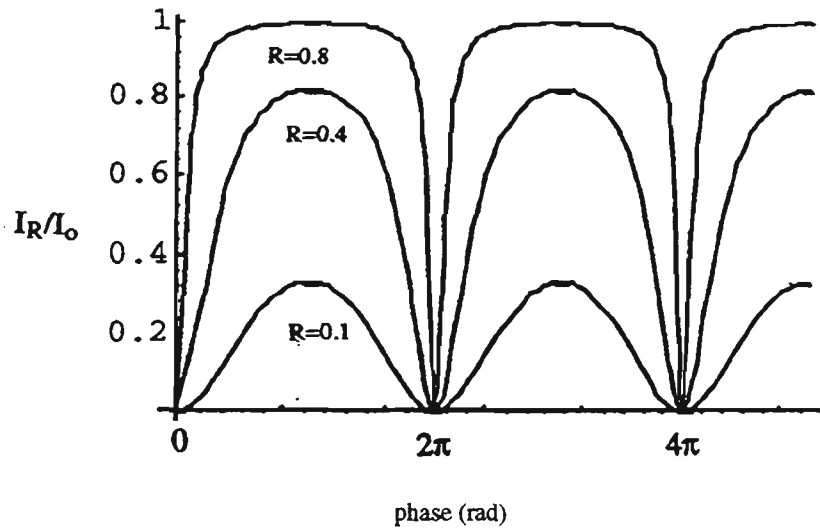


Figure 6.2. Transfer function in reflection of an FFP cavity for three values of  $R$ .

The minima in equation 6.3 correspond to those values for which  $\phi = (2m + 1)\pi$ , where  $m$  takes integer values. Defining the FFPI effective finesse  $F_e$  as the ratio of the Airy minima spacing (free spectral range) to the full width at half-maximum (FWHM) of the reflection minima [Nichelatti and Salvetti, 1995]

$$F_e = \frac{2\pi}{\text{FWHM}}, \quad (6.6a)$$

$$= \frac{\pi}{2\sin^{-1}(1/\sqrt{F})}, \quad (6.6b)$$

$$F_e \approx \frac{\pi}{2}\sqrt{F}, \quad (\text{for } F \text{ large}) \quad (6.6c)$$

$$F_e = \frac{\pi\sqrt{R}}{1-R}. \quad (6.6d)$$

When the value of R is small the finesse is also small. The FFP sensors being fabricated are generally of low finesse (low mirror reflectances,  $4\% \leq R \leq 20\%$ ), and owing to the small value of reflectance, it can be assumed that the higher order reflections in the optical cavity are negligible. In this case, on expanding the expression in equation 6.1c and retaining only the first term in F, gives

$$I_R / I_o \approx F \sin^2(\phi / 2) ,$$

$$= F(1 - \cos \phi) / 2 , \quad (6.7)$$

which is characteristic of the transfer function of two beam interferometry. This has been utilised in low finesse FFP sensors for this work. The fringes are broad for low values of reflectance and as the value of R increases the value of F rapidly becomes larger and the fringes become sharper (figure 6.2).

## 6.2 Thermal properties of the FFP sensor

Although, the primary interest in this thesis is the strain response of the FFPI sensor the thermal properties must be considered as they also affect the optical phase shift  $\phi$ , given in equation 6.4. The phase change is produced by changes in either the fibre length, due to thermal expansion or contraction, or changes in refractive index with temperature. Normally, for silica glass, the change in index with temperature is the dominant term. The fractional phase shift per unit temperature change, neglecting the effects of fibre diameter changes, is given by [Lagakos *et al.*, 1981, Rogers, 1988]

$$\frac{\Delta \phi}{\phi \Delta T} = \frac{\Delta l}{l \Delta T} + \frac{\Delta n}{n \Delta T} , \quad (6.8a)$$

$$\frac{\Delta\phi}{\phi\Delta T} = \alpha_f + \frac{1}{n} \frac{\Delta n}{\Delta T} , \quad (6.8b)$$

where  $\alpha_f$  is the coefficient of thermal linear expansion of the fibre. Using bulk optic silica parameters,  $dn/dT = 10 \times 10^{-6}/K$ ,  $\alpha_f = 5.0 \times 10^{-7}/K$ ,  $n = 1.456$  [Hocker, 1979] gives

$$\frac{\Delta\phi}{\phi\Delta T} = 7.4 \times 10^{-6} / K . \quad (6.9)$$

In general,  $\alpha_f$  and  $dn/dT$  are dependent on glass composition [Hocker, 1979]. For example  $\alpha_f$  can take values between  $4 \times 10^{-6} - 13 \times 10^{-6}/K$ , while  $dn/dT$  may have values ranging from  $-10 \times 10^{-6}$  to  $+19 \times 10^{-6}/K$ , and in addition  $dn/dT$  is a function of temperature and operating wavelength. Accordingly, the experimentally measured value of  $\Delta\phi/\phi\Delta T$  will differ somewhat from that predicted in equation 6.9.

### 6.3 FFPI strain response

If the FFPI is attached to a stressed structure the strain in the structure introduces an optical phase change in the light propagating in the sensor. The approach used for the strain sensitivity assumes a weakly guiding condition [Egalon and Rogowski, 1993]. This provides good results for surface mounted sensors, which is the case for this work, however for embedded sensors a suitable analysis can be found elsewhere [Tay *et al.*, 1989; Valis, *et al.*, 1991; Measures, 1992]. The round-trip phase retardance,  $\phi$ , (equation 6.4) of light after propagating through an FFP sensor of cavity length,  $l$ , can be expressed as

$$\phi = 2\beta l , \quad (6.10a)$$

where  $\beta$  is the propagation constant of the guided mode in the fibre and can be approximated by  $\beta = 2\pi n/\lambda$ ,  $\lambda$  is the wavelength of light in vacuum and  $n$  is the core refractive index. The variation in  $\phi$  due to incremental changes in strain is expressed as

$$\Delta\phi = 2(\beta\Delta l + l\Delta\beta) , \quad (6.10b)$$

where  $\beta\Delta l$  refers to the physical extension of the fibre, and  $l\Delta\beta$  is caused by two effects, namely; (i) the dependence of the fibre index on strain, and (ii) the waveguide dispersion (change in fibre diameter ( $D$ )). The physical extension of the fibre is usually the dominant term.  $l\Delta\beta$  can be expressed as

$$l\Delta\beta = l\frac{\partial\beta}{\partial n}\Delta n + l\frac{\partial\beta}{\partial D}\Delta D . \quad (6.11a)$$

$\beta$  is related to the vacuum propagation constant  $k$  by  $\beta = n_{\text{eff}}k$ , where  $n_{\text{eff}}$  is the effective index which lies between the core and cladding indices. The core and cladding indices typically differ by the order of 1% so it could be assumed that  $n_{\text{eff}} \approx n$  (the refractive index of the core), such that  $\beta \approx nk$ . Thus,  $\partial\beta/\partial n = k = \beta/n$ . Substituting for  $\partial\beta/\partial n$  in equation 6.11a

$$l\Delta\beta = l\frac{\beta}{n}\Delta n + l\frac{\partial\beta}{\partial D}\Delta D . \quad (6.11b)$$

Realising that  $\Delta\left(\frac{1}{n^2}\right) = -\frac{2}{n^3}\Delta n$ , equation 6.10b can be written as

$$\Delta\phi = 2\left[\beta\Delta l - l\frac{\beta n^2}{2}\Delta\left(\frac{1}{n^2}\right) + l\frac{\partial\beta}{\partial D}\Delta D\right] . \quad (6.12)$$

Elasto-optic theory describes the changes in the optical indicatrix  $\Delta\left(\frac{1}{n^2}\right)_j$  due to an applied strain as [Measures, 1992] ,

$$\Delta\left(\frac{1}{n^2}\right)_j = \sum_{k=1}^6 p_{jk}\epsilon_k , \quad (6.13)$$

where  $\epsilon_k$  are the components of the strain vector and  $p_{jk}$  are the averaged strain-optic coefficients of the medium. If an isotropic, elastic optical fibre oriented in the z-direction, is subjected to a longitudinal strain  $\epsilon_z$ , the resulting strain (first order approximation) is given from the elastic theory [Measures, 1992]

$$\epsilon_k = \begin{bmatrix} -\vartheta\epsilon_z \\ -\vartheta\epsilon_z \\ \epsilon_z \end{bmatrix}, \quad (6.14)$$

where  $\epsilon_z$  is the longitudinal strain,  $-\vartheta\epsilon_z$  is the corresponding transverse strain and  $\vartheta$  is the Poisson's ratio of the fibre material. For an isotropic medium  $p_{jk}$  has only two independent values:  $p_{11}$  and  $p_{12}$  ( $k = 1, 2$ ). Using the symmetry of the tensor it follows that the change in the optical indicatrix in the x and y directions simplifies to

$$\Delta(1/n^2) = \epsilon_z[p_{12} - (p_{11} + p_{12})\vartheta]. \quad (6.15)$$

Therefore, the propagating light in the fibre will see a change in the refractive index  $\Delta n$  given by

$$\Delta n = \frac{-\epsilon_z n^3}{2} [p_{12} - (p_{12} + p_{11})\vartheta], \quad (6.16)$$

where  $\epsilon_z$  is longitudinal strain defined by  $\Delta/l$ . The last term in equation 6.12, due to waveguide dispersion, can be obtained from the change in diameter of the fibre  $\Delta D = \epsilon\vartheta D$  and from the value of  $d\beta/dD$ . Using the normalised frequency [Senior, 1992]

$$V = kD(n^2 - n_{cl}^2)^{1/2}, \quad (6.17)$$

and the normalised propagation constant

$$b = \frac{\left(\frac{\beta}{k}\right)^2 - n_{cl}^2}{n^2 - n_{cl}^2}, \quad (6.18)$$

$\partial\beta/\partial D$  can be evaluated. Here  $n$  and  $n_{cl}$  are the refractive indices of the core and cladding respectively. Writing

$$\frac{\partial\beta}{\partial D} = \frac{\partial\beta}{\partial b} \frac{\partial b}{\partial V} \frac{\partial V}{\partial D}, \quad (6.19)$$

and differentiating equations 6.17 and 6.18 gives

$$\frac{\partial V}{\partial D} = k(n^2 - n_{cl}^2)^{1/2} = \frac{V}{D}, \quad (6.20)$$

$$\frac{\partial\beta}{\partial b} = \frac{k^2(n^2 - n_{cl}^2)}{2\beta} = \frac{V^2}{2\beta D^2}, \quad (6.21)$$

and hence

$$\frac{\partial\beta}{\partial D} = \frac{V^3}{2\beta D^3} \frac{\partial b}{\partial V} \quad (6.22)$$

while  $\partial b/\partial V$  defines the slope of the  $b$ - $V$  curve at the point corresponding to the waveguide mode. Substituting for the relevant expressions in equation 6.12, the fractional phase shift per unit strain (which can be interpreted as the FFPI's gauge factor) is given by

$$\frac{\Delta\phi}{\phi\varepsilon} = 1 - \frac{n^2}{2} [p_{12} - (p_{12} + p_{11})\vartheta] + \frac{V^3\vartheta}{4\beta^2 D^2} \frac{\partial b}{\partial V}. \quad (6.23)$$

Substituting for  $n = 1.46$ ,  $\vartheta = 0.16$ ,  $p_{12} = 0.252$ ,  $p_{11} = 0.113$  [Bertholds and Dandliker, 1988],  $D = 8 \times 10^{-6}$  m,  $\lambda = 1300$  nm,  $db/dV = 0.5$  in equation (6.23)

$$\begin{aligned} \frac{\Delta\phi}{\phi\epsilon} &= 1 - 0.2063 + 0.0002, \\ &= 0.794 \text{ (FFPI gauge factor)}. \end{aligned} \quad (6.24)$$

It can be seen clearly that the contribution from the waveguide dispersion term is negligible, and therefore the fractional phase shift per unit strain can be simply given by

$$\frac{\Delta\phi}{\phi\epsilon} = 1 - \frac{n^2}{2} [p_{12} - (p_{12} + p_{11})\nu]. \quad (6.25)$$

#### 6.4 Apparent strain analysis

An ideal optical fibre strain gauge bonded to a structure would respond only to the applied strain in the structure and be virtually insensitive to other environmental parameters. Unfortunately, optical fibre sensors, like all other sensors, are sensitive to both strain and temperature, as discussed in the previous two sections. The co-dependency on temperature and strain may significantly affect strain measurements if not accounted for. Any change in ambient temperature for an optical gauge adhered to a structure results in a phase change at the output, and this change will be mistaken as a change in strain of the structure. This change in phase is caused by two concurrent and algebraically additive effects, namely: (i) the free sensor thermal sensitivity, and (ii) the difference in thermal expansion coefficients between the structure to which the sensor is bonded and the silica fibre. Temperature changes cause the structure to expand or contract and, since the optical FFP gauge is firmly adhered to the structure, it is forced to undergo the same expansion or contraction. The amount of extra strain on the FFPI gauge is dependent on the difference between the coefficients of thermal expansion of the structure and FFP gauge. This effect of temperature change being misinterpreted as strain change is called the thermally induced apparent strain or apparent strain and it does not depend on, and neither does it have any bearing on, the mechanical (stress-induced) strain in the test structure. The magnitude of the apparent strain may be greater in some circumstances than the static strain being measured. The bonded sensor temperature sensitivity may be obtained by

following a treatment similar to that used by Measurement Group Inc.[1993] when correcting for thermal strain in resistive strain gauges, as

$$B_s = F + G(\alpha_s - \alpha_f) , \quad (6.26)$$

where  $B_s$  is the bonded sensor temperature sensitivity,  $\left(\frac{d\phi}{\phi dT}\right)_s$ .  $F$  the free sensor temperature sensitivity,  $\left(\frac{d\phi}{\phi dT}\right)_f$ ,  $G$  the bonded sensor strain sensitivity,  $\Delta\phi/\phi\varepsilon$ , and  $\alpha_s$  and  $\alpha_f$  are the coefficients of thermal expansion of the structure and sensor fibre respectively.

$$\text{apparent strain} = \frac{F + G(\alpha_s - \alpha_f)}{G} = F/G + \alpha_s - \alpha_f . \quad (6.27)$$

Using the following strain and temperature sensitivities [Kaddu *et al.*, 1993] of

$\frac{\Delta\phi}{\phi\Delta T} = 7.5 \times 10^{-6}/^\circ\text{C}$  and  $\frac{\Delta\phi}{\phi\varepsilon} = 0.84$  at  $\lambda = 1300$  nm for a 4.5 mm FFP sensor gives,

$$F = \frac{\Delta\phi}{l\Delta T} = \frac{\Delta\phi}{\phi\Delta T} \frac{\phi}{l} = \frac{7.5 \times 10^{-6} \times 4\pi \times 1.46 \times 4.5 \times 10^{-3}}{1300 \times 10^{-9} \times 0.45} \text{ rad K}^{-1} \text{ cm}^{-1} ,$$

$$F = 1.06 \text{ rad K}^{-1} \text{ cm}^{-1} ,$$

$$= 60.6 \text{ deg K}^{-1} \text{ cm}^{-1} , \quad (6.28)$$

and

$$G = \frac{\Delta\phi}{\mu\varepsilon.l} = \frac{\Delta\phi}{\phi\varepsilon \times 10^6} \frac{\phi}{l} = \frac{0.84 \times 4\pi \times 1.46 \times 4.5 \times 10^{-3}}{10^6 \times 1300 \times 10^{-9} \times 0.45} \text{ rad } \mu\varepsilon^{-1} \text{ cm}^{-1} ,$$

$$= 0.119 \text{ rad } \mu\varepsilon^{-1} \text{ cm}^{-1}$$

$$= 6.8 \text{ deg } \mu\varepsilon^{-1} \text{ cm}^{-1} \quad (6.29)$$

Substituting for  $F$  and  $G$  and also for an FFP ( $\alpha_f = 0.55 \mu\epsilon/K$  [Lagakos *et al.*, 1981] bonded to a steel cantilever ( $\alpha_s = 11.7 \mu\epsilon/K$  [Weast *et al.*, 1970]) in equation 6.27 gives,

$$\text{apparent strain} = 60.6/6.8 + (11.7 - 0.55) = 20 \mu\epsilon/^\circ\text{C}. \quad (6.30)$$

Therefore a temperature change of the substrate of  $1^\circ\text{C}$  would be misinterpreted as a  $20 \mu\epsilon$  change in strain. This effect of apparent strain was experimentally corrected for during static strain measurements, and its correction is discussed in chapter 7.

### 6.5 White light interferometry (WLI)

WLI employs broadband sources (section 4.5), with two interferometers linked in series. Various light sources have been used in white light interferometry including LEDs (which are the most commonly used), multimode laser diodes and superluminescent diodes (SLDs). The path difference of the sensing interferometer is made much longer than the coherence length of the source, so that the two beams reflected from the FFP sensor are incoherent. In order to observe interference fringes, the path difference of the receiving interferometer is matched closely to that of the sensor so that the two beams are brought back into temporal coherence. In WLI systems, the lower the value of coherence length of the source  $l_c$ , the smaller the spatial extent of the interference pattern with the advantage that the central fringe is identified more accurately (section 6.5.2). Most low coherence sources are not suitable for WLI systems because it is very difficult to couple incoherent light from large area sources, resulting in inadequate injected powers and signal-to-noise ratio problems, which would complicate attempts to locate the centre of the interference pattern accurately. Multimode laser diodes have been used as a compromise between the requirement for small  $l_c$  and a reasonable amount of optical power injected into single-mode fibres. However, there may exist a disadvantage in using multimode laser diodes to perform accurate measurements if certain considerations including the nature of the interference fringe pattern formed when using a multimode laser

diode are not taken into account. In this thesis both multimode laser diodes and SLDs are used as sources for WLI. In this section use of multimode laser diode sources in WLI sensing systems is discussed.

### 6.5.1 WLI sensing with multimode laser diodes

The use of multimode laser sources, having a periodic spectrum with cavity modes spaced evenly in frequency at  $\Delta f = c/(2n_{cav}l_{cav})$ , where  $n_{cav}$  is the refractive index of the laser medium and  $l_{cav}$  the cavity length of laser diode, is considerably more complicated than would be expected by simply assuming the linewidth  $\Delta\lambda$  (FWHM) given by the mode envelope. The output from a multimode laser diode consists of a set of longitudinal oscillation modes superimposed on a continuous, wideband, spontaneous emission spectrum [Gerges *et al.*, 1990; Ning *et al.*, 1990]. When the light from a multimode laser diode is injected into a two-beam interferometer, each of the longitudinal modes produces its own interference pattern that is amplitude modulated by an envelope. The output optical power from the interferometer with a path imbalance  $\Delta l$  is given by [Gerges *et al.*, 1990]

$$P_{out} = P_s[1 + V_s \cos\Delta\phi_o(\Delta l)] + \sum_{j=-m}^m P_j[1 + V_j \cos\Delta\phi_j(\Delta l)], \quad (6.31)$$

where  $P_s$  and  $V_s$  are the optical power and visibility function respectively, corresponding to the spontaneous emission, while  $\Delta\phi_o(\Delta l)$  is the optical phase corresponding to the centre frequency. The total number of modes is  $2m + 1$  (including the central one).  $P_j$ ,  $V_j$  and  $\Delta\phi_j(\Delta l)$  are the optical power, visibility function and optical phase of the  $j$ th mode respectively. The optical phase for the  $j$ th mode is given by

$$\Delta\phi_j = \frac{2\pi\nu_j}{c} \Delta l, \quad (6.32)$$

where  $c$  is the speed of light in vacuum and  $\nu_j$  is the frequency of the  $j$ th mode. The output power of the interferometer may be written in the usual form

$$P_{\text{out}} = P_{\text{av}} \left[ 1 + V(\Delta l) \cos \left( \frac{2\pi\nu_0}{c} \Delta l \right) \right], \quad (6.33)$$

where  $P_{\text{av}} = P_s + \sum_{j=-m}^m P_j$  is the average optical power of the laser diode, and  $V(\Delta l)$  is the visibility function of the interferogram. The output power comprises of two terms: a dc term  $P_{\text{av}}$  and an interference term  $P_{\text{osc}}$ , where

$$P_{\text{osc}} = P_s V_s \cos \Delta\phi_0(\Delta l) + \sum_{j=-m}^m P_j V_j \cos \Delta\phi_j(\Delta l). \quad (6.34)$$

The source auto-correlation function  $|\gamma(\Delta l)|$  is given by [Gerges *et al.*, 1990]

$$|\gamma(\Delta l)| = \frac{P_{\text{osc}}}{P_{\text{av}} \cos \Delta\phi_0(\Delta l)}. \quad (6.35)$$

If chromatic dispersion within the laser medium is neglected, and the following conditions are satisfied [Gerges *et al.*, 1990]

$$(i) V_n = V, \text{ for } n = -m, \dots, 0, \dots, m, \quad (6.36a)$$

$$(ii) P_{-j} = P_j, \quad (6.36b)$$

$$(iii) \nu_j = \nu_0 + j\Delta\nu \quad (\text{for } \Delta\nu = c/(2n_{\text{cav}}l_{\text{cav}})), \quad (6.36c)$$

then the source auto-correlation function simplifies to

$$|\gamma(\Delta l)| = \frac{(P_o V + P_s V_s) + 2V \sum_{j=1}^m P_j \cos \frac{2\pi \Delta l_j \Delta v}{c}}{P_{av}} \quad (6.37)$$

Here  $P_o$  is the optical power in the central mode. The visibility function  $V$  has a Lorentzian distribution [Gerges *et al.*, 1990], such that  $V = \exp(-|\Delta l|/l_{cm})$ , where  $l_{cm}$  is the coherence length associated with the modal linewidth, whereas  $V_s$  is a Gaussian function given by [Gerges *et al.*, 1990]  $V_s = \exp\left[-\frac{\pi}{2}(\Delta l/l_{sc})^2\right]$ , where  $l_{sc}$  is the coherence length associated with the spontaneous emission linewidth of the laser diode. It should be noted that  $l_{sc} \ll l_{cm}$ . When the path imbalance ( $\Delta l$ ) in the interferometer is zero, the source auto-correlation function (degree of coherence)  $|\gamma(0)|$  becomes unity, and fringes with unity visibility are observed. As  $\Delta l$  increases, the longitudinal modes rapidly dephase because they oscillate at different frequencies [Gerges *et al.*, 1990] and therefore the amplitude of the resulting interference signal, and thus  $|\gamma(\Delta l)|$  decreases dramatically. Large amplitude interference “packets” appear [Santos and Jackson, 1991] as the differential phase between each adjacent mode approaches  $2\pi$ , (i.e.  $2\pi\Delta l\Delta f/c = 2\pi$ ), giving  $\Delta l = 2n_{cav}l_{cav}$ . Similar interference packets occur for  $\Delta l = 2pn_{cav}l_{cav}$ , where  $p$  is an integer. As  $p$  increases the amplitude of the interference packets will monotonically decrease and will vanish when  $\Delta l \gg l_{cav}$  (figure 6.3).

This type of pattern can be used for low coherence interferometry but it should be observed that there could arise additional noise considerations that must be accounted for [Gerges *et al.*, 1990]. Gerges *et al.* observed noise enhancement of  $\sim 10.8$  dB for small  $\Delta l (< l_{cav})$ , which returned to the noise floor when  $\Delta l \geq 20l_{cav}$ , for a multimode laser diode with a centre wavelength of  $\sim 784$  nm,  $l_{cav} \sim 1.1$  mm and the mode spacing is 134.4 MHz. To meet the requirements of low coherence sensing using multimode laser diodes, the path imbalances of the sensing and receiving interferometers ( $\Delta l_1$  and  $\Delta l_2$  respectively) should be chosen to be either much greater than the coherence length associated with the modal spectral line width (giving a large operating range, which is only limited by the scanning range of receiving

interferometer) or in a range between successive interference packets (i.e.  $< l_{cav}$ ; giving a limited working range defined by the properties of the multimode laser). FFP sensors of optical path difference (50 - 60 mm) which are much greater than 20 times the laser cavity length were used in this work. FFP sensor lengths were chosen so that the optical path difference in the sensor did not coincide with  $2pn_{cav}l_{cav}$ .

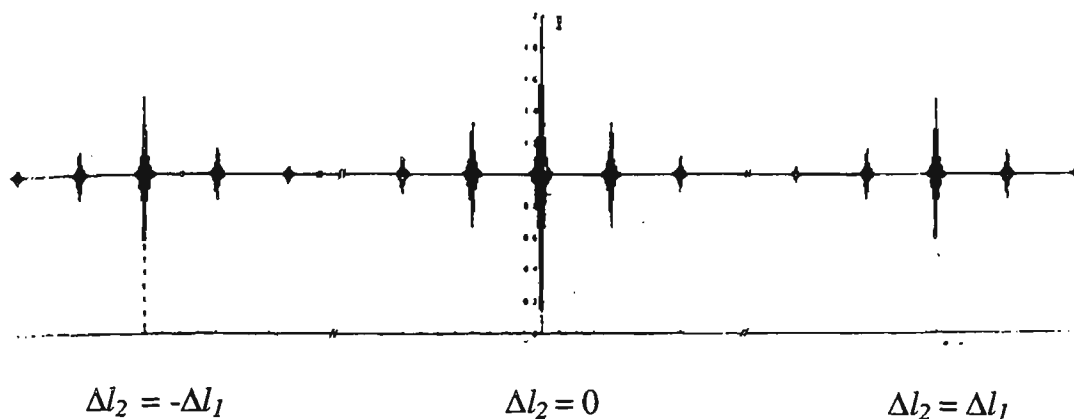


Figure 6.3 Typical WLI interference patterns formed using a multimode laser diode [Gerges *et al.*, 1990]. The horizontal axis is the path imbalance in the receiver interferometer ( $\Delta l_2$ ).  $\Delta l_1$  is the path imbalance in the sensing interferometer.

### 6.5.2 Central fringe determination

The technique of white light interferometry requires signal processing to locate the central (zero order) fringe without ambiguity. A further consideration is the accuracy with which the receiver interferometer's optical path length can be determined. The WLI output is a cosine function modulated by a Gaussian profile. The zero order fringe of a WLI pattern is a bright fringe or dark fringe (depending on the characteristics of the interferometer) with maximum fringe contrast. This fringe defines the centre of the WLI fringe pattern where the optical path difference is zero. It is not possible to identify the central fringe through its maximum visibility, because the visibility profile of a WLI fringe pattern is fairly flat around the central region.

Furthermore, the presence of noise in the output signal imposes considerable limitations in identifying the zero order fringe. Failure to identify the central fringe correctly implies optical path difference measurement errors of more than one wavelength. Therefore, the central fringe must be identified accurately before any sensible measurement can be made. This is achieved via a two stage process, namely: identification of the central fringe, and then determination of the centre of this fringe by interpolation.

Various methods have been used to identify the central fringe, including fast Fourier transform algorithms [Norton, 1992], for which complex signal processing techniques were required. Dandliker *et al.*, [1992] used a “centre of gravity” approach based on calculation of weighted mean of data. The technique first calculates the total power of the ac part of the signal and then its first moment with respect to a specified origin. These two values allow the calculation of the centre of gravity of the interference pattern. The centre of gravity of the interference pattern could be determined to about 1/250 of a fringe for a signal-to-noise ratio of 51 dB. The technique has advantages of simplicity and fairly high resistance to noise. An elaborate procedure of central fringe identification involving a series of digital processing techniques [Chen *et al.*, 1992] and intrafringe resolution enhancement methods [Chen *et al.*, 1992a] has been reported, and has advantages of resistance to noise and improved accuracy for locating the position of zero path difference. The method first pre-filters the noise from the measured data before using an approach similar to the weighted mean of data technique to identify the central fringe. Intra-fringe resolution enhancement methods are then used to get a better estimate of the centre of this fringe. These include a linear interpolation technique that identifies the zero crossing points (first quadrature) on the negative slope of the fringe. This allows an estimate of an offset value (from centre of central fringe) from which the absolute phase can be obtained. In the second approach to finding the centre of central fringe, Chen *et al.* used either the positive data within the central fringe or considered all data points within the entire fringe. Using either set of data points in the central fringe a weighted mean of data approach is used to calculate the centre of this fringe. These intra-fringe resolution enhancement methods performed well with

the full-fringe approach offering the best performance. Using these methods, a phase resolution of 1/400 of a fringe at a signal-to-noise ratio of 26 dB and a sample rate of 13 pixels/fringe was obtained.

Dual broadband sources having a substantial difference in their centre wavelength have also been used in combination to simplify the problem of identifying the central WLI fringe through its maximum visibility [Chen *et al.*, 1993; Wang *et al.*, 1994; Rao and Jackson, 1995]. This technique is based on generation of a synthesised signal which gives rise to low coherence fringes at the average source frequency together with a modulation at the beat frequency. This modulation can considerably reduce the width of the central fringe packet of the low coherence fringes. At zero total path difference the central fringes arising from the two sources are in phase, and as a result the amplitude of the central fringe becomes dominant allowing its identification without the use of sophisticated digital processing techniques. Chen *et al.* [1993] used two laser diode sources operated below threshold with coherence lengths of 30 and 28 fringes and central wavelengths of 670 and 810 nm, respectively. In their system, if either one of the laser diodes were used alone as the optical source, the minimum SNR required to identify the central fringe would be as high as 53 dB, but use of the two laser diode source technique lowered the required SNR to 22 dB. However, this comes at the cost of an extra light source and an extra  $2 \times 2$  optical coupler. The use of multiple wavelength sources is discussed in more detail in chapter 8.

In this present work the central fringe was identified using both a chi-squared fitting technique and the Dandliker *et al.* method for each interferogram. This was coupled with intrafringe resolution enhancement using the full fringe method of Chen *et al.* [1992a]. These central fringe identification methods were generally found to be quite adequate although perhaps they do not perform as well as some more complicated processing schemes which pre-filter the noise. Computer simulations were used to test the performance of the technique and to compare it to the method of Dandliker *et al.* [1992].

### 6.5.3 Chi-squared fitting

The mathematical equation which describes the form of the low coherence fringe pattern (without noise) is well known. One method which can be used to identify the central fringe is to simply fit this equation to the measured data and find the best estimate of the variable parameters in this equation from the data. The quantity that is often used to quantify the fit is called the  $\chi^2$ . Although this fitting technique has long been used [William, 1986], it has not been applied before to fitting a complex signal of WLI fringe pattern with the sole aim of identifying its central fringe. This work presents a new application of the  $\chi^2$  fitting method to identify the central fringe of a white light interference pattern.

Suppose that a set of  $n$  data points,  $y_i$ , have been measured at positions,  $x_i$ , with each data point having its own standard deviation  $\sigma_i$ . If  $f_i$  is the expected measurement value, according to some known distribution (model), the value of chi-squared is defined by [William *et al.*, 1986]

$$\chi^2 = \frac{1}{N_f} \sum_{i=1}^n \frac{(y_i - f_i)^2}{\sigma_i^2}. \quad (6.38)$$

Here  $N_f$  is the number of degrees of freedom of the fit which is equal to the number of data points minus the number of parameters being varied. A large value of  $\chi^2$  indicates a poor fit of the model to the measured data, while a small value of  $\chi^2$  indicates a good fit. If the model includes a function with parameters  $K_j$ , these can be altered to make  $\chi^2$  smaller. Minimisation of  $\chi^2$  results in optimum values of  $K_j$  which give the best fit of the assumed model to the measured data. The parameters have their optimum values for

$$\frac{\partial \chi^2}{\partial K_j} = 0 \quad \text{for all } j. \quad (6.39)$$

The problem of finding the optimum fit to the data is now simply reduced to the problem of determining the parameters  $K_j$  which minimise the  $\chi^2$  function. This is achieved via a suitable computer program. Because of the uncertainty in the result of the algorithm with the representation of the function by discrete points and also the presence of noise in the signal, the determined parameters  $K_j$  have a systematic error and a statistical error. For example, even for an ideal set of data without noise, the measured parameters may not be the same as the actual values, and this deviation defined as the systematic error of the algorithm, is in part a function of the sample rate [Dandliker *et al.*, 1992]. The error estimate in the calculated parameters can be found by finding how much the parameters can vary before  $\chi^2$  increases by 1 from its minimum value [Bevington and Robinson, 1992]. This can be done in two ways; either by keeping all other parameters constant or allowing them to vary. The first estimate gives the change in  $K_j$  required to change  $\chi^2$  by 1 when all other parameters are fixed, and the second estimate gives the change in  $K_j$  required to change  $\chi^2$  by 1 when all other parameters are allowed to vary. The latter gives a more conservative and better error estimate while the former is easier to calculate. The central fringe was identified using the chi-squared fitting method introduced above. In locating the central fringe by using the  $\chi^2$  technique, the equation describing the expected output of the interferometer needs to be considered.

The normalised output of a WLI interference pattern as a function of receiver path difference,  $x$ , can be expressed as [Dandliker *et al.*, 1992]

$$P_{norm.}(x) = 1 + V \exp\left[\frac{-(x - x_s)^2}{(\Delta x)^2}\right] \cos\left[\frac{2\pi}{\Lambda}(x - x_s)\right] \quad (6.40)$$

where,  $V$  is the visibility and  $\Lambda$  the period of the fringes, and  $\Delta x$  is the width and  $x_s$  the centroid of the Gaussian envelope.

Two approaches, both utilising the  $\chi^2$  minimisation technique, were employed in identifying the zero order fringe in this investigation. A model having the form of equation (6.40) was used together with the measured data points and the parameters were allowed to vary until  $\chi^2$  is minimised, thus giving a value for the centroid  $x_s$ . In the second approach, a chi-squared fitting method using only the interference peaks of the fringe pattern was employed to find the centre of the modulation envelope. A program sorts out the interference peaks from the data points of the WLI fringe pattern and a Gaussian function is fitted to the resulting envelope; the centroid being obtained from the optimal fitted parameters. The two different methods are expected to identify the same fringe and the fringe in which this centroid position  $x_s$  is included is taken to be the central fringe.

#### 6.5.4 Centre of the central fringe

The ability to locate the central fringe accurately is the basis for determining the centre of the WLI fringe pattern. The centre of the central fringe,  $x_o$  (that is the position of zero path imbalance), can be determined using a “centroid position” method [Chen *et al.*, 1992a]. The centre of the central fringe is given by

$$x_o = \frac{\sum_{i=1}^k x_i P_{norm.}(x_i)}{\sum_{i=1}^k P_{norm.}(x_i)} , \quad (6.41)$$

where  $x_i$  are the sample points (all positive numbers in this data) and  $k$  is the number of data points lying within the full central fringe. Clearly, this value of  $x_o$  is expected to produce a much more accurate estimate of the centre of the white light fringe pattern than the value of  $x_s$  above. The position of zero path imbalance (when receiver interferometer path difference matches the sensor’s path difference) allows an absolute measurement of the sensor path imbalance.

## 6.6 Modelling of multiplexed system performance

In a fibre optic sensor network, a certain portion of the optical power coupled into the sensor system is lost at splices, connectors, couplers and sensor elements. When these optical losses are accounted for, it is possible to determine the power margin available to each sensor, which in turn gives the possible signal-to-noise ratio and dynamic range of the sensor. Depending on the desired dynamic range and the multiplexed sensor scheme adopted, it is possible to evaluate the number of sensors that can be usefully addressed in a network. The analysis in this work used to predict the maximum number of sensors that can be simultaneously addressed assumes  $N$  low-finesse intrinsic fibre optic Fabry-Perot sensors monitored in reflection. Figure 6.4 shows the arrangement of this serial sensor network. In this multiplexed arrangement low finesse sensors are required in order that sufficient optical power reaches the last sensor. The assumption of low finesse also simplifies calculations because the transfer function of low finesse FFP sensors approximates that of two beam interferometers [Dakin, 1987; section 6.1], and the sensors are normally monitored in reflection since the visibility is generally poor if monitored in transmission. In this arrangement, a single receiver interferometer at the output selectively reconstructs the interference associated with each sensor by tuning its optical path difference to match that of the sensor to within the coherence length of the source. An important consideration for a low coherence multiplexed sensor network is to ensure that only the paths intended to interfere are closely matched. This is achieved by choosing the coherence length of the source,  $l_c$ , to be much less than the path imbalance,  $l_n$ , in each interferometer, so that a change in relative phase between the reference and sensing signal will not be converted into a detectable intensity modulation at the output. Also, each successive path length should be longer than the previous by at least some amount,  $l_o$ , ( $l_o \gg l_c$ ) which ensures that cross talk is minimised.

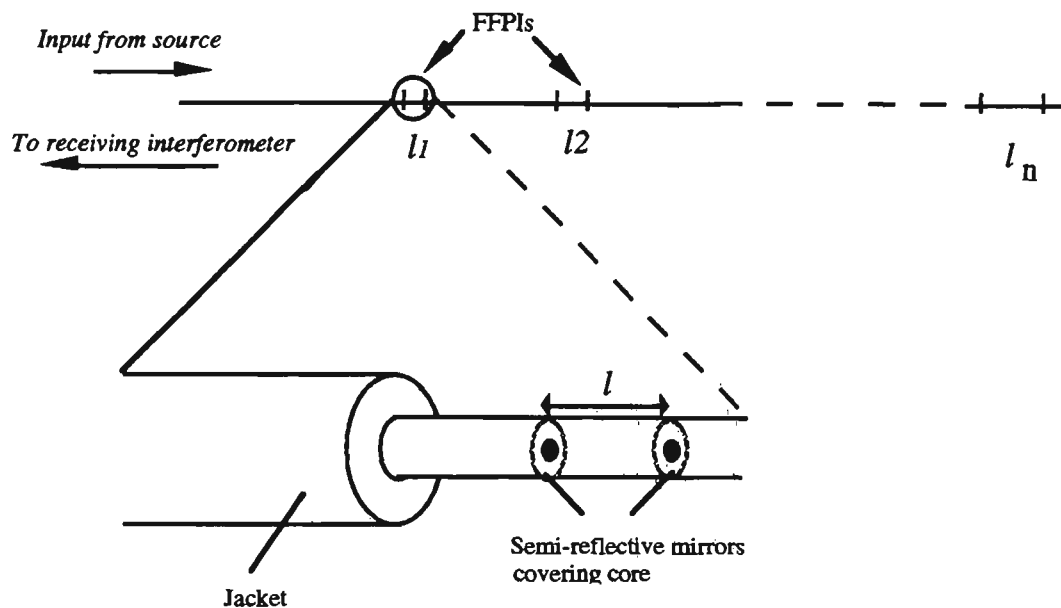


Fig. 6.4 Schematic diagram of  $N$  serially multiplexed in-line FFPI sensors. The semi-reflective mirrors are confined to a region of  $\sim 25 \mu\text{m}$  diameter which includes the core.

### 6.6.1 Interferometer transfer function

To obtain the interferometer transfer function, a single FFPI sensor is considered and a receiver interferometer of Mach-Zehnder type (could be a Fabry-Perot) as shown in figure 6.5. The incident electric field of amplitude  $E_0$  is partially reflected at mirror A (reflection coefficient  $r_a$ ) and partially transmitted (transmission coefficient  $t_a$ ). When the transmitted field strikes mirror B it is multiplied by  $r_b$  on reflection, and by  $t_b$  on transmission, where  $r_b$  and  $t_b$  are the fraction of the electric field amplitude reflected and transmitted at B respectively. For reasons of simplicity all rays are assumed to be normal to the mirror surfaces.

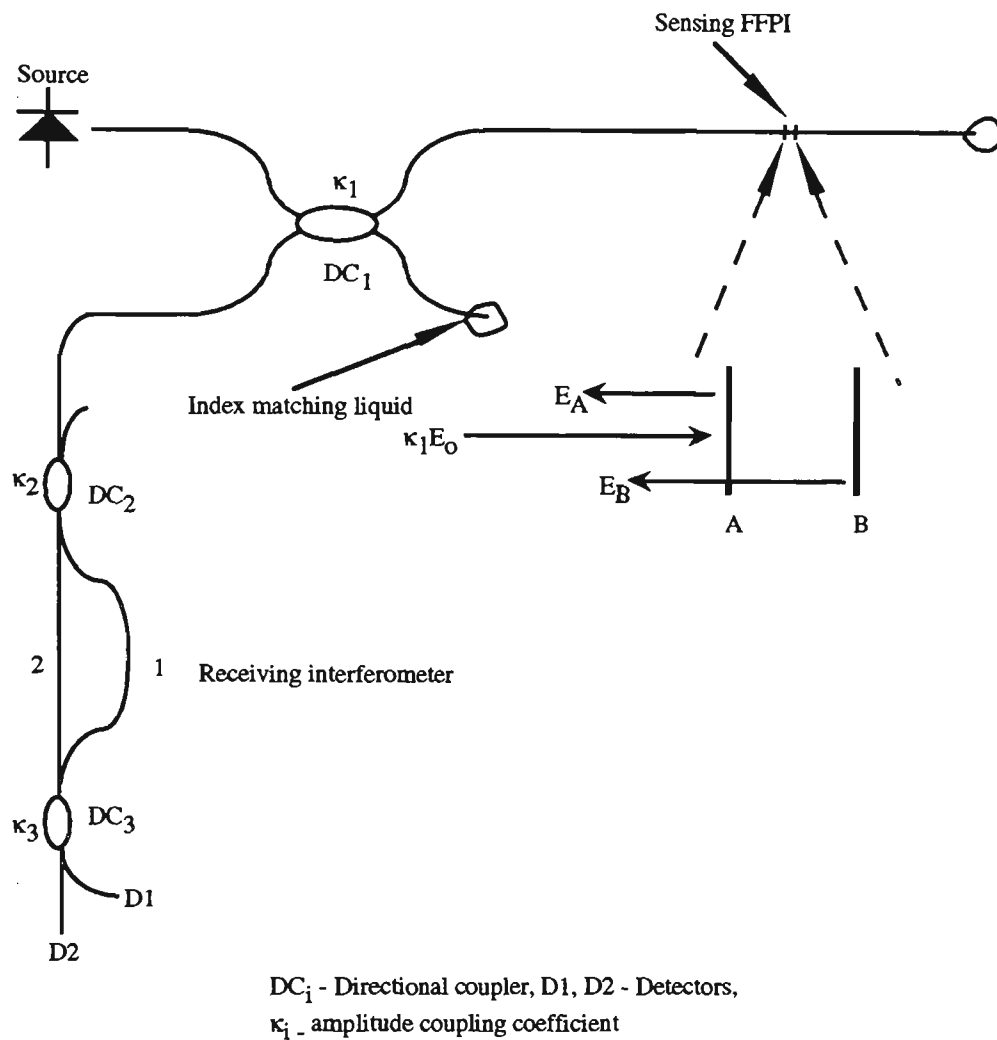


Fig. 6.5 Schematic diagram of WLI arrangement with a single sensing and receiving interferometer

In addition, it is assumed that the state of polarisation of the guided beam remains unchanged. For identical dielectric coatings  $r_a = r_b = r$  and  $t_a = t_b = t$ , and therefore the total electric field at the detector can be given by

$$E = E_{A1} + E_{A2} + E_{B1} + E_{B2} \quad , \quad (6.42)$$

where  $E_{jk}$  ( $j = A, B, k=1, 2$ ) is the component of the electric field observed at the detector output, from mirror  $j$  of the sensing interferometer and propagated via the  $k$ th arm of the receiving interferometer. Following a similar treatment to that described by others [Culshaw and Dakin, 1989; Al-Raweshidy and Uttam, 1990], the four component electric fields can be written as

$$E_{A1} = \kappa_1^2 \kappa_2 \kappa_3 r E_o(\tau_{A1}) e(i\omega\tau_{A1}),$$

$$E_{A2} = \kappa_1^2 \kappa_2 \kappa_3 r E_o(\tau_{A2}) e(i\omega\tau_{A2}),$$

$$E_{B1} = \kappa_1^2 \kappa_2 \kappa_3 t^2 r E_o(\tau_{B1}) e(i\omega\tau_{B1}),$$

$$E_{B2} = \kappa_1^2 \kappa_2 \kappa_3 t^2 r E_o(\tau_{B2}) e(i\omega\tau_{B2}), \quad (6.43)$$

where  $E_o(0)$  is the electric field amplitude of the source,  $\tau_{jk}$  are the propagation times from the source to the detector via sensing and receiving interferometers, and  $\kappa_1, \kappa_2, \kappa_3$  are the electric field amplitude coupling coefficients. The electric fields and coupling coefficients are scalar quantities since polarisation effects have, in this case, been neglected. However, to account for changes of phase during coupling, the coupling coefficients are complex quantities. The output optical power observed at the detector is given by

$$I_{out} = \langle E \cdot E^* \rangle \quad (6.44)$$

By assuming 50% coupling (i.e.  $\kappa_i = 1/\sqrt{2}$ ) and a lossless system, the resulting output optical power relative to the input power  $I_o$  may therefore be represented by (using equations 6.41, 6.42 and 6.43)

$$\begin{aligned} \frac{I_{out}}{I_o} = \frac{1}{16} \times \{ & 2r^2 + 2r^2t^4 + \gamma(\tau_{A1}-\tau_{A2})r^2e^{i\omega(\tau_{A1}-\tau_{A2})} + \gamma(\tau_{A1}-\tau_{B1})r^2t^2e^{i\omega(\tau_{A1}-\tau_{B1})} + \\ & \gamma(\tau_{A2}-\tau_{A1})r^2e^{i\omega(\tau_{A2}-\tau_{A1})} + \gamma(\tau_{A1}-\tau_{B2})r^2t^2e^{i\omega(\tau_{A1}-\tau_{B2})} + \gamma(\tau_{A2}-\tau_{B1})r^2t^2e^{i\omega(\tau_{A2}-\tau_{B1})} + \\ & \gamma(\tau_{A2}-\tau_{B2})r^2t^2e^{i\omega(\tau_{A2}-\tau_{B2})} + \gamma(\tau_{B1}-\tau_{A1})r^2t^2e^{i\omega(\tau_{B1}-\tau_{A1})} + \gamma(\tau_{B1}-\tau_{A2})r^2t^2e^{i\omega(\tau_{B1}-\tau_{A2})} + \\ & \gamma(\tau_{B1}-\tau_{B2})r^2t^4e^{i\omega(\tau_{B1}-\tau_{B2})} + \gamma(\tau_{B2}-\tau_{A1})r^2t^2e^{i\omega(\tau_{B2}-\tau_{A1})} + \gamma(\tau_{B2}-\tau_{A2})r^2t^2e^{i\omega(\tau_{B2}-\tau_{A2})} + \\ & \gamma(\tau_{B2}-\tau_{B1})r^2t^4e^{i\omega(\tau_{B2}-\tau_{B1})} \} \quad , \end{aligned} \quad (6.45)$$

where the degree of coherence of the source has been defined [Born and Wolf, 1969] as

$$\gamma(\tau_x - \tau_y) = \langle E_O(\tau_x).E_O^*(\tau_y) \rangle / I_o . \quad (6.46)$$

There are only 2 path imbalances, so we may define

$$\tau_{A1} - \tau_{A2} = \tau_{B1} - \tau_{B2} = \tau_m , \quad \tau_{A2} - \tau_{B2} = \tau_{B1} - \tau_{A1} = \tau_s , \quad \text{and} \quad r^2 = R, \quad t^2 = T , \quad (6.47)$$

where  $\tau_m$  and  $\tau_s$  are the differential propagation time delays in the receiving (measurement) and sensing interferometers, respectively.  $R$  is the intensity reflection coefficient and  $T$  is the intensity transmission coefficient. The degree of coherence may be related to the coherence time  $\tau_c$  of the source by [Born and Wolf, 1969]

$$\gamma(\tau) = e^{-|\tau| / \tau_c} . \quad (6.48)$$

The output optical power then becomes

$$\begin{aligned} I_{out} = \frac{1}{16} \times I_o \{ & 2R + 2RT^2 + 2\gamma(\tau_m)R(T^2+1).\cos\omega\tau_m + 4\gamma(\tau_s)RT.\cos\omega\tau_s + \\ & 2\gamma(\tau_m-\tau_s)RT.\cos\omega(\tau_m-\tau_s) + 2\gamma(\tau_m+\tau_s)RT.\cos\omega(\tau_m+\tau_s) \} . \end{aligned} \quad (6.49)$$

For interference to be observed at the detector, one of the following conditions has to be satisfied:

$$\tau_m, \tau_s, \tau_m - \tau_s, \text{ or } \tau_m + \tau_s \leq \tau_c \quad .$$

If the sensing and receiver interferometer differential propagation time delays  $\tau_s$  and  $\tau_m$  are chosen to be greater than the coherence time  $\tau_c$ , then the terms  $\gamma(\tau_m)$ ,  $\gamma(\tau_s)$ ,  $\gamma(\tau_m + \tau_s)$ , and  $\gamma(\tau_m - \tau_s)$  become negligibly small, so that equation 6.49 reduces to

$$I_{out} = \frac{I_o}{8} [R + R(1 - R)^2] = I_A \quad . \quad (6.50)$$

Thus the output irradiance does not contain any interference terms when the sensing and receiving interferometers are not balanced.

White light interferometry requires both the sensor and receiver path imbalances to be greater than the coherence length of the source, but in order to observe an interference pattern, their relative path difference should be within the coherence length of the source such that  $\tau_m \approx \tau_s$ . Then the term  $\gamma(\tau_m - \tau_s)$  approaches unity while  $\gamma(\tau_m)$ ,  $\gamma(\tau_s)$  and  $\gamma(\tau_m + \tau_s)$  tend to zero. Using these limits in conjunction with equation 6.49, the observed optical power at the detector is

$$I_{out} = I_A [1 + V \cos \omega(\tau_m - \tau_s)] \quad (6.51)$$

where (noting that  $R + T = 1$ )

$$V = \frac{R(1 - R)}{R + R(1 - R)^2} \quad . \quad (6.52)$$

Equation 6.51 applies where  $\tau_m \approx \tau_s$ , i.e. near the centre of the fringe pattern and shows that the centre of the fringe pattern is an intensity maximum. However, away from the centre of the pattern  $\gamma(\tau_m - \tau_s)$  is no longer unity and this means the fringe visibility reduces as indicated by equation 6.40.

### 6.6.2 Multiplexed sensors

To obtain the possible number of FFPI sensors that can be addressed in the network, the transmission characteristics of these sensors needs to be considered. Consider an incident plane wave of amplitude  $E_0$  which is successively reflected between two plane parallel surfaces, separated by a distance  $d$ . The incident beam makes an angle of  $\theta$  with the second plane surface as shown in figure 6.6. The reflection coefficients at each surface are equal to  $r$  and the transmission coefficients are equal to  $t$ .

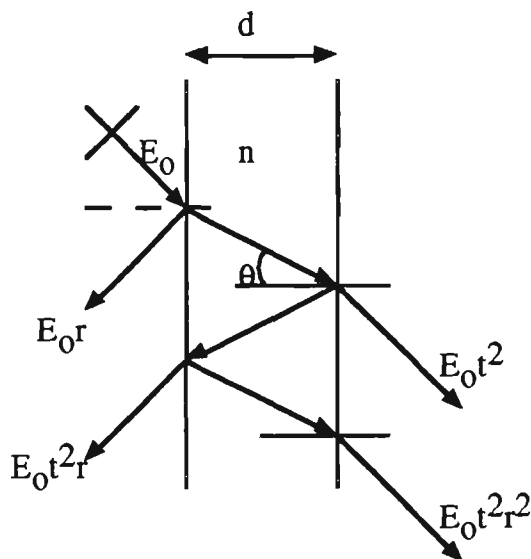


Fig. 6.6 Amplitudes of successive rays reflected back and forth between two plane surfaces

The transmitted electric field,  $E_t$ , neglecting higher order terms is given by

$$E_t = E_o t^2 e^{i\omega t} + E_o t^2 r^2 e^{i(\omega t - \phi)} , \quad (6.53)$$

where  $\phi$  is the phase lag between any two adjacent reflected beams corresponding to a double passage of the cavity and is given by [Vaughan, 1989],  $\phi = 2\pi(2n_{\text{eff}}d\cos\theta)/\lambda$ , with  $n_{\text{eff}}$  being the effective index of refraction inside the cavity and  $\lambda$  the free space wavelength. The transmitted intensity for this first FFPI,  $I_{t1}$ , is (given by  $\langle E_t E_t^* \rangle$ )

$$I_{t1} = I_o T^2 (1 + R^2 + 2R\cos\phi_1) , \quad (6.54)$$

where  $I_o$  is the incident intensity, and as stated earlier  $R$  and  $T$  are reflection and transmission coefficients. For a system without losses within the Fabry-Perot,  $R$  and  $T$  are related by  $R + T = 1$ , and thus substituting for  $T$  gives

$$I_{t1} = I_o [(1-R)^2 + R^2(1-R)^2 + 2R(1-R)^2\cos\phi_1] . \quad (6.55)$$

If there are two FFPI sensors multiplexed in series and monitored in transmission, assuming the reflection coefficient is the same for every FP mirror, the intensity transmitted through the second Fabry-Perot cavity,  $I_{t2}$ , is obtained by analogy from equation 6.55, i.e.

$$I_{t2} = I_{t1} [(1-R)^2 + R^2(1-R)^2 + 2R(1-R)^2\cos\phi_2] . \quad (6.56)$$

For  $N$  serially multiplexed FFPI sensors, the intensity incident on the  $n$ th sensor ( $2 \leq n \leq N$ ) will be that transmitted through the  $(n-1)$ th sensor. The intensity  $I_{T(n-1)}$  transmitted through the  $(n-1)$ th FFPI sensor can therefore be written as

$$I_{T(n-1)} = I_o \prod_{i=1}^{n-1} l_i (W + Q\cos\phi_i) , \quad (6.57)$$

where

$$W = (1 - R)^2 + R^2(1 - R)^2 ,$$

$$Q = 2R(1 - R)^2 ,$$

$\phi_i$  = phase delay in  $i$ th sensor .

Here the term  $l_i$  has been incorporated to allow for losses which are observed within these fusion-spliced fibre Fabry-Perot interferometers.

For a low reflectivity FFPI interferometer in reflection the intensity returned  $I_R$  as a function of the incident intensity  $I_i$  can easily be shown to be

$$I_R = I_i[R + R(1 - R)^2 + 2R(1 - R)\cos\phi] , \quad (6.58)$$

and thus the optical power returned from the  $n$ th sensor,  $I_{Rn}$ , towards the processing unit is deduced to be

$$\begin{aligned} I_{Rn} &= I_{T(n-1)}[R + R(1 - R)^2 + 2R(1 - R)\cos\phi_n] , \\ &= I_o(U + Z\cos\phi_n) \prod_{i=1}^{n-1} l_i(W + Q\cos\phi_i) , \end{aligned} \quad (6.59)$$

(substituting from equation 6.57) where

$$U = R + R(1 - R)^2 ,$$

and

$$Z = 2R(1 - R).$$

Therefore, the intensity leaving the network from sensor  $n$ ,  $I_n$ , after passing through sensors (n-1) to 1 can be expressed as (by analogy with equation 6.57)

$$I_n = I_{Rn} \prod_{i=n-1}^1 l_i (W + Q \cos \phi_i) ,$$

$$I_n = I_o (U + Z \cos \phi_n) \prod_{i=1}^{n-1} l_i (W + Q \cos \phi_i) \prod_{i=n-1}^1 l_i (W + Q \cos \phi_i),$$

$$I_n = I_o (U + Z \cos \phi_n) \prod_{i=1}^{n-1} l_i^2 (W + Q \cos \phi_i)^2 . \quad (6.60)$$

Equation 6.60 applies for all  $n$ , such that  $2 \leq n \leq N$ . For  $N = 1$ , the returned intensity is simply

$$I_1 = I_o (U + Z \cos \phi_1) . \quad (6.61)$$

Up to this point the analysis includes coherence effects as phase terms have been kept. The intensity at the detector  $I_{Dn}$  from sensor  $n$  is obtained by considering the receiver interferometer, having a path delay  $\phi_m$ , and includes a term  $\eta_r$  which incorporates the attenuation of the signal beam by optical components placed between the series of sensors and the detector

$$I_{Dn} = I_o \eta_r [U + Z \cos(\phi_m - \phi_n)] \prod_{i=1}^{n-1} l_i^2 [W + Q \cos(\phi_m - \phi_i)]^2 . \quad (6.62)$$

For the situation in which all path differences are much greater than the coherence length of the source then all phase terms disappear, i.e.  $\cos(\phi_m - \phi_i) = 0$ . Alternatively, if the receiver interferometer is tuned so that for a single sensor  $n$ , the total optical path difference is less than the source coherence length, then the intensity will be

$$I_{Dn} = \eta_r I_o [U + Z \cos(\phi_m - \phi_n)] \prod_{i=1}^{n-1} l_i^2 W^2 . \quad (6.63)$$

Figure 6.8 shows an example of the normalised return power from the last sensor (i.e.  $I_{DN}$  from equation 6.63) when 2, 3, 4 or 5 FFPI sensors are arranged in series. The graphs plot  $I_{DN}/(\eta_r I_o)$  as a function of reflectance (assumed uniform for all mirrors) and include a one-way total sensor loss ( $l_t$ ) of 0.7 dB which is the lowest value obtained for the sensors manufactured by fusion splicing in this work.

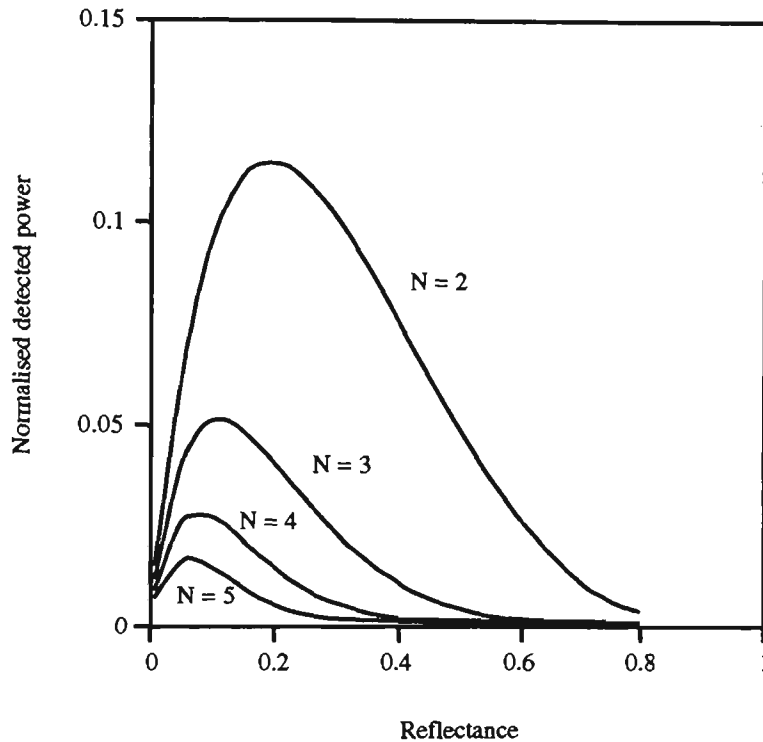


Figure 6.8 Normalised detected power  $I_{DN}/(\eta_r I_o)$  intensity from the last sensor in an N sensor array as a function of reflectance. The one way total loss assumed for each sensor in this calculation is 0.7 dB.

Figure 6.8 clearly indicates that there exists an optimum reflectance which maximises the power received from a particular sensor in the series. This is to be expected since for very small values of R most of the incident power is transmitted and reflected signals are small; while for large R most of the power is reflected from the first sensor and little is incident on subsequent ones. Figure 6.9 is a plot of the mirror reflectance required to optimise the signal from the last sensor

as a function of the number of sensors. It can be seen from this figure that most practical multiplexing situations will require mirror reflectivities of about 2% - 10%.

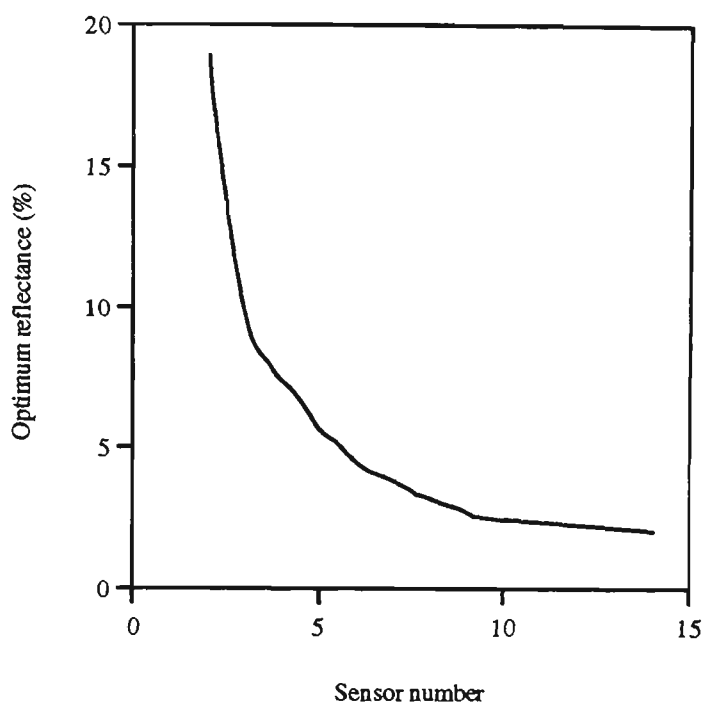


Fig. 6.9 A plot of optimum value of reflectance against number of sensors.

From the analysis above, the maximum number of sensors, which can be addressed for a given reflectivity and launched power, can be determined. The maximum number of sensors is dependent on the maximum power at the detector which will give a signal-to-noise ratio sufficient for reliable determination of the central fringe. Figure 6.10 shows an example of a plot of the detected power from the last sensor in a series, plotted as a function of the number of sensors included in the series. This data has been produced using equation 6.62 with  $\eta_r$  set arbitrarily to 1,  $l_i$  having a range of values from 0.7 to 3.5 dB and with a mirror reflectivity of 10%. Also, the minimum power for satisfactory determination of central fringe position was set arbitrarily at -50 dBm. For the purposes of the example, the value is not important and in fact the real situation (see chapter 7) is not too different from this.

From the figure it can be seen that, under the assumed conditions the number of sensors which can be placed in series are 8, 6 and 4 for values of  $l_t$  of 0.7 dB, 1.5 dB and 3.5 dB respectively. When the receiver efficiency is included by incorporating the value of  $\eta_r$  then these values will be reduced. For example for  $\eta_r = 0.1$ , the maximum numbers of sensors which can be used are 4, 3 and 2 for values of  $l_t$  of 0.7 dB, 1.5 dB, and 3.5 dB respectively.

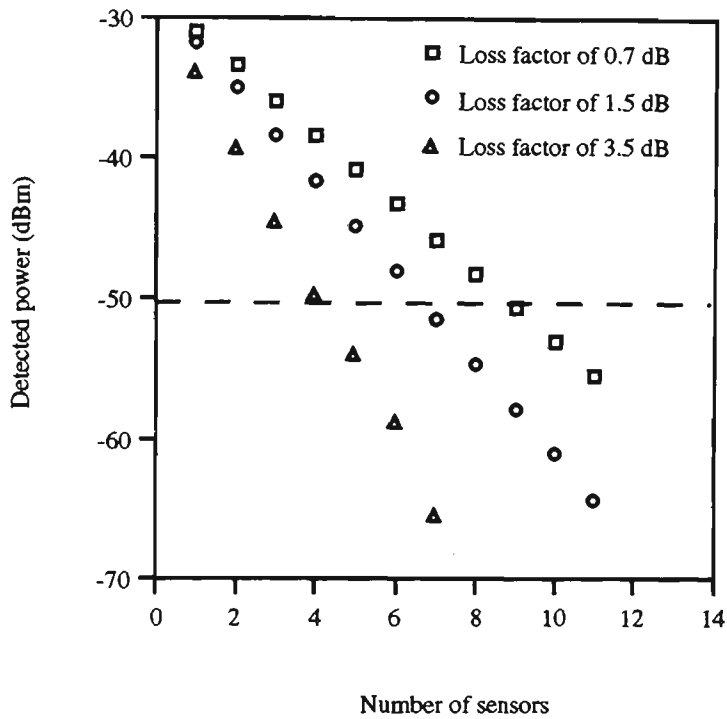


Figure 6.10 Detected power from the last sensor in series against sensor number at various values of loss factor  $l_t$ . For the calculation the reflectivity of each mirror is 10%,  $\eta_r$  is 1 and power launched into sensor network is - 23 dBm.

Figure 6.11 is similar to figure 6.10, except that in this case the effect of varying the mirror reflectivity can be seen. Clearly higher reflectivities significantly increase the signal from the near sensors and also decrease the total number of sensors which can be used. A suitable value of the mirror reflectance depends on the number of sensors which need to be addressed as

discussed earlier. Again it can be seen this will be somewhere in the range 2% - 10%. For such reflectivities, the assumption of low finesse which was used in the calculations will certainly be valid.

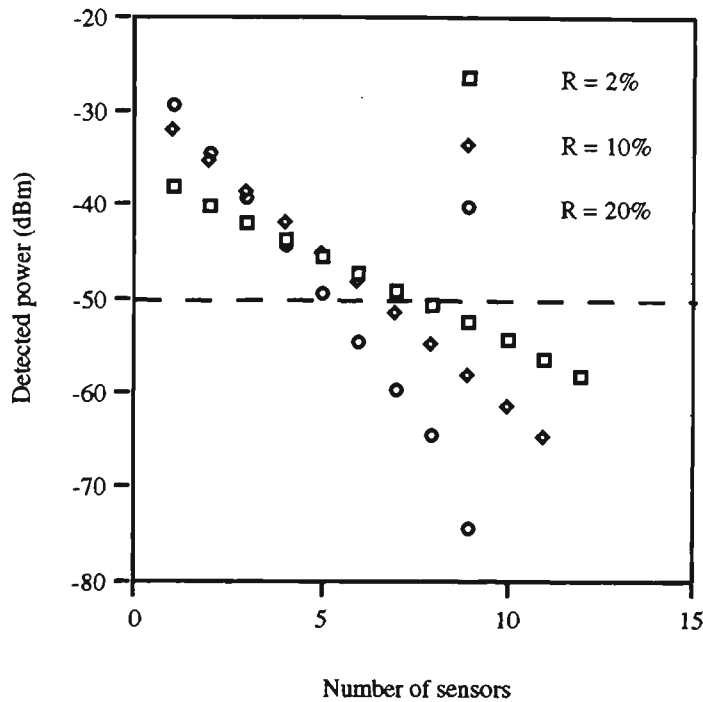


Figure 6.11 Optical power received at the detector from the nth sensor against number of sensors. For this calculation  $\eta_r = 1$  and  $l_t = 3.5$  dB.

The fringe visibility given in equation 6.52 is shown in figure 6.12 plotted as a function of reflectance where it can be seen that the fringe contrast decreases with R; this is a further indication of the requirement for low finesse FFPI sensors.

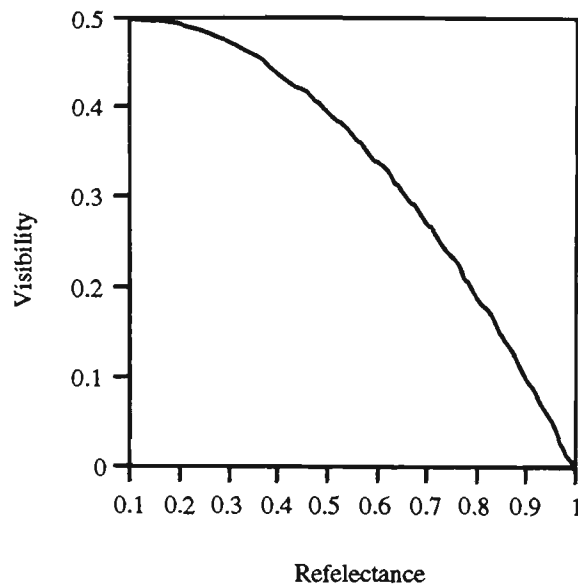


Figure 6.12 Fringe visibility versus reflectance of the FFPI sensor

## 6.7 Conclusion

The basic theory of a fibre Fabry-Perot interferometer has been described and the method used to identify the centre of the low coherence interference pattern discussed. An estimation has been given for the measurement sensitivity when sensing strain or temperature. The intrinsic FFPI is well suited for static strain measurement, however, its co-dependency on temperature and strain can complicate its application as a strain sensor. With a single measurement of phase shift, it is not possible to distinguish between the effects of changes in strain or temperature. Therefore, compensation or correction for apparent strain is required if meaningful static strain measurements are to be made. Chapter 7 presents strain measurements using fusion-spliced sensors as well as measurements of the thermally-induced apparent strain.

Calculations have been performed which give the reflected and transmitted intensity from a single FFPI sensor. These were extended to  $N$  identical FFPI sensors connected in series. The results obtained from these calculations have been used to estimate a suitable value of reflectance for each FFPI sensor suitable for use in a multiplexed system by optimising the intensity of light returned to the detector from the last sensor (which has the worst signal-to-

noise ratio). The power available per sensor is not the only limiting factor determining the maximum number of addressable sensors (without cross modulation effects). Another important consideration limiting the number of sensors in WLI schemes is the scanning range of the receiver interferometer required to match the different optical paths length of various multiplexed sensors. The path imbalances of these sensors increase with the number of sensors. The receiver interferometer used in this work had a maximum displacement range of 25 mm which made it well-suited for serially multiplexing several sensors of different free spectral ranges. It would be desirable to have equal power returned from each sensor to the central processing unit, but this requires each sensor to have a different finesse value. The reflectances of successive sensors would have to increase with increased number of sensors, but without compromising the low finesse condition, which inevitably reduces the number of sensors able to be multiplexed. The analysis becomes more complex than when the same value of reflectance is assumed for each sensor mirror. However, since the Fabry-Perot interferometers are of low reflectance (2-10%), significant optical power is transmitted and is available for sensors further down the fibre. This can mean that FFPIs with different reflectances are not necessarily required. In this model only sensors of equal reflectance were considered. The model is verified experimentally in chapter 7 where intrinsic FFPI sensors monitored in reflection are investigated in a multiplexed array.

## CHAPTER 7

# EXPERIMENTAL MEASUREMENTS WITH FUSION-SPLICED SENSORS

### 7.1 Measurements with one sensor

Following the successful development and fabrication of intrinsic FFPI sensors, their temperature and static strain response was investigated. FFPIs fabricated using a 1300 nm single-mode fibre were tested for their temperature and strain response using a 1.3  $\mu\text{m}$  laser diode source having sufficient coherence length to give a coherent response from the sensor. To demonstrate absolute measurement of temperature and strain using white light interferometry, intrinsic FFPI sensors fabricated from an 850 nm single-mode Flex core fibre were used.

#### 7.1.1 Thermal characteristics of the FFPIs

The temperature induced phase shift was measured in an intrinsic fibre Fabry-Perot interferometer of nominal cavity length of 5 mm and mirror reflectances of approximately 4% and 6%. Figure 7.1 shows the experimental set-up, in which the sensor FFPI was monitored in reflection. The FFPI was spliced to the output of the coupler (port 3), and light from a stabilised laser diode, having sufficient coherence length to produce interference fringes was launched into the fibre Fabry-Perot sensor via a 2 $\times$ 2 directional coupler arrangement. The two

reflected beams overlap coherently and were monitored using an ANDO optical power meter. The other output arm of the coupler (port 4) and the end of the sensing fibre were index matched to avoid unwanted reflections. Any change in temperature of the sensing fibre alters the optical path length of the sensor, thus introducing a corresponding change in the optical phase of the reflected light (section 6.2). This change in phase of the light (received at the detector) allows the measurement of temperature via determination of the fringe shift.

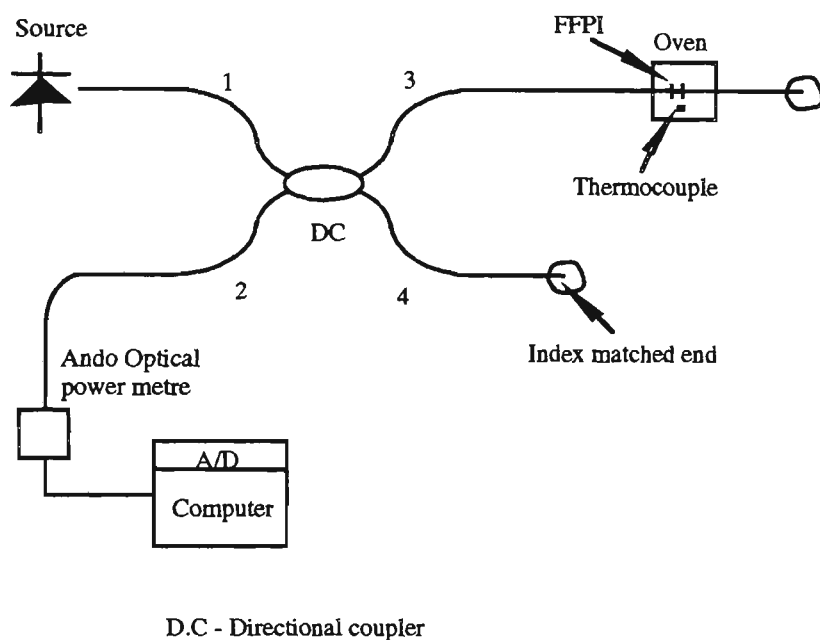


Figure 7.1 Experimental arrangement for FFPI temperature characterisation.

### 7.1.2 Thermal results

The thermal sensitivity of the sensor was measured by monitoring the variation of reflectance of the FFPI as its temperature was changed. The temperature of the FFPI sensor was varied by a miniature oven fixed to a current-controlled hot plate and monitored independently by a thermocouple placed adjacent to the sensor. The optical power reflected from the sensor and the temperature read by the thermocouple were recorded as the temperature of the oven was slowly raised. Figure 7.2 shows the reflected intensity from the FFPI sensor over the range of

25 - 145 °C. The reflectance variation of the FFPI sensor with temperature produces typical cosine like fringes on the detector as expected from such a low finesse interferometer. In figure 7.3 the phase shift calculated using the data of figure 7.2, is plotted as a function of temperature. The graph obtained in figure 7.3 is linear with a constant relative phase shift per unit temperature ( $\Delta\phi/\phi\Delta T$ ) of  $7.0 \times 10^{-6}/K$  ( $\lambda = 1300$  nm). This value is in good agreement with the approximate value of  $7.4 \times 10^{-6}/K$  obtained in the theoretical prediction using bulk silica parameters (section 6.2).

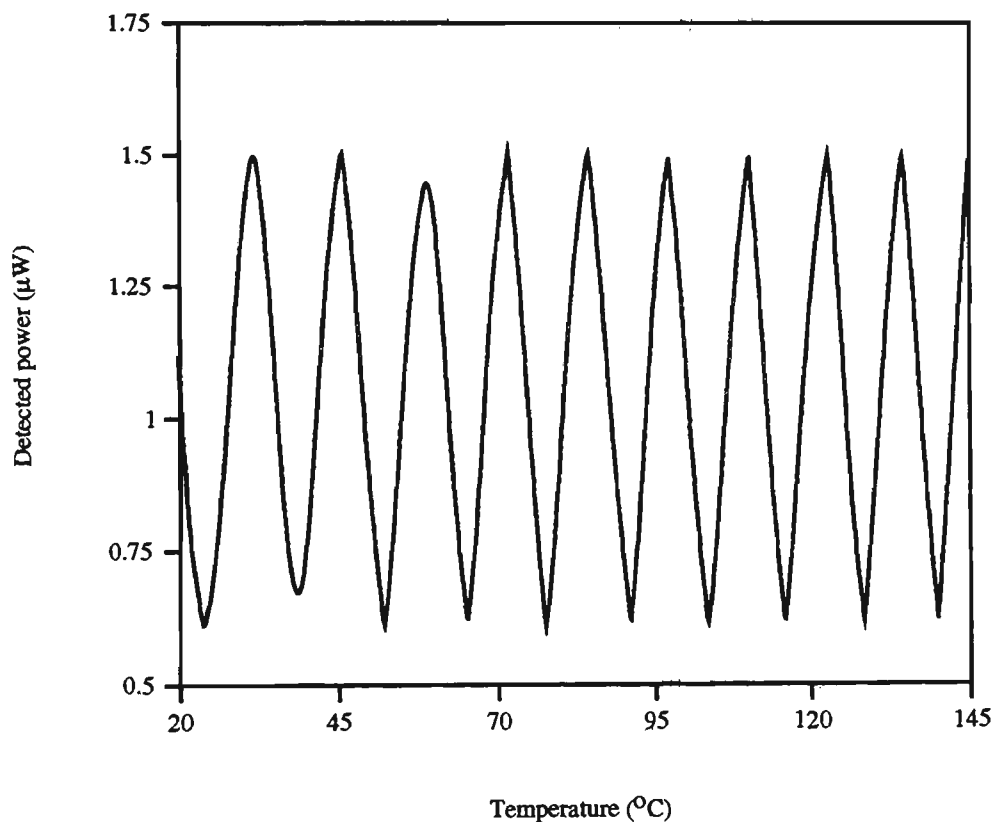


Figure 7.2 Power reflected from the FFPI sensor (cavity length ~ 5 mm, mirror reflectances ~ 4% and 6%) against temperature measured by the thermocouple.

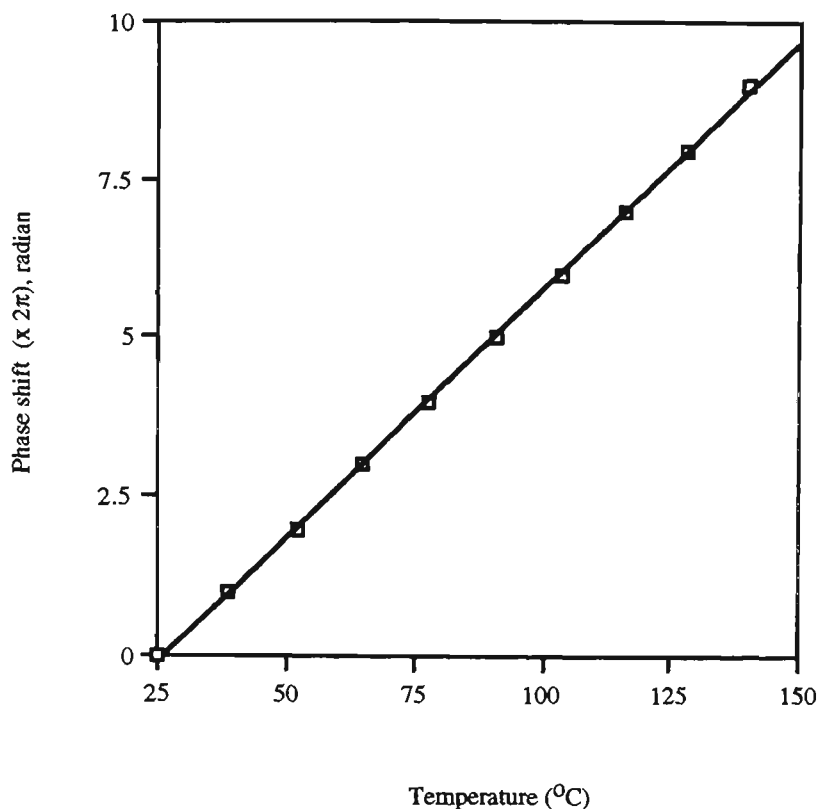


Figure 7.3 Phase shift versus temperature for an FFPI sensor of length  $\sim 5$  mm, mirror reflectances  $\sim 4\%$  and  $6\%$ , using a laser diode source of centre wavelength of 1300 nm.

### 7.1.3 Results for Static strain

An experiment was also performed to examine the static strain response of the fabricated FFPI sensors. The experimental arrangement used for strain monitoring was similar to that shown schematically in figure 7.1, except for the oven, which was replaced by a cantilever beam. The strain sensitivity measurements for the FFPI were obtained for an FFPI of length around  $\sim 4.5$  mm and effective mirror reflectance of  $8\%$ . The FFPI strain sensor, along with a resistance strain gauge of similar length were adhered to the upper surface of a mild steel cantilever, parallel to the direction of principal strain with epoxy adhesive using a procedure recommended for resistive strain gauges. The optical power returned from the FFPI sensor and the electrical

strain gauge reading were recorded as the cantilever was stressed. Figure 7.4 is a plot of the phase shift against the strain measured by the electrical strain gauge as the beam was stressed.

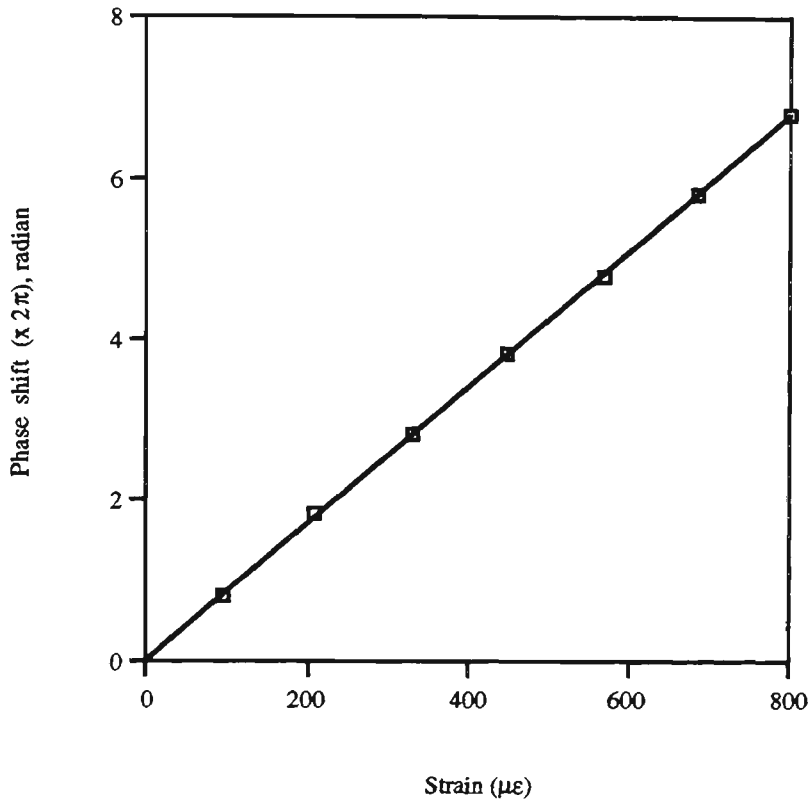


Figure 7.4 Sensor phase shift (cavity length  $\sim 4.5$  mm, effective mirror reflectance  $\sim 8\%$ ,  $\lambda = 1300$  nm) as a function of longitudinal strain.

The experimentally measured optical phase shift per unit strain is nearly constant, with a value of the optical gauge factor  $(\Delta\phi/\phi\epsilon)$   $G_{\text{FFPI}} = 0.840 \pm 0.004$ . This value is in close agreement with the predicted value of 0.794 (section 6.3). These preliminary FFPI strain measurements using a coherent source were carried out in order to give an initial assessment of the sensor performance and sensitivity. During these measurements the temperature of the sensor was not controlled but merely remained at room temperature (assumed constant).

## 7.2 Summary of temperature and strain measurements

The above observations show that the FFPIs developed and fabricated performed well as both temperature and strain sensors. The experimental temperature and strain sensitivities obtained with these FFPIs were in agreement with the predicted values. These sensors are lead insensitive and satisfy the initial criteria of small size, ease of handling and are simple to bonding to structures. They were thus considered for use in serial multiplexing of low coherence demodulated fibre Fabry-Perot sensors for absolute strain measurements. Table 7.1 summarises the measured characteristics.

Fibre used	single-mode, 8/125 $\mu\text{m}$ communications grade
Cavity length	4 - 5 mm
Sensor diameter	125 $\mu\text{m}$
Operating wavelength	1300 nm
Temperature sensitivity	$7.0 \times 10^{-6}/\text{K}$
FFPI optic gauge factor	$0.840 \pm 0.004$

Table 7.1 The FFPIs temperature and strain response.

## 7.3 WHITE LIGHT INTERFEROMETRY MEASUREMENTS

### 7.3.1 WLI measurements with a single FFPI sensor

In this section experimental results are presented for low finesse FFPI sensors used to measure temperature and strain. The FFPIs were produced in the manner described in section 5.3 by arc fusion splicing of titanium dioxide-coated single-mode fibre onto an similar uncoated fibre. The optical fibre used for this present investigation was Corning Flexcore 780 single-mode fibre of diameter  $5/125\ \mu\text{m}$ , attenuation 3 dB/km @ 850 nm and cut off wavelength of 750 nm. The sensing scheme employs a multimode laser diode source (coherence length  $\sim 150\ \mu\text{m}$ ) and two interferometers, an intrinsic FFPI sensing interferometer and a Fabry-Perot type receiving interferometer (figure 7.5). The receiving interferometer was formed by a cleaved end of a single-mode fibre and a planar mirror, which is driven by a computer controlled Melles-Griot Nanomover having 50 nm displacement resolution and 25 mm travel. The path difference of the sensing interferometer was made much longer than the coherence length of the source, to ensure that the two beams reflected from the FFPI sensor do not interfere.

### 7.3.2 Experimental arrangement for temperature measurement

The FFPI sensor reflectance was approximately 6% with a nominal cavity length of 2 cm. Figure 7.5 shows the WLI experimental arrangement, in which the sensor FFPI was monitored in reflection. Light from a multimode laser diode (LT016MD: centre wavelength 810 nm, coherence length  $\sim 150\ \mu\text{m}$ ) was launched into the sensor via a  $2\times 2$  directional coupler arrangement. The two reflections from the FFPI enter the receiving interferometer via the second directional coupler. Lens L collimates the beam before reflection from the mirror M and refocusses the reflected light into the same fibre. The mirror of the receiving interferometer is mounted on a translation stage which is driven by a computerised precision Nanomover. This

mirror arrangement in the receiving interferometer must exhibit great mechanical stability for accurate and reliable measurements.

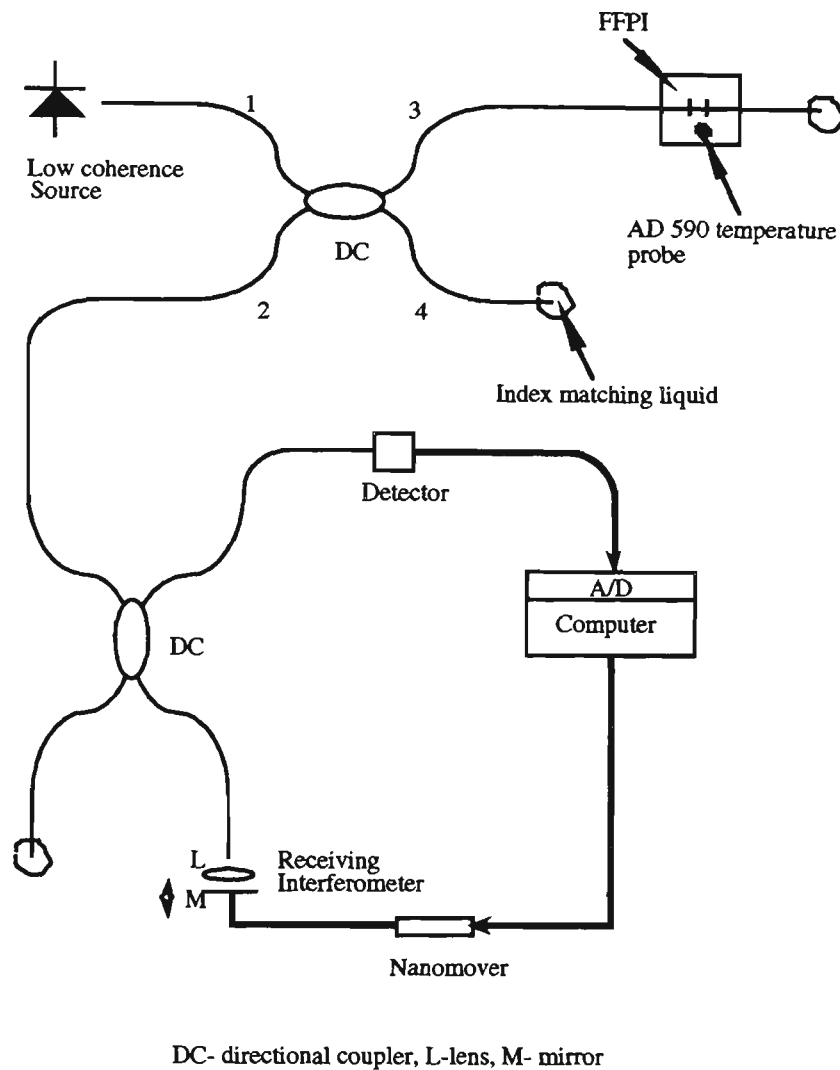


Figure 7.5 Schematic diagram showing experimental set up of WLI.

By scanning the receiving interferometer, its optical path difference could be matched to that of the sensor so that parts of the two reflections are brought back into temporal coherence. Thus, as the time delay between the two signals was varied, a fringe pattern was produced at the photodetector. The photodetector output was digitised and recorded on-line as the receiving interferometer was scanned. Unwanted reflections from the unused output port of the coupler

and that from the end of the fibre housing the FFPI sensor were suppressed using index matching liquid. The temperature of the sensing FFPI was controlled using a miniaturised temperature controlled oven. The temperature control circuit was capable of controlling the temperature between room temperature and 70°C, with a precision of about 0.1°C. An AD590 temperature transducer was placed adjacent to the sensor FFPI to monitor the temperature. Any change in temperature of the oven alters the optical path length of the sensor. Thus, by adjusting the mirror position of the receiving interferometer, the WLI pattern could be tracked. This procedure allowed the measurement of temperature by monitoring the shift of the centre of the WLI fringe pattern.

### 7.3.3 Central fringe determination

For fibre optic white light interferometer systems utilising the path-matched differential techniques, it is required that the central fringe of the WLI interference pattern be rapidly identified with a very high repeatability. The Chi-square fitting method described in chapter 6 was used to identify the central fringe of the WLI interference pattern. However, since this method was new, the method of Dandliker *et al.*, [1992] was also used and the results of the two methods compared. Intrafringe resolution enhancement techniques were applied to the identified central fringe to improve the accuracy of the estimated position of zero path imbalance. (Full central centroid technique of Chen *et al.*, [1992a]).

### 7.3.4 Computer simulations

A. To evaluate the performance of the fitting techniques, computer simulated data was generated by adding random noise to a signal having the form of equation 6.40, and fitted using  $\chi^2$  minimisation. Figure 7.6 shows an example of a simulated WLI fringe pattern having noise amplitude up to 10% of the maximum signal amplitude.

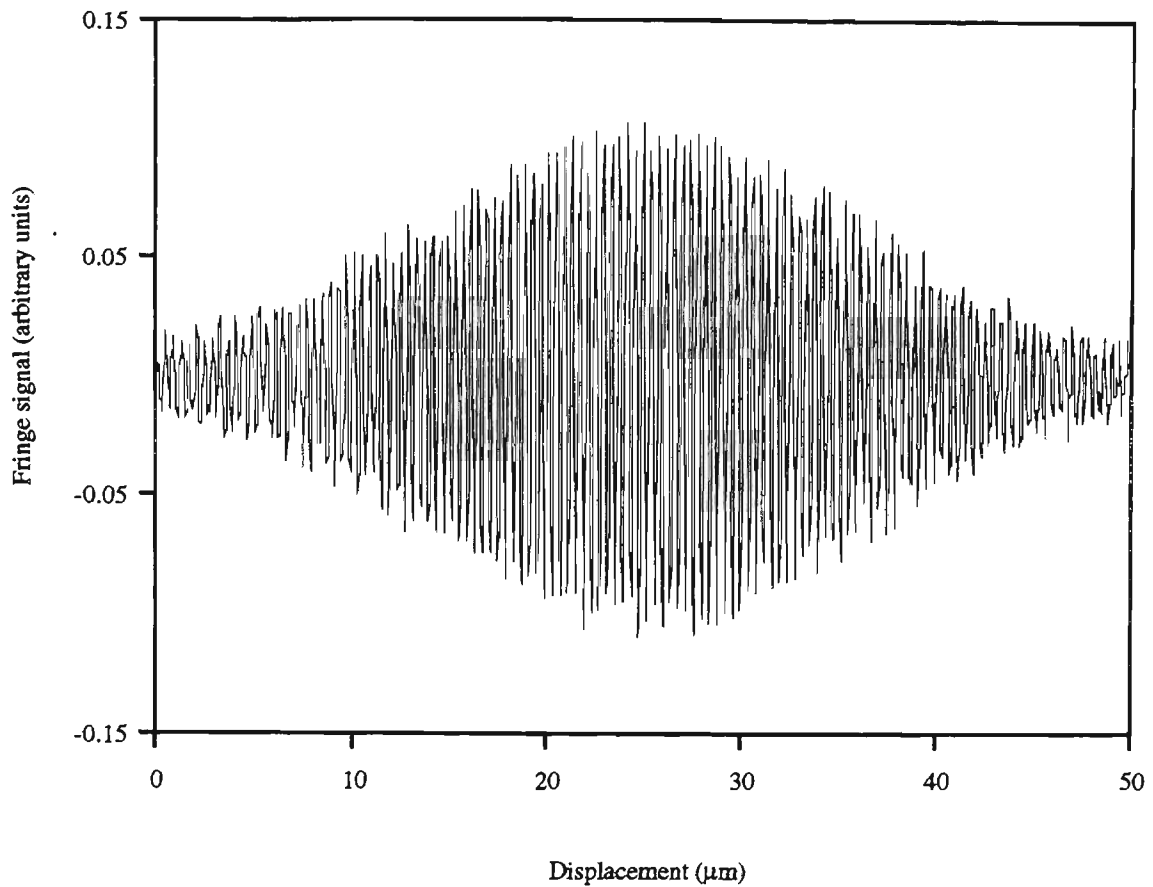


Figure 7.6 Computer simulated WLI fringe pattern with 10% added noise.

The simulation assumed 8 samples per fringe, an optical coherence length equivalent to 31 fringes and a visibility of 0.1. This noise value represent the upper limit of what might be reasonably expected from experimental data, taking into consideration the sensor arrangement, coherence length, centre wavelength, and minimum step size of the Nanomover. Various WLI fringe pattern simulations having noise levels ranging from 1 - 30% of maximum signal amplitude were added to the signal and used to verify the fitting technique. The central fringe is considered to be correctly determined if the value of (the central fringe)  $x_s$  obtained agrees with the expected value to within less than 4 sample points (half a fringe). Figure 7.7 shows a plot of the number of incorrectly identified central fringes using the Chi-squared fitting technique against noise level in the signal.

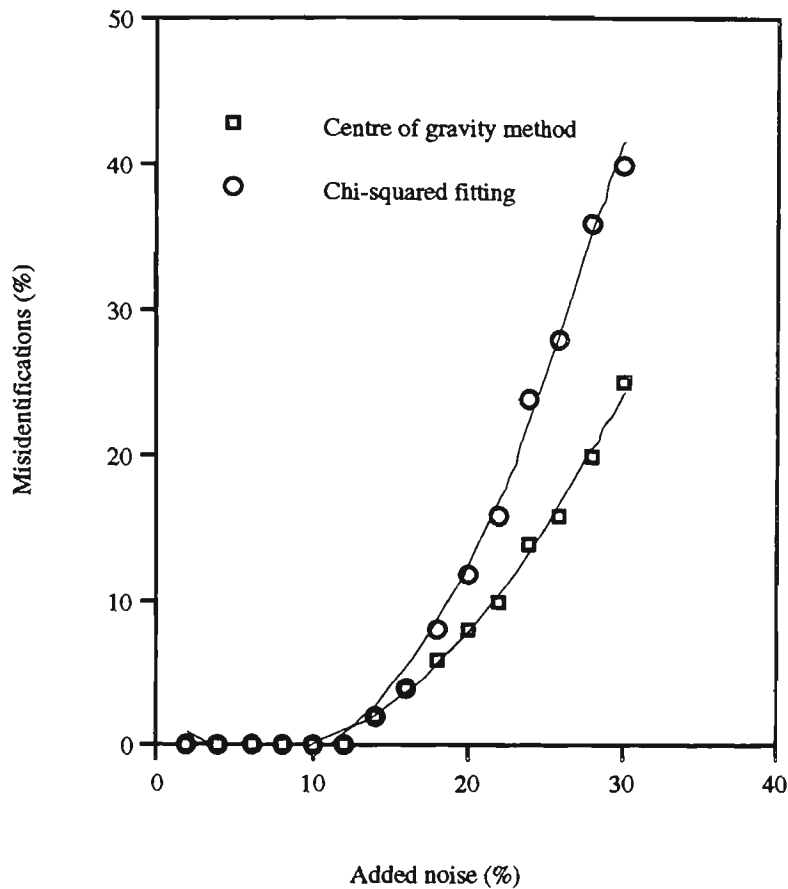


Figure 7.7 Comparison of misidentifications obtained from Chi-squared fitting technique and centre of gravity method applied to simulated data.

A set of 100 simulated WLI fringe patterns (for each noise level) were investigated using the  $\chi^2$  technique. The  $\chi^2$  fitting method was also compared to the centre of gravity method used by Dandliker *et al.*, [1992]. The number of incorrectly identified central fringes using the centre of gravity method was also plotted as a function of the amount of added noise (figure 7.7). The two methods both perform very well up to about 10% added noise. Above this value the centre of gravity method and the  $\chi^2$  method began to give errors. For added noise  $\geq 20\%$ , the centre of gravity method performed better. However, both methods were considered to be unreliable at these signal to noise levels and hence it is necessary to ensure the voltage signal-to-noise ratio is kept above about 10 dB for practical sensing. Above these levels the error in length of the

FFPI is generally one fringe rather than a small fraction of a fringe as is the case when the central fringe is correctly identified.

B. Computer simulations of the WLI fringe patterns were also performed at a constant noise level of 10% of the maximum signal amplitude (SNR = 10 dB) as the source coherence length was varied in the range of 10 - 80 fringes. For each value of the coherence length, 100 different simulations were studied and the number of incorrectly identified central fringes was plotted as a function of the coherence length figure 7.8. The Chi-squared fitting methods and that of Dandliker *et al.* were compared as before. This is a useful graph as it gives an indication of the appropriate light sources (in terms of coherence length) when using these signal processing methods. The two methods both performed very well for up to about a coherence length of 35 fringes (~ 178  $\mu\text{m}$ ) for a signal-to-noise ratio of 10 dB. Above this value both methods were prone to errors and became unreliable. The  $\chi^2$  method showed a slightly better performance for relatively high coherence lengths ( $\geq 50$  fringes (~ 250  $\mu\text{m}$ )). At these values of coherence lengths both methods are regarded as unreliable, and it would be necessary to use sources of coherence lengths shorter than 35 fringes at a voltage signal-to-noise ratio of 10 dB if the central fringe has to be identified with certainty when using these two methods. However, it is likely that if the voltage signal to-noise-ratio is better than 10 dB (lowest limit), sources with coherence lengths longer than 178  $\mu\text{m}$  would perform satisfactorily.

C. Having determined the central fringe without ambiguity, the centre of the central fringe was determined in the manner described in section (6.5.4) using the full central fringe centroid method [Chen *et al.*, 1992a]. The method was tested on simulated data with a signal-to-noise ratio of 10 dB. The simulation assumed a centre wavelength of 810 nm, 8 data points lying in the central fringe (8 samples/fringe) and an optical coherence length equivalent to 31 fringes. A set of 50 simulated phase measurements were carried out. The deviations were evaluated for this technique and found to be 2 nm in a 50 nm step. Since there are 8 steps (or data points) lying in the central fringe, this gives an uncertainty of  $2/(50 \times 8)$  of a fringe. Thus, using this

interpolation method between data points, it is estimated that the value of the centre of central fringe  $x_0$  (at SNR of 10 dB) could be determined to an accuracy of 1/200 of a fringe.

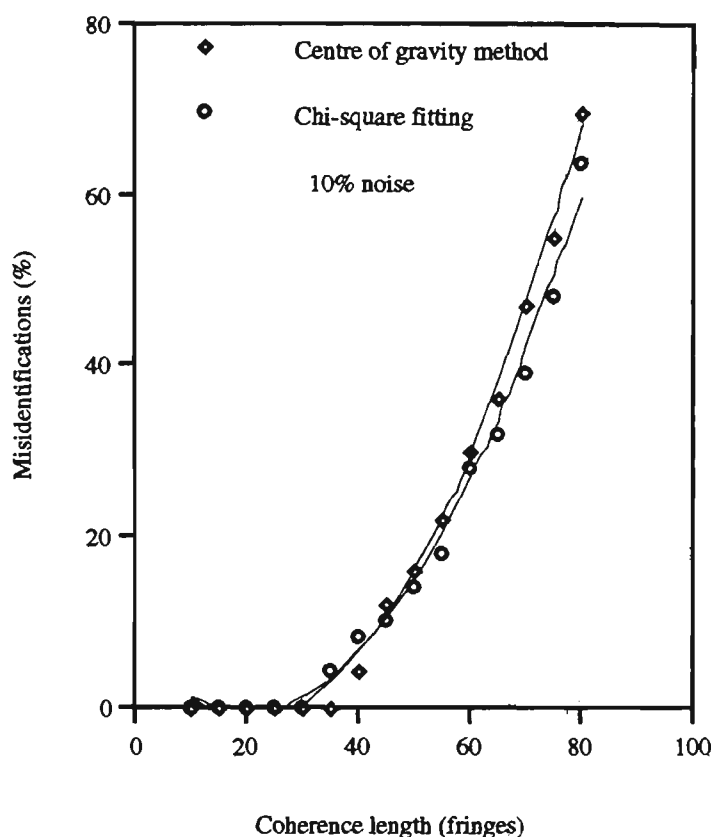


Figure 7.8 Percentage of wrongly identified central fringes (when the  $\chi^2$  technique and centre of gravity method were applied on simulated data of SNR = 10 dB) as a function of coherence length of the source.

### 7.3.5 Experimental results

The WLI pattern was first measured at room temperature, allowing a plot of photodetector voltage versus mirror displacement to be made, as shown in figure 7.9. The white light interference pattern observed experimentally in figure 7.9 confirm the computer simulation shown in figure 7.6. The signal-to-noise ratio of the experimental interference fringe signal is 15.1 dB (much higher than the lowest limit). The central fringe of the WLI pattern was identified using the same  $\chi^2$  approach as in the previous section. A model having the form of

equation 6.40 was assumed and fitted to the experimental data by determining the best fit parameters by  $\chi^2$  minimisation. The minimisation proceeds iteratively through a procedure that optimises the model, thus giving a value for the centroid  $x_s$ . An example of the fit between the optimised  $\chi^2$  model and the experimental data is shown in figure 7.10. This figure shows the central part of the white light fringe pattern where the visibility remains fairly constant. In this example the value of  $x_s$  was determined to be 491.4 steps (with each step 50 nm) from the chosen origin . It can be seen from figure 7.10 that the model was well optimised.

An alternative  $\chi^2$  fitting method using only the crests of the interference fringes was also investigated. A Gaussian function was fitted to the resulting envelope and its centroid,  $x_s$ , obtained from the best-fit parameters. Figure 7.11 shows a Gaussian fitted to the experimental peak data points. The value of  $x_s$  obtained in this manner for the same WLI interference fringe pattern of figure 7.10 was  $488.6 \pm 0.1$  steps. The two centroid values agreed within less than half a fringe, and were in agreement with those obtained using the centre of gravity method by Dandliker *et al.*, [1992] provided the signal-to-noise ratio was not below 10 dB. Thus the fringe containing the centroid was taken to be the central fringe. Applying the centre of gravity method to the WLI fringe pattern gave a value of  $488.6 \pm 0.1$  steps for the centre of gravity of the pattern.

After identifying the central fringe, the most accurate estimate of the position of the centre of this fringe,  $x_o$ , was determined as described in section (6.5.4) using the full central fringe centroid method. As stated earlier, this procedure used 8 data points lying within the central fringe, as shown in figure 7.12. The estimated centre of the central fringe of WLI pattern obtained by interpolating between points was  $489.54 \pm 0.04$  steps. The value of  $x_s$  obtained earlier by applying the  $\chi^2$  on peak data points of the interferogram was  $488.6 \pm 0.1$  steps.

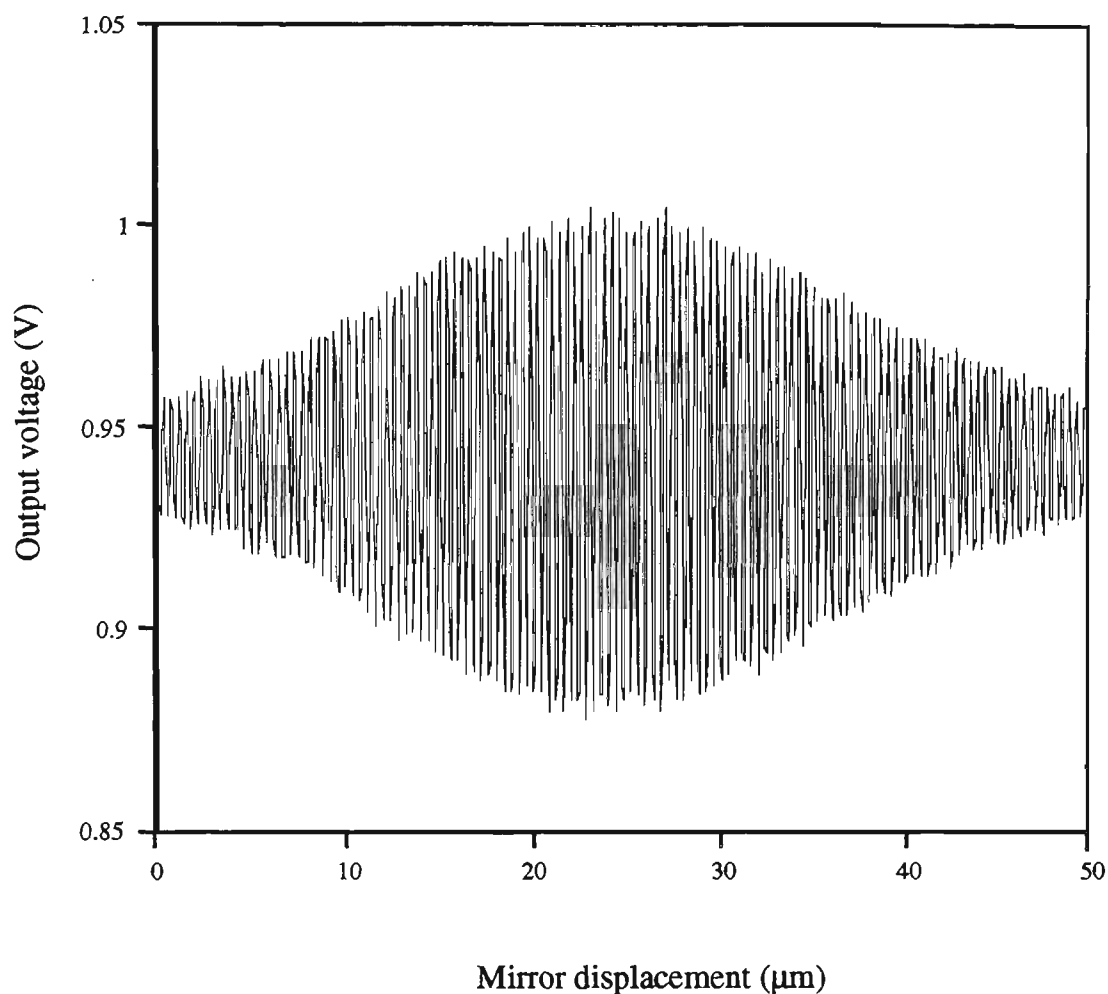


Figure 7.9 WLI fringe pattern obtained experimentally at room temperature ( voltage SNR = 15.1 dB).

### 7.3.6 Temperature measurements

The temperature of the receiving interferometer was kept at room temperature, while that of the sensor was slowly raised. Using the procedures of central fringe determination and intrafringe resolution enhancement described above (i.e. both the  $\chi^2$  along with Dandiliker methods and the centroid of the full central fringe method), the central fringe shift could be determined as the temperature of the oven was altered. The dependence of Fabry-Perot cavity length on

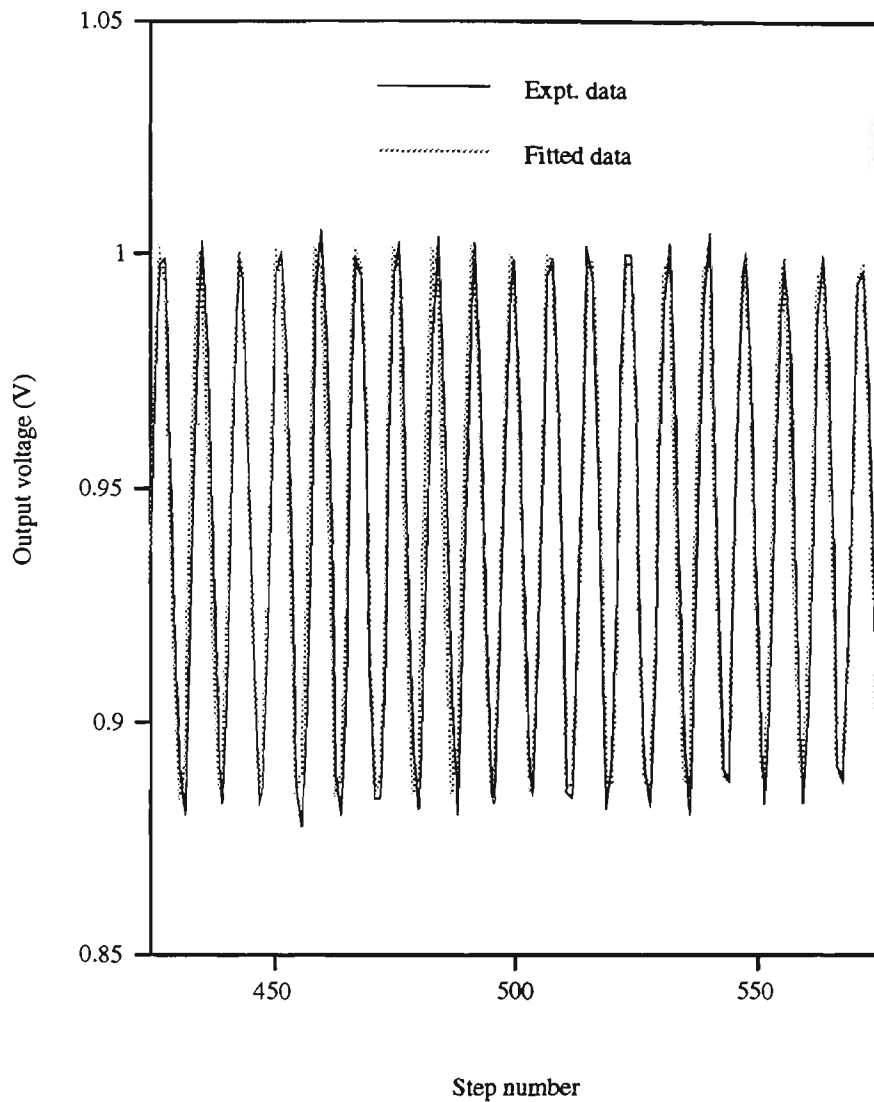


Figure 7.10 Calculated fit using  $\chi^2$  technique showing fringes around the central region of the WLI fringe pattern superimposed on the experimental data.

temperature, in the range of 20°C to 67 °C is displayed graphically in figure 7.13. The central fringe shift (in air) per unit temperature change over this range is seen to be constant, with a value of  $223 \pm 3$  nm/K. The relative phase sensitivity with temperature had previously been measured by counting fringes using a single mode laser diode source at 1300 nm and found to be  $(7.90 \pm 0.34) \times 10^{-6}/K$  which corresponds to  $230 \pm 10$  nm/K. The fringe visibility obtained

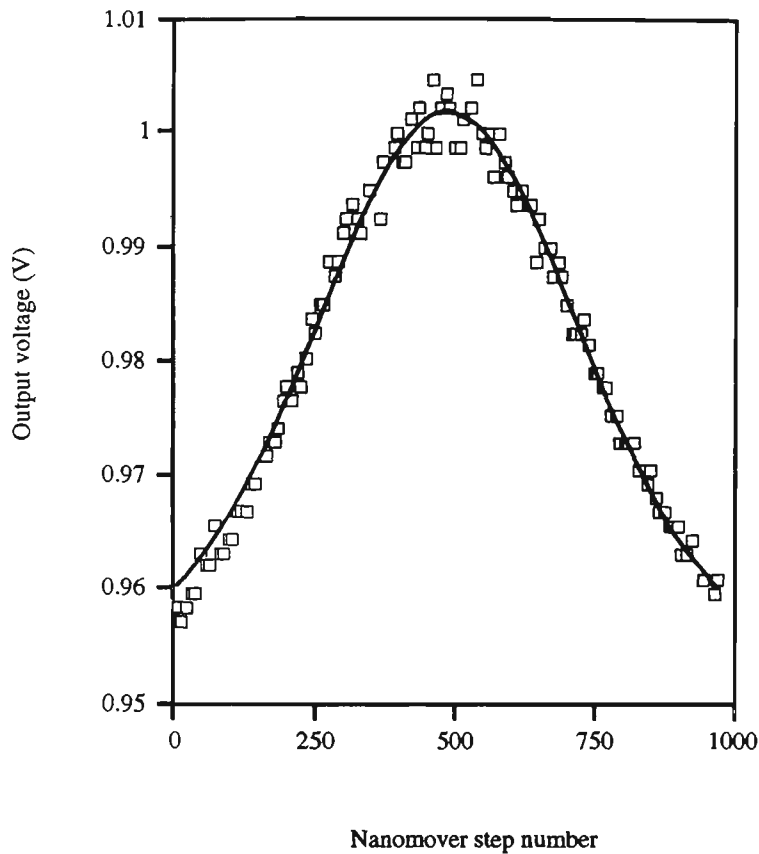


Figure 7.11 Gaussian fitted to the experimental peak data points using  $\chi^2$  technique.

The peak data points correspond to the WLI fringe pattern obtained at room temperature.

in this investigation was found to be 0.12. The low value of the visibility could be attributed to the low power reflected at the cleaved end ( $R \sim 3.6\%$ ) in the receiving interferometer. Using the intrafringe resolution enhancement technique described above, the measured temperature in this investigation (with voltage SNR = 15.1 dB) can be obtained to an estimated resolution of better than  $0.01^\circ\text{C}$ .

Because of the nature of the interference fringe patterns formed by multimode laser diodes when used as low coherence source in WLI sensor systems (section 6.5.1), it was possible to determine the cavity length of the laser diode used. This was determined experimentally by measuring in the receiver output pattern the distance between two successive interference fringe packets and was found to be  $\sim 1.02$  mm.

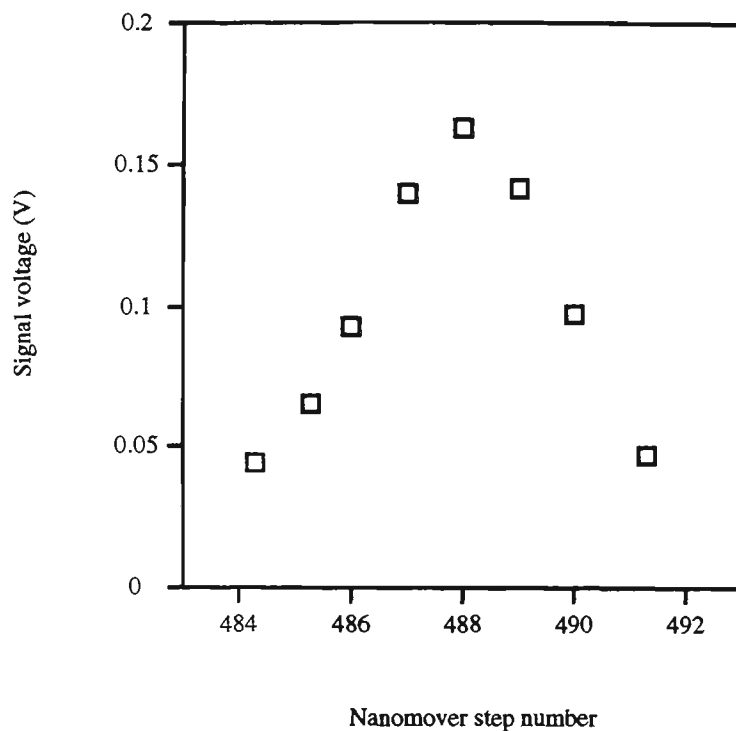


Figure 7.12 Illustration of the central fringe of the WLI interference pattern identified by the  $\chi^2$  fitting technique.

### 7.3.7 Static strain measurements

The experimental arrangement to demonstrate the performance of fabricated FFPI sensors as strain gauges using white light interferometry is similar to that shown in figure 7.5. An FFPI gauge was adhered to the surface of a mild steel cantilever beam parallel to the direction of principal strain and the beam was subjected to longitudinal stress. The adhesive used to attach FFPI sensor to the cantilever was polyester P-2 type. A self-temperature-compensated resistive strain gauge was also bonded adjacent to the FFPI sensor to monitor the strain. The FFPI sensor length was approximately 1.7 cm, with an effective mirror reflectance of about 10%. The same multimode laser diode used for the temperature experiment was used. Any change in

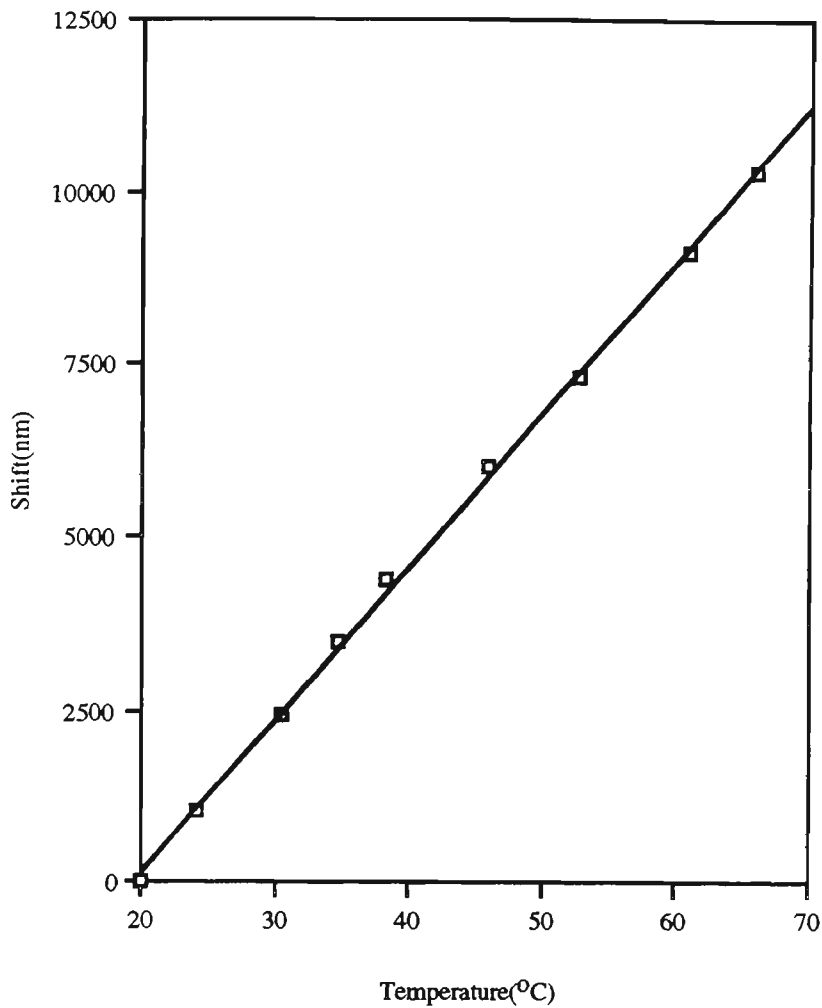


Figure 7.13 Central fringe shift of WLI pattern against temperature for an FFPI sensor of length  $\sim 2$  cm, combined reflectance  $\sim 6\%$ , at a wavelength of 810 nm.

the strain of the cantilever introduces a change in the optical path length of the FFPI strain gauge. The optical path difference change in the sensing interferometer is followed by scanning the receiving interferometer to match the sensor imbalance as described in section 7.3.2. This enables the measurement of the axial strain in the structure via the shift of the centre of the WLI fringe pattern. The optical FFPI strain sensor is sensitive to both temperature and strain (section 6.4), and therefore it is necessary to allow for thermally induced strain if realistic static strain measurements are to be made in circumstances which involve temperature changes. This

effect was corrected for and a description of the procedure used is given in the following section.

### 7.3.7.1 Correction for thermally induced strain

Apparent strain corrections were made by determining the shift of the centre of the WLI fringe pattern with ambient temperature. When the FFPI bonded to the cantilever beam was under no load the WLI pattern was tracked as a function of ambient temperature and the shift of the centre of the fringe pattern per unit temperature obtained. Figure 7.14 shows the shift of the centre of the WLI pattern against ambient temperature. A value for the FFPI's bonded temperature sensitivity (central fringe shift in air per unit temperature change) of  $446 \pm 24$  nm/K was obtained for a 1.7 cm FFPI sensor. In order to estimate the value of apparent strain that would be expected as a result of ambient temperature fluctuations, the calculated fractional phase shift per unit strain ( $\frac{\Delta\phi}{\phi\epsilon} = 0.794$  (section 6.3)) is used. This value corresponds to a phase shift per microstrain of about 20 nm/ $\mu\epsilon$  for a 1.7 cm FFPI sensor. From equation 6.29 the calculated value of apparent strain of 20  $\mu\epsilon/^\circ\text{C}$  enables calculation of the apparent strain. Thus, the predicted apparent strain becomes  $20 \mu\epsilon/\text{K} \times 20 \text{ nm}/\mu\epsilon = 400 \text{ nm}/\text{K}$ . The experimental value of  $446 \pm 24$  nm/K correlates quite closely with this calculated value. Correction for this effect was made by simply monitoring the ambient temperature and subtracting algebraically (with sign) the apparent strain from the indicated strain. Such corrections are readily made provided the apparent strain is not too large.

### 7.3.7.2 Static strain results

The detected power reflected from the FFPI sensor was measured as a function of mirror displacement allowing a fringe pattern similar to that in figure 7.9 to be produced at the detector. A reference scan with zero load was obtained before measurement with successively

increased loads. The FFPI sensor was strained by loading the end of the cantilever and the receiver interferometer was scanned to obtain the WLI fringe pattern. The reading of the

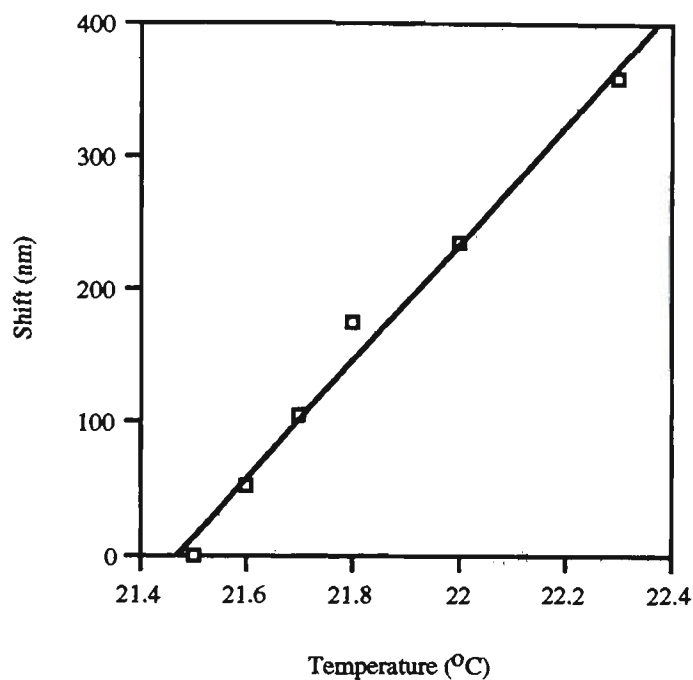


Figure 7.14 Results of the measurement of apparent strain using an FFPI sensor of cavity length  $\sim 1.7$  cm, combined reflectance  $\sim 10\%$  bonded to a cantilever illustrating graphically the shift of centre of WLI fringe pattern versus ambient temperature.

resistive strain gauge was recorded at each load as was the ambient temperature, thus, enabling temperature correction during strain measurements. The central fringe and the centre of this fringe were determined as described in sections 6.5.3 and 6.5.4. Figure 7.15 shows a plot of the corrected shift of the centre of the WLI fringe pattern versus strain measured by the resistive strain gauge. The graph is linear with a central fringe shift of the centre of WLI pattern per unit strain (in air) of  $24.3 \pm 0.1$  nm/ $\mu\epsilon$ . This value is in reasonable agreement with calculated value (which used bulk silica constants) of relative phase sensitivity per unit strain  $\Delta\phi/\phi\epsilon$  of 0.794 which corresponds to a fringe shift of 23 nm/ $\mu\epsilon$  for an FFPI of similar gauge length. Using intrafringe resolution techniques described above, the measured strain in this investigation (with voltage SNR = 15.1 dB) can be obtained to an estimated resolution of better than 0.07  $\mu\epsilon$ .

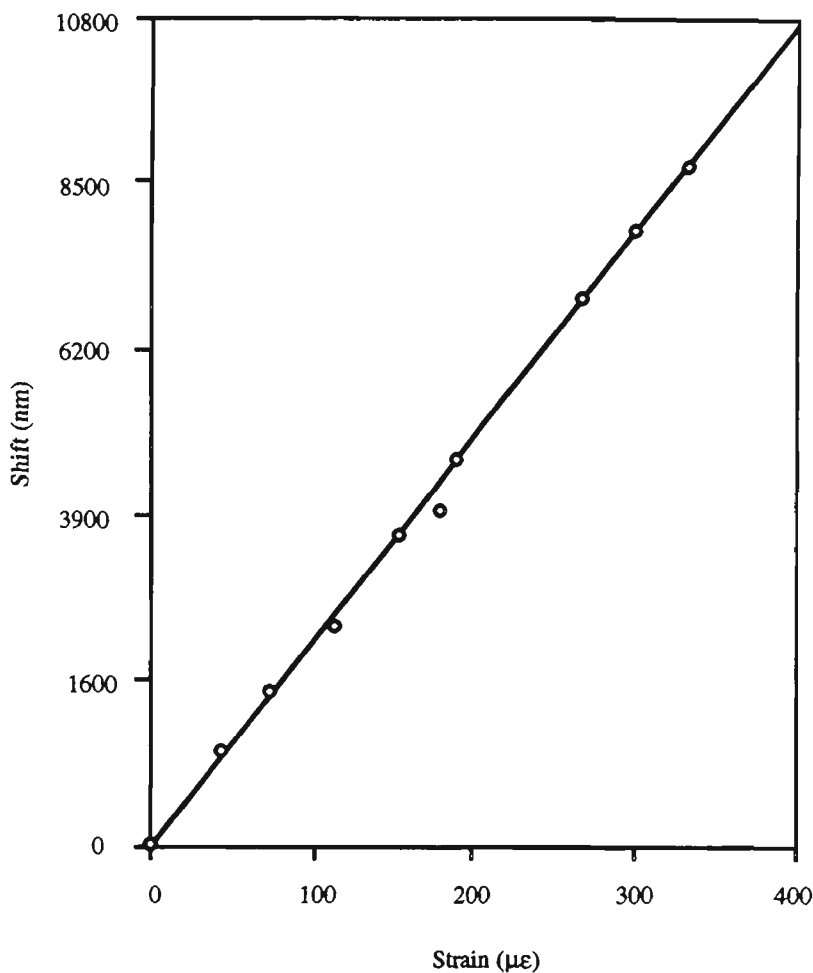


Figure 7.15 Shift of centre of WLI fringe pattern against strain measured by a resistive strain gauge, for an FFPI of gauge length  $\sim 1.7$  cm,  $R \sim 10\%$ , ( $\lambda = 810$  nm).

#### 7.4 Conclusion

An optical fibre interferometric sensor system for absolute measurement of static strain, or temperature, based on white light interferometry has been demonstrated. It offers a large measurement range and is designed to be suitable for the multiplexing of sensors having different free spectral ranges. The chi-squared fitting technique used for identifying the central fringe is simple and enables the central fringe of an interferogram to be identified with a greatly reduced signal-to-noise ratio (up to a minimum SNR of 10 dB). This technique allows a wide choice of low coherence sources like LEDs, SLDs or multimode laser diodes. Intrafringe

resolution improves the accuracy of the system. The measured values of central fringe shift (in air) per unit temperature of  $223 \pm 3 \text{ nm/}^\circ\text{C}$  and central fringe shift (in air) per unit strain of  $24.3 \pm 0.1 \text{ nm/}\mu\text{e}$  are in agreement with values observed in sensors with a single FFPI using long coherence length source. For a voltage signal to noise ratio of 15.1 dB temperature resolution of better than  $0.01 \text{ }^\circ\text{C}$  and strain resolution of better than  $0.07 \mu\text{e}$  are possible. Table 7.2 compares the central fringe identification methods and gives the overall performance of the sensors investigated in this section.

## **7.5 MEASUREMENTS WITH LOW COHERENCE MULTIPLEXED FUSION-SPLICED FFPI SENSORS**

### **7.5.1 Introduction**

Following the WLI measurements with single Fabry-Perot sensor systems in section 7.3, measurements were made with multiplexed sensors. The intrinsic fibre optic Fabry-Perot sensors examined were of different cavity lengths formed in a continuous length of Flexcore 780 single mode fibre and multiplexed in series. The sensors were investigated for the measurement of temperature and strain and demodulated by scanning the Nanomover to the relevant fringe pattern. A parallel arrangement of FFPIs was also investigated for the measurement of static strain. However, use of such an arrangement is limited by the need to use  $2 \times 2$  fibre couplers which attenuate the optical power by a total factor of 4. Losses soon become prohibitive with increasing numbers of sensors as the number of couplers required is equal to the number of sensors (loss =  $4^N$ ). The other disadvantage of the parallel arrangement is that there are as many optical fibre lines as there are sensors. Of particular interest in this work is the serial arrangement because it allows localised and quasi-distributed measurements. The maximum number of sensors that may be multiplexed is mainly limited by the optical power loss and the minimum signal-to-noise ratio for reliable identification of the central fringe. A

**Example of WLI pattern obtained at room temperature, voltage SNR = 15.1 dB**

**Central fringe identification**

Centroid of the entire pattern = 491.449 steps

Centroid of Gaussian envelope = 488.627 steps

(using chi-square fitting methods)

“Centre of gravity” of pattern = 488.614 steps

(Using method of Dandliker *et al.*, 1992)

*All methods identify the same fringe*

*Centre of central fringe* = 489.54 ± 0.04 steps

**Temperature and strain measurements using WLI, voltage SNR = 15.1 dB**

Fibre type	single-mode, Corning Flexcore 780	
Cavity length	17 - 20	mm
Sensor diameter	125	µm
Operating wavelength	810	nm
Temperature resolution	0.01	°C
FFPI length resolution	$\lambda/200$	nm
Strain resolution	0.07	µε
Apparent strain based on a strain sensitivity of 24.3 nm/µε for the 1.7 cm FFPI bonded on mild steel cantilever .	18.4	µε/°C

Table 7.2 Summary of results for a typical WLI measurement.

multimode laser diode source was used as broad band source. The system performance, resolution, absolute accuracy and noise limitations are described in the following sections.

## **7.5.2 Temperature measurements**

### **7.5.2.1 Experimental arrangement**

Absolute measurement of temperature was demonstrated with two serially multiplexed FFPI sensors. Light from the 810 nm multimode laser diode was launched into the sensor system via a 2×2 fibre optic directional coupler as with previous measurements. The sensing interferometers were intrinsic fusion-spliced fibre optic Fabry-Perot sensors of cavity lengths  $l_1 \sim 1.9$  and  $l_2 \sim 1.7$  cm, having combined reflectances of 10% and 17% respectively. Figure 7.16 shows the experimental arrangement in which the sensors are monitored in reflection. The cavity length of each sensor defines the size of the sensing element, and these are chosen to be long enough for low-noise use with a multimode laser diode and of sufficiently different length to avoid overlap of the individual WLI fringe patterns and cross modulation effects. The receiver and detector system was the same as that used in previous FFPI measurements. The white light fringe pattern associated with each sensor was first measured at room temperature by scanning the mirror of the receiving interferometer to match the imbalance of each sensor, allowing a plot of photodetector voltage versus mirror displacement to be made. A separate WLI fringe pattern was obtained for each interferometer, and figure 7.17 illustrates the dependence of the output voltage on the relative path imbalance between the sensing and receiving interferometers. It is observed from figure 7.17 that the amplitude of the WLI pattern becomes smaller as the number of sensor interferometers is increased. This is expected because of the losses incurred by two-way transmission through the first sensor.

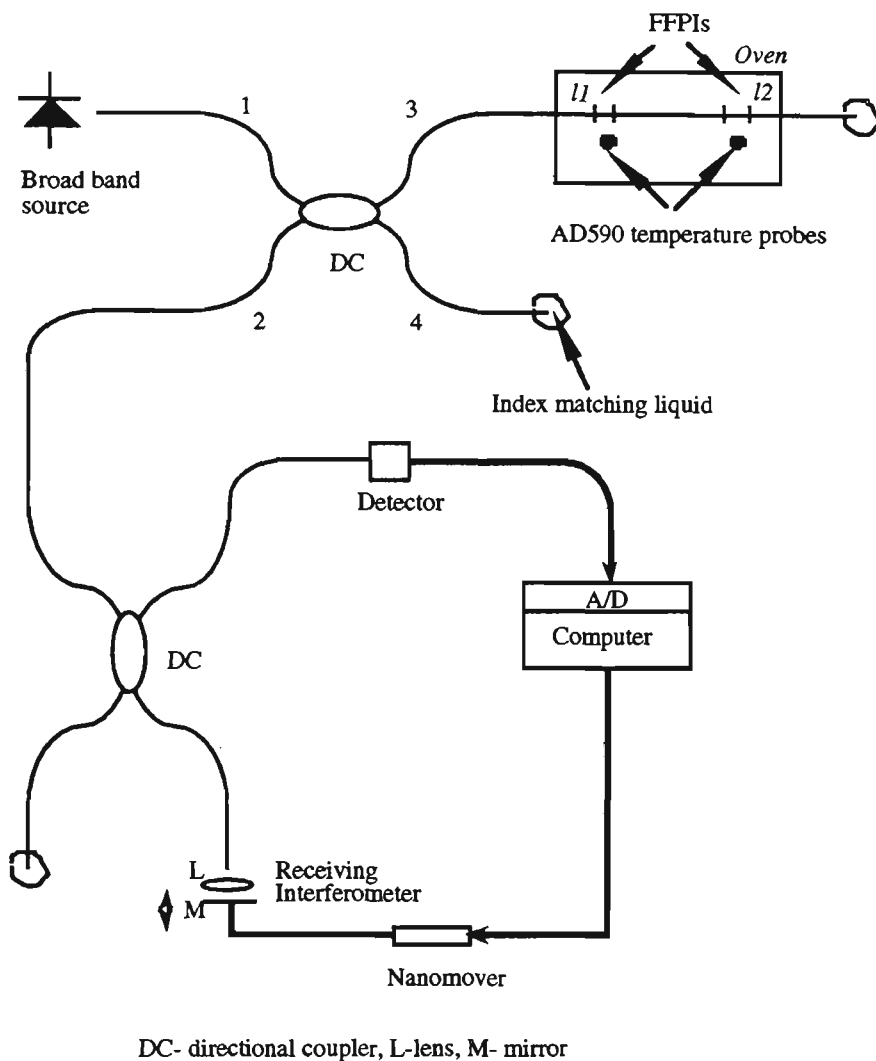


Figure 7.16 Schematic experimental arrangement for serially multiplexed FFPI sensors based on white light interferometry.

### 7.5.2.2 Signal processing and results

Analysis of the data was performed using the signal processing techniques described earlier (sections 6.5.3 and 6.5.4). After identifying the central fringe, its centre was evaluated in a similar manner described using the centroid approach. As stated earlier the accuracy of the procedure depends on the signal-to-noise ratio. The voltage signal-to-noise ratio of the WLI fringe pattern corresponding to the first sensor was 14.91 dB, while that of the fringe pattern

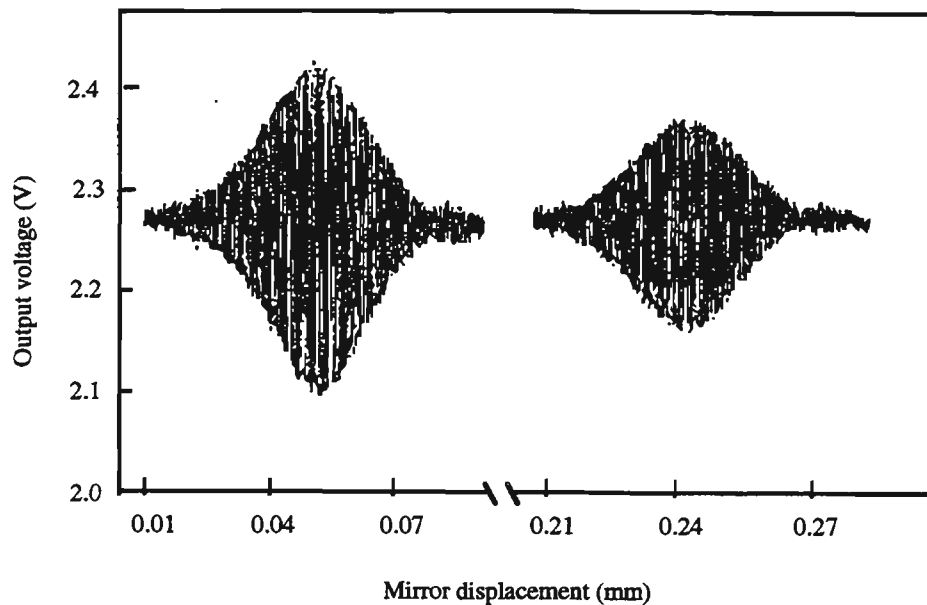


Figure 7.17 WLI fringe patterns obtained with two FFPI sensors multiplexed in series. The first FFPI sensor had a cavity length of  $\sim 1.9$  cm, combined reflectivity  $\sim 10\%$  and the second FFPI sensor had a sensor length of  $\sim 1.7$  cm and reflectivity of  $\sim 17\%$ . Voltage signal-to-noise ratio of sensor 1 was 14.91 dB and that of sensor 2 was 13 dB. (The origin of the mirror displacement is not zero path imbalance in the sensor beams).

associated with the second sensor was 13.0 dB. The number of possible sensors in a serial array is governed by the signal-to-noise of the last sensor. If this value of voltage SNR falls below 10 dB, then there is a significantly increased uncertainty in identifying the central fringe. This limits the possible number of sensors. Since the SNR of the last sensor was + 3 dB above the lowest limit, other sensors can be deployed along the same fibre until the SNR of the last sensor falls below 10 dB. The temperature of the sensors were varied using the temperature-controlled oven and an AD590 temperature transducer was placed adjacent to the FFPI sensors to allow for continued monitoring of temperature. The temperature of the oven was slowly raised and the fringe pattern associated with each sensor was simultaneously tracked by adjusting the mirror position of the receiving interferometer using the computer controlled Nanomover.

The temperature was varied over the range of 20 to 70°C. The white light interference patterns were similarly tracked during cooling of the interferometers after the oven was switched off. The overall performance of the multiplexed sensors in terms of fringe shift versus temperature during heating and cooling cycle is given in figure 7.18. The response is again linear over the range of 20 - 70°C with a central fringe shift (in air) per unit temperature of  $219.3 \pm 0.5$  nm/K for the 1.9 cm FFPI and  $181 \pm 1$  nm/K for the 1.7 cm FFPI. These values correspond to a fringe shift (in air) per unit temperature per cm length of FFPI cavity of  $\sim 115$  nm K<sup>-1</sup> cm<sup>-1</sup> and  $106$  nm K<sup>-1</sup> cm<sup>-1</sup> respectively and show good agreement with the calculations of section 6.2. The fringe visibility at the output of the first and second interferometers were found to be 0.10 and 0.07, respectively. The difference in the FFPI sensor cavity lengths was determined experimentally by finding the difference between the centres of the individual WLI fringe patterns corresponding to each sensor at room temperature. The value obtained was 0.181 cm and is in close agreement with the nominal length difference of 0.2 cm.

## **7.6 Static strain measurements**

### **7.6.1 Experimental arrangement and results**

To investigate the sensitivity of the FFPI sensors to static strain, two fibre optic FP sensors were arranged in parallel. The use of a parallel arrangement here was purely for convenience and the measurements could equally well be made in series. Figure 7.19 shows the sensor arrangement in which light from the multimode laser diode ( $\lambda = 810$  nm) was launched into the system via a 2×2 coupler. Light modulated by the sensors was transmitted back through the same fibres. As in the previous section, each sensing interferometer has a unique path imbalance, which was chosen in such a way that the sum or difference of differential path delays from each interferometer cannot duplicate the differential delay of a single interferometer to within the coherence length of the source  $l_c$ , thus ensuring no significant cross-modulation.

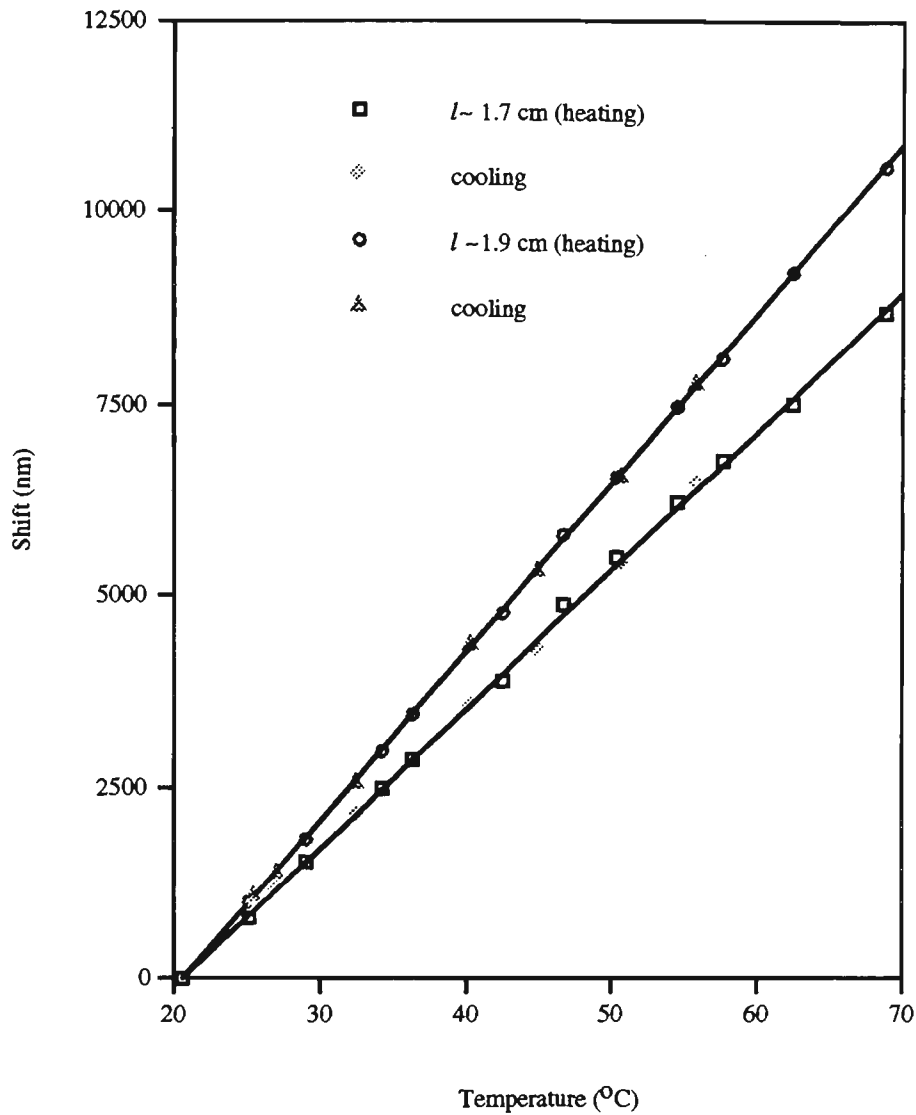


Figure 7.18 Temperature measurements obtained from two FFPI sensors multiplexed in series. The measurements were obtained during heating and cooling of sensor fibres. The sensor lengths for the first FFPI sensor was  $\sim 1.9$  cm and that of the second FFPI sensor was  $\sim 1.7$  cm, ( $\lambda = 810$  nm).

The FFPI sensors were fusion-spliced to each output port of the coupler (i.e. ports 3 and 4), and one was adhered to the upper surface (parallel to the direction of the principal strain) of the mild steel cantilever while the other was bonded to the lower side of the cantilever. The FFPI

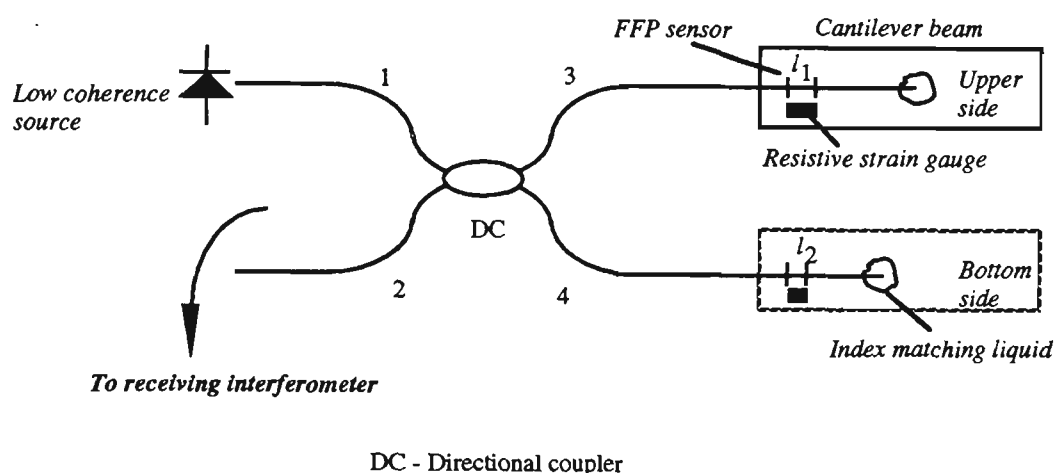


Figure 7.19 Sensor arrangement for multiplexed low coherence FFPI sensors addressed in parallel

attached to the upper surface suffered elongation while the other experienced compression. Resistive strain gauges were also bonded adjacent to each sensor to monitor the strain. The sensor combined reflectances were 7% for the top-bonded FFPI sensor and 10% for the bottom-bonded sensor, with a cavity length of  $\sim 1.8$  cm and  $\sim 1.7$  cm respectively. The WLI pattern for each optical strain gauge was obtained at room temperature. The longitudinal strain of the cantilever was varied from zero up to  $\sim 400 \mu\epsilon$  and the corresponding shift in WLI pattern was monitored in the usual way. The temperature at each measurement was obtained to allow for temperature-induced strain correction. The centre of each fringe pattern was obtained as described previously in sections 6.5.3 and 6.5.4, and correction for thermally induced strain was performed in a manner described in section 7.3.7.1. The corrected shift of the centre of WLI pattern versus strain is shown in figure 7.20 for the sensor in extension, while in figure 7.21 is a plot of corrected central fringe shift (in air) against strain for the sensor in compression. The measured values of central fringe shift per unit strain (in air) for the FFPI sensors used were  $25.5 \pm 0.4 \text{ nm}/\mu\epsilon$  for a 1.8 cm FFPI under tension and  $23.4 \pm 0.7 \text{ nm}/\mu\epsilon$  for a 1.7 cm FFPI under compression. These values are again in agreement with calculations

(section 6.3). The signal-to-noise ratio of the WLI fringe pattern associated with the top-bonded FFPI sensor was 14.1 dB while that obtained for the WLI fringe pattern corresponding to the bottom-bonded FFPI sensor was 14.4 dB. The difference in measured cavity lengths of the two sensors was 0.69 mm, in agreement with the nominal length difference.

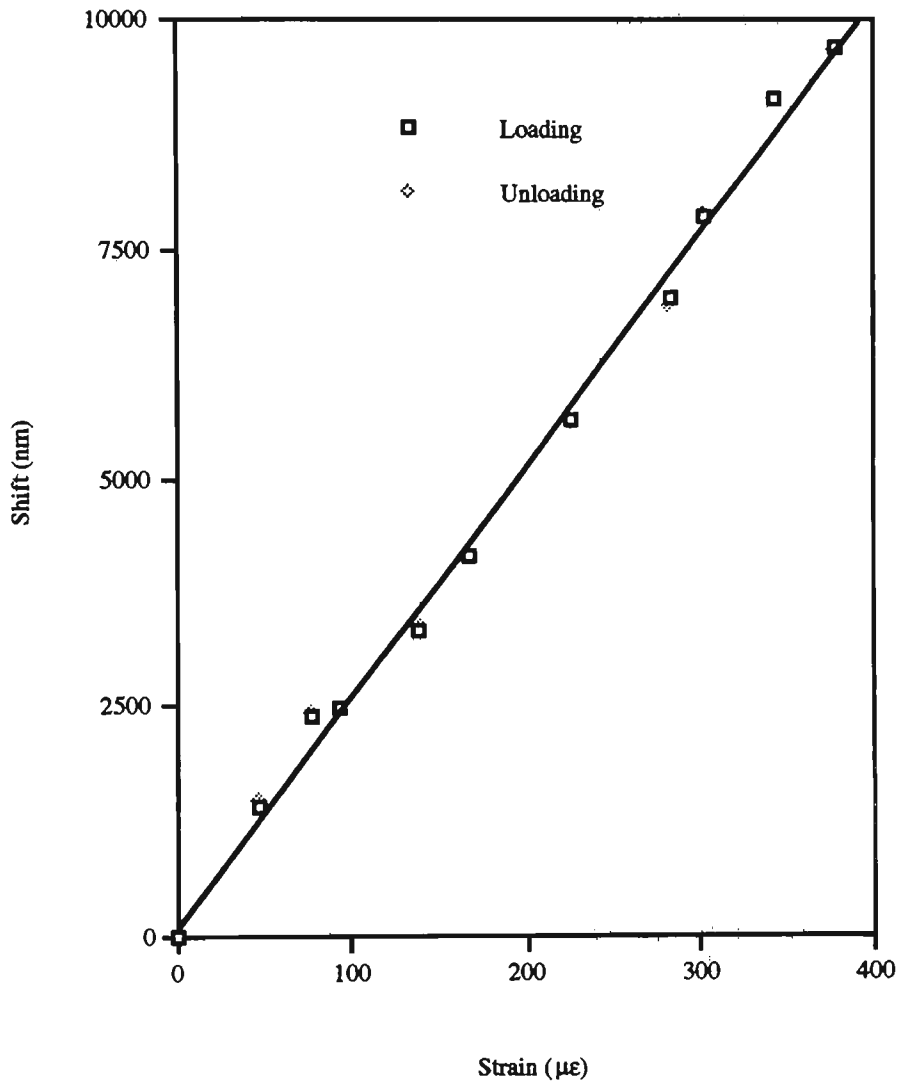


Figure 7.20 Strain response of the upper surface adhered FFPI sensor in extension. Sensor cavity length  $\sim 1.8$  cm, sensor combined reflectance  $\sim 7\%$ , ( $\lambda = 810$  nm). Strain measurements made with co-located resistive strain gauge.

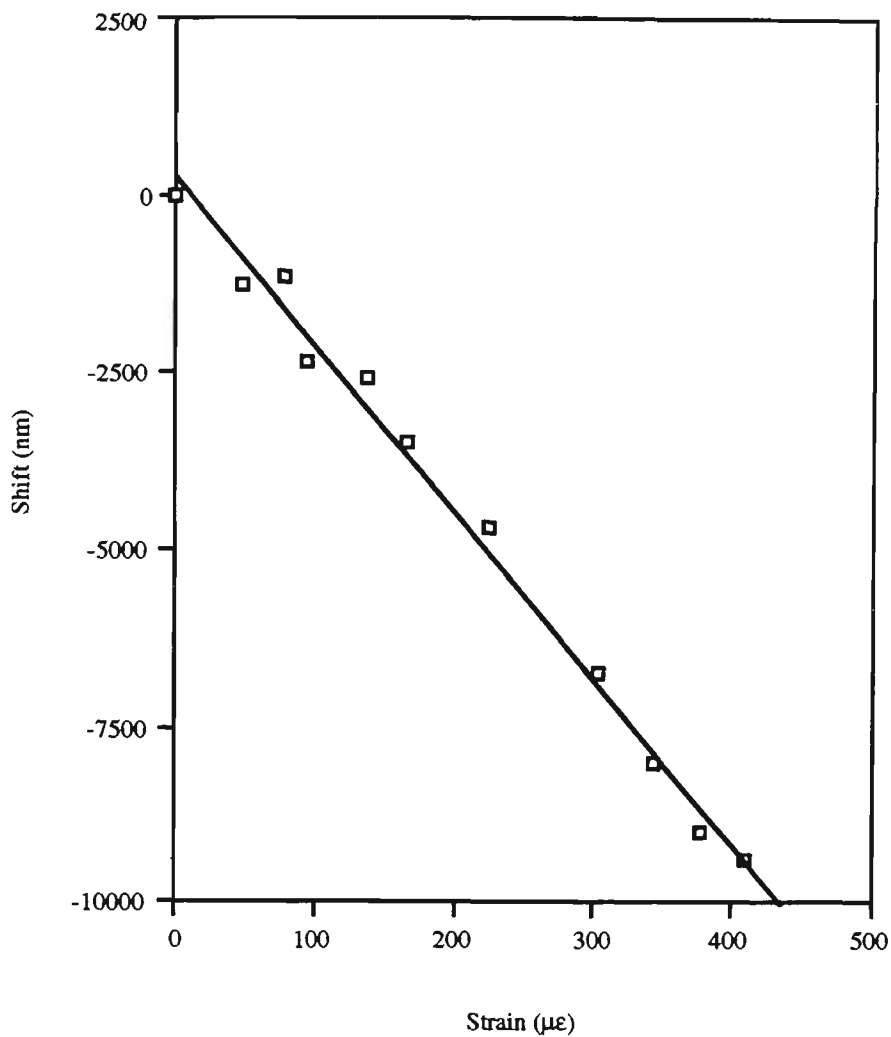


Figure 7.21 Strain response of the lower-surface-adhered FFPI sensor in compression. The FFPI sensor length was  $\sim 1.7$  cm with an combined sensor reflectance of  $\sim 10\%$ , ( $\lambda = 810$  nm). Strain measurements were made with a co-located resistive strain gauge.

## 7.7 System limitation

This section discusses the noise contribution to the sensing system and also possible approaches to minimise this noise. As indicated in section 2.5 the performance of optical sensing systems is typically limited by a number of noise sources and other factors including environmental noise, sample rate, shot and thermal noise.

Data acquisition and processing involves sampling the data. For optimal efficiency the data should be sampled in such a way that the sample rate is at least twice the highest frequency in the signal, as required by Nyquist sampling theorem. Although an optimal sampling rate does not destroy any signal information, it does alter the appearance of the interferogram and may complicate central fringe identification. The sample rate in this investigation was fixed at 8 samples per fringe governed by the minimum step size of the Nanomover of 50 nm, which is a factor of 4 greater than the minimum specified by the Nyquist limit.

A complete scan of a low coherence fringe pattern normally requires about 10 minutes, faster rates being precluded by environmental noise. During a scan of the receiving interferometer, vibrational noise adds to the signal, limiting the system resolution. This was reduced to an acceptable level by allowing a settling time for the moving mirror in the receiver interferometer prior to each reading of a scan. In some cases signal averaging techniques could also be used to further reduce the vibration effects to a minimum. The sensing system was placed on a vibration isolated table to minimise environmental noise effects. As a further means to minimise the environmental noise, the receiving interferometer was shielded from environmental perturbations using a styrofoam enclosure.

Normally measurements were performed with optical powers of about  $\sim 80 \mu\text{W}$  ( $-11 \text{ dBm}$ ) incident into the sensor network (i.e. about  $\sim 160 \mu\text{W}$  ( $-8 \text{ dBm}$ ) launched into port 1, figure 7.16). The average output power of the multimode laser diode was 15 mW. The power received at the detector with this sort of launched power was about 100 nW ( $-40 \text{ dBm}$ ). This low level of power received at the detector is mainly because of the very low signal returned from the cleaved end of a single-mode fibre which forms one of the reflecting surfaces of the receiving interferometer. It has also been possible to make measurements with a reasonable signal-to-noise ratio using this WLI scheme with powers much lower than  $-65 \text{ dBm}$ . At these low levels of optical signal received at the detector, thermal noise is the dominant detector noise. Phase noise arising from frequency instabilities of the source was not observed to be

significant in this sensing arrangement. This type of noise is proportional to the various path unbalances in the interferometers, and since a white light interferometer operates near zero optical path imbalance, it has negligible levels of phase induced noise. For the optical sensor system described in this chapter the overall RMS noise measured at the output of the receiver electronics was 1 mV, and this sets a limit to the detectable optical power of  $\sim -70$  dBm. The intrafringe resolution obtained at a voltage SNR of 10 dB is of 1/200th of a fringe. There is scope for improvement in detected power levels with improvement in launch optics. This was done before using SLD sources (see chapter 8).

For comparison purposes with the model predicting the multiplexed sensor performance, an optical power of -23 dBm was launched into the multiplexed sensor arrangement (i.e - 20 dBm launched into port 1). This figure was chosen so that the experimental conditions would be similar to those assumed in the calculations. Table 7.3 summarises the experimental results obtained under these conditions.

From table 7.3 the voltage signal-to-noise ratio of the WLI fringe pattern associated with the 2nd sensor prior to multiplexing was  $\sim 13.9$  dB, and this decreased to  $\sim 12.5$  dB after multiplexing, giving a drop in the voltage SNR of 1.4 dB. Since for this power the detector is thermal noise limited, this decrease of 1.4 dB is produced by optical power reflected by the first sensor together with the two-way transmission loss of the first sensor. Considering  $N$  sensors of similar properties multiplexed in series and a minimal signal-to-noise ratio of 10 dB required for the  $\chi^2$  technique to identify the central fringe with a high degree of reliability, the value of  $N$  can be obtained approximately as,  $N \approx \frac{13.9 - 10}{1.4} = 2.78 \approx 3$ . Thus, with -23 dBm optical power launched into the sensor array, up to 3 intrinsic FFPI sensors could be deployed on the same fibre.

The above figure can be approximately compared with the model of chapter 6 using the data of figure 6.10. For the present circumstances, the minimum acceptable power at the detector is

Source used	multimode laser diode LT016MD
Laser diode output power ( <i>average</i> )	15 mW
Centre wavelength	810 nm
Optical power incident into sensor array	- 23 dBm
Power received at the detector from sensor 1 only	-50 dBm
Power received at the detector from both sensors 1 and 2	- 48 dBm
System RMS noise	1 mV
Sensor transmission loss ( <i>1 way loss figure, both sensors similar</i> ) (reflectivity dependent)	~ 1.5 dB
Voltage signal-to-noise ratio of sensor 1 ( <i>prior to multiplexing</i> )	14.33 dB
Voltage signal-to-noise ratio of Sensor 1 ( <i>after multiplexing</i> )	14.33 dB
Cross talk	<i>No detectable cross talk</i>
Visibility for sensor 1	~ 0.10
Voltage signal-to-noise ratio of sensor 2 ( <i>prior to multiplexing</i> )	13.90 dB

Voltage signal-to-noise ratio of sensor 2 ( <i>after multiplexing</i> )	12.50 dB
Visibility for sensor 2	0.07
Combined reflectance of sensor 1	~ 10%
Cavity length $l_1$	~ 1.9 cm
Combined reflectance of sensor 2	~ 17%
cavity length $l_2$	~ 1.7 cm
Cavity length $l_2$	~ 1.7 cm
Difference in sensor cavity lengths	~ 0.181 cm

Table 7.3 Multiplexed system evaluation

- 54.33 dBm (voltage signal-to-noise ratio of 10 dB). The one-way power loss factor for these sensors is ~ 1.5 dB which corresponds to one of the lines of figure 6.10. A minimum detector power of - 54.33 dBm can be seen from the diagram to allow approximately 8 sensors with  $\eta_r = 1$ . The measured value of 2.78 corresponds to a detected power of - 37.8 dBm. The difference of 16.5 dBm between these two values implies a value of  $\eta_r$  for the couplers and Fabry-Perot receiving interferometer of about 0.02. It is difficult to estimate the light throughput of the receiver interferometer as there are unknown losses in coupling in and out of the fibre but this overall figure seems quite reasonable.

There was no cross-talk observed with the two FFPI sensors multiplexed in series. The effect of cross-talk was investigated by monitoring both the position of the centre of the WLI interference pattern and also the visibility of this pattern associated with the first sensor (sensor 1) whose temperature was maintained at room temperature, as the temperature of the second sensor (sensor 2) was varied. Figures 7.22a and 7.22b display the cross-talk measurements, where as expected, the position of the central fringe (squares) and the value of the visibility were nearly constant, indicating that there was no cross-talk between the two sensors.

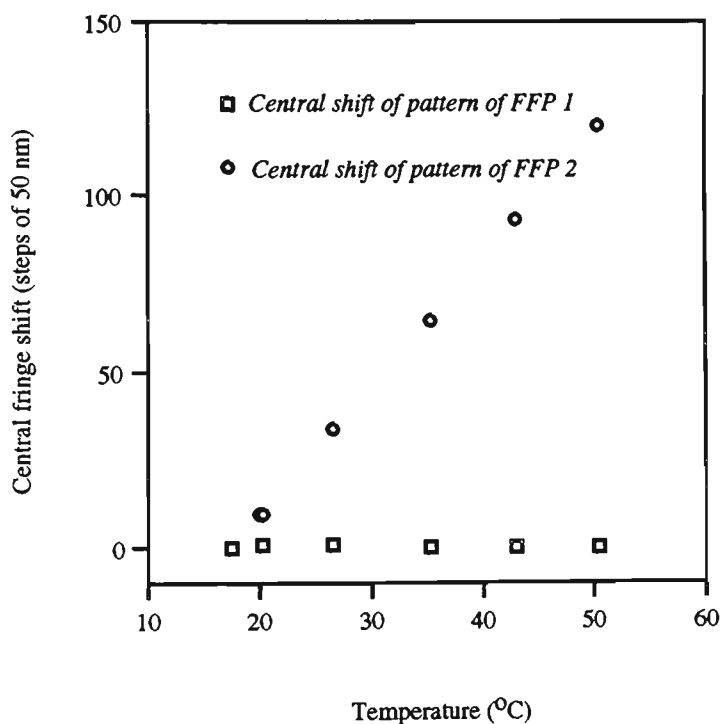


Figure 7.22a Shift of centre of WLI fringe patterns of sensor 1 (□) and that of sensor 2 (●) for the two sensors multiplexed in series when the temperature of sensor 2 is varied

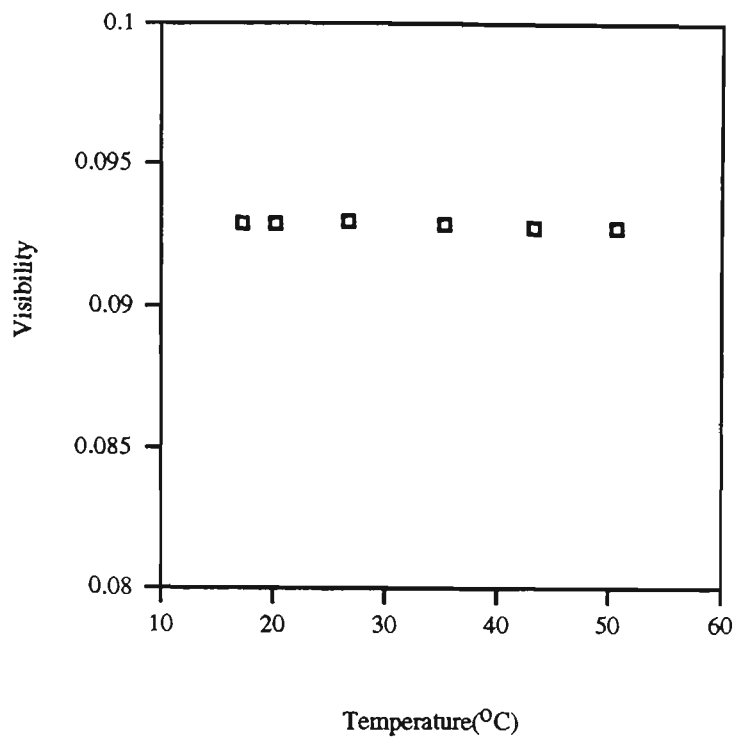


Figure 7.22b Dependence of the visibility of the first sensor (sensor 1) fringe pattern on temperature of the second sensor (sensor 2) for the two sensors multiplexed in series.

## 7.8 Conclusion

A multiplexed sensor system for the absolute measurement of static strain and temperature has been demonstrated, with two sensors multiplexed either in a serial arrangement for the measurement of temperature or in a parallel arrangement for the measurement of strain. The sensor resolution has been measured. These FFPIs sensors have been successfully multiplexed in series and in parallel with no observable cross-talk between them, and no hysteresis was evident. The experimental measurements agree reasonably with the theoretical predictions. The serial arrangement allows a compact network of interferometric fibre optic sensors formed in a single strand of optical fibre to be efficiently interrogated and demodulated. Indeed, the multiplexed fibre optic FP sensors can be used for multiparameter monitoring. The demodulation technique employing white light interferometry enables multiplexing of several sensors because of the large operating range of the receiver interferometer, and it has been

possible to multiplex FFPIs using an economical single source and detector arrangement. The advantages of this low coherence sensing include remote sensing application, a large dynamic measurement range limited only by the strength and thermal stability of the sensor, self initialisation and the achievement of absolute measurements.

## CHAPTER 8

### GRATING FIBRE FABRY-PEROT INTERFEROMETERS

Intrinsic fibre Fabry-Perot sensors based on semi-reflective fusion splices have been found to possess several advantages including high sensitivity, potential for multiplexing and easy embodiment or attachment to structures (chapter 7). However, fusion spliced fibre Fabry-Perot interferometers (FFPIs) are difficult to fabricate, particularly with birefringent fibres where alignment of eigenaxes is required, and also the strain performance ( $+3500 \mu\epsilon$  (section 5.3.3)) obtained with these sensors is less than one would like. Therefore it was necessary to look for an alternative simpler way to make FFPIs suitable for use in high stress environments. Bragg gratings when configured as FFPIs should overcome both problems; however these are difficult to make with a broad spectral reflectance. A fibre Fabry-Perot interferometer formed by two single gratings has a rather narrow bandwidth. This works well with normal FFPIs based on long coherence interferometry but is not really usable for low coherence FFPI sensing as the white light fringe pattern formed by reflection from these structures is too long and its central region rather flat. Thus there is a high probability of large errors occurring in identifying the central fringe (section 7.3.4) and hence in the measurement of the measurand. This is unacceptable in a practical system. Chirped Bragg gratings written using holographic techniques may be used to provide a broad reflection bandwidth and high reflectivity [Poladian *et al.*, 1992; Eggleton *et al.*, 1993; Farries *et al.*, 1994]. However, the technique used to

fabricate such gratings was not available with our research laboratories which uses diffraction phase masks.

There have been two types of previous approaches to making synthetic broadband sources for low coherence interferometry namely (i) by using a multimode laser diode [Gerges *et al.*, 1990], (ii) by using two broadband sources widely spaced in their centre wavelengths [Chen *et al.*, 1993; Wang *et al.*, 1994; Rao and Jackson, 1995]. The latter works particularly well but suffers from the slight disadvantage that it requires two separate broadband sources.

By using a two wavelength technique with closely-spaced coherent sources, it is possible to extend the unambiguous measurement range associated with measurement of fringe shifts in interferometric sensors [Berkoff and Kersey, 1992]. Berkoff and Kersey demonstrated a two wavelength operation of an interferometric optical fibre sensor using such a source which is in effect produced by reflecting broadband light from two in-fibre Bragg gratings to provide two closely spaced wavelengths. Using this technique with a Mach-Zehnder interferometer, an unambiguous sensor range ( $\Delta\phi = 2\pi$ ) in the optical path difference of the interferometer of about  $\pm 0.5$  mm was achieved with the two gratings separated by about 2.5 nm. This system suffers from the disadvantage that there is no absolute reference and thus information obtained is lost when the system is interrupted. This problem is overcome with white light interferometry.

The use of two widely-spaced broadband sources to produce a synthetic source for use in conjunction with WLI interferometry has been discussed by a number of authors [Chen *et al.*, 1993; Rao *et al.*, 1993; Wang *et al.*, 1993a, 1993b, 1994]. This technique has been used to enhance the amplitude of the central fringe making it easier to identify this fringe. Chen *et al.* showed that the minimum signal-to-noise ratio required to identify the central fringe through its maximum visibility could be significantly reduced when two broadband sources of wide wavelength separation are used. Two laser diodes operated below threshold were used and a

reduction in the minimum SNR from about 53 dB (for a single source) to about 22 dB (when using dual broadband sources) was obtained. Rao *et al.*, [1993] were able to produce a source of very short coherence length by summing the autocorrelation function of two multimode laser diodes. The centre wavelengths of these diode lasers were 676 nm (coherence length of 45  $\mu\text{m}$ ) and 784 nm (coherence length of 80  $\mu\text{m}$ ). At the output of the interferometer an interference signal with a significantly reduced equivalent coherence length of about 4  $\mu\text{m}$  was obtained. This was an important achievement because the narrow spectral extent of the central low coherence pattern greatly simplifies the identification of the central fringe through its maximum visibility.

Wang *et al.*, [1994] considered the matter of the optimum choice of wavelength separation for the two low coherence sources used together as a synthetic broadband source in a white light interferometric system. They developed a method of finding the optimum wavelength separation and verified their calculations experimentally using a number of laser diode sources which were operated below threshold. The wavelength combinations used in the experimental study included 635 nm, 655 nm, 688 nm and 830 nm, all with approximately the same coherence length of 15 - 16  $\mu\text{m}$ . Other experiments were performed using sources with differences in both wavelength and coherence length. Combinations of wavelength (coherence length) used included (a)  $\lambda_1 = 635 \text{ nm}$  (16  $\mu\text{m}$ ),  $\lambda_2 = 670 \text{ nm}$  (20  $\mu\text{m}$ ); (b)  $\lambda_1 = 635 \text{ nm}$  (16  $\mu\text{m}$ ),  $\lambda_2 = 750 \text{ nm}$  (40  $\mu\text{m}$ ); (c)  $\lambda_1 = 635 \text{ nm}$  (16  $\mu\text{m}$ ),  $\lambda_2 = 786 \text{ nm}$  (35  $\mu\text{m}$ ). The optimum wavelength separation for the first series of experiments (with  $\sim 16 \mu\text{m}$  coherence length) was about 175 nm. This was reduced in the second series of experiments where the second source had increased coherence length. For all cases the predicted and experimental results agreed quite well.

Wang *et al.* [1993b] showed that the use of a synthetic source involving the combination of three separate wavelengths can result in WLI patterns in which the central fringe is extremely easy to identify (even easier than with two-wavelength synthetic sources). They used three laser

diodes operated below threshold at wavelengths of 635 nm, 688 nm and 830 nm, all with coherence lengths of about 16 mm. The three-wavelength source gave a reduction of almost 6 dB in minimum signal-to-noise ratio (as defined by them) compared to a two-wavelength source using 635 nm and 830 nm laser diodes.

Recently Wang *et al.* [1995] showed that it was possible to do away with the receiving interferometer in a WLI based scheme by interrogating a sensor interferometer with two broadband sources and tuning the wavelength of one of the sources. Tuning the wavelength of one source causes a shift in all the side peak positions in the fringe pattern. If a measurand induces an optical path difference change in the sensing interferometer a corresponding shift in the entire fringe pattern will be manifest. By appropriately tuning the wavelength of one source, the side peaks could be brought back to their original position. This provides a measure of optical path difference change in the interferometer via the wavelength change of the tuned source. A measurement resolution of 1.4  $\mu\text{m}$  was obtained with this scheme. The sensitivity and scanning range with this technique depends on the properties of the tunable source. A practical system is clearly possible when tunable sources with suitable characteristics for the application are available.

Dual and multiple broadband techniques are attractive because they simplify the identification of the central fringe, but the use of several sources and the associated optical splitters is a drawback with these schemes. It was realised that this type of result could be obtained with in-fibre Bragg grating FFPIs by writing two or more closely spaced pairs of IFBGs with identical separation and different Bragg wavelengths. When used with single broadband source illumination, the wavelength separation of these Bragg grating FFPIs is limited only by the spectral width of the source.

This chapter describes an extension of this work to an intrinsic FFPI of high mechanical strength which is amenable to multiplexing and is compatible with white light interferometry.

The work used a completely new technique utilising “dual/triple in-fibre Fabry-Perot interferometers” based on in-fibre Bragg gratings. Computer simulations of dual interferometers were carried out and the success of this new method has been experimentally verified by constructing suitable dual in-fibre Bragg grating FFPIs and demonstrating their use in a sensing situation. The simulations were extended to triple Bragg grating FFPIs (6 gratings) at three distinct wavelengths and a device was made to check the accuracy of the predictions for this case also. In general it turns out that within the spectral limitations imposed by the SLD source used, triple grating FFPIs are not a substantial improvement over double grating FFPIs (with the same overall spectral separation) and hence it is perhaps best to initially concentrate on using the maximum possible wavelength spacing and spectral width for the Bragg Fabry-Perot interferometers.

### **8.1 Bragg grating writing techniques**

IFBGs consist of a long series of regular periodic refractive index variations written into the fibre core. The first report of Bragg gratings written into cores of optical fibres was made by Hill *et al.* [1978]. They observed that it was possible to induce a periodic index modulation in germanium-doped silica optical fibres by coupling highly intense counter-propagating laser beams from an argon ion laser operated at 488 nm or 514.5 nm. The counter-propagating waves form a standing wave in the fibre which results in a permanent refractive index change in the GeO<sub>2</sub>-doped core in silica fibres. The mechanism responsible for the refractive index changes has been shown to be a photon absorption process [Meltz *et al.*, 1989; Morey *et al.*, 1989]. Germanium doped silicate fibres have an oxygen-vacancy ‘defect’ absorption band at about 245 nm which can be bleached using ultra-violet radiation. During the chemical vapour deposition process involved in the formation of these fibres, oxygen deficiencies occur [Morey *et al.*, 1989] such that photons in the 245 nm region can readily break the Si - Si, Ge - Ge and Si - Ge bonds which occur without the bridging oxygen, thus giving rise to a refractive index variation.

Similar work using the Hill *et al.*, technique was done [Lam and Garside, 1981] where gratings were written in single-mode fibres using an argon ion laser operated at 514.5 nm, with 1 W output power. Lam and Garside indicated that the grating strength increased with the square of the writing power, suggesting a two photon absorption process. These optical fibre gratings are of advantage because of their intrinsic nature and low-loss. However, this method allows writing gratings only at the pump wavelength. La Rochelle *et al.* [1990] also used the same technique when fabricating Bragg gratings into elliptical-core polarisation preserving fibres. They used an argon-ion laser at a wavelength of 488 nm and gratings were written typically with optical powers of 42 mW launched into the fibre and a maximum grating reflectivity of 96% was achieved.

## 8.2 Holographic techniques

The holographic technique has found considerable application in writing Bragg gratings [Meltz *et al.* 1989; Xie *et al.*, 1993; Mizrahi and Sipe, 1993] into the cores of optical fibres. This method involves irradiating the core through the side of the cladding by an ultra violet two-beam interference pattern. The wavelength of the irradiation is chosen to be in the UV region corresponding to the oxygen defect band of germania. A permanent periodic refractive index variation results from the irradiation. Generally, CW or pulsed laser sources have been used to write these type of gratings [Meltz, *et al.*, 1989; Kashap *et al.*, 1990; Xie *et al.*, 1993]. Meltz *et al.* used a tunable excimer-pumped dye laser used in the wavelength region of 486 - 500 nm. A frequency doubling crystal was used to provide a UV source that was in the 244 nm range and had sufficient coherence length. A prism/cylindrical lens combination allowed the splitting of the UV beam into two equal intensity beams and recombining of these beams to produce an interference pattern on the fibre core. Pulse radiation having an average power between 4 - 24 mW were used to write these Bragg gratings with centre wavelength of 577 - 591 nm and grating length in the range of 4 - 10 mm. Xie *et al.* [1993] similarly used a pulsed laser

source to write their gratings. An ultraviolet interference pattern from a XeCl-pumped frequency-doubled dye laser was used. Gratings were written at a wavelength of 243 nm with typical writing energies per pulse in the range of 150 - 300 mJ/cm<sup>2</sup>. Unlike Meltz *et al.* and Xie *et al.* who used pulsed laser sources, Kashap *et al.* used an intra-cavity doubled Argon ion laser operated at 257.5 nm, with an output CW power of about 100 mW. The beam was initially expanded and split into two equal parts by using fused silica prisms (placed on a rotation stage to allow for angular variation of the two beams), and then recombined using similar prisms in such a way that it was made to interfere on one of the desired optical fibre surfaces. The holographic method of writing gratings is of advantage because it allows gratings of various Bragg wavelengths to be written by either changing the wavelength of UV beam (within the limits of the absorption band) or by altering the angle of the interfering beams. However, it demands high mechanical stability of the interferometer and freedom from vibrations.

### 8.3 Phase mask technique

A diffraction phase mask is composed of a silica plate with regular channels formed on one surface by electron beam lithography or reactive etching techniques [Verdiell *et al.*, 1993]. The depth of the channels is adjusted to introduce a  $\pi$  phase shift in the direct beam at the illuminating wavelength and this suppresses the zero order beam in the diffraction pattern from the mask. When it is illuminated with the appropriate UV laser beam, the mask generates two strong first order diffraction beams which interfere to produce UV fringes in the near field. This provides a means of writing fibre gratings when the fibre is placed in contact with, or in very close proximity to, the mask (the depth of field is very small). The phase mask technique has the advantage that the Bragg grating periodicity is half that of the phase mask and is insensitive to the angle of incidence of the writing beam. This lessens the requirement of mechanical stability. Normally, the fibre is clamped to the phase mask during the writing process, further reducing the requirement for mechanical stability. A phase mask writes gratings only at one

wavelength defined by the spatial period of the mask. Bragg gratings have been written using this technique by Hill and co-workers [1993] who indicated that long length gratings and hence narrow bandwidth gratings could be written by translating either the UV beam or the fibre phase mask assembly. Short length fibre gratings can also be made with this technique with inclusion of an aperture. The smallest length which can be written (i.e. smallest aperture which can be used) is limited by the depth of field problem.

#### 8.4 Characteristics of in-fibre Bragg gratings

The Bragg wavelength reflected by the grating is governed by the refractive index of the core and the period of the grating. Assuming that the grating is uniform along the length of the fibre, the refractive index variation  $n(z)$  has the approximate form [Russel , *et al.*, 1993]

$$n(z) = n_1 + \Delta n \cos\left(\frac{2\pi z}{\Lambda}\right), \quad (8.1)$$

where  $n_1$  is the average refractive index of the core,  $\Delta n$  is the refractive index modulation,  $z$  is the distance along the fibre core and  $\Lambda$  is the grating period. The reflectivity of the grating can be obtained using coupled mode theory [Yariv, 1973] and shown to be [Lam and Garside, 1981]

$$R(L_g, \lambda) = \frac{\kappa_c \sinh^2(SL_g)}{\Delta\beta^2 \sinh^2(SL_g) + S^2 \cosh^2(SL_g)}. \quad (8.2)$$

Where

$L_g$  is the grating length,

$\lambda$  is the wavelength in vacuum,

$\Delta\beta = \left( \beta_o - \frac{\pi}{\Lambda} \right)$  is the wave-vector detuning from Bragg resonance (phase mismatch constant),

$\beta_o$  is the propagation constant of the mode in the optical fibre and is approximated by

$$\beta_o = \frac{2\pi n_1}{\lambda} ,$$

$\kappa_c = \frac{\eta\pi\Delta n}{\lambda}$  is the coupling coefficient,

$\eta \sim 0.9$  is the fraction of fundamental mode intensity within the core,

and

$$S^2 = \kappa_c^2 - \Delta\beta^2 .$$

When the wavelength of the reflected light satisfies the Bragg condition, the reflected beams add constructively and ideally a narrow peak is observed at a Bragg wavelength  $\lambda_B$ , given by [Melle *et al.*, 1993]

$$\lambda_B = 2n\Lambda , \tag{8.3}$$

where  $n$  is effective refractive index. Under the phase matching condition,  $\Delta\beta = 0$ ,  $\lambda = \lambda_B$  equation 8.2 simplifies to the Bragg reflectivity  $R_B(\Delta n, L_g)$  which is given by

$$R_B(\Delta n, L_g) = \tanh^2\left(\pi\Delta n\eta L_g / \lambda_B\right) . \tag{8.4}$$

## 8.5 Temperature and strain characteristics of a Bragg grating sensor

Any change in either the refractive index or the grating period due to an environmental parameter,  $P$ , (e.g. temperature or strain) will alter the Bragg wavelength  $\lambda_B$  such that,

$$\Delta\lambda_B = 2 \left( \frac{\Lambda \partial n}{\partial P} + \frac{n \partial \Lambda}{\partial P} \right) \Delta P \quad . \quad (8.5)$$

It has been shown [Melle *et al.*, 1993] that the fractional change in Bragg wavelength per unit wavelength caused by simultaneous changes in strain and temperature is given by

$$\frac{\Delta\lambda_B}{\lambda_B} = \frac{\Delta n}{n} + \frac{\Delta \Lambda}{\Lambda} = (1 - p_e) \Delta \epsilon + (\alpha + \xi) \Delta T \quad , \quad (8.6)$$

where  $p_e = \frac{n^2}{2} \{p_{12} - (p_{11} + p_{12})\vartheta\}$ ,  $\Delta \epsilon$  is the change in the axial strain,  $\Delta T$  is the temperature change, and  $p_{ij}$  are the components of the strain optic tensor,  $\vartheta$  is Poisson's ratio of the fibre,  $\alpha$  is the coefficient of thermal expansion, and  $\xi$  is the thermo-optic coefficient. Using the estimated values for the constants for germano-silicate glass of  $n = 1.465$ ,  $p_{11} = 0.121$ ,  $p_{12} = 0.27$ ,  $\vartheta = 0.17$ ,  $\xi = 8.3 \times 10^{-6}/K$  and  $\alpha = 0.56 \times 10^{-6}/K$  [Xu *et al.*, 1993a], gives

$$\frac{\Delta\lambda_B}{\lambda_B \Delta \epsilon} = 0.78 \quad (8.7)$$

and

$$\frac{\Delta\lambda_B}{\lambda_B \Delta T} = 8.86 \times 10^{-6} / K \quad . \quad (8.8)$$

The thermal and static strain sensitivity of the Bragg grating were experimentally measured and are discussed in section below.

## 8.6 Bragg grating characterisation

### 8.6.1 Thermal sensitivity of IFBG

Following the analysis of in-fibre Bragg grating sensors given in the previous section 8.5, the thermal and static strain response was determined experimentally by measuring the wavelength shift as these parameters were varied. The temperature sensitivity was measured for a grating of length approximately 5.6 mm (formed in a Corning Flexcore 780 single-mode fibre, centre wavelength 835 nm, reflection bandwidth 0.3 nm (FWHM) with a 15% peak reflectivity).

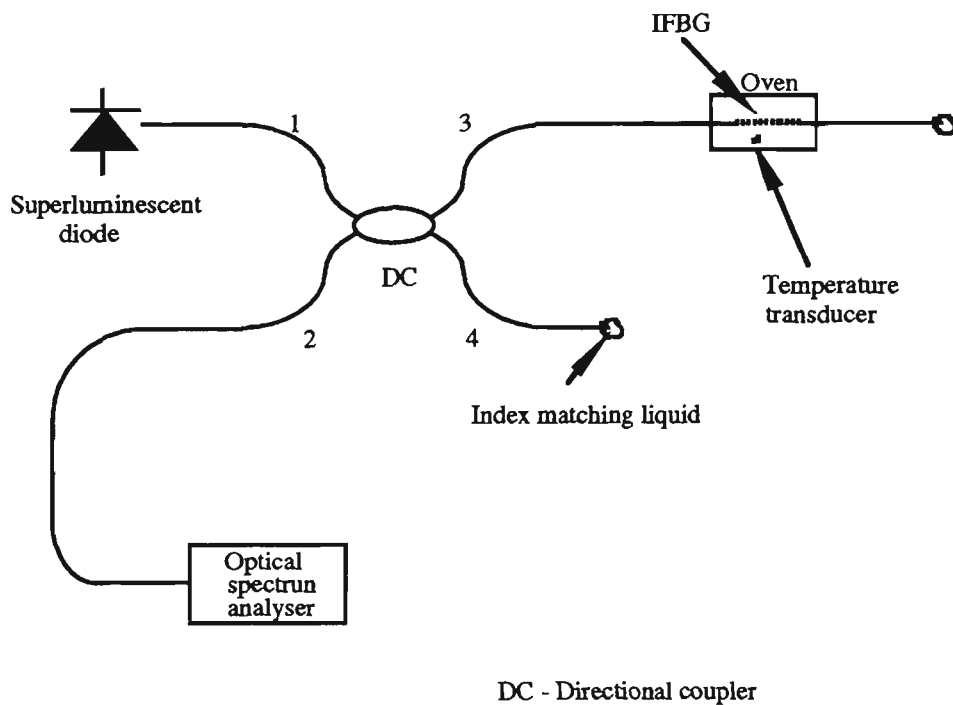


Figure 8.1 Experimental arrangement for the determination of thermal response of an in-fibre Bragg grating sensor.

An 835 nm superluminescent diode (Hamamatsu L3302) peak power 2.4 mW at 90 mA and a line-width of 10 nm (FWHM) was used as a broadband source. Light was coupled into the

IFBG via a 3 dB directional coupler. The back reflected light was analysed using an optical spectrum analyser (AQ-6310B) with a resolution of 0.1 nm. Figure 8.1 shows the experimental arrangement used to test the temperature sensitivity of the fibre grating. The unused port of the fibre coupler and the end of the fibre containing the grating were index matched to avoid unwanted reflections. The temperature of the IFBG was varied using a temperature controlled oven and monitored by an AD590 temperature transducer placed near the sensor. A typical spectral output of the back reflected light from a fibre grating sensor is shown in figure 8.2. The peak wavelength is 835 nm with a 0.3 nm bandwidth (FWHM).

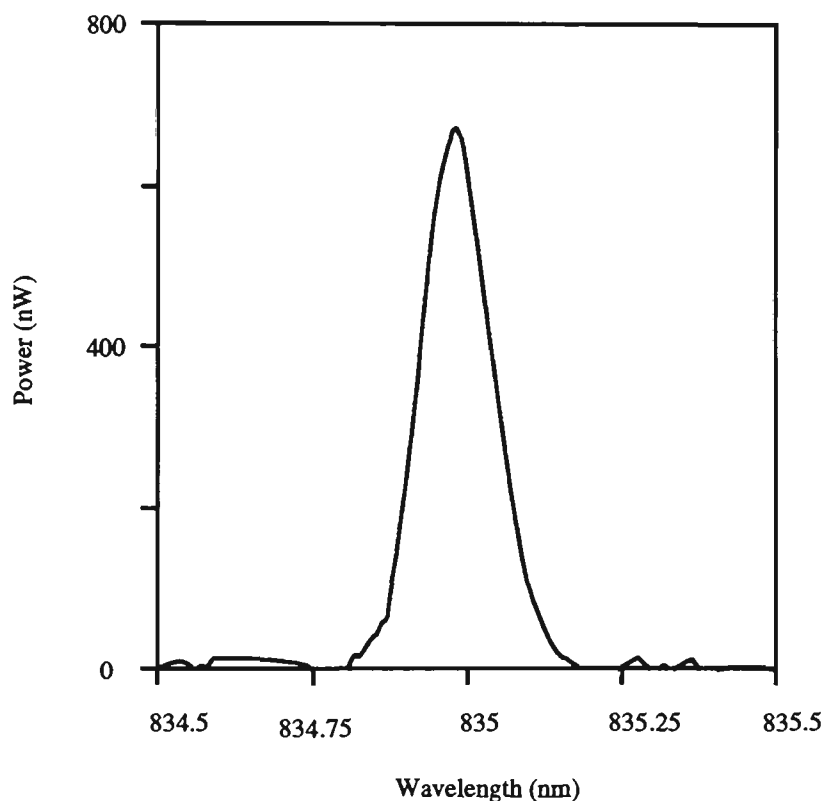


Figure 8.2 Typical back reflection spectrum from an IFBG of centre wavelength 835 nm, reflection bandwidth of 0.3 nm (FWHM) and reflectivity of 15% at room temperature.

Figure 8.3 shows a plot of reflected Bragg wavelength against temperature in the range of 20 - 70°C. The graph is approximately linear with a wavelength shift per unit temperature of  $0.0061 \pm 0.0002$  nm/K. This corresponds to a relative wavelength shift per unit temperature ( $\Delta\lambda/\lambda\Delta T$ ) of  $7.2 \times 10^{-6}/K$ . This value is in reasonable agreement with the calculation in section 8.5 of  $8.86 \times 10^{-6}/K$  considering that the properties of Flexcore fibre in which the grating was formed are very likely to be different from germano-silicate glass constants used in the calculation. The optical spectrum analyser readout gave the Bragg wavelength to  $\sim 0.01$  nm even though the spectral resolution was only 0.1 nm. Therefore, this is a very limited experiment which gives the temperature shift of the Bragg wavelength only approximately due to the limitations of the optical spectrum analyser.

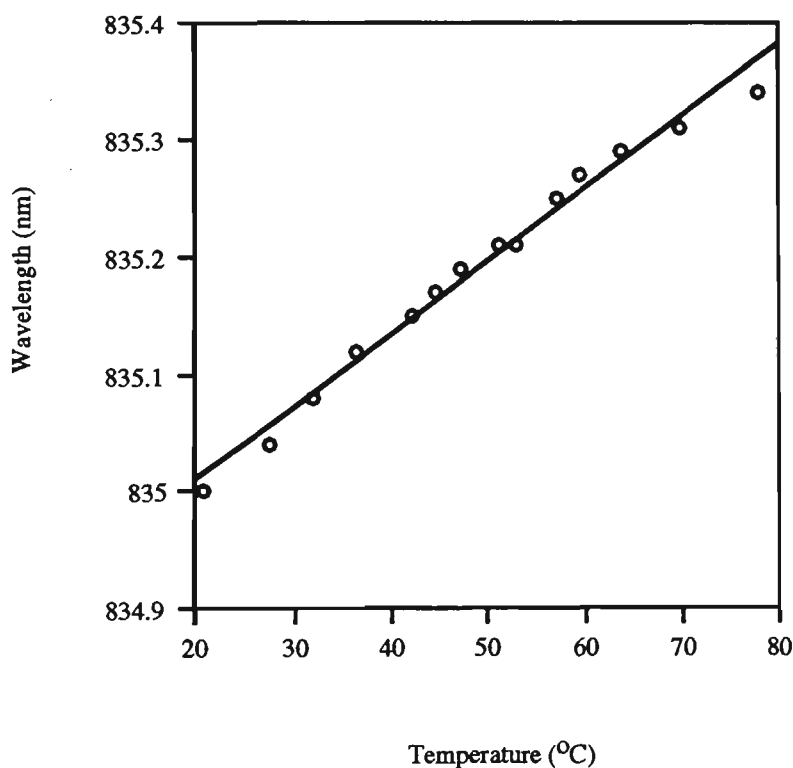


Figure 8.3 Thermal sensitivity of an in-fibre Bragg grating sensor measured with an optical spectrum analyser of resolution 0.1 nm.

### 8.6.2 Static strain sensitivity of IFBG

The in-fibre Bragg grating was also characterised for its static strain performance. The experimental arrangement is similar to the one shown in figure 8.4. The same grating as used above was adhered on the surface of a cantilever so that the grating was aligned in a direction parallel to the strain direction of the cantilever. A resistive strain gauge was similarly bonded adjacent to the IFBG to monitor the strain. Light from an SLD used in the previous experiment was injected into the system and the back reflected light again analysed using the optical spectrum analyser.

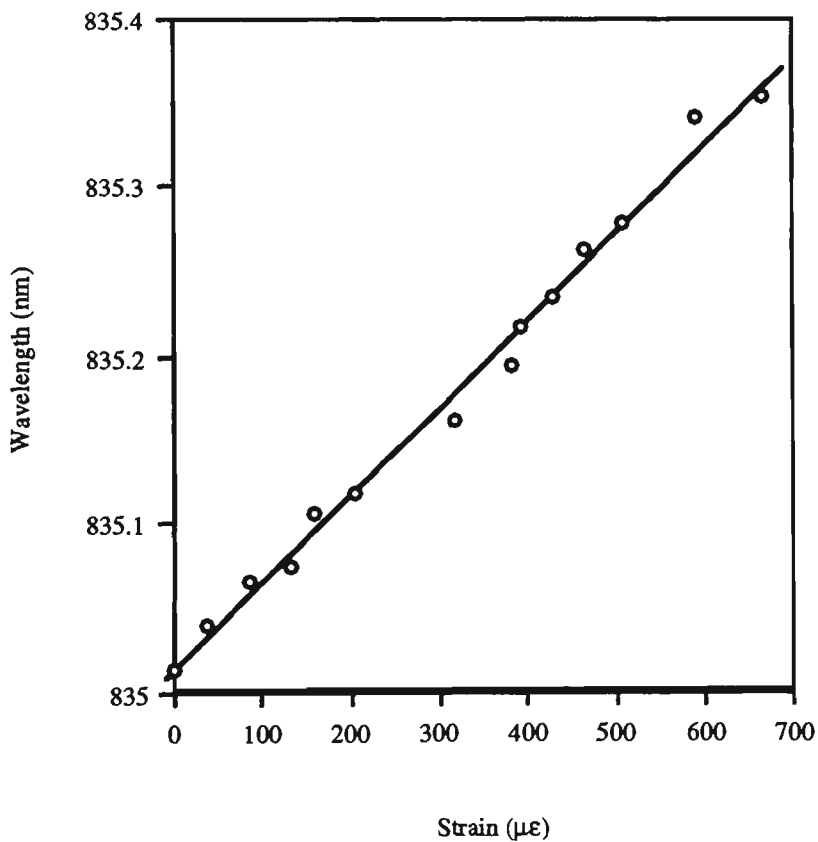


Figure 8.4 Strain sensitivity of a surface-adhered in-fibre Bragg grating sensor measured with an optical spectrum analyser of resolution 0.1 nm.

The Bragg grating is also sensitive to temperature as already indicated in section 8.5, so the sensor wavelength readings at different axial strains were taken at the same indicated temperature. An approximately linear response was displayed by the IFBG sensor (figure 8.4) over the region of 0 to about 700  $\mu\epsilon$  with a rate of change of wavelength with strain of  $\sim 0.60 \pm 0.04 \text{ pm} / \mu\epsilon$ . Given the limitation in resolution of the optical spectrum analyser this strain sensitivity is approximate only.

### **8.7 Fabrication of Dual FFP interferometer based on Bragg gratings**

The Bragg grating FFPI sensors used in this work were fabricated using the phase mask technique. To form the gratings, the fibres were initially photo-sensitised using hydrogen. Hydrogen sensitising of the fibres was done by keeping them under a pressure of 100 atmospheres of hydrogen for at least 24 hours. Normally the temperature of the “hydrogen bomb” was raised to about 100°C for 6 -12 hours of this time. In fact it appeared that satisfactory sensitisation could be achieved with somewhat less storage time and without the need to raise the temperature but this was not really investigated as the procedure used above was really quite simple and convenient to use. Use of hydrogen sensitisation changed the writing time for Bragg gratings from hours to minutes. To form the gratings, a section of the sensitised fibre that was a little longer than the grating to be written was first chemically stripped using dichloromethane. Chemical stripping ensured that minimum mechanical damage was introduced on the fibre surface. The fibre was then clamped in a special jig which could allow the fibre to be mechanically strained along its axis using a micrometer-coupled tension device. To assist the critical fibre translations required, micropositioners were used for the x-y-z movements. Figure 8.5 shows schematically the experimental arrangement. The UV beam was obtained from Spectra Physics Nd:YAG laser pumped Master Oscillator/Power Oscillator (MOPO) optical parametric oscillator. For this work the MOPO was tuned to 490 nm and this output was frequency doubled to 245 nm using an external BBO crystal. The system had a pulse repetition rate of 10 Hz, a pulse length of 6 ns and output of 50 - 100 mJ per pulse at

490 nm and up to 7 mJ per pulse at 245 nm. A dispersive prism was used to separate the fundamental (490 nm) and the UV beam emerging from the BBO crystal, and a beam dump was used to block the fundamental beam. Using a cylindrical lens to control the power density, the UV beam was partially focused through the phase mask and onto the fibre core. An aperture of 0.4 mm wide was placed between the lens and phase mask so that the length of the exposed core was restricted to about this figure.

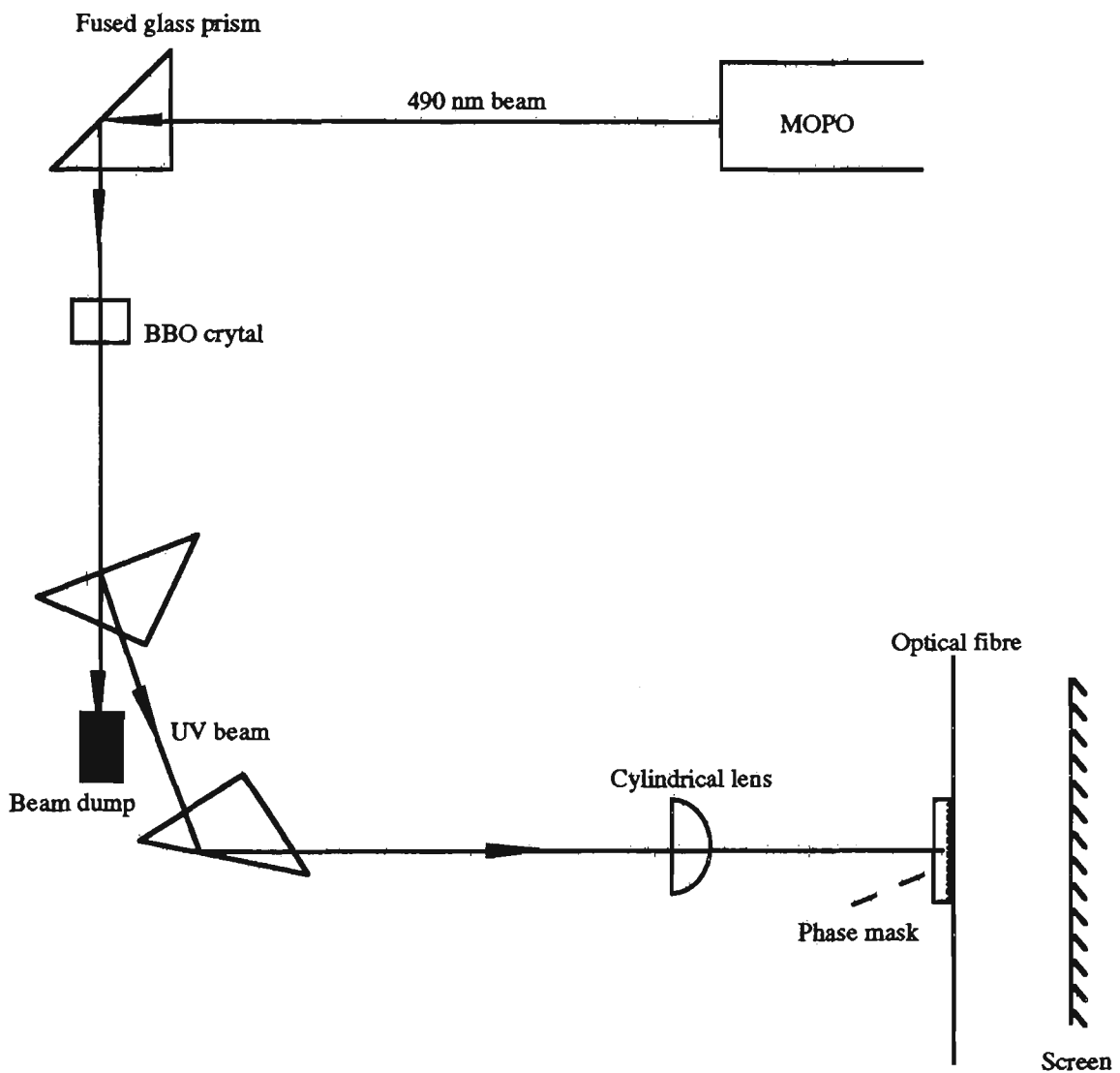


Figure 8.5 Schematic diagram of the experimental arrangement for writing Bragg gratings using a phase mask.

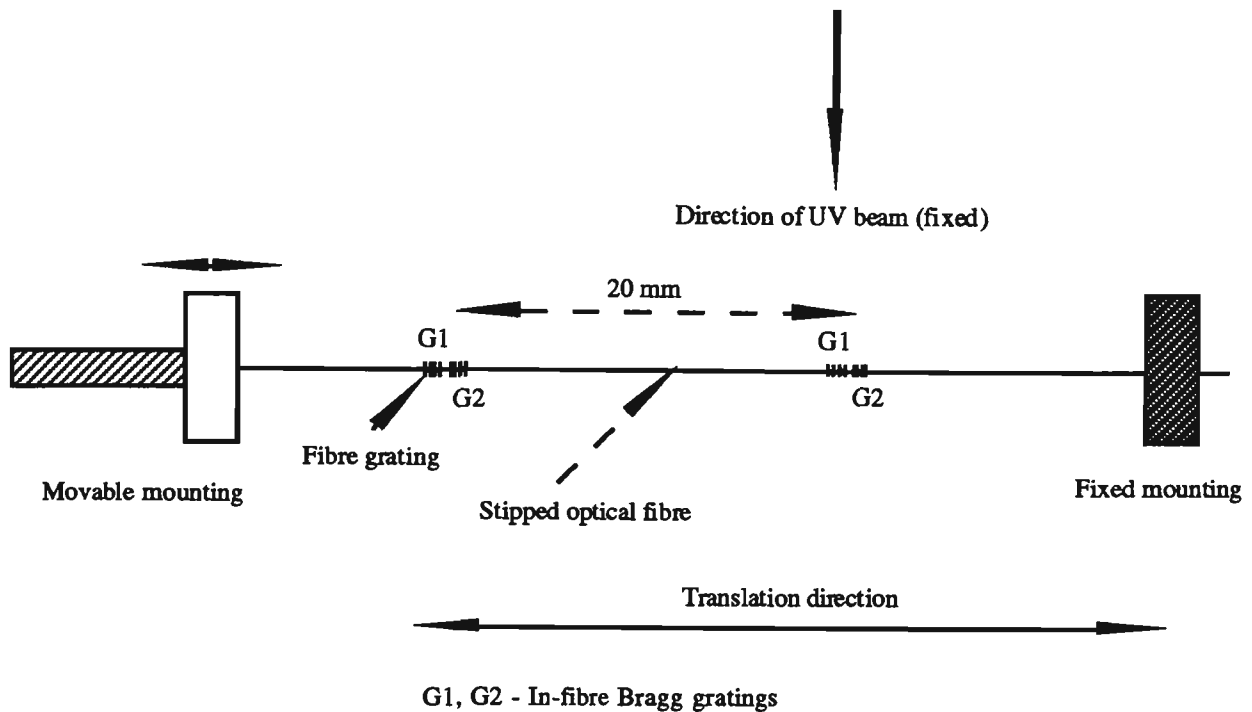


Figure 8.6 Optical fibre mounted in a special jig showing the gratings being written and also the movement of the fibre relative to the UV beam direction during grating writing process.

When tension is applied between two points of a fibre, the resulting strain is constant throughout the fibre. If a Bragg grating is written while the fibre is strained, on removing the stress there is a uniform Bragg wavelength shift (to shorter wavelength) with no change in shape in the reflection spectrum of the grating. In this way, using strains of up to 0.8%, Bragg grating-based FFPIs were written at a range of closely-spaced wavelength. The first pair of gratings forming the first FFP interferometer was written when the fibre was under maximum desired tension and subsequent pairs were written into the same fibre with reduced tension. Each writing processes followed a careful and precise movement of the fibre in its longitudinal direction. In this way it was possible to ensure that the first gratings of each FFPI pair were all written very close to each other and the spacing of each pair was the same. Figure 8.6 depicts in

a simplified way the mounted fibre and its translation relative to UV beam direction. The chosen cavity length of the FFPIs was 20 mm.

While the series of gratings were written, the spectral transmission of the fibre was monitored using a white light source and an optical spectrum analyser. In this way it was possible to carefully monitor wavelength shifts and the reflectivity and bandwidth of each grating.

### 8.7.1 Fabrication results

Figures 8.3 (a - c) show a typical transmission spectra for a set of 4 gratings which constitute a dual FFPI. Figure 8.3a shows the transmission spectrum while under tension of a pair of gratings (G1) which were written into the core of a single-mode fibre when the fibre was under tension.

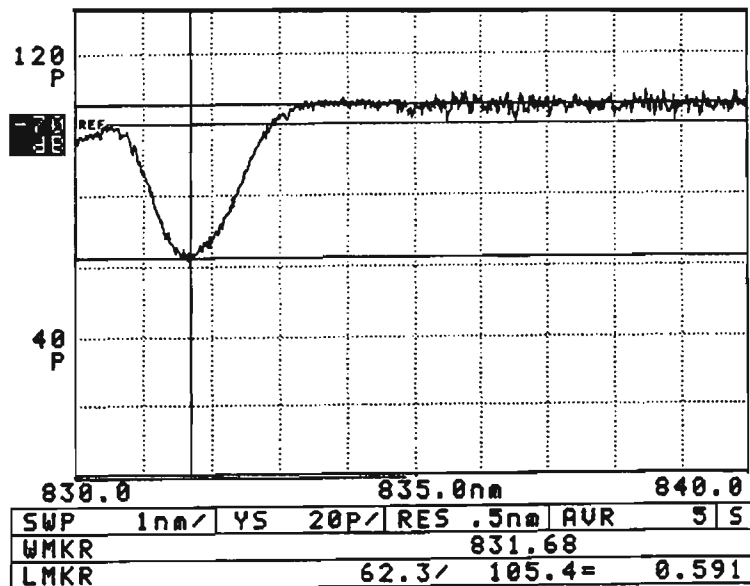


Figure 8.3a Transmission spectrum of a pair of gratings (G1) forming the first FFPI sensor written under axial tension as monitored by the optical spectrum analyser while still under tension.

Figure 8.3b shows the spectrum of the same pair of gratings (G1) when the tension had been released. As seen from figure 8.3b, the expected shift of the spectrum to the lower wavelength is observed. In figure 8.3c is shown the spectral transmission of the final dual grating fibre Fabry-Perot interferometer after a second pair of gratings were written into the unstrained fibre.

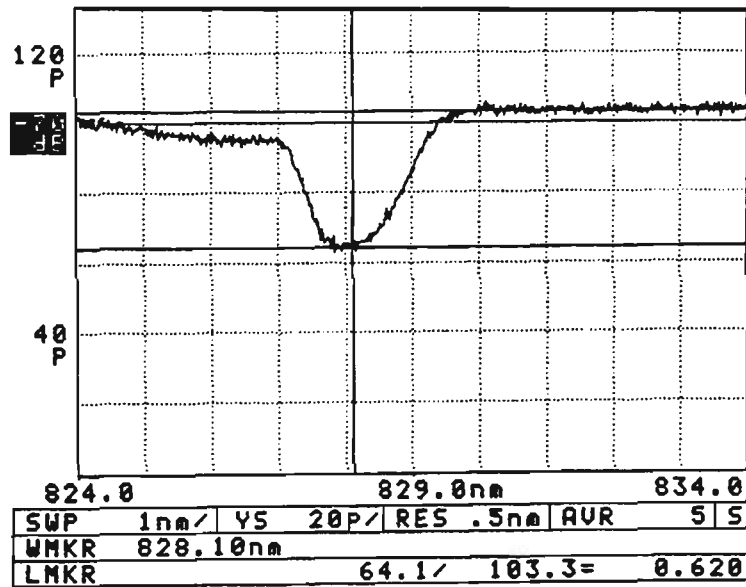


Figure 8.3b Transmission spectrum of pair of gratings G1 which form the first FFPI sensor when tension was released.

The results of the fabrication process show that the reflection Bragg wavelength of the two gratings which form the first FFPI sensor written under tension shifted about 3.7 nm when the tension was released. When the two FFPI formed by the four Bragg gratings are illuminated by broadband light, the result is equivalent to the use of two independent optical sources with a wavelength separation of 3.7 nm reflected from a FFPI with broadband mirrors.

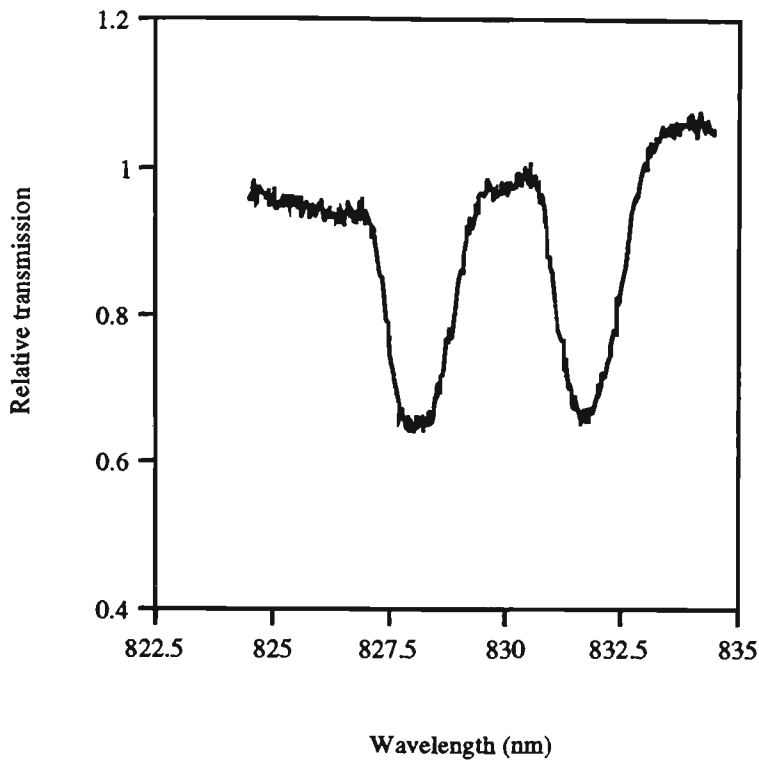
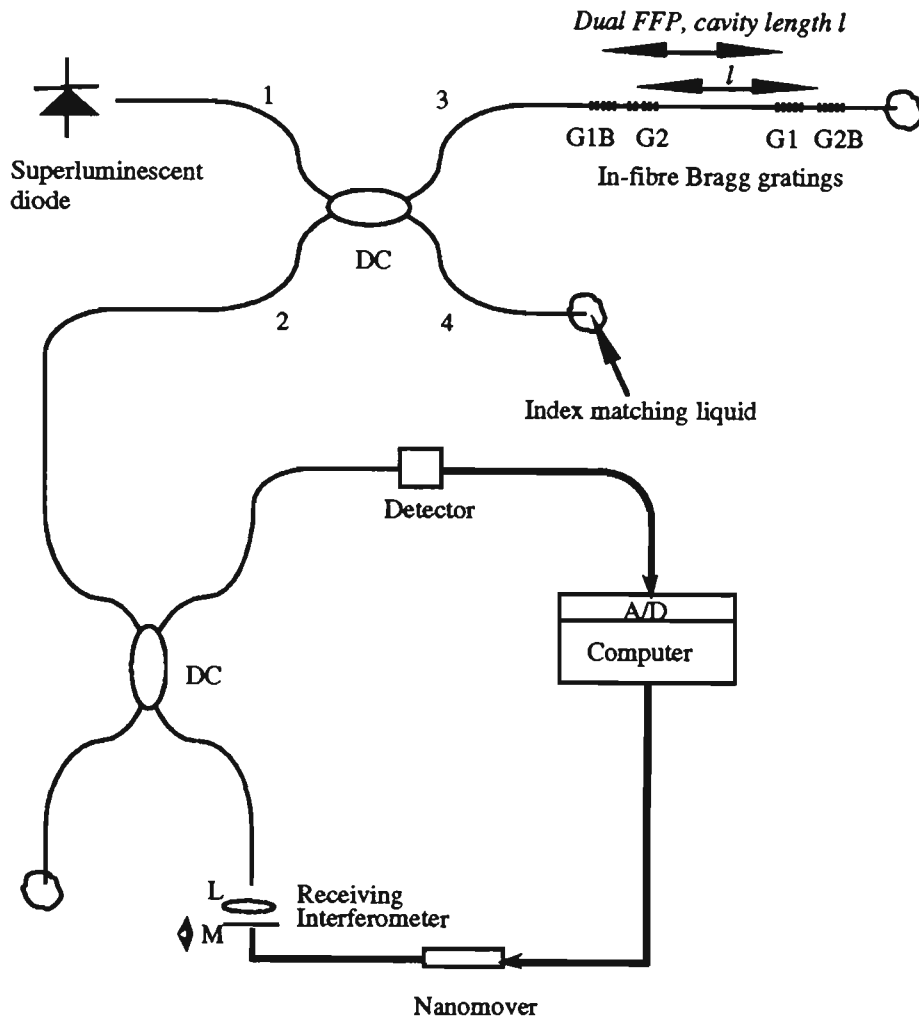


Figure 8.3c Transmission spectrum of the dual FFPI-based grating sensor (4 gratings) monitored using an optical spectrum analyser.

### 8.7.2 Predicted performance of dual FFP interferometer based on Bragg gratings

The schematic diagram of a WLI sensing scheme using a dual grating FFP interferometer as the sensor element is shown in figure 8.4. Each pair of similar Bragg gratings reflects a distinct wavelength say  $\lambda_1$  and  $\lambda_2$  of the incident light from a broadband source. In this case the two wavelengths for the dual FFP are centred at  $\lambda_1 \sim 828$  nm ( $\Delta\lambda_1 \sim 1.2$  nm (FWHM)), and  $\lambda_2 \sim 832$  nm ( $\Delta\lambda_2 \sim 1.2$  nm (FWHM)).



DC- directional coupler, L-lens, M- mirror

Figure 8.4 Schematic diagram of the experimental set up of a dual FFP sensor based on fibre Bragg gratings with WLI sensing.

Because the dual grating FFPI provides two sources with a specified difference in wavelength, the scheme is similar in principle to the dual broadband source technique described earlier [Wang *et al.*, 1994; Rao and Jackson, 1995].

For an interferometer illuminated with a superluminescent diode, assuming a Gaussian spectral profile for the SLD, the normalised ac component of the output intensity obtained is given by [Wang *et al.*, 1995a]

$$V \times \exp\left[-\left(\frac{2(x - x_o)}{l_c}\right)^2\right] \cos[4\pi(x - x_o) / \lambda], \quad (8.14)$$

where  $\lambda$  is the centre wavelength of the source,  $V$  is the visibility,  $l_c$  is the coherence length of the reflected light and  $(x - x_o)$  is the optical cavity length difference between sensor and receiver interferometers.

The two beams from the dual Bragg grating pair (which form the 2 FFPI sensors) are mutually incoherent, and therefore the resultant interference signal intensity, in the case of the two wavelengths combination source, is the superposition of the two output signal intensities generated by each grating pair. Following a similar treatment by Wang *et al.* [1994] the resultant normalised ac signal intensity can be written as

$$I_{ac}(x) = V \times \exp\left[-\left(\frac{2(x - x_o)}{l_{c1}}\right)^2\right] \cos\frac{4\pi}{\lambda_1}(x - x_o) \\ + V \times \exp\left[-\left(\frac{2(x - x_o)}{l_{c2}}\right)^2\right] \cos\frac{4\pi}{\lambda_2}(x - x_o), \quad (8.15)$$

where  $\lambda_1, \lambda_2$  and  $l_{c1}, l_{c2}$  are the centre wavelengths and coherence lengths of the two “sources” formed by reflections from the two Bragg grating pairs. Here the intensities of the two signals have been assumed equal as the reflectivities of all the Bragg gratings are assumed equal.

Since the linewidths of the two sources are the same and the wavelengths are closely spaced, the coherence length of the two sources are nearly the same i.e.  $l_{c1} \approx l_{c2} = l_c$ , and considering  $\lambda_1 < \lambda_2$  equation 8.15 becomes

$$I_{ac}(x) = V \times \exp\left[-\left(\frac{2(x-x_o)}{l_c}\right)^2\right] \cos\left[\frac{4\pi(x-x_o)}{\lambda_a}\right] \cos\left[\frac{4\pi(x-x_o)}{\lambda_m}\right], \quad (8.16)$$

where

$\lambda_a = \frac{2\lambda_1\lambda_2}{\lambda_1 + \lambda_2}$  is the wavelength at the average frequency (often termed the average wavelength),

$\lambda_m = \frac{2\lambda_1\lambda_2}{\lambda_2 - \lambda_1}$  is the modulation wavelength.

Equation 8.16 can be described as a cosine wave of wavelength  $\lambda_a$  whose amplitude is being modulated by another wave of equivalent wavelength  $\lambda_m$ , and the overall envelope of the output intensity is modulated by a Gaussian function of the type  $\exp[-2((x-x_o)/l_c)^2]$ . The beat wavelength is  $\lambda_{beat} = \lambda_m/2$ . If there is an optical path variation as a result of the measurand in the interferometer, the whole fringe pattern will shift accordingly. This allows the measurement of the measurand via the shift of the centre of wave packet.

For a triple grating FFP interferometer (6 grating elements), three sources with specified wavelengths originate from the grating assembly when illuminated by a single broadband source, thus the normalised output ac interference signal intensities can be obtained by analogy from equation 8.15 (see also Wang *et al.* [1993]), i.e.

$$I_{ac}(x) = V \times \exp\left[-\left(\frac{2(x-x_o)}{l_{c1}}\right)^2\right] \cos\left[\frac{4\pi(x-x_o)}{\lambda_1}\right]$$

$$\begin{aligned}
& +V \times \exp\left[-\left(\frac{2(x-x_0)}{l_{c2}}\right)^2\right] \cos\left[\frac{4\pi(x-x_0)}{\lambda_2}\right] \\
& +V \times \exp\left[-\left(\frac{2(x-x_0)}{l_{c3}}\right)^2\right] \cos\left[\frac{4\pi(x-x_0)}{\lambda_3}\right], \quad (8.17)
\end{aligned}$$

where  $\lambda_1, \lambda_2, \lambda_3$  and  $l_{c1}, l_{c2}, l_{c3}$  are the centre wavelengths and coherence lengths of the three reflections from the 3 grating pairs. The reflections are assumed to have same bandwidth and intensity and be closely spaced. hence their coherence lengths are nearly the equal such that  $l_{c1} = l_{c2} = l_{c3} = l_c$  and therefore equation 8.17 simplifies to

$$\begin{aligned}
I_{ac}(x) = V \times \exp\left[-\left(\frac{2(x-x_0)}{l_c}\right)^2\right] \{ & \cos[4\pi(x-x_0)/\lambda_1] \\
& + \cos[2\pi(x-x_0)/\lambda_2] + \cos[4\pi(x-x_0)/\lambda_3] \}. \quad (8.17a)
\end{aligned}$$

### 8.7.3 Computer simulations

Simulations have been done for a single grating FFPI using equation 8.14 and for both a dual FFPI-based sensor (2 optical sources) using equation 8.16 and for a triple FFPI-based sensor (3 optical sources) using equation 8.17a. The simulations for the dual grating FFP are based on combining the outputs of two sources with wavelengths of  $\lambda_1 \sim 832$  nm,  $\lambda_2 \sim 829$  nm and source bandwidth  $\sim 1.2$  nm (FWHM). Based on these parameters, the individual source coherence length  $(\lambda^2/\Delta\lambda) \sim 577$   $\mu\text{m}$  and the synthesised beat wavelength is about 230  $\mu\text{m}$ . Simulations for a triple FFPI sensor assumed three sources of centre wavelengths of 828 nm, 830 nm and 832 nm and a common bandwidth of  $\sim 1.2$  nm. These assumptions are based on

the wavelength at which the phase mask writes the gratings (i.e. 832 nm) and on the tension that can be applied safely to the fibre before fracture. To see the effect of source bandwidth on the output interference pattern, additional computer simulations for the triple FFPI were done at wavelengths of 827, 829, and 831 nm and a bandwidth of 0.6 nm. This gives an individual source coherence length of  $\sim 1154 \mu\text{m}$ .

Figure 8.5 shows a typical simulated output of the system with a single grating-based FFP sensor of reflection bandwidth  $\sim 1.2 \text{ nm}$  (FWHM). Clearly, for a single FFPI sensor, the central region of the interference fringe pattern is relatively flat and the fringe pattern extends over many hundreds of  $\mu\text{m}$ . In figure 8.6 the results of a simulation when a dual grating-based FFPI is used are displayed. The dual FFPI sensor significantly reduces the equivalent coherence length as can be seen from the simulation. The effect of increasing the wavelength separation on the interference fringe pattern is shown in figure 8.7. Here a wavelength separation of 7 nm is assumed (i.e.  $\lambda_2 - \lambda_1 = 7 \text{ nm}$ ). It can be seen that as the wavelength difference is increased the equivalent coherence length is reduced. The output of the system with a triple FFPI sensor is shown in figures 8.8a and 8.8b. With particular parameters assumed, the triple FFPI sensor does not give a significant reduction in equivalent coherence length in comparison with the dual FFP with same overall wavelength separation. This is because the modulation wavelength depends mainly on the overall wavelength separation. The overall spatial extent of the pattern in figure 8.8b is greater than that in figure 8.8a because of the longer coherence length of the 0.6 nm wide reflections.

The SLD used in this study has a rather narrow bandwidth (10 nm) and other SLDs are available with bandwidths over 30 nm. With such sources it would be possible to obtain much narrower central fringe packets while using a single optical source. This would greatly simplify the identification of the central fringe and lower the required signal-to-noise ratio for reliable identification of that fringe. In order to demonstrate this, figures 8.9 (a), (b) and (c) show the low coherence interferogram pattern obtained with a dual FFPI having reflection wavelengths

of 818 nm and 842 nm and an optical bandwidth (FWHM) for each reflection of 1.2 nm, 5 nm and 10 nm respectively.

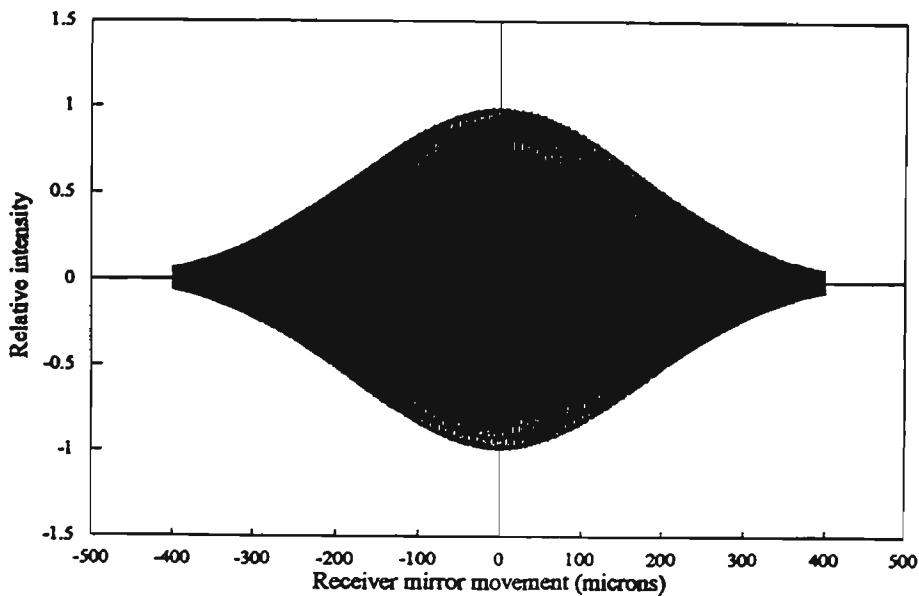


Figure 8.5 Typical simulated output interference fringe pattern using a single grating-based FFPI sensor of centre wavelength 832 nm, reflection bandwidth of 1.2 nm (FWHM).

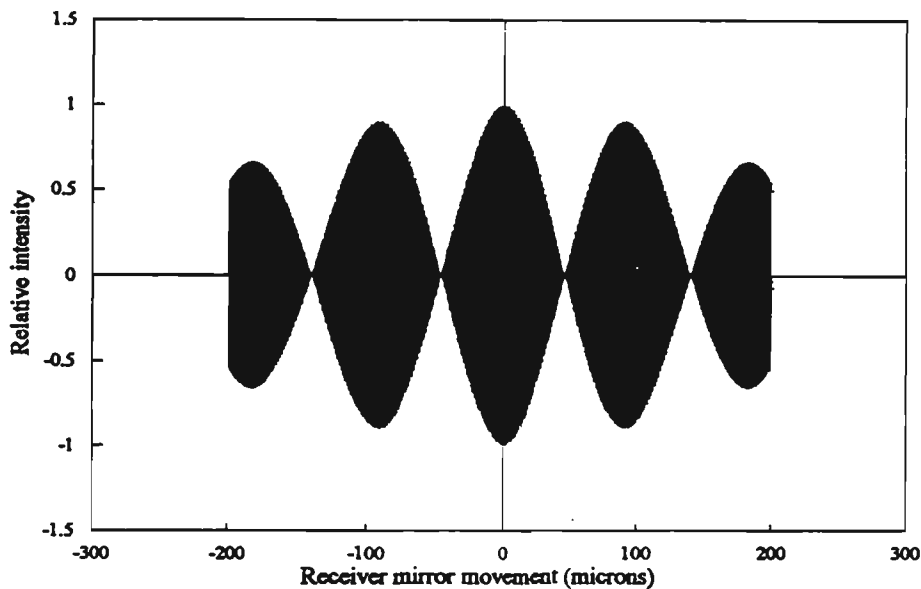


Figure 8.6 Simulated output interference fringe pattern formed by a dual FFPI sensor element reflecting at centre wavelengths of 831.7 nm and 828 nm, each having a reflection bandwidth of 1.2 nm (FWHM).

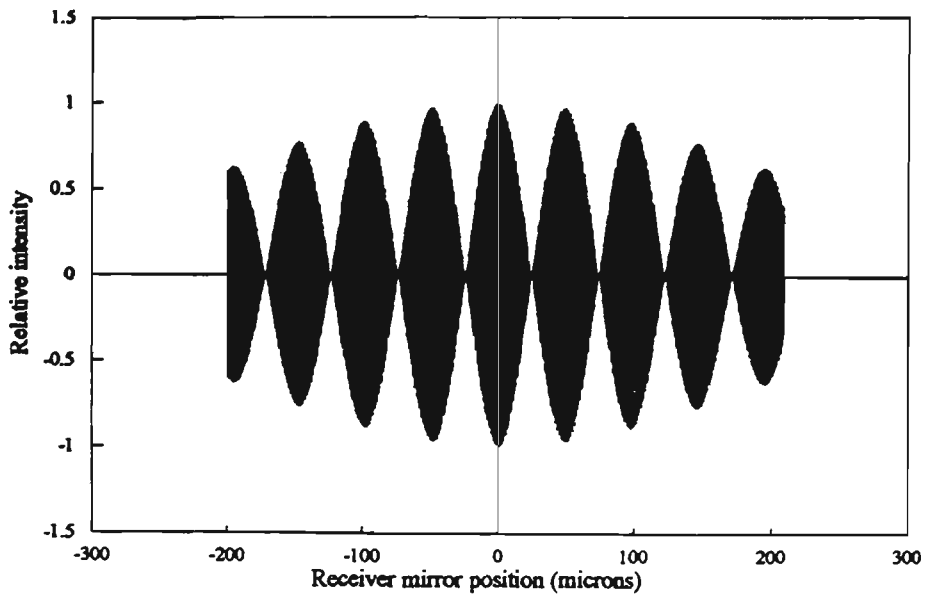


Figure 8.7 Simulated WLI interference pattern for a dual FFPI sensor with a wavelength separation of 7 nm, reflection centre wavelengths of 824.7 nm and 831.7 nm, each having a reflection bandwidth of 1.2 nm (FWHM).

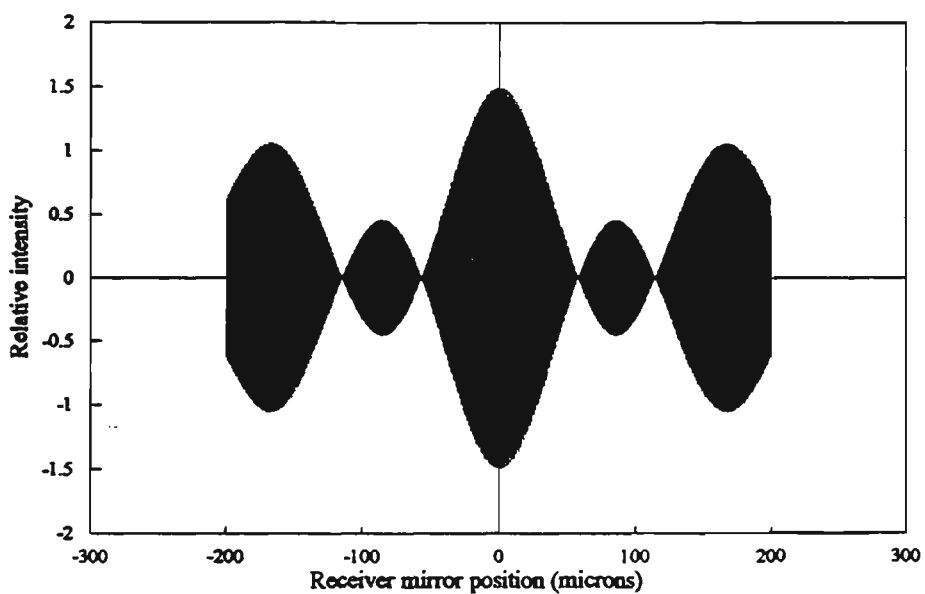


Figure 8.8a Simulation of the WLI fringe pattern formed by a triple FFPI (6 grating elements). Reflection centre wavelengths of 827 nm, 829 nm and 831 nm with a common bandwidth of 1.2 nm (FWHM).

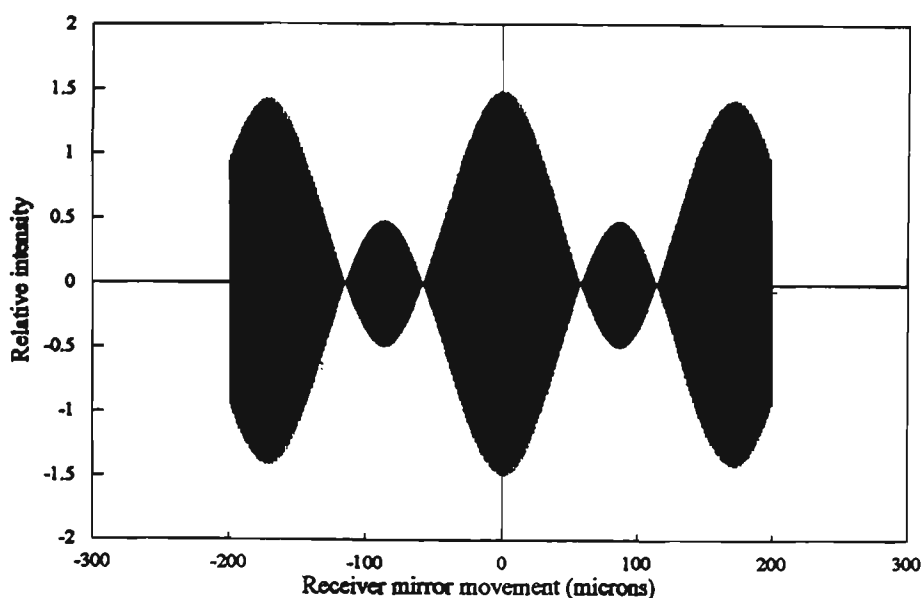
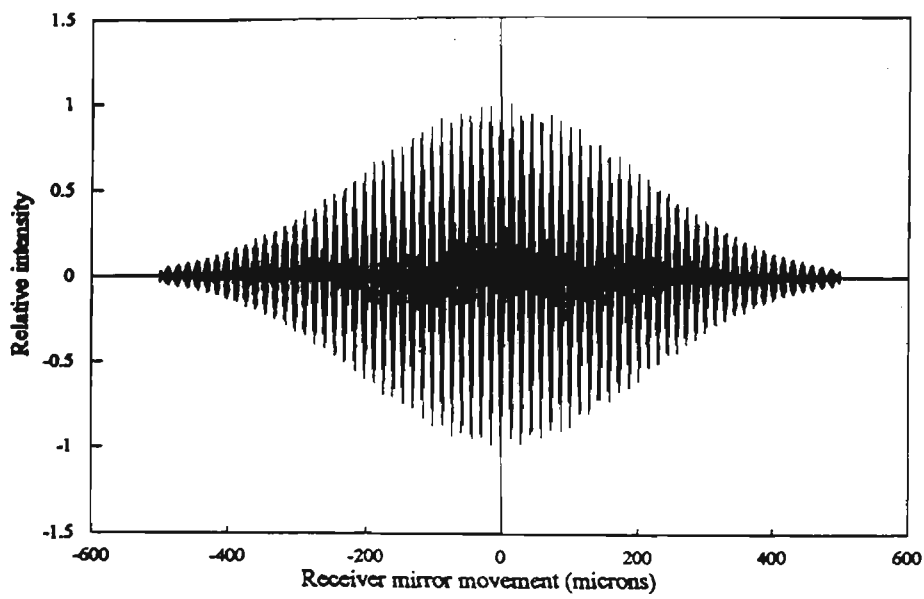


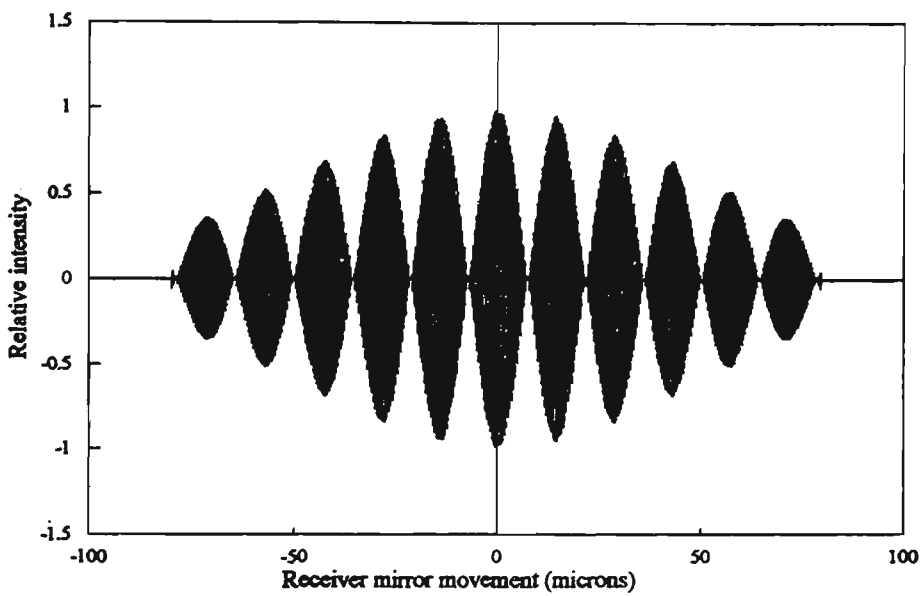
Figure 8.8b Computer simulation of the interference pattern obtained with a triple FFPI (6 grating elements), with reflection centre wavelengths of 827 nm, 829 nm, and 831 nm and a common bandwidth of 0.6 nm (FWHM).

The improvement (i.e. decrease) in width of the central fringe packet and ease of identification of the central fringe is obvious.

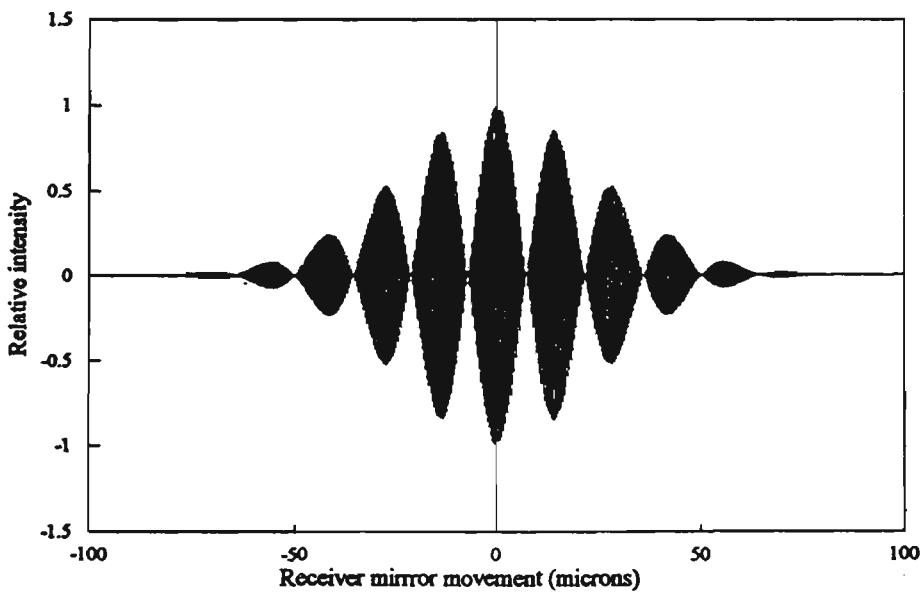
Very broad Bragg gratings are possible using holographically-produced chirped gratings. This is the reason that larger bandwidths have been included in figure 8.9. In fact gratings with widths as large as 44 nm have been produced [Farries *et al.*, 1994]. Gratings of this type can be produced at any desired wavelength and are very suitable for use with SLD sources or laser diodes operated below threshold. With the use of two or more such sources in a manner similar to others [Wang *et al.*, 1994; Rao and Jackson, 1995], even narrower central fringe



(a)



(b)



(c)

Figure 8.9 Simulated low coherence interferogram for  $\lambda_1 = 842$  nm and  $\lambda_2 = 818$  nm and FWHM reflection bandwidth of (a) 1.2 nm, (b) 5 nm and (c) 10 nm.

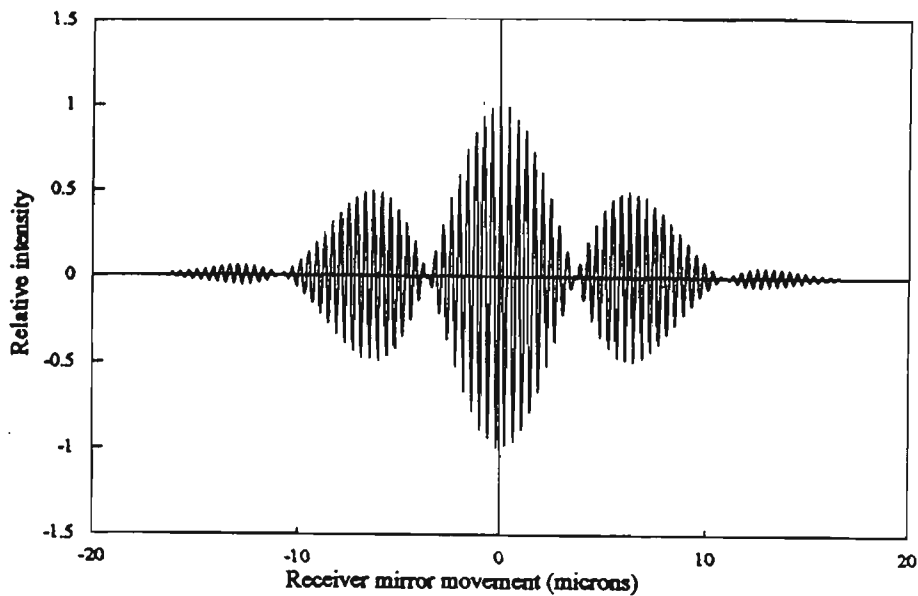


Figure 8.10 Simulated low coherence interferogram for  $\lambda_1 = 830$  nm and  $\lambda_2 = 785$  nm and FWHM reflection bandwidth of 40 nm.

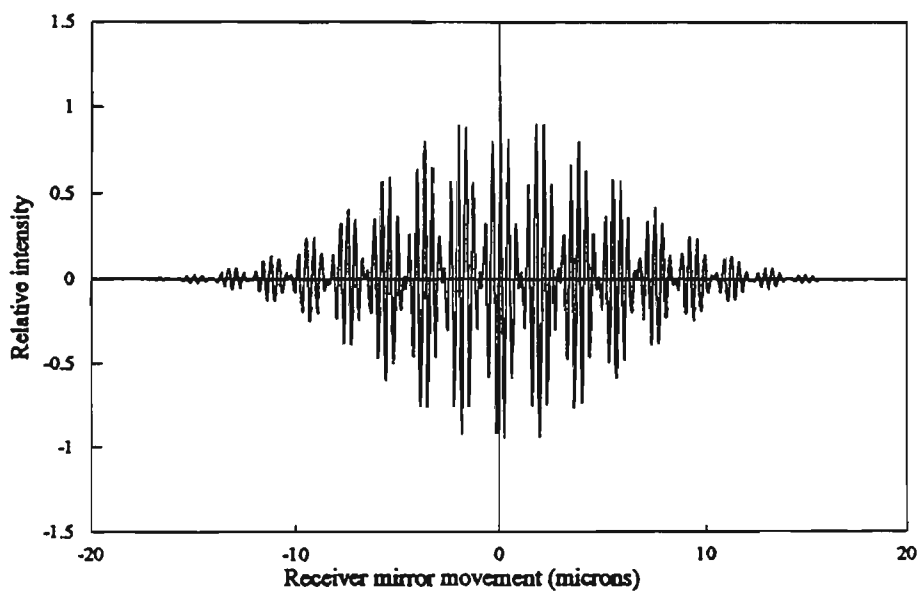


Figure 8.11 Simulated low coherence interferogram for  $\lambda_1 = 830$  nm and  $\lambda_2 = 680$  nm and FWHM reflection bandwidth of 40 nm.

packets are achievable with appropriately designed multiple FFPI sensors. Figure 8.10 is an example of such an interferogram using grating wavelengths of 785 nm and 830 nm with a bandwidth for each reflection of 40 nm (coherence length of approximately 16  $\mu\text{m}$ ). Figure 8.11 is a similar interferogram for reflection wavelengths of 830 nm and 680 nm. This latter choice corresponds approximately to the optimum wavelength separation as defined by Wang *et al.* [1994].

Clearly multiple grating-based FFPI sensors have the potential to combine all the advantages of using Bragg gratings as reflectors with the established advantages of using synthetic light sources.

#### 8.7.4 Experimental results

The experimental arrangement used to verify the above concepts with a dual FFPI sensor is shown in figure 8.4. Light at a centre wavelength of 832 nm from a superluminescent diode (Hamamatsu L3302), having a FWHM bandwidth of  $\sim 10$  nm was launched into the sensor via a  $2 \times 2$  single-mode directional coupler as discussed earlier. The temperature sensitivity was measured for a dual FFPI sensor of grating spacing  $20.00 \pm 0.01$  mm, centre wavelengths of  $\sim 829$  nm and  $\sim 832$  nm, reflection bandwidth of  $\sim 1.2$  nm (FWHM) with each grating FFPI having a reflectivity of  $\sim 20\%$  (see transmission spectrum, figure 8.3c). These reflectivities were a little high for low finesse sensors suitable for multiplexing but were adequate to verify the concepts and the higher reflectivity improved the signal-to-noise ratio. The receiving interferometer and detection arrangement was the same as in previous WLI measurements. The unused ports of the fibre couplers together with the distal end of the fibre containing the Bragg gratings were index matched to avoid spurious back reflections. Figure 8.12 shows the measured output signal obtained at the detector as the mirror of the receiver interferometer was scanned. It shows the sum of both outputs of wavelength  $\lambda_1$  and  $\lambda_2$ , where a beat signal is

clearly evident. The fringe pattern obtained experimentally agrees well with the simulation in figure 8.6. The experimental beat interval was  $96 \mu\text{m}$  compared to a simulated one of  $93 \mu\text{m}$ . The temperature of the dual FFP sensor was varied using the temperature controlled oven and an AD590 temperature probe served as a reference. The central interference packet was tracked as the temperature of the oven was varied. The central fringe and centre of this fringe were identified using the signal processing techniques described in sections 6.5.3 and 6.5.4. Figure 8.13 shows a plot of the shift of the centre of the central fringe against temperature measured by the AD590 temperature probe. The graph is linear with a central fringe shift (in air) per unit temperature of  $209 \text{ nm/K}$ . This corresponds to a relative phase shift per unit temperature ( $\Delta\phi/\phi\Delta T$ ) of  $7.2 \times 10^{-6}/\text{K}$ . The equivalent coherence length is smaller than would be obtained with a single FFPI sensor. The voltage signal-to-noise ratio obtained with this arrangement was  $15.64 \text{ dB}$  with a fringe visibility of  $\sim 0.3$ .

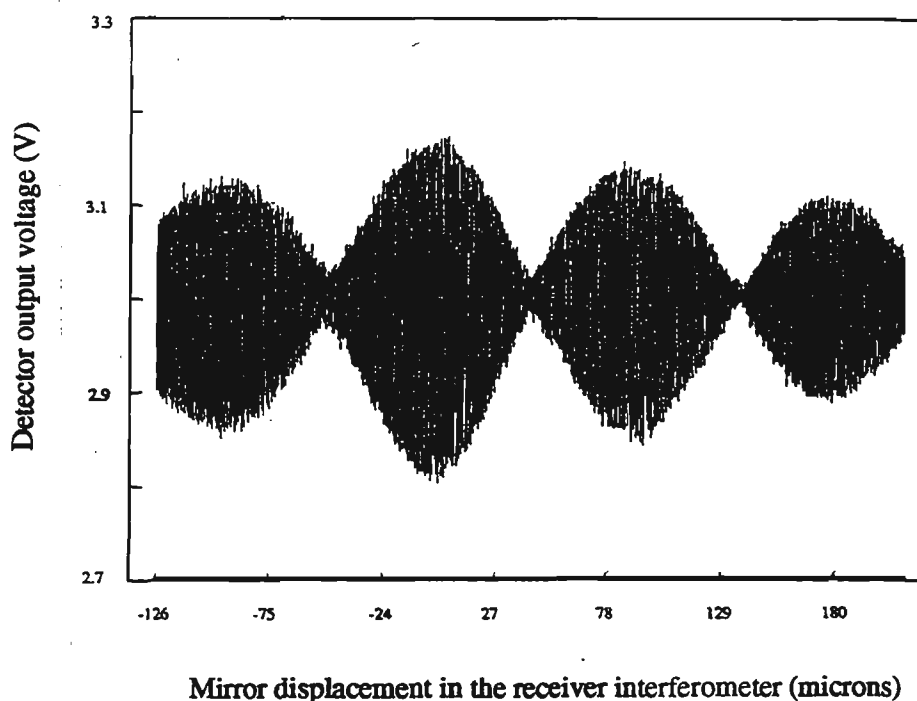


Figure 8.12 Measured interference fringe pattern obtained with a dual FFPI sensor as the receiver interferometer is scanned. Sensor parameters are: wavelength separation  $3.7 \text{ nm}$  (centres  $\sim 828 \text{ nm}$  and  $\sim 832 \text{ nm}$ ), FWHM reflection bandwidth  $\sim 1.2 \text{ nm}$ , reflectivity  $\sim 20\%$ . The source used was an SLD with FWHM bandwidth  $\sim 10 \text{ nm}$ .

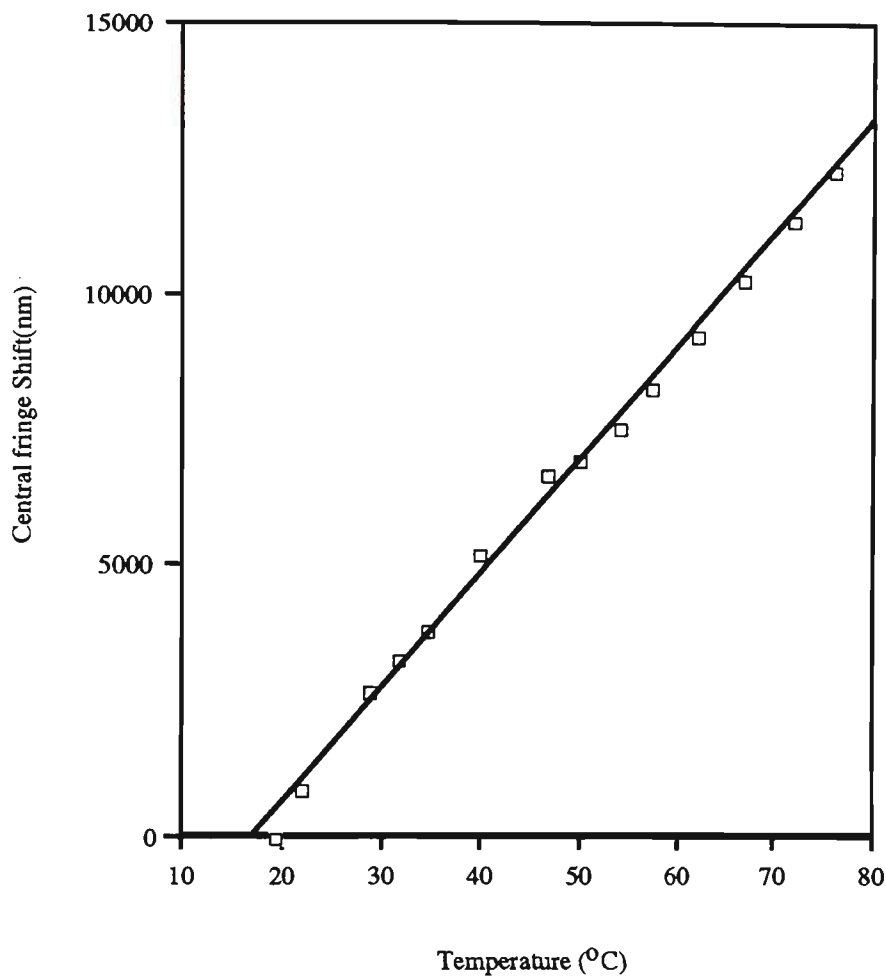


Figure 8.13 Shift of the centre of fringe pattern against temperature for the grating-based dual FFPI sensor.

### 8.7.5 Results with triple FFPI sensor

Following a similar procedure described in section 8.7, a triple FFPI sensor was fabricated. The sensor was constructed using 3 FFPIs, each with a pair of gratings reflecting at a different wavelength. The central wavelengths were equally spaced over a 3.7 nm interval with centres at approximately 831 nm, 829 nm and 827 nm. The grating spacing was  $20.00 \pm 0.01$  mm with a reflectance for each grating of  $\sim 17\%$  and a bandwidth of 0.6 nm (FWHM). Figure 8.14

shows the transmission spectrum of a triple FFP based grating observed using an optical spectrum analyser.

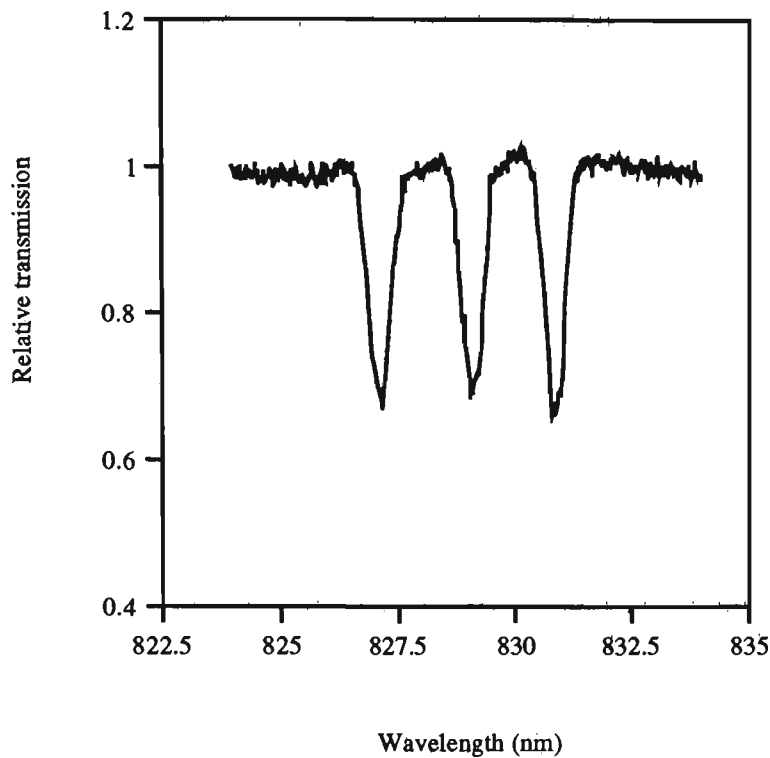


Figure 8.14 Transmission spectrum of a triple fibre Fabry-Perot grating based sensor, reflectance  $\sim 17\%$ , bandwidth  $\sim 0.6$  nm (FWHM), total wavelength separation  $\sim 3.7$  nm.

The triple FFPI sensor was characterised for its thermal sensitivity using the same arrangement shown as used in the previous section. Figure 8.15 shows the measured output fringe pattern for a triple FFP sensor. The results agree reasonably well with the computer simulation in figure 8.8b although there are some shape differences which are possibly due to the visibility being less than unity for the experimental measurements. In this case the experimental beat interval was  $92 \mu\text{m}$  and the simulated one was  $84 \mu\text{m}$ . The temperature of the sensor was slowly raised in the range of  $18^\circ\text{C}$  to about  $54^\circ\text{C}$  and the central fringe packet tracked as the temperature was varied. The central fringe and centre of this fringe were identified as described

in sections 6.5.3. and 6.54. Figure 8.13 shows a graph of the shift of the centre of the central fringe versus temperature read by an AD590 temperature transducer. The graph is linear with a central fringe shift (in air) per unit temperature of 211 nm/K for a 20 mm length of sensing cavity. The voltage signal-to-noise ratio was 13.3 dB and the fringe visibility obtained experimentally was 0.14.

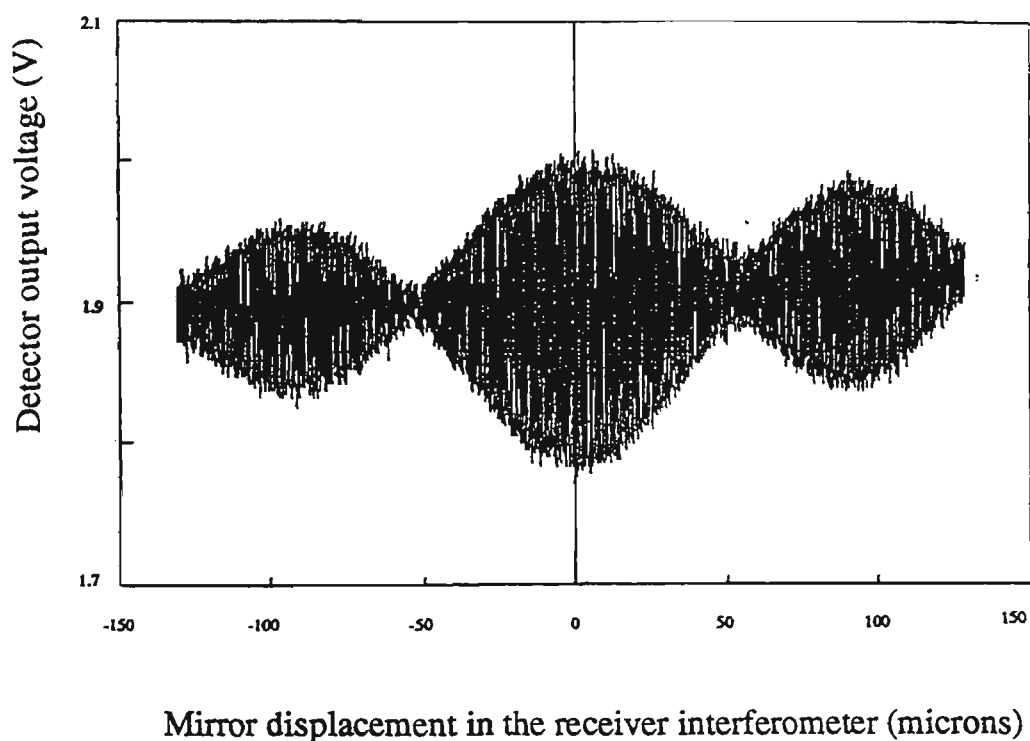


Figure 8.15 Measured interference fringe pattern obtained with a triple FFPI sensor as the receiving interferometer was scanned. The reflection centre wavelengths were  $\sim 827$  nm, 829 nm, and 831 nm with a bandwidth of  $\sim 0.6$  nm (see figure 8.14). The source used was an SLD with FWHM bandwidth of  $\sim 10$  nm.

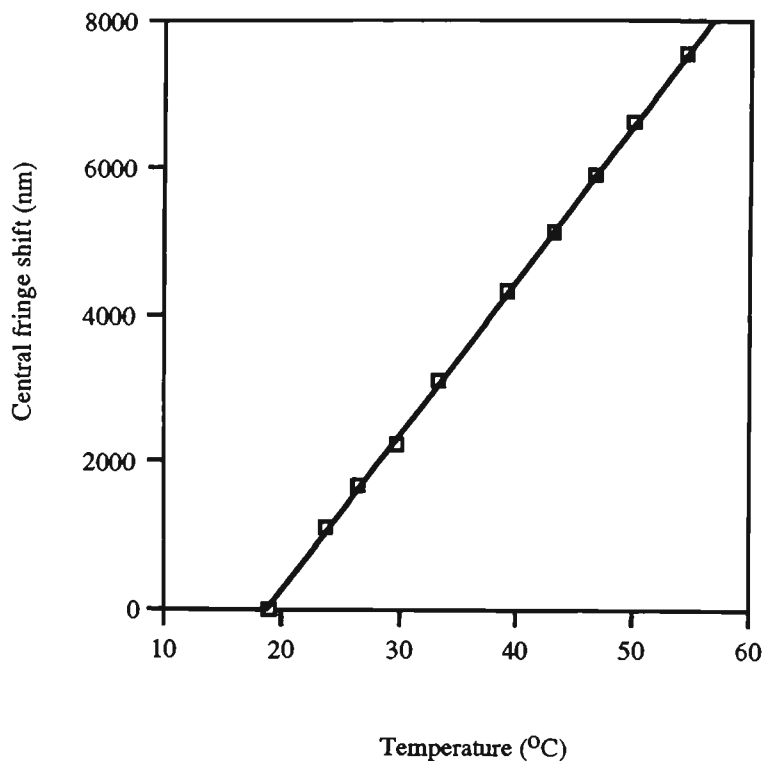


Figure 8.16 Thermal sensitivity of a triple FFPI sensor, reflectivity ~ 17%, sensing length 20 mm, total wavelength separation 3.7 nm (centre wavelengths ~ 827, ~ 829, and ~ 831 nm), bandwidth ~ 0.6 nm (FWHM) (see figure 8.14).

### 8.7.6 Mechanical strength of grating sensors

The mechanical breaking strength was investigated for both normal Corning Flexcore fibres which were chemically stripped at their centres but without any gratings written in them and on similar fibres into which gratings had been written. The number of such fibres was very limited (4 normal and 2 Bragg grating) and so the data can only be regarded as giving very approximate values for the breaking strain. The fibres were strained until fracture and an average breaking strain of about +35,000  $\mu\epsilon$  was obtained for the normal fibres compared to an average breaking strain of about +12,000  $\mu\epsilon$  for fibres with Bragg gratings (the actual figures were 12,270  $\mu\epsilon$  and 12,007  $\mu\epsilon$ ). The fibres which included Bragg grating both broke at the grating. The breaking strength of a grating-based FFPI appears to be a factor of about 3 higher

than that obtained with the fusion spliced FFPIs of +3500  $\mu\epsilon$ . This is a significant improvement in mechanical strength and makes Bragg grating FFPIs suitable for applications where larger stresses are envisaged. The higher breaking strength of the grating FFPIs may be in part attributed to the use of chemical stripping which was not done during fabrication of fusion spliced FFPIs. The difficulty of manufacturing fusion-spliced FFPIs was such that it was not considered worthwhile to investigate the improvement which could be gained from chemical stripping of the jacket.

### **8.7.7 Conclusion**

In this chapter, a totally new type of fibre Fabry-Perot sensor, which is suitable for use in low coherence sensing, has been proposed, modelled and experimentally verified. FFPI sensors which are based on a single pair of IFBGs written into the core of a single-mode fibre using normal writing techniques are not very suitable for low coherence systems. This is because the narrowband reflections have a long coherence length and thus very long WLI patterns are produced. By writing multiple independent Fabry-Perot interferometers, using grating pairs at different wavelengths with the same grating spacing and occupying a length of fibre only slightly longer than the grating spacing, it is possible to obtain WLI fringes having a central fringe pattern of much reduced spatial extent. The advantages offered by these sensors are completely analogous to those offered by systems which use multiple wavelength sources together with broadband mirrors in a single FFPI. The grating-based multiple FFPI sensors may be tailored to use the maximum bandwidth available from a single broadband source or be designed for use with multiple broadband sources.

Double and triple grating-based FFPI sensors which are designed to be used with a single SLD source of bandwidth 10 nm have been constructed and used to measure temperature.

These grating-based FFPI sensors appear to have significantly improved mechanical strength compared to those made using cleaving, coating and fusion splicing techniques, even when the latter is combined with CO<sub>2</sub> laser annealing.

## **CHAPTER 9**

### **CONCLUSION AND FUTURE WORK**

#### **9.1 Conclusion**

The objectives of this thesis, outlined in chapter 1, of fabricating an optical fibre sensor suitable for the measurement of strain in structural materials, and evaluating its performance in an effective multiplexed arrangement, have been realised. The optical device developed was all-fibre, intrinsic and based on Fabry-Perot interferometry with gauge lengths in the range of 4 - 20 mm. Demodulation was achieved by white light interferometry. Two approaches were used to fabricate the internal mirrors of the sensor elements; the first method used vacuum deposition on the cleaved fibre end followed by fusion splicing which resulted in reflectances in the range of 4%- 20%. These sensors were successfully fabricated and surface adhered onto a mild steel cantilever for static strain monitoring. The second method was a new technique of fabricating multiple FFPIs based on low reflectance Bragg gratings as Fabry-Perot mirrors. These were introduced into the cores of single-mode fibres by exposing the fibre to a UV beam through a diffraction phase mask. A single sensor was evaluated first and then a multiplexed arrangement was assessed. Experimental measurements were carried out at wavelengths of 810 nm and 1300 nm for the fusion spliced FFPIs and at approximately 832 nm for the grating FFPIs.

For the evaluation of the fusion spliced FFPI sensors which were fabricated in a 1300 nm single-mode communication fibre, a long coherence source of centre wavelength of 1300 nm was used. The sensor response was linear in both tension and compression with negligible hysteresis. The relative phase sensitivity per unit strain  $\Delta\phi/\phi\epsilon$  obtained experimentally was found to be  $0.840 \pm 0.004$ ,  $\lambda = 1300$  nm for a 4.5 mm FFP sensor. The sensors were also calibrated for temperature during both heating and cooling cycle, and there was no observable hysteresis. The relative phase sensitivity per unit temperature,  $\Delta\phi/\phi\Delta T$ , was found to be  $7.0 \times 10^{-6}$  /K for a 5 mm FFP cavity.

Methods to reliably identify the central fringe of a WLI fringe pattern have been discussed and an intrafringe resolution of 1/200 of a fringe was shown to be possible. Using white light interferometry, the central fringe shift (in air) per unit strain for a  $\sim 1.7$  cm FFPI sensor was found to be  $23.4 \pm 0.7$  nm/ $\mu\epsilon$  at  $\lambda = 810$  nm. The thermal response for these sensors was also investigated and a central fringe shift (in air) per unit temperature of  $223 \pm 3$  nm/K ( for a  $\sim 2$  cm FFPI sensor) was obtained at a wavelength of 810 nm . This corresponds to a relative phase shift per unit temperature of  $7.7 \times 10^{-6}$ /K. Temperature measurements with an estimated resolution of 0.01 °C and strain measurements with a resolution of 0.07  $\mu\epsilon$  are possible with this technique.

The FFPI sensors were multiplexed both in a series and in a parallel arrangement and their performance obtained for both static strain and temperature measurement, with no observable cross-talk. By adopting the serial arrangement and demodulation using WLI interferometry, it is possible to multiplex several FFP sensors of different free spectral ranges without any cross-modulation. This arrangement has the potential to realise a localised and quasi-distributed sensor system for monitoring of most fields of practical and industrial interest over several sites with good sensitivity. The fibre Fabry-Perot sensor was demonstrated to be easily bonded to a structure without any hysteresis problems being evident in the final bonded sensor. FFPI sensors which can withstand high mechanical strains are important in many of the potential applications areas for these devices. In order to improve their mechanical strength, the sensors

were annealed using a CW CO<sub>2</sub> laser beam. This is the first report of such a technique and if more fully developed CO<sub>2</sub> laser annealing may have great potential for producing stronger fusion-spliced sensors. Fusion spliced sensors were fabricated by coating only a localised region of the core with TiO<sub>2</sub> in order to maximise glass to glass fusion of the cladding to give higher mechanical strength of the internal mirror splice. In this study with TiO<sub>2</sub>-coated fibres, it was found that fusion splice conditions for optimum splices were very different from those required for an uncoated fibre. This contrasts with the experience of Hogg et al., [1991] using aluminium coatings. A major advantage of intrinsic FFPI sensors is their small cross-sectional area which is no larger than the diameter of the fibre itself. This allows their consolidation into structures with minimal disturbance of the measurement environment. Other advantages are their high sensitivity, small sensor size and lead insensitivity since light is transmitted to the sensor and back through the same fibre.

The WLI multiplexing arrangement is economical because it uses a single fibre, a single source and detector. The advantages offered by white light interferometry are considerable since with this method absolute phase or path imbalance measurements are possible. WLI measurements are also insensitive to intensity variations, support self initialisation and capable of addressing several sensors with negligible cross-talk. One difficulty with the use of intrinsic FFPI sensors with dielectric internal mirrors is that fabrication of these sensors is a difficult process which requires particular attention to the uniformity of the deposited films. Other requirements for successful fabrication include properly cleaved end faces of the single-mode fibres and optimised fusion parameters so as to give good splices with minimal internal transmission losses. The in-fibre Bragg grating does not require a fusion splice and offers an advantage in this regard. However because fibre Bragg gratings normally have narrow bandwidth, a single FFPI based on a pair of such gratings is not suitable for WLI as the fringe pattern is too long for reliable determination of the central fringe.

A new means of making intrinsic FFPI sensors based on intracore Bragg reflectors has been demonstrated. The technique was demonstrated in temperature sensor configuration and

operated in dual and triple wavelength mode. The synthesising of low coherence reflections from multiple FFPIs at different wavelengths enables the white light interferometry technique to be applied with a significant reduction in equivalent coherence length compared to a single grating pair. These grating-based multiple FFPI sensors may be purpose-designed to optimise their performance in measuring a number of physical parameters including strain, temperature and pressure. In addition to being able to be multiplexed in the usual power splitting way used in this thesis, they also have potential for spectral multiplexing. Multiple grating-based FFPIs offer advantages of being fully intrinsic, having low loss and having superior mechanical strength compared to fusion spliced FFPIs. Although the multiple FFPIs constructed using this investigation are not optimum for low coherence sensing, they nevertheless were demonstrated to perform well as temperature sensors.

In conclusion, a serial array of reflectively-monitored FFPI sensors with internal dielectric mirrors, addressed using white light interferometry, has been demonstrated to be suitable for measuring strain in structures. These sensors possess most of the desired qualities for practical strain measurements. The inherent advantages of optical fibres coupled with the sensitivity of an intrinsic fibre Fabry-Perot sensor, make the FFPI gauge a viable alternative to the conventional resistive strain gauge. Demodulation and de-multiplexing using white light interferometry has a number of advantages over conventional coherent fringe shift or fringe counting techniques. Although mechanical scanning of the receiver interferometer requires high mechanical stability, it offers a large measurement range and is practical in a number of measurement situations.

## **9.2 Future work**

There are a number of fairly obvious improvements which can be made to the experimental system which would improve its performance. In addition, the study has opened up a number

of issues which could usefully be investigated further. These areas of investigation and further improvement include:

- (i) The efficiency of the receiver interferometer could be readily improved by the use of a suitable dielectric coating on the cleaved end of the fibre.
- (ii) When the WLI pattern is not too long, the time taken for a strain measurement could be considerably reduced by the inclusion of a PZT stretcher into the receiver interferometer. In this way the Nanomover could be used for coarse tuning followed by a rapid fine scan of the fringes using the PZT.
- (iii) Compensation for thermally induced strain could be automatically incorporated if a reference FFPI sensor was incorporated into the unused arm of the first directional coupler so that temperature could be monitored.
- (iv) There is a need for a thorough evaluation of the performance of the grating-based FFPI sensors developed in the latter stages of this present project. The use of broader or multiple sources together with suitably designed multiple FFPIs should be quite straightforward. However longer chirped gratings will have some implications for sensor design. Finally there is a need to consider carefully the effect of small differences in FFP cavity length when writing multiple sets of gratings.
- (v) Alternative multiplexing schemes which at least partially use the spectral multiplexing capability of the grating-based FFPIs should be modelled.

## **PUBLICATIONS RESULTING FROM THE RESEARCH DESCRIBED IN THIS THESIS**

Caranto, N.R.Y., Kaddu, S.C., Szajman, J., Murphy, M.M., Collins, S.F., and Booth, D.J., "An Optical Fibre-Based Thin Film Thickness Monitor", *Proc. International Conference on Physics and Technology in the 1990's*, pp. 129 - 135, Physical Society of the Philippines, Quezon City, Philippines, 1992.

Caranto, N.R.Y., Kaddu, S.C., Szajman, J., Murphy, M.M., Collins, S.F., and Booth, D.J. "An Optical Fibre Thin Film Thickness Monitor", *Meas. Sci. Technol.*, **4**, pp. 865-9, 1993.

Kaddu, S.C., Caranto, N.R.Y., Murphy, M.M., Collins, S.F., Booth, D.J., "Construction of Fibre Fabry-Perot Sensors for Temperature or Strain Measurement", *Proc. 18th Australian Conf. on Optical Fibre Technol.*, pp. 245-8, 1993.

Kaddu, S.C., Collins, S.F., and Booth, D.J., "A Large Operating Range Optical Fibre Temperature Sensor Employing Low Coherence Interferometry", *Proc. 19th Australian Conf. on Optical Fibre Technol.*, pp. 150-3, 1994.

## REFERENCES

1. Alcoz, J. J., Lee, C.E., and Taylor, H.F., "Embedded Fiber-Optic Fabry-Perot Ultra Sound Sensor", *J. IEEE Transactions on Ultrasonics, Ferroelectrics and Frequency Control*, **37**(4), pp. 302-6, 1990.
2. Akhavan, L.P., Jones, J.D.C., and Jackson, D.A., "Interferometric Strain Measurement Using Optical Fibres", *Proc. SPIE, Fibre Optic Sensors*, **586** pp. 230-7, 1985.
3. Al-Chalabi, S.A., Culshaw, B., and Davies, D.E.N., "Partially Coherent Sources in Interferometric Sensors", *Proc. 1st Int. Conf., Optical Fibre Sensors*, pp. 132-7, London, 1983.
4. Al-Raweshidy, H. S., and Uttamchandani, D., "Spread Spectrum Technique for Passive Multiplexing of Interferometric Sensors", *Proc. SPIE , Fibre Optics*, **1314**, pp. 342-7, 1990.
5. Andonovic, I., and Uttamchandani, D., *Principles of Modern Optical Systems*, Artech House, Inc., 1989.
- 5b Atkins, R.A., Gardiner, J.H., Gibler, W.N., Lee, C.E., Oakland, M.D., Spears, M.O., Swenson, V.P., Taylor, H.F., McCoy, J.J. and Beshouri, G., "Fibre-optic Pressure Sensors for Internal Combustion Engines", *Appl. Opt.*, **33** (7), pp 1315 - 20, 1994.
6. Beheim, G., Fritsch, K., Flatico, J.M., and Azar, M.T., "Silicon-Etalon Fibre-Optic Temperature Sensor, *Proc. SPIE Fibre Optic and Laser Sensors VII*, **1169**, pp 504-11, 1989.
7. Behrisch, R., and Wittmaack, K., *Sputtering by Particle Bombardment III, Characteristics of Sputtered Particles, Technical Applications*, Springer-Verlag, 1991.
8. Bennett, J.M., Pelletier, E., Albrand, G., Borgogno, J.P., Lazarides, B., Charles, K. C., Schmall, R.A., Thomas, H.A., Trudy, T.H., Karl, H.G., and

- Saxer, A., "Comparison of the Properties of Titanium Dioxide Films Prepared by Various Techniques", *Appl. Opt.*, **28**(15), pp. 3303-17, 1989.
9. Bergh, A.A., and Dean, P.J., *Light Emitting Diodes*, Oxford University Press, 1976.
  10. Berkoff, T.A., and Kersey, A.D., "Dual Wavelength Interrogation of a Fibre Interferometer Using a Broadband source and Fibre Gratings", *Proc. 8th Int. Conf. Optical Fibre Sensors*, PD8, Monterey, 1992.
  11. Bertholds, A., and Dandiliker, R., "Determination of the Individual Strain-Optic Coefficients in Single-mode Optical Fibres", *J. Lightwave Technol.* **1**(6), pp. 17-20, 1988.
  12. Bevington, P.R., and Robinson, D.K., *Data Reduction and Error Analysis for the Physical Sciences*, McGraw-Hill, 1992.
  13. Blake, J.N., Huang, S.Y., Kim, B.Y. and Shaw H.J., "Strain Effects on Highly Elliptical Core Two-Mode Fibres" *Opt. Lett.*, **12**(9), pp. 732-4, 1987.
  14. Bosselmann, Th., and Ulrich, R., "High-Accuracy Position Sensing with Fibre-Coupled White Light Interferometers", *Proc. 2nd Int. Conf. Optical Fibre Sensors*, Stuttgart, pp. 361-4, 1984.
  15. Born, M., and Wolf, E., *Principles of Optics*, Pergamon, London, 1969.
  16. Brady, G.P., Hope, S., Ribeiro, A.B.L., Webb, D.J., Reekie, L., Archambault, J.L., and Jackson, D.A., "Bragg Grating Temperature and Strain Sensors", *Proc. SPIE 10th Int. Conf. Optical Fibre Sensors*, **2362**, pp. 510-3, 1994.
  17. Brooks, J. L., Robert, H., Wentworth, R., C., Youngquist, Moshe, T., Byoung, Y. K., and Shaw, H. J., "Coherence Multiplexing of Fibre-Optic Interferometric Sensors", *IEEE J. Lightwave Technol.*, **LT-3**, pp. 1062-70, 1985.
  18. Brooks, J.L., Tur, M., Kim, B.Y., Fesler, K.A., and Shaw, H.J., "Fibre-Optic Interferometric Sensor Arrays with Freedom from Source Phase-Induced Noise", *Opt. Lett.*, **11**(7), pp. 473-5, 1986.

19. Brooks, J. L., Moslehi, B., Kim, B. Y., and Shaw, H. J. "Time-Domain Addressing of Remote Fibre-Optic Interferometric Sensor Arrays", *IEEE J. Lightwave Technol.* **LT-5**, pp. 1014-23, 1987.
20. Budiansky, B., Drucker, D.C., Kino, G.S., and Rice, J.R., "Pressure Sensitivity of a Clad Optical Fibre", *Appl. Opt.*, **18**(14), pp. 4085-8, 1979.
21. Butter, C.D., and Hocker, G.B., "Fiber Optics Strain Gauge", *Appl. Opt.* **17**(18) pp. 2867-9, 1978.
22. Caranto, N.R.Y., Kaddu, S.C., Szajman, J., Murphy, M.M., Collins, S.F., and Booth, D.J. "An Optical Fibre Thin Film Thickness Monitor", *Meas. Sci. Technol.*, **4**, pp. 865-9, 1993.
23. Charasse, M.N., Turpin, M., and Pesant, J.P., "Dynamic Pressure Sensing with a Side-Hole Birefringent Optical Fibre", *Opt. Lett.*, **16**(13), pp. 1043-5, 1991.
24. Chen, S., Meggitt, B.T., and Rogers, A.J., "Novel Electronic Scanner for Coherence Multiplexing in a Quasi-Distributed Pressure Sensor", *Electron. Lett.*, **26**(17), pp. 1367-9, 1990.
25. Chen, S., Meggitt, B.T., and Rogers, A.J., "Electronically-Scanned White Light Interferometry With Enhanced Dynamic Range", *Electron. Lett.*, **26**(20), pp. 1663-5, 1990a.
26. Chen, S., Palmer, A.W., Grattan, K.T.V., Meggitt, B.T., and Martin, S., "Study of Electronically Scanned Optical-Fibre White-Light Fizeau Interferometer", *Electron. Lett.*, **27**(12), pp. 1032-3, 1991.
27. Chen, S., Giles, I.P., and Fahadiroushan, M., "Quasi-Distributed Pressure Sensor Using Intensity Type Optical Coherence Domain Polarimetry", *Opt. Lett.*, **16**(5), pp. 342-4, 1991a.
28. Chen, S., Rogers, A. J., and Meggitt, B.T., "A large Dynamic Range Electronically Scanned White-Light Interferometer with Optical-Fibre Young's Structure", *Proc. SPIE, Fibre Optic Sensors; Engineering and Applications*, **1511**, pp. 67-77, 1991c.

29. Chen, S., Palmer, A.W., Grattan, K.T.V., and Meggitt, B.T., "Fringe Order Identification in Optical Fibre White-Light Interferometry Using Centroid Algorithm Method", *Electron. Lett.*, **28**(6), pp. 553-5, 1992.
30. Chen, S., Palmer, A. W., Grattan, K. T. V., and Meggitt, B. T., "Digital Signal-Processing Techniques for Electronically Scanned Optical-Fibre White Light Interferometry", *Appl. Opt.*, **31**, pp. 6003-10, 1992a.
31. Chen, S., Grattan, K.T.V., Meggitt, B.T., and Palmer, A.W., "Instantaneous Fringe Identification Using Dual Broadband Sources with Widely Spaced Wavelength", *Electron. Lett.*, **29**(4), pp. 334-5, 1993.
32. Chung, E.L., and Taylor, H.F., "Interferometric Fibre Optic Temperature Sensor Using a Low-Coherence Light Source", *Proc. SPIE, Fibre Optic Smart Structures and Skins III*, **1370**, pp. 356-64, 1990.
33. Corke, M., Kersey, A.D., Jackson, D.A., and Jones, J.D.C., "All-Fibre Michelson Thermometer", *Electron. Lett.* **19**(13), pp. 471-3, 1983.
34. Corke, M., Jones, J.D.C., Kersey, A.D., and Jackson, D.A., "Combined Michelson and Polarimetric Fibre Optic Interferometric Sensor" *Electron. Lett.* **21** pp.148-9, 1985.
35. Culshaw, B., and Dakin, J., *Optical Fiber Sensors : Principles and Components/Systems and Applications* , Vol.1 & 2, Artech House, Inc., 1988/1989.
36. Dakin, J. P., "Multiplexed and Distributed Optical Fibre Sensor Systems", *J.Phys .E: Sci. Instrum.*, **20** pp. 954-66, 1987.
37. Dakin, J.P., and Kahn, D.A., "A Novel Fibre-Optic Temperature Probe", *Optical and Quantum Electronics*, **9**, pp. 540-4, 1977.
38. Dally, J.W., and Riley, W.F., *Experimental Stress Analysis*, McGraw Hill, New York, 1978.
39. Dandliker, R., Zimmermann, E., and Frosio, G., "Noise Resistant Signal Processing for Electronically Scanned White-Light Interferometry", *Proc. 8th Int. Conf.Optical fibre Sensors*, Monterey, pp. 53-6, 1992.

40. Dandridge, A., Tevten, A.B., Kersey, A. D., and Yurek, A.M., "Multiplexed Interferometric Sensors Using Phase Generated Carrier Techniques", *IEEE, J. Lightwave Technol.*, **LT-5**, pp. 947-50, 1987.
41. Douglas, L., F., and Kim, E.M., "Long Optical-Fibre Fabry-Perot Interferometers", *Appl. Opt.* **20**(23), pp. 3991-2, 1981.
42. Egalon, C.O., and Rogowski, R.S., "Exact Solution for Phase shift of TE and TM Modes in an Optical Fibre due to Axial Strain", *Optical Engineering*, **32**(7), pp. 1638-43, 1993.
43. Eggeleton, B., Krug, P.A., and Poladian, L., "Chirped Bragg Grating Filters for Dispersion Compansation and Pulse Compression", *Proc. 18th Australian Conf. on Optical Fibre Technol.*, pp. 63-6, 1993.
44. Eickhoff, W., "Temperature Sensing by Mode-Mode Interference in Birefrigent Optical Fibres", *Opt. Lett.*, **6**(4), pp. 204-6, 1981.
45. Escobar, P., Gusmeroli, V., and Martinelli, M., "Fibre-Optic Interferometric Sensors for Concrete Structures", *Proc. SPIE*, **1777**, pp. 215-8, 1992.
46. Farahi, F., Webb, D.J., Jones, J.D.C., and Jackson, D.A., "Simultaneous Measurement of Temperature and Strain Using Fibre Optic Interferometric Sensors", *Proc. SPIE Fibre Optics*, **1314**, pp. 270-7, 1990.
47. Faramarz, F., Webb, D., Jones, J.D.C., Jackson, D.A., "Simultaneous Measurement of Temperature and Strain: Cross-Sensitivity Considerations", *IEEE J. Lightwave Technol.*, **8**(2), pp. 138-42, 1990.
48. Farries, M.C., Sugden, K., Reid, D.C.J., Bennion, I., Molony, A., and Goodwin, M.J., "Very Broad Reflection Bandwidth (44 nm) Chirped Fibre Gratings and Narrow Bandpass Filters Produced by the use of an Amplitude Mask", *Electron. Lett.*, **30**(11), pp.891-2, 1994.
49. Fields, J.N., and Cole, J.H., "Fibre Microbend Acoustic Sensor", *Appl. Opt.*, **19**, pp. 3265-7, 1980.

50. Fuhr, P.L., Huston, D.R., Spillman, W.B., "Multiplexed Fibre Optic Pressure Vibration Sensors for Hydroelectric Dam", *Proc. SPIE, Fibre Optic Smart Structures and Skins V*, **1798**, pp. 247-52, 1992.
51. Furstenau, N., Schmidt, W., and Goetting, H.C., "Simultaneous Interferometric and Polarimetric Strain Measurements on Composites using a Fibre-Optic Strain Gauge", *Appl. Opt.*, **31**(16), pp. 2987-93, 1992.
52. Gale, M.T., Lehmann, H.W., Heeb, E., and Frick, K., "A Simple Optical Thin Film Deposition Monitor Using LEDs and Fibre Optics", *J. Vac. Sci. Technol.*, **20**(1), pp. 16-20, 1982.
53. Gerges, A.S., Farahi, F., Newson, T.P., Jones, J.D.C., and Jackson, D.A., "Interferometric Fibre Optic Sensor Using a Short Coherence Length Source", *Electron. Lett.* **23**(21), pp. 1110-1, 1987.
54. Gerges, A.S., Newson, T.P., and Jackson D.A., "Coherence Tuned Fibre Optic Sensing System, with Self-Initialisation Based on a Multimode Laser Diode", *Appl. Opt.*, **29**(30), pp. 4473-80, 1990.
55. Giallorenzi, T.G., Bucaro, J.A., Dandridge, A., Sigel, G.H., Cole, J.H., Rashleigh, S.C., and Pries, R. G., "Optical Fibre Sensor Technology", *IEEE, J. of Quantum Electronics*, **QE-18**(4) pp. 626-65, 1982.
56. Giovannini, H.R., Konan, K.D., Huard, S.J., Gonthier, F., Lacroix, S., and Bures, J., "Modal Interference in All-Fibre Sensor Measured by Coherence Multiplexing Technique", *Electron. Lett.*, **29**(1), pp. 29-31, 1993.
57. Giles, I.P, Uttam, D., Culshaw, B., Davies, D.E.N., "Coherent Optical Fibre Sensors with Modulated Laser Sources", *Electron. Lett.*, **19**(1), pp. 14-5, 1983.
58. Gloge., D., "LED Design for Fibre Systems", *Electron. Lett.*, **13**(4), pp. 399-400, 1977.
58. Gunderson, L.C., "Fibre Optic Sensor Applications Using Fabry-Perot Interferometry", *Proc. SPIE 1267, Fibre Optic Sensors IV*, pp. 194 - 204, 1990.

60. Handerek, V.A., and Rogers, A.J., "Sensor System Architecture for Spatially-Resolved Dynamic Strain Measurement Using Optical Fibres", *Proc. SPIE, 1st Int. Conf. on Smart Structures and Materials*, Glasgow, pp. 31-4, 1992.
61. Hatakeyama, I., Tachikura, M., and Tsuchiya, H., "Mechanical Strength of Fusion-Spliced Optical Fibres", *Electron. Lett.*, **14**(19), pp. 613-4, 1978.
62. Hetenyi, M., *Handbook of Experimental Stress Analysis*, Wiley & Sons, New York, 1950.
63. Hill, K.O., Fujii, Y., Johnson, D.C., and Kawasaki, B.S., "Photosensitivity in Optical Fibre Waveguides: Application to Reflection Filter Fabrication", *Appl. Phys. Lett.* **32**(10), pp. 647-9, 1978.
64. Hill, K.O., Malo, B., Bilodeau, F., Johnson, D.C., and Albert, J., "Bragg Grating Fabricated in Monomode Photosensitive Optical Fibre by UV Exposure Through a Phase Mask", *Appl. Phys. Lett.*, **62**, pp. 1035-7, 1993.
65. Hocker, G.B., "Fiber-Optic Sensing of Pressure and Temperature", *Appl. Opt.*, **18**(9), pp. 1445-8, 1979.
66. Hogg, W.D., Turner, R., and Measures, R.M., "Dual Wavelength All-Localised Polarimetric Strain Sensor", *Proc. SPIE, Fibre Optic Structures and Skins 11*, **1170**, pp. 542-50, 1989.
67. Hogg, D., Janzen, D., Valis, T., and Measures, R. M., "Development of Fibre Fabry-Perot Strain Gauge", *Proc. SPIE, Fibre Optic Smart Structure and Skins IV*, **1588**, pp. 300-7, 1991.
68. Inci M.N., Kidd, S.R., Barton, J.S., and Jones, J.D.C., "Fabrication of Single-Mode Fibre Optic Fabry-Perot Interferometers Using Fusion Spliced Titanium Dioxide Optical Coatings", *Meas. Sci. Technol.*, **3**, pp. 678-84, 1992.
69. Jackson, D. A., "Monomode Optical Fibre Interferometers for Precision Measurement", *J. Phys E: Sci. Instrum.*, **18** , pp. 981-1001, 1985.
70. Jackson, D.A., "Recent progress in Monomode Fibre-Optic Sensors", *Meas. Sci. Technol.*, **5**, pp. 621-38, 1994.

71. Jenkins, F.A., and White, H.E., *Fundamentals of Optics*, McGraw-Hill, 1976.
72. Kaddu, S.C., Caranto, N.R.Y., Murphy, M.M., Collins, S.F., Booth, D.J., "Construction of Fibre Fabry-Perot Sensors for Temperature or Strain Measurement", *Proc. 18th Australian Conf. on Optical Fibre Technol.*, pp. 245-8, 1993.
73. Kaddu, S.C., Collins, S.F., and Booth, D.J., "A Large Operating Range Optical Fibre Temperature Sensor Employing Low Coherence Interferometry", *Proc. 19th Australian Conf. on Optical Fibre Technol.*, pp. 150-3, 1994.
74. Kashyap, R., Armitage, J.R., Wyatt, R., Davey, S.T., and Williams, D.L., "All-Fibre Narrowband Reflection Gratings at 1500 nm", *Electron. Lett.*, **26**(11), pp. 730-1, 1990.
75. Kersey, A.D., and Dandridge, A., "Phase-Noise Reduction in Coherence-Multiplexed Interferometric Fibre Sensors", *Electron. Lett.*, **22**(11), pp. 616-7, 1986.
76. Kersey, A. D., and Dandridge, A., "Distributed and Multiplexed Fibre-Optic Sensor Systems", *J. of the Institution of Electronic and Radio Engineers*, **58**, pp. s99-s111, 1988.
77. Kersey, A. D., and Dandridge, A., "Fibre-Optic Multisensor Networks", *Proc. SPIE, Fibre Optic and Laser Sensors VI*, **985**, pp. 90-104, 1988a.
78. Kersey, A. D., "Analysis of Intrinsic Crosstalk in Tapped-Serial and Fabry-Perot Interferometric Fibre Sensor Arrays", *Proc. SPIE Fibre Optic and Laser Sensors VI*, **985**, pp. 113-124, 1988b.
79. Kersey, A.D., Dorsey, K.L., Dandridge, A., "Demonstration of An Eight-Element Time Division Multiplexed Array", *Electron. Lett.*, **24**(11), pp. 689-91, 1988c.
80. Kersey, A.D., Dorsey, K.L., Dandridge, A., "Characterisation of an Eight-Element Time Division Multiplexed Interferometric Fibre Sensor Array", *Proc. SPIE, Fibre Optic and Laser Sensors VI*, **985**, pp. 105-12, 1988d.

81. Kersey, A.D., Davis, M.A., and Marrone, M.J., "Differential Polarimetric Fibre-Optic Sensor with Dual Wavelength Operation", *App. Opt.* **28**(2), pp. 204-6, 1989.
82. Kersey, A.D., and Dandridge, A., "Multiplexed Mach-Zehnder Ladder Array with Ten Sensor Elements", *Electron. Lett.*, **25**(19), pp. 1298-9, 1989.
83. Kersey, A.D., "Demonstration of a Hybrid Time/Wavelength Division Multiplexed Interferometric Fibre Sensor Array", *Electron. Lett.*, **27**(7), pp. 554-5, 1991.
84. Kersey, A.D., and Berkoff, T.A., "Fibre-Optic Bragg Grating Differential-Temperature Sensor", *IEEE Photonics Technol. Lett.*, **4**(10), pp.1183-5, 1992.
85. Kersey, A.D., Berkoff, T.A., and Morey, W.W., "High-Resolution Fibre-Grating Based Strain Sensor with Interferometric Wavelength-Shift detection", *Electron. Lett.* **28**(3), pp. 236-8, 1992a.
86. Kidd, S.R., Sinha, P.G., Barton, J.S., and Jones, J.D., "Interferometric Fibre Sensors for Measurement of Surface Heat Transfer Rates on Turbine Blades", *Opt. Laser Eng.*, **14**, pp. 201-21, 1992.
87. Kist, R., Ramakrishnan, S., and Wölfescneider, H., "The Fibre Fabry-Perot and its Applications as a Fibre-Optic Sensor Element", *Proc. SPIE, Fibre Optic Sensors*, **586**, pp. 126-33, 1985.
88. Koch, A., and Ulrich, R., "Displacement Sensor with Electronically Scanned White-Light Interferometer", *Proc. SPIE, Fibre Optic Sensors*, **1267**, pp. 126-33, 1990.
89. Koch, A., and Ulrich, R., "Fibre-Optic Displacement Sensor with 0.02  $\mu\text{m}$  Resolution by White-Light Interferometry", *Sensors and Actuators, A*, **25-27**, pp. 201-7, 1991.
90. Krause, J.T., Kurkjian, C.R., and Paek, U.C., "Tensile Strength > 4 GPa for Lightguide Fusion Splices", *Electron. Lett.*, **17**(21), pp. 812-3, 1981.
91. Krause, J.T., Kurkjian, C.R., and Paek, U.C., "Strength of Fusion Splices for Fibre Lightguides", *Electron. Lett.*, **17**(6), pp. 232-3, 1981a.

92. Lagakos, N., Litovitz, T., Macedo, P., Mohr, R., and Meister, R., "Multimode Optical Fibre Displacement Sensor", *Appl. Opt.*, **20**, pp. 167-8, 1981.
93. Lagakos, N., Bucaro, J.A., and Jarzynski, J., "Temperature-Induced Optical Phase Shifts in Fibres", *Appl. Opt.*, **20**(13), pp. 2305-8, 1981a.
94. Lam, D.K.W., and Garside, B.K., "Characterisation of Single-mode Optical Fibre Filters", *Appl. Opt.*, **20**(3), pp. 440-5, 1981.
95. La Rochelle, S., Mizrahi, V.M., Simmons, K.D., and Stegeman, G.I., "Photosensitive Optical Fibres Used as Vibration Sensors", *Opt. Lett.*, **15**(7), pp. 399-401, 1990.
96. Lee, C.E., and Taylor, H.F., "Interferometric Optical Fibre Sensors using Internal Mirrors", *Electron. Lett.*, **24**, pp. 193-4, 1988.
97. Lee, C.E., Atkins, R.A., and Taylor, H.F., "Performance of a Fibre-Optic Temperature Sensor from - 200 to 1050°C", *Opt. Lett.*, **13**(11), pp. 1038-40, 1988a.
98. Lee, C.E., Taylor, H.F., Markus, A.M., and Udd, E., "Optical Fibre Fabry-Perot Embedded Sensor", *Opt. Lett.*, **14**(21), pp. 1225-7, 1989.
99. Lefevre, H.C., "White Light Interferometry in Optical Fibre Sensors", *Proc. 7th. Int. Conf., Optical Fibre Sensors*, pp. 345-51, Sydney, 1990.
100. Leilabady, P.A., and Corke, M., "All-Fibre-Optic Remote Sensing of Temperature Employing Interferometric Techniques", *Opt. Lett.*, **12**(10), pp. 772-4, 1987.
101. Lesko, J.J., Carman, G.P., Fogg, B.R., Miller, W.V., Vengsarkar, A.M., Reifsnider, K.L., and Claus, R.O., "Embedded Fabry-Perot Fibre Optic Strain Sensors in the Macromodel Composites", *Optical Engineering*, **31**(1), pp. 13-22, 1992.
102. Lin, C., Kobrinski, H., Frenkel, A., Brackett, C.A., "Wavelength-Tunable 10 Optical Channel Transmission Experiment at 2 Gbit/s and 600 Mbit/s for Broadband Subscriber Distribution", *Electron. Lett.*, **24**(19), pp. 1215-6, 1988.

103. Lu, Z., and Blaha, F.A., "Optic Strain and Impact Sensor System for Composite Materials", *Proc. SPIE*, **1170**, pp. 239-48, 1989.
104. Mardi, C. H., Chiu, B., Myers, D.J., and Chang, T., "Evaluation of Special Communication Grade Fibres in Interferometric and Microbend Sensors for Measurements with Ambient Temperature Fluctuations", *Proc. SPIE, Fibre Optic and Laser Sensors X*, **1795**, pp. 227-35, 1992.
105. Martin, S.O., Meggitt, B.T., and Chen, S., "A White Light Wedge Interferometer and an Optical Fibre Pressure Sensor", *Proc. 16th Australian Conf. on Optical Fibre Technol.*, pp. 214-7, 1991.
106. Mason, B., Valis, T., and Hogg, D., "Commercialisation of Fibre-Optic Strain Gauge Systems", *Proc. SPIE, Fibre Optic and Laser Sensors X*, **1795**, pp. 215-21, 1992.
107. McGarrity, C., and Jackson, D.A., "4 Sensor Time Division Multiplexed Michelson Topology for Low Frequency Measurands", *Proc. SPIE*, **1797**, pp. 218-27, 1992.
108. Measurement Group, Tech. Note TN-504-1, *Strain Gage Thermal Output and Gage Factor Variation with Temperature*, Measurement Group Inc. USA, 1993.
109. Measures, R.M., Hogg, D., Turner, R.D., Valis, T., and Giliberto, M.J., "Structurally Integrated Fibre Optic Strain Rosette", *Proc. SPIE, Fibre Optic Smart Structure and Skins 11*, **986**, pp.32-42, 1988.
110. Measures, R. M. , "Fibre Optics in Composite Materials....Materials with Nerves of Glass" *Proc. SPIE, Fibre Optic Sensors IV*, **1267**, pp 241- 55, 1990.
111. Measures, R.M., "Fibre Optic Sensor Advances Pertinent to Smart Structure Development", *Proc. SPIE, Fibre Optics*, **1314**, pp. 255-60, 1990a.
112. Measures, R.M., "Advances Toward Fibre Optic Based Smart Structures", *Optical Eng.*, **31**(1), pp. 34-47, 1992.

- 112b Meggit, B.T., Boyle, W.J.O., Grattan, K.T.V., Palmer, A.W. and Ning, Y.N., "Fibre Optic Anemometry Using an Optical Delay cavity Technique", *Proc. SPIE*, **1314**, Fibre Optics, pp 321 - 6, 1990.
113. Melle, M.S., Liu, K., and Measures, R.M., "Practical Fibre Optic Bragg Grating Strain Gauge System" *Appl. Opt.*, **32**(19), pp.3601-9, 1993.
114. Meltz, G., Morey, W.W., and Glenn, W.H., "Formation of Bragg Gratings in Optical Fibres by a Transverse Holographic Method", *Opt. Lett.* **14**, pp. 823-5, 1989.
115. Mitchell, G.L., "A Review of Fabry-Perot Interferometric Sensors", *Springer Proc. in Physics Optical Fibre Sensors*, **44**, pp. 450-7, 1989.
116. Miyajima, Y., Ohnishi, M., and Kawata, O., "Strain Required in Proof Test for High-Strength Fibre Splices", *J. IEEE Lightwave Technol.*, **LT-3**(2), pp. 332-7, 1985.
117. Mizrahi, V., and Sipe, J.E., "Optical Properties of Photosensitive Fibre Phase Gratings", *J. IEEE Lightwave Technol.*, **11**(10), pp. 1513-17, 1993.
118. Morey, W.W., Meltz, G., and Glenn, W.H., "Bragg-Grating Temperature and Strain Sensors", *Springer Proc. in Physics Optical Fibre Sensors*, **44**, pp. 526-31, 1989.
119. Morey, W.W., Meltz, G., Dunphy, J.R., and D'Amato, F.X, "In-fibre Bragg Gratings", *Proc. 17 th Australian Conf. on Optical Fibre Technol.*, pp. 162-9, 1992.
120. Morey, W.W., Ball, G.A., and Meltz, G., "Photoinduced Bragg Gratings in Optical Fibres", *Optics and Photonics News*", pp. 8-14, 1994.
121. Murphy, K.A., Gunther, M.F., Vengsakkar, A.M., and Claus, R.O., "Quadrature Phase Shifted, Extrinsic Fabry-Perot Optical Fibre Sensors" *Opt. Lett.* **16**(4), pp. 273-5, 1991.
122. Murphy, K. A., Gunther, M.F., Vengsarkar, A.M., and Claus, R.O., "Fabry-Perot Fibre-Optic Sensors in Full-Scale Fatigue Testing on an F-15 Aircraft", *Appl. Opt.*, **31**(4), pp. 431-3, 1992.

123. Nellen, M.Ph., Pierhofer, H., Bronnimann, R., and Sennhauser, U., "Absolute Strain Measurements with Multiplexed Low Coherence Demodulated Fibre Fabry-Perot Sensors", *Proc. SPIE 10th Int. Conf. Optical Fibre Sensors*, **2562** pp. 518-21, 1994
124. Neubert, H.K.P., *Strain Gauges Kinds and Uses*, Macmillan, 1967.
125. Nguyen, T.T., and Birch, L.N., "Fibre Optic Laser Doppler Anemometer", *Appl. Phys. Lett.*, **45**, pp. 1163, 1984.
126. Nichelatti, E., and Salvetti, G., "Spatial and Spectral Response of a Fabry-Perot Interferometer by a Gaussian Beam", *Appl. Opt.*, **34**(22), pp. 4703-12, 1995.
- 126b Ning, Y.N., Grattan, K.T.V., Palmer, A.W. and Meggit, B.T., "Characteristics of a Multimode Laser Diode Source in Several Types of Dual-Interferometer Configurations", *Proc. SPIE 1367*, Fibre Optics and Laser Sensors VIII, pp. 347 - 56, 1990.
127. Norton, D.A., "System for Absolute Measurements by Interferometric Sensors", *Proc. SPIE, Fibre Optic Laser Sensors X*, **1795**, pp. 371-6, 1992.
128. Ohba, R., Kakuma, S., Yamane, H., and Uehira, I., "Static Strain Monitoring OFS Using a FM Laser Diode", *Springer Proc. in Physics .Optical Fibre Sensors*, **44**, pp. 400-7, 1989.
129. Ohtsuka, Y., and Tanaka, S., "Tension-Induced Modal Birefringence in a Single-Fibre Interferometric Strain Gauge", *Fibre and Integrated Optics*, **9** pp. 245-53, 1990.
130. Palais, J.C., *Fibre Optic Communications*, Prentice Hall, 1988.
131. Picherit, F., and Mineau, J.L., "Interferometric-Polarimetric Force and Temperature Sensor Using High and Low Birefringence Fibres with a Short Coherence Source", *Optics Communications*, pp. 295-9, 1990.
132. Pitt, C.W., Kirk, I.H., and Stevens, R.J., "Automatic Monitoring of Deposition Conditions During RF Sputtering of Dielectric Materials", *Vacuum*, **25**(6), pp. 265-71, 1975.

133. Poladian, L., Sipe, J.E., and Sterke, M.D., "Behaviour of Chirped and Tapered Gratings", *Proc. 17th Australian Conf. on Optical Fibre Technol.*, pp. 170-3, 1992.
134. Pulker, H.K., Paesold, G., and Ritter, E., "Refractive Indices of TiO<sub>2</sub> Films Produced by Reactive Evaporation of Various Titanium-Oxygen Phases", *Appl. Opt.*, **15**(12), pp. 2986-91, 1976.
135. Rao, Y.J., Ning, Y.N., and Jackson, D.A., "Compounded Source for White-Light Interferometric systems", *Proc. 9th Int. Conf. Optical Fibre Sensors*, pp. 275-8, 1993.
136. Rao, Y.J., and Jackson, D.A., "Long-Distance Fibre-Optic White Light Displacement Sensing Systems Using a Source-Synthesising Technique", *Electron. Lett.*, **31**(4), pp. 310-12, 1995.
137. Ribeiro, A.B.L., Liu, T.Y., Rao, Y.J., and Jackson, D.A., "Simple Multiplexing-Schemes for Sensor Networks Exploiting Low Coherence Interferometry", *Proc. 9th Int. Conf. Optical Fibre Sensors*, pp. 63-6, 1993.
138. Rogers, A.J., "Distributed Optical-Fibre Sensors for the Measurement of Pressure, Strain and Temperature", *J. of the Institution of Electronic and Radio Engineers*, **58**(5) (Supplement), pp. s113-s122, 1988.
139. Rowe, J.W., Rausch, E.O., and Dean, P.D., "Embedded Optical Fibre Strain Sensor for Composite Structural Application" *Proc. SPIE, Fibre Optics and Laser Sensors IV*, **718**, pp. 266-73, 1986.
140. Russell, P.S.J., Archambault, J, and Reekie, L., "Fibre Gratings", *Physics World*, pp.42-6, 1993.
141. Sakai, I., "Multiplexing of Optical Fibre Sensors Using a Frequency-Modulated Source and Gated Output", *IEEE J. Lightwave Technol.*, **LT-5**, pp. 932-5 1987.
142. Santos, J.L., and Jackson, D.A., "Coherence Sensing of Time-Addressed Optical-Fibre Sensors Illuminated by a Multimode Laser Diode", *Appl. Opt.*, **30**(34), pp. 5068-76, 1991.

143. Santos, J.L., and Leite, A.P., "Multiplexing of Polarimetric Sensors Addressed in Coherence", *Proc. 9th Int. Conf. Optical Fibre Sensors*, Firenze, pp. 59-62, 1993.
144. Senior, J. M., *Optical Fibre Communications Principles and Practice* (Prentice-Hall), 1992.
145. Severin, P.J., "In-Situ Film Thickness Monitoring in CVD and Other Film Deposition Processes", *Proc. SPIE, In-process Measurements and Industrial Methods*, **1266**, pp. 130-6, 1990.
146. Severin, P.J., and Severijns, A.P., "In Situ Film Thickness Monitoring in CVD Processes", *J. Electrochem. Soc.*, **137**(4), pp. 1306-9, 1990.
147. Sirkis, J., "Interferometric Optical Fibre Strain Sensor Under Biaxial Loading", *OSA Technical Digest Series. Proc. 6th Int. Conf. Optical Fibre Sensors*, pp. 203-7, 1988.
148. Sorin, W.V., "Low Coherence Reflectometry for High Accuracy Sensing", *Proc. 9th Int. Conf., Optical Fibre Sensors*, pp. 243-5, Firenze, 1993.
149. Stone, J., "Optical-Fibre Fabry-Perot Interferometer with Finesse of 300", *Electron. Lett.*, **21**(11), pp 504-5, 1985.
150. Stone, J., and Stulz, L.W., "High-Performance Fibre Fabry-Perot Filters", *Electron. Lett.*, **27**(24), pp. 2239-40, 1991.
151. Stuart, R.V., *Vacuum Technology, Thin Films*, Academic Press, 1983.
152. Swanepoel, R., "Determination of the Thickness and Optical Constants of Amorphous Silicon", *J. Phys. E: Sci. Instrum.*, **16**, pp. 1214-22, 1983.
153. Tachikura, M., and Haibara, T., "Devitrification Effect on Optical-Fibre Reduction by Fusion Splicing", *IEEE J. Lightwave Technol.* **LT-3**(3) pp. 662-8, 1985.
154. Tay, A., Wilson, D.A., and Wood, L., "Strain Analysis of Optical Fibres Embedded in Composite Materials Using Finite Element Modelling", *Proc. SPIE, Fibre Optic Smart Structures and Skins*, **1170**, pp. 521-33, 1989.

155. Thomas, N.L., "Optical Thin Film Monitoring Using Optical Fibres", *Proc. SPIE , Optical Thin Films II: New Developments*, **678**, pp. 123-9, 1986.
156. Trouchet, D., Desforges, F.X., Graindorge, P., and Lefevre, H.C., "Remote Fibre Optic Measurement of Air Index with White Light Interferometry", *Proc. 8th Int. Conf., Optical Fibre Sensors*, pp. 57-60, 1992.
157. Udd, E., "Fibre Sensors for Smart Structures", *Springer Proc. in Physics, Optical Fibre Sensors*, **44**, pp. 392-9, 1989.
158. Urquhart, P., "Review of Rare Earth Doped Fibre Lasers and Amplifiers", *IEE Proc. J.* **135**(6), pp. 385-407, 1988.
159. Uttam, D., Culshaw, B., Ward, J.D., and Carter, D., "Interferometric Optical Fibre Strain Measurement", *J. Physics E: Sci. Instrum. :* **18**, pp. 290-3, 1985.
160. Valis, T., Hogg, D., and Measures, R.M., "Composite Material Embedded Fibre Optic Fabry-perot Strain Rosette" *Proc. SPIE Fibre Optic Smart Structures and Skins 111*, **1370**, pp. 154-61, 1990.
161. Valis, T., Hogg, W.D., and Measures, R.M., "Optic Fabry-Perot Strain Gauge" *IEEE Photonics Techn. Lett.* **2** pp. 227-8, 1990b.
162. Valis, T., Tapanes, E., Liu, K., and Measures, R.M., "Passive-Quadrature Demodulated Localised-Michelson Fiber-Optic Strain Sensor Embedded in Composite Materials", *IEEE J. Lightwave Technol.*, **9**(4), pp. 535-44, 1991.
163. Varnham, M.P., Barlow, A.J., Payne, D.N., and Okamoto, K., "Polarimetric Strain Gauges Using High Birefringence Fibre", *Electron. Lett.*, **19**(17), pp. 699-700, 1983.
164. Vaughan, J. M., *The Fabry-Perot Interferometer, History, Theory, Practice and Applications*, IOP Publishing LTD, 1989.
165. Verdiel, J.M., Koch, T.L., Tennant, D.M., Freder, K., Gnall, R.P., Young, M.G., Miller, B.I., Koren, U., Newkirk, M.A., and Tell, B., "8-Wavelength DBR Laser Array Fabricated with a Single Bragg Grating Printing Technique", *IEEE Photonics Technol. Lett.*, **5**(6), pp. 619-21, 1993.

166. Wang, D.N., Ning, Y.N., Grattan, K.T.V., Palmer, A.W., and Weir, K., "Characteristics of Synthesized Light Sources for White-Light Interferometric Systems", *Opt. Lett.* **18**(22), pp.1884-6, 1993a.
167. Wang, D.N., Ning, Y.N., Grattan, K.T.V., Palmer, A.W., and Weir, K., "Three-Wavelength combination for White-Light Interferometry", *IEEE Photonics Technol. Lett.*, **5**(1), pp.1350-2, 1993b.
168. Wang, D.N., Ning, Y.N., Grattan, K.T.V., Palmer, A.W., and Weir, K., "The Optimised Wavelength Combinations of Two Broadband Sources for White Light Interferometry", *J. Lightwave Technol.*, **12**(5), pp. 908-15, 1994.
169. Wang, A., Wang, G.Z., Murphy, K.A., and Claus, R.O., "Fibre-Optic Temperature Sensors Based on Differential Spectral Transmittance/Reflectivity and Multiplexed Sensing Systems", *Appl. Opt.*, **34**(13), pp. 2295-300, 1995.
170. Wang, D.N., Ning, Y.N., Palmer, A.W., Grattan, K.T.V., and Weir, K., "An Alternative to White Light Interferometric Sensing", *J. Lightwave Technol.*, **13**(5), pp. 961-6, 1995a.
171. Weast, R.C., Tuve, G.L., Selby, S.M., and Sunshine, I., *Handbook of Chemistry and Physics*, 51st edn., Chemical Rubber Co., 1970.
172. William, H.P., Flannery, B.P., Teukolsky, S.A., and Vettering, W.T., *Numerical Recipes : The Art of Scientific Computing*, Cambridge University Press, pp. 454-546, 1986.
173. Woolsey, G.A., and Lamb, D.W., "Absorption of Polarised 10.6  $\mu\text{m}$  CO<sub>2</sub> Laser Radiation by Fused Silica Optical Fibres", *Proc. SPIE , Fibre Optic and Laser Sensors X*, **1795**, pp. 247-55, 1992.
174. Wosinski, L., Breidue, M., Stubbe, R., Sahlgren, B., and Jean-Pierre, B.B., "Experimental System Considerations for Distributed Sensing with Grating Fabry-Perot Interferometers", *Proc. SPIE 10th Int. Conf. Optical Fibre Sensors*, pp. 146-9, 1994.
175. Xie, W.X., Niay, P., Bernage, P., Douay, M., Bayon, J.F., Georges, T., Monerie, M., and Poumellec, B., "Experimental Evidence of two Types of

- Photorefractive Effects Occuring During Photoinscriptions of Bragg Gratings within Germanosilicate Fibres”, *Optics Communications*, pp. 185-195, 1993.
176. Xu, M.G., Johnson, M., Faradiroushan, M., Dakin, J.P., “Thermally-Scanned, In-Line Fibre Polarimetric Interferometer for White Light Intereferometry”, *Proc. 9th. Int.Conf.Optical Fibre Sensors*, pp. 267-70, 1993.
177. Xu, M.G., Reekie, Y.T., Chow, Y.T., and Dakin, J.P., “Optical in-Fibre Grating High Pressure Sensor”, *Electron. Lett.*, **29**(4), pp. 398-9, 1993a.
178. Yariv, A., “Coupled-Mode Theory for Guided-Wave Optics”, *IEEE J. Quantum Electronics*, **QE-9** (9), pp. 919-33, 1973.
179. Yoshino, T., Kurosawa, K., Itoh, K., and Ose, T., “Fibre-Optic Fabry-Perot Interferometer and its Sensor Applications”, *IEEE J. Quantum Electronics*, **QE-18**(10), pp. 1624-33, 1982.
180. Zoller, A., Boos, M., Herrmann, R., Klug, W., and Lehnert, W., “Photometer Monitors Film Thickness During Optical Coating”, *Laser Focus World*, pp. 149-52, 1990.

## **SYMBOLS AND ACRONYMS**

$\alpha$	= Coefficient of thermal expansion
$B_s$	= Bonded sensor temperature sensitivity
$\beta$	= Propagation constant of guided mode
$\Delta\beta$	= wave vector detuning from Bragg wavelength
$\beta_o$	= propagation constant of mode in the optical fibre
$D$	= Fibre diameter
$d$	= Diameter of rod
$E$	= Electric field
FFP	= Fibre Fabry-Perot
FFPI	= Fibre Fabry-Perot interferometer
$E_e$	= Youngs modulus
$F_e$	= Effective finesse
$F$	= Finesse
$F$	= Free sensor temperature sensitivity
IFBG	= In-fibre Bragg grating
$\Delta n$	= Refractive index modulation
$n_1$	= Refractive index of core
$n_2$	= Refractive index of cladding
$n_{\text{eff}}$	= Effective refractive index
$n_{\text{cav}}$	= Refractive index of laser cavity
$z$	= Distance along the fibre
$l$	= FFP cavity length
$L_g$	= Grating length
$\lambda$	= wavelength in vacuum
$\kappa_c$	= Amplitude coupling coefficient
$\eta$	= Fraction of fundamental mode in fibre
$S^2$	= $\kappa_c^2 - \Delta\beta^2$

$\lambda_B$	= Bragg wavelength
$R_B$	= Reflectivity at Bragg wavelength
$P$	= Environmental parameter
$p_{ij}$	= Strain optic coefficients
$\nu$	= Poisons' ratio
$\xi$	= Thermo optic coefficient
$\epsilon$	= Axial strain
$\Delta T$	= Temperature change
$l_w$	= Length of wire
$G1, G2$	= Gratings
$I_{out}$	= Normalised output intensity
$m$	= Mode number
$x_0$	= Centroid of Gaussian envelope
$x$	= Receiver path difference
$I_0$	= Incident intensity
$I_R$	= Reflected intensity
$A(\phi)$	= Airy shape function
$\Omega_f$	= Free spectral mng
$V$	= Normalised frequency
$G$	= Bonded FFP sensor strain sensitivity.
$\mu\epsilon$	= Microstrain
$\Delta\lambda$	= linewidth of the source
$\Delta f$	= Laser cavity mode spacing
$\Delta l$	= Interferometer path imbalance
$P_{out}$	= Output optical power
$P_s$	= Optical power corresponding to spontaneous emission
$V$	= Visibility
$V_s$	= Visibility function corresponding to spontaneous emission
$m$	= Number of cavity modes

$P_{av}$	= Average optical power (spontaneous and stimulated)
$P_{osc}$	= Optical power associated with the interference term
$l_{cm}$	= Coherence length associated with modal linewidth
$\gamma(0)$	= Degree of coherence
$p$	= Integer
$\chi^2$	= Chi-squared
$N_f$	= Degrees of freedom
$K_j$	= Variable parameters for the function (model)
$f_i$	= Expected measurement value of model
$n$	= Set of data points
$y_i$	= Measured data points
$x_i$	= Position corresponding to $y_i$
$\Lambda$	= Period of the fringes
$Dx$	= Width of Gaussian envelope
$x_o$	= Centre of central fringe
$P_{norm}$	= Normalised output power of WLI interference pattern
$N$	= Number of FFP sensors
$l_c$	= Coherence length of source
$l_n$	= Path imbalance in each interferometer
$l_o$	= Difference in path imbalance between adjacent sensors
$E_o$	= Incident electric field
$r_a$	= Electric field reflection coefficient at mirror A
$t_a$	= Amplitude transmission coefficient
$t_b$	= Transmission amplitude coefficient for mirror B
$r_b$	= Reflection amplitude coefficient for mirror B
$k$	= Amplitude coupling coefficient
$\tau$	= Propagation time delay in sensing and receiving interferometer
$R$	= Intensity reflection coefficient
$T$	= Intensity transmission coefficient

- W =  $(1-R)^2 + R^2(1-R)^2$
- Q =  $2R(1-R)^2$
- U =  $R + R(1-R)^2$
- Z =  $2R(1-R)$
- $I_{ac}$  = a.c signal intensity
- $l_{av}$  = Average wavelength
- $l_{sy}$  = Modulation (sythetic) wavelength
- $L_o$  = Original length of rod
- $\Delta L$  = Change in length
- $\sigma$  = Stress
- j = Order number
- $\rho$  = Volume density
- K = Resisitivity
- LED = Light emitting diode
- SLD = Superluminescent diode